Gas adsorption and separation in porous metal–organic framework

A thesis submitted to the University of

Manchester for the degree of Doctor of

Philosophy in Faculty of Science and Engineering

2023

Lixia Guo

School of Natural Sciences, Department of Chemistry

[Blank page]

List of Contents

List of Abbreviations

CO_2	Carbon Dioxide
H_2	Hydrogen
CH_4	Methane
NH_3	Ammonia
C_2H_2	Acetylene
C_2H_4	Ethylene
C_2H_6	Ethane
C_3H_4	Propyne
C_3H_6	Propylene
C_3H_8	Propane
SO_2	Sulfur Dioxide
H_2SO_4	Sulfuric Acid
N_2	Nitrogen
MOF	Metal–Organic Frameworks
OMS	Open Metal Sites
–OH	Hydroxyl group
–COOH	Carboxyl group
$–NH_2$	Amino group
sPXRD	Synchrotron Powder X-ray Diffraction
NPD	Neutron Powder Diffraction
SRIR	Synchrotron Infrared Micro-Spectroscopy
INS	Inelastic Neutron Scattering
BET	Brunauer–Emmett–Teller
UiO	University of Oslo

MFM	Manchester Framework Material
NOTT	Nottingham University
D	Deuterium
Q_{st}	Isosteric Enthalpy
DRIFTS	Diffuse Reflectance Infrared Fourier Transform Spectroscopy
BTDD	Bis(1*H*-1,2,3-Triazolo[4,5-b],[4′,5′*i*])Dibenzo[1,4]Dioxin
BBTA	1*H*,5*H*-Benzo(1,2-d:4,5-*d*′)Bistriazole
IAST	Ideal Adsorbed Solution Theory
HIAM	Hoffmann Institute of Advanced Materials
GCMC	Grand canonical Monte Carlo
ELM	Elastic Layer Structured Metal–organic Frameworks
ssNMR	Solid-State Nuclear Magnetic Resonance
CAU	Christian-Albrechts-University
MIL	Materials of Institute Lavoisier
1D	One-Dimensional
H_4BPTC	BiPhenyl-3,3,5,5-TetraCarboxylic acid
DMF	Dimethylformamide
MIRIAM	Multimode InfraRed Imaging And Micro Spectroscopy
MAS	Magic Angle Spinning
SOLA	Solid Line shape Analysis
FTIR	Fourier-Transform Infrared Spectroscopy
DFT	Density Functional Theory
VASP	Vienna Ab initio Simulation Package
PAW	Projector Augmented Wave
PBE	Perdew-Burke-Ernzerhof

GGA	Generalized Gradient Approximation
TGA	Thermal Gravimetric Analysis
TPD	Temperature-Programmed Desorption
TCD	Thermal Conductivity Detector
ABR	Automated Breakthrough Reactor
PSD	Pore Size Distributions
ΔS	Entropy
U_{iso}	Isotropic Displacement Parameters
MIL	Materials of Institute Lavoisier
CCDC	Cambridge Crystallographic Database Centre
IUPAC	International Union of Pure and Applied Chemistry
ppm	Parts per Million

List of Figures

Figure 2.2 (a) Views of the co-ordination environment of binuclear Sc(III) centres with $BPTC^{4-}$ and TDA^{2-}. (b) Space-filling views of the structure of NOTT-400 along the b-axis showing 8.1 Å channels, and the structure of NOTT-401 along the c-axis showing the 6.3 Å channels (scandium: green; sulfur: yellow; oxygen: red; carbon: grey; hydrogen: small grey).
Figure 2.3. $Zr_6O_4(OH)_4$ secondary building units (SBUs) are connected with organic linkers to form MOFs of **fcu** topology.
Figure 2.4. (a) Structures of linkers of L1 to L3 for MFM-126 to MFM-128. Views of crystal structure of MFM-126. (b) Cage A; (c) cage B. (d) View of the alternate packing of cages A (void space coloured orange) and B (void space coloured plum). (e) View along the c-axis of the Kagomé lattice in MFM-126. Colours: C, grey; H, white; O, red; N, blue; Cu, teal.
Figure 2.5. (a) PXRD patterns of simulated (black), as-synthesised (blue) sample for Al-bttotb. (b) Adsorption-desorption isotherms of N_2 at 77 K for Al-bttotb (solid: adsorption; open: desorption). (c) Adsorption-desorption isotherms of NH_3 at 273 K for Al-bttotb (solid: adsorption; open: desorption). (d) PXRD patterns of as-synthesised (blue), after dosing NH_3 for 1 day (magenta), after NH_3 adsorption isotherms (red) for Al-bttotb.
Figure 2.6. (a) PXRD patterns of simulated (black), as-synthesised (red) sample for NOTT-401. (b) Adsorption-desorption isotherms of N_2 at 77 K for pristine NOTT-401 (solid: adsorption; open: desorption). (c) Adsorption-desorption isotherms of NH_3 at 273 K for NOTT-401 (solid: adsorption; open: desorption). (d) PXRD patterns of as-synthesised (blue), after dosing NH_3 for 1 day (magenta), after NH_3 adsorption isotherms (red) for NOTT-401.
Figure 2.7. (a) PXRD patterns of simulated (black), as-synthesised (blue) sample for MOF-801. (b) Adsorption-desorption isotherms of N_2 at 77 K for pristine MOF-801 (solid: adsorption; open: desorption). (c) Adsorption-desorption isotherms of NH_3 at 273 K for MOF-801 (solid: adsorption; open: desorption). (d) PXRD patterns of as-synthesised (blue), after dosing NH_3 for 1 day (magenta), after NH_3 adsorption isotherms (red) for MOF-801.
Figure 2.8. (a) PXRD patterns of simulated (black), as-synthesised (blue) sample for Zr-ndc. (b) Adsorption-desorption isotherms of N_2 at 77 K for pristine Zr-ndc (solid: adsorption; open: desorption). (c) Adsorption-desorption isotherms of NH_3 at 273 K for Zr-ndc (solid: adsorption; open: desorption). (d) PXRD patterns of as-synthesised (blue), after dosing NH_3 for 1 day (magenta), after NH_3 adsorption isotherms (red) for Zr-ndc.
Figure 2.9. (a) PXRD patterns of simulated (black), as-synthesised (blue) sample for Zr-cca. (b) Adsorption-desorption isotherms of N_2 at 77 K for pristine MOF- Zr-cca (solid: adsorption; open: desorption). (c) Adsorption-desorption isotherms of NH_3 at 273 K for Zr-cca (solid: adsorption; open: desorption). (d) PXRD patterns of as-synthesised (blue), after dosing NH_3 for 1 day (magenta), after NH_3 adsorption isotherms (red) for Zr-cca.
Figure 2.10. PXRD patterns of simulated (black), as-synthesised (red) sample for MFM-126 (a), and MFM-127 (c). Adsorption-desorption isotherms of C_2H_4 and C_2H_6 at 293 K for MFM-126 (b), and MFM-127 (d) (solid: adsorption; open: desorption).
Figure 2.11. IAST selectivity of C_2H_4/C_2H_6 at 293 K for MFM-127.
Figure 3.1. Schematic illustration. Schematic illustration of selected linkers, the self-assembly processes through *cis*- and/or *trans*-μ_2-OH connected [AlO_6] octahedral and the resulting MOFs.

Figure 3.2. Adsorption and thermodynamics data. (a) Adsorption-desorption isotherms for four Al-MOFs at 298 K (red: MIL-160; blue: CAU-10-H; magenta: Al-fum; olive: MIL-53(Al); solid: adsorption; open: desorption). (b) Adsorption-desorption isotherms for MIL-160 at 273–308 K (red: 273 K; blue: 283 K; magenta: 298 K; dark yellow: 308 K; solid: adsorption; open: desorption). (c) Dynamic breakthrough plots for NH_3 (1000 ppm diluted in He) with an inlet gas flow rate of 25 mL min^{-1} through a fixed-bed packed with (olive) MIL-53(Al), (magenta) Al-fum, (blue) CAU-10-H and (red) MIL-160 samples at 298 K. (d) Plots for isosteric heats of adsorption (Q_{st}) and entropies of adsorption (ΔS) (red: Q_{st}; black: ΔS). The error bars were derived by least-squares linear fitting from four isotherms at different temperatures.

Figure 3.3. Stability data of MIL-160. (a) 16 cycles of NH_3 adsorption-desorption at 298 K between 0 and 0.2 bar in MIL-160 (pressure-swing conditions) (red bars represents the uptake capacity and blue bars indicate the residual NH_3 in the pore upon pressure swing desorption). (b) PXRD patterns of simulated (black), as-synthesised (blue), after dosing NH_3 for 1 week (magenta), after 16 cycles of NH_3 adsorption (purple) and regenerated sample (red) for MIL-160. (c) Adsorption-desorption isotherms of N_2 at 77 K for pristine MIL-160 (red) and sample regenerated after 16 cycles of NH_3 adsorption (black) (solid: adsorption; open: desorption). (d) PXRD patterns of MIL-160 for as-synthesised (black), after NH_3 ad/desorption isotherms (blue), breakthrough experiments (red), and samples soaked in solutions with pH = 1 (magenta), 2 (dark yellow), 8 (wine), 10 (olive), 12 (orange) and in boiling water (purple) for 12 h.

Figure 3.4. *In situ* NPD analysis. Views of the host–guest interactions in ND_3-loaded MIL-160 determined by *in situ* NPD at 10 K. The occupancy of each site has been converted into ND_3 per Al for clarity. (a) Views of ND_3 in MIL-160·$(ND_3)_{0.4}$ along the *c*-axis and (b) detailed views of host–guest interactions between MIL-160 and ND_3 (Site I: pink, Site II: orange); (c) Views of ND_3 in MIL-160·$(ND_3)_{1.5}$ along the *c*-axis and (d) detailed views of host–guest interactions between MIL-160 and ND_3 (Site I: pink; Site II: orange; Site III: green).

Figure 3.5. Solid-state NMR spectra. (a) ^{27}Al direct excitation and (b) $\{^{1}H\text{-}\}^{13}C$ cross-polarization MAS NMR spectra of treated MIL-160 samples: pristine (black curve), partial ammonia adsorption (red curve), ammonia saturation after 1 week sealed in a rotor (blue curve) and after active desorption (250 ºC for 12 hours under dynamic vacuum) (grey curve). Daggers denote peaks arising due to structural decomposition. Simulated ^{27}Al NMR spectra (purple dashed lines) were produced using the following non-zero parameters: MIL-160 C_Q = 5.2 MHz, η_Q = 0.4, δ_{iso} = 3.8 ppm, NH_3-MIL-160' C_Q = 4.8 MHz, δ_{iso} = 4.0 ppm (Gaussian Isotropic Distribution Model) and C_Q = 5.5 MHz, η_Q = 0, δ_{iso} = -5.4 ppm, NH_3-MIL-160 C_Q = 4.8 MHz, δ_{iso} = 6.0 ppm, NH_3-MIL-160_{250} C_Q = 5.2 MHz, η_Q = 0.46, δ_{iso} = 4.0 ppm.

Figure 3.6. *In situ* synchrotron IR spectra. (a) *In situ* synchrotron IR spectra for activated MIL-160; *In situ* synchrotron IR spectra for MIL-160 as a function of adsorption of NH_3 (diluted in dry N_2) and after regeneration under a dry N_2 flow at 10 mL min^{-1} at 423 K for 2 h: (b) 3800-3500 cm^{-1}, (c) 1700-1600 cm^{-1}, (d) 1600-1500 cm^{-1}, (e) 1300-1000 cm^{-1}, (f) 850-750 cm^{-1}. Activated MIL-160 (black), 1% NH_3-loaded MIL-160 (blue), 2% NH_3-loaded MIL-160 (pink), 5% NH_3-loaded MIL-160 (magenta), 10% NH_3-loaded MIL-160 (dark yellow), 20% NH_3-loaded MIL-160 (purple), 40% NH_3-loaded MIL-160 (wine), 60% NH_3-loaded MIL-160 (olive), 80% NH_3-loaded MIL-160 (orange), 100% NH_3-loaded MIL-160 (violet), regenerated MIL-160 (red).

Figure 4.1. Isotherms and breakthrough data. (a) Adsorption isotherms for NH_3 in MFM-300(Sc) at 273 K (red), 283 K (black), 293 K (blue), 298 K (magenta), 303 K (dark yellow) and 313 K (violet) (adsorption: solid symbols; desorption: open symbols). (b) 90 cycles of adsorption-desorption of NH_3 in MFM-300(Sc) under pressure-swing conditions. (c) Dynamic breakthrough curve for NH_3 (1000 ppm diluted in He) with an inlet gas flow rate of 25 mL min^{-1} through a fixed-bed packed with MFM-300(Sc) at 298 K and 1.0 bar (Dry NH_3: red; He: black). (d) Comparison of NH_3 uptake at 1.0 bar under 298 K for selected materials plotted against their surface areas (solid symbols: reversible sorption; hollow symbols: irreversible sorption; full details are given in the supplementary information).

Figure 4.2. *In situ* NPD analysis. Views of binding sites for ND_3 in MFM-300(Sc) determined by NPD at 10 K (Sc: green; C: grey; O: red; H: light yellow; D: orange; N: blue). The occupancy of each site has been converted into ND_3/Sc for clarity. (a, c) Views along the *c*-axis showing packing of the guest molecules of NH_3 in MFM-300(Sc)·$(ND_3)_{1.25}$ and MFM-300(Sc)·$(ND_3)_{2.6}$, respectively. (b, d) Detailed views of host–guest interactions between MFM-300(Sc) and adsorbed molecules of ND_3.

Figure 4.3. ssNMR and *in situ* FTIR spectra analysis. ^{1}H-^{45}Sc Heteronuclear dipolar correlation spectroscopy (HETCOR) MAS NMR spectra of (a, c) pristine and (b, d) NH_3-loaded MFM-300(Sc), with corresponding ^{45}Sc MAS NMR spectra (top). The spectra were recorded at 9.4 T using a MAS frequency of 12 kHz. The dashed blue lines highlight correlations between the Sc(III) site and various proton environments. *In situ* FTIR spectra of MFM-300(Sc) as a function of NH_3 loading (diluted in dry N_2) and re-activated under a flow of dry N_2 at 100 mL min^{-1} at 298 K for 2 h: (e) 3800−3200 cm^{-1}, (f) 1650−1400 cm^{-1}. Activated MFM-300(Sc) (black), 1% NH_3-loaded MFM-300(Sc) (blue), 2% NH_3-loaded MFM-300(Sc) (blue), 5% NH_3-loaded MFM-300(Sc) (pink), 10% NH_3-loaded MFM-300(Sc) (magenta), 20% NH_3-loaded MFM-300(Sc) (dark yellow), 40% NH_3-loaded MFM-300(Sc) (purple), and regenerated MFM-300(Sc) (red).

Figure 4.4. Dynamic studies by INS. (a) Experimental and simulated INS difference spectra of the adsorbed NH_3 within MFM-300(Sc), denoted as Expt-Diff (olive) and Simu-Diff (red), respectively. (b) Comparison of the INS spectra of adsorbed NH_3 of Expt-Diff (olive) and Simu-Diff (red) with solid NH_3 (blue). (c) Experimental INS spectra of bare MFM-300(Sc) (blue), NH_3-loaded MFM-300(Sc) (magenta) and the difference spectrum at the higher energy region (olive).

Figure 5.1. Structure and adsorption data. (a) View of infinite chain of $[InO_4(OH)_2]_\infty$ linked by tetracarboxylate ligands (In: green; C: grey; O: red; H: light yellow; hydrogen atoms on the ligands are omitted for clarity). Single-component adsorption isotherms for (b) C_2 and (c) C_3 hydrocarbons in MFM-300(In) at 293 K. (d) Analysis of IAST selectivity of C_2H_6/C_2H_4 for MFM-300(In) at 293 K and 1 bar. (e) Isosteric heats of adsorption (Q_{st}) for C_2 and C_3 hydrocarbons in MFM-300(In). (f) Adsorption kinetics of C_2 and C_3 hydrocarbons of MFM-300(In) at 293 K (30-70 mbar). C_2H_2 (black), C_2H_4 (blue), C_2H_6 (red), C_3H_4 (magenta), C_3H_6 (olive) and C_3H_8 (purple).

Figure 5.2. Breakthrough curves. Dynamic breakthrough plots for single-component (a) C_2H_4, (b) C_2H_6, (d) C_3H_4, and (e) C_3H_6 with an inlet target gas flow rate of 2.0 mL min^{-1} diluted in He (total flow rate: 20 mL min^{-1}). Dynamic breakthrough plots for equimolar mixtures of (c) C_2H_6/C_2H_4 and (f) C_3H_4/C_3H_6 with an inlet gas flow rate of 2.0 mL min^{-1}/2.0 mL min^{-1} diluted in He (total flow rate: 20 mL min^{-1}) through a fixed-bed packed with MFM-300(In) at 293 K. C_2H_4 (blue), C_2H_6 (red), C_3H_4 (magenta), and C_3H_6 (olive).

Figure 5.3. *In situ* NPD analysis. Binding sites (site I, orange; site II, green) of (a) acetylene, (b) ethylene, (c) ethane, (d) propyne, (e) propylene and (f) propane in MFM-300(In) obtained from NPD refinements (In: green; C: grey; O: red; H: light yellow; the $[InO_4(OH)_2]$ moiety is shown in green octahedron). The e.s.d. values of the bond distances are typically within 0.05 Å.

Figure 5.4. *In situ* INS studies. Comparison of the INS spectra of bare MFM-300(In) and MFM-300(In) loaded with (a) C_2D_2 (black: solid C_2H_2; red: 1.0 C_2H_2 difference; blue: 2.0 C_2H_2 difference), (b) C_2D_4 (black: solid C_2H_4; red: 1.0 C_2H_2 difference), and (c) C_2D_6 (black: solid C_2H_6; red: 1.0 C_2H_6 difference; blue: 1.5 C_2H_6 difference). For comparison, INS spectra of the condensed gas in the solid state are also included.

Supplementary Figure 3.1. PXRD patterns of simulated (black), as-synthesised (blue), activated (magenta) and NH_3-loaded (red) samples of (a) MIL-160, (b) CAU-10-H, (c) Al-fum and (d) MIL-53(Al). MIL-53*as* (Al) is the form occupied by free terephthalic acid ligand; MIL-53*ht* (Al) is the calcined form with empty channels; MIL-53*lt* (Al) is the room temperature form with water molecule in the channels.

Supplementary Figure 3.2. TGA curves of acetone-exchanged and activated samples for (a) MIL-160, (b) CAU-10-H, (c) Al-fum and (d) MIL-53(Al) measured under an air flow (black: activated sample; red: activated MIL-160; blue: activated CAU-10-H; magenta: activated Al-fum; olive: activated MIL-53(Al)).

Supplementary Figure 3.3. (a) N_2 adsorption and desorption isotherms at 77 K (solid symbols: adsorption; hollow symbols: desorption) and (b) micropore size distribution for MIL-160.

Supplementary Figure 3.4. (a) N_2 adsorption and desorption isotherms at 77 K (solid symbols: adsorption; hollow symbols: desorption) and (b) micropore size distribution for CAU-10-H.

Supplementary Figure 3.5. (a) N_2 adsorption and desorption isotherms at 77 K (solid symbols: adsorption; hollow symbols: desorption) and (b) micropore size distribution for Al-fum.

Supplementary Figure 3.6. (a) N_2 adsorption and desorption isotherms at 77 K (solid symbols: adsorption; hollow symbols: desorption) and (b) micropore size distribution for MIL-53(Al).

Supplementary Figure 3.7. (a-d) Fitting of isotherm by Dual-Site Langmuir Freundlich (DSLF) model for NH_3-loaded MIL-160 at 273, 283, 298 and 308 K up to 1.0 bar. (e) van't Hoff linear fittings.

Supplementary Figure 3.8. NH_3-temperature programmed desorption (TPD) curve for MIL-160.

Supplementary Figure 3.9. PXRD patterns of (a) CAU-10-H, (b) Al-fum and (c) MIL-53 (Al) for as-synthesised samples and samples after NH_3 isotherms and dynamic breakthrough experiments and samples after soaked in solutions with pH=1, 2, 8, 10, 12 and in boiling water for 12 h.

Supplementary Figure 3.10. Adsorption kinetics of NH_3 in MIL-160 from 1.9 to 3.0 mbar at 298 K.

Supplementary Figure 3.11. Rietveld refinement patterns of the NPD data of bare MIL-160 from bank 1 to 5.

Supplementary Figure 3.12. Rietveld refinement patterns of the NPD data of MIL-160·$(ND_3)_{0.4}$ from bank 1 to 5. Due to excessively dosed ND_3 and rapid cooling, trace amount of solid ammonia with cubic structure was identified through Pawley refinement and related peaks were treated as anomalous background in the Rietveld refinement.

Supplementary Figure 3.13. Neutron powder diffraction and Rietveld fit profiles of MIL-160· $(ND_3)_{1.5}$ from bank 1 to 5. Due to excessively dosed ND_3 and presence of trace moisture in the pipeline, a series of ammonia monohydrate was identified via Pawley refinement and related peaks were treated as anomalous background in Rietveld refinement.

Supplementary Figure 3.14. ^{1}H Hahn-echo MAS NMR spectra of the MIL-160 samples. 1 rotor period was used as the delay either side of the π-pulse for the Hahn-echo. NH_3-MIL-160-*ap* is the MIL-160 sample as-prepared after NH_3 dosing, NH_3-MIL-160-*aw* is this dosed sample after one week of ambient storage, and NH_3-MIL-160_{250} is this latter sample after heating to 250 °C.

Supplementary Figure 3.15. {^{1}H-}^{13}C CPMAS (left) and ^{1}H Hahn-echo MAS (right) NMR spectra of select MIL-160 samples. 1 rotor period was used as the delay either side of the π-pulse for the Hahn-echo. The ^{1}H Hahn-echo MAS NMR spectra of MIL-160 and NH_3-MIL-160-*aw* are reproduced from Supplementary Figure 14 for comparison. After loading with NH_3, subsequent desorption at 150 ºC does not fully regenerate the MOF structure.

Supplementary Figure 3.16. ^{1}H-^{13}C heteronuclear dipolar correlation spectrum (left) of NH_3-MIL-160-*aw* and corresponding cross-sectional slices (right) taken at the positions indicated by the coloured dashed lines. The ^{1}H Hahn-echo MAS NMR spectrum for this sample is also reproduced (right, black) for comparison.

Supplementary Figure 3.17. Comparison of {^{1}H-}^{13}C CPMAS (left) and ^{1}H Hahn-echo MAS (right) NMR spectra of NH_3 loaded and desorbed (250 ºC) MIL-160 (top) and activated pristine MIL-160 that has undergone heating at 250 ºC (bottom). 1 rotor period was used as the delay either side of the π-pulse for the Hahn-echo.

Supplementary Figure 4.1. View of the three-dimensional framework structure of MFM-300(Sc). Colour code for atoms: Sc, green; O, red; C, grey; H, tan; N, blue.

Supplementary Figure 4.2. Adsorption isotherm for N_2 in MFM-300(Sc) at 77 K (solid symbols: adsorption; hollow symbols: desorption).

Supplementary Figure 4.3. Thermogravimetric analysis of acetone-exchanged MFM-300(Sc) under a flow of N_2 at a heating rate of 5 °C min^{-1}.

Supplementary Figure 4.4. PXRD patterns of MFM-300(Sc) after being immersed in (a) solutions at pH 7 to pH12, and (b) different organic solvents.

Supplementary Figure 4.5. PXRD patterns of as-synthesised MFM-300(Sc), activated sample, and samples after 90 consecutive cycles of adsorption of NH_3 and after NH_3 breakthrough experiment.

Supplementary Figure 4.6. (a) Adsorption isotherms for NH_3 in MFM-300(Sc) at 273 K, first cycle (black) and second cycle (red). (b) Adsorption isotherms for N_2 at 77 K in MFM-300(Sc) before and after two cycles NH_3 adsorption. Solid symbols: adsorption; hollow symbols: desorption.

Supplementary Figure 4.7. (a-d) IAST fitting of isotherms for NH_3-loaded MFM-300(Sc) at different temperatures and up to 1.0 bar. (e) van't Hoff linear fittings and (f) isosteric enthalpy and entropy of adsorption for NH_3 in MFM-300(Sc) at different loadings.

Supplementary Figure 4.8. Neutron diffraction patterns and Rietveld refinement of bare MFM-300(Sc) (bank 1 to 5).

Supplementary Figure 4.9. Neutron diffraction patterns and Rietveld refinement of MFM-300(Sc)·$(ND_3)_{1.25}$ (bank 1 to 5).

Supplementary Figure 4.10. Neutron diffraction patterns and Rietveld refinement of MFM-300(Sc)·$(ND_3)_{2.6}$ (bank 1 to 5).

Supplementary Figure 4.11. (a) ^{45}Sc and (b) {^{1}H-}^{13}C CP MAS NMR spectra of pristine (black) and NH_3-loaded (red) MFM-300(Sc). The dashed lines in (a) are from simulated spectra with the following parameters: δ_{iso} = 59.6 ppm, C_Q = 10.8 MHz, η_Q = 1, Gaussian broadening = 1.41 kHz for pristine MFM-300(Sc) and δ_{iso} = 68.6 ppm, C_Q = 11.5 MHz, η_Q = 1, Gaussian broadening = 1.14 kHz for NH_3-loaded MFM-300(Sc).

Supplementary Figure 4.12. Experimental INS spectra of bare MFM-300(Sc) (dark cyan) and of NH_3-loaded MFM-300(Sc) (olive).

Supplementary Figure 4.13. Simulated INS spectra of bare MFM-300(Sc) (pink) and NH_3-loaded MFM-300(Sc) (wine).

Supplementary Figure 5.1. Scheme of the column dynamic breakthrough experiments.

Supplementary Figure 5.2. PXRD patterns of as-synthesised, activated MFM-300(In), and sample after breakthrough experiments (black: simulated MFM-300(In); blue: as-synthesised; red: activated; olive: after breakthrough experiments).

Supplementary Figure 5.3. TGA curves for as-synthesised (black), acetone-exchanged (blue) and activated MFM-300(In) (red).

Supplementary Figure 5.4. N_2 adsorption/desorption isotherms for (a) MFM-300(Al) and (c) MFM-300(In) at 77 K (solid symbols: adsorption; hollow symbols: desorption). Micropore size distribution plots for (b) MFM-300(Al) and (d) MFM-300(In).

Supplementary Figure 5.5. Adsorption/desorption isotherms for acetylene in MFM-300(In) (black: 195 K; red: 273 K; blue: 283 K; olive: 293 K; magenta: 303 K) (solid symbols: adsorption; hollow symbols: desorption).

Supplementary Figure 5.6. Adsorption/desorption isotherms for ethylene in MFM-300(In) (black: 195 K; red: 273 K; blue: 283 K; olive: 293 K; magenta: 303 K) (solid symbols: adsorption; hollow symbols: desorption).

Supplementary Figure 5.7. Adsorption/desorption isotherms for ethane in MFM-300(In) (black: 195 K; red: 273 K; blue: 283 K; olive: 293 K; magenta: 303 K) (solid symbols: adsorption; hollow symbols: desorption).

Supplementary Figure 5.8. Adsorption/desorption isotherms for propyne in MFM-300(In) (black: 273 K; red: 283 K; blue: 293 K; olive: 303 K) (solid symbols: adsorption; hollow symbols: desorption).

Supplementary Figure 5.9. Adsorption/desorption isotherms for propene in MFM-300(In) (black: 273 K; red: 283 K; blue: 293 K; olive: 303 K) (solid symbols: adsorption; hollow symbols: desorption).

Supplementary Figure 5.10. Adsorption/desorption isotherms for propane in MFM-300(In) (black: 273 K; red: 283 K; blue: 293 K; olive: 303 K) (solid symbols: adsorption; hollow symbols: desorption).

Supplementary Figure 5.11. Adsorption isotherms at 273 K of C_2H_2 (black), C_2H_4 (blue), C_2H_6 (red), C_3H_4 (magenta), C_3H_6 (olive) and C_3H_8 (purple) in MFM-300(In) to a pressure of 1 bar. Desorption isotherms are omitted for clarity; the nature of reversible adsorption has been demonstrated above.

Supplementary Figure 5.12. Adsorption isotherms at 303 K of C_2H_2 (black), C_2H_4 (blue), C_2H_6 (red), C_3H_4 (magenta), C_3H_6 (olive) and C_3H_8 (purple) in MFM-300(In) to a pressure of 1 bar. Desorption isotherms are omitted for clarity; the nature of reversible adsorption has been demonstrated above.

Supplementary Figure 5.13. Linear fitting of 1/T vs ln$P$ at intervals of 0.1 mmolg^{-1} for substrates in MFM-300(In) to determine the isosteric heat of adsorption by the Van t' Hoff method.

Supplementary Figure 5.14. Entropy of adsorption for C_2 and C_3 hydrocarbons in MFM-300(In) calculated from isotherm data. C_2H_2 (black), C_2H_4 (blue), C_2H_6 (red), C_3H_4 (magenta), C_3H_6 (olive) and C_3H_8 (purple).

Supplementary Figure 5.15. Selectivities as a function of pressure for C_2 and C_3 hydrocarbons in MFM-300(In) calculated by IAST from single component adsorption isotherms.

Supplementary Figure 5.16. Breakthrough plots for single component (a) C_2H_2 and (b) C_3H_8 with an inlet gas flow rate of 2.0 mL min^{-1} diluted in He through MFM-300(In) at a total flow of 20 mL min^{-1} at 293 K.

Supplementary Figure 5.17. Dynamic breakthrough plots for equimolar mixtures of (a) C_2H_4/C_2H_2, (b) C_2H_6/C_2H_2, (c) C_3H_8/C_3H_4 and (d) C_3H_8/C_3H_6 with an inlet gas flow rate of 2.0 mL min^{-1}/2.0 mL min^{-1} diluted in He through a fixed-bed packed with MFM-300(In) at a total flow of 20 mL min^{-1} at 293 K. C_2H_2 (black), C_2H_4 (blue), C_2H_6 (red), C_3H_4 (magenta), C_3H_6 (olive) and C_3H_8 (purple).

Supplementary Figure 5.18. Dynamic breakthrough experiments for 1:99 mixtures of (a) C_2H_2/C_2H_4, (b) C_2H_2/C_2H_6, and (c) C_2H_4/C_2H_6 with an inlet gas flow rate of 0.2 mL min^{-1}/19.8 mL min^{-1} through a fixed-bed packed with MFM-300(In) at a total flow rate of 20 mL min^{-1} at 293 K. C_2H_2 (black), C_2H_4 (blue), and C_2H_6 (red).

Supplementary Figure 5.19. Rietveld fit profiles of the NPD data of MFM-300(In)·1.32(C_2D_2).

Supplementary Figure 5.20. Rietveld fit profiles of the NPD data of MFM-300(In)·1.66(C_2D_4).

Supplementary Figure 5.21. Rietveld fit profiles of the NPD data of MFM-300(In)·0.72(C_2D_6).

Supplementary Figure 5.22. Rietveld fit profiles of the NPD data of MFM-300(In)·0.2(C_3D_4).

Supplementary Figure 5.23. Rietveld fit profiles of the NPD data of MFM-300(In)·0.48(C_3D_6).

Supplementary Figure 5.24. Rietveld fit profiles of the NPD data of MFM-300(In)·0.46(C_3D_8).

Supplementary Figure 5.25. NPD structure of MFM-300(In)·0.2(C_3D_4).

Supplementary Figure 5.26. NPD structure of MFM-300(In)·0.48(C_3D_6).

Supplementary Figure 5.27. NPD structure of MFM-300(In)·0.46(C_3D_8).

Supplementary Figure 5.28. Comparison of bare and C_2H_2 loaded MFM-300(In) (black: bare MFM-300(In); red: 1.0 C_2H_2 per metal; blue: 2.0 C_2H_2 per metal).

Supplementary Figure 5.29. Comparison of bare and C_2H_4 loaded MFM-300(In) (black: bare MFM-300(In); red: 1.0 C_2H_4 per metal).

Supplementary Figure 5.30. Comparison of bare and C_2H_6 loaded MFM-300(In) (black: bare MFM-300(In); red: 1.0 C_2H_6 per metal; 1.5 C_2H_6 per metal).

List of Tables

List of Graphical Abstract

WORD COUNT: 40450

Abstract

This thesis is dedicated to the development and evaluation of efficient methods for mitigating greenhouse gas emissions and reducing global energy consumption to contribute net zero carbon emissions goal. This endeavour involves exploring alternative gas fuels as a substitute for fossil fuels, and with efforts to decrease global energy consumption by employing advanced separation technology. Specifically, this research spotlights the potential of porous metal–organic frameworks (MOFs) for the storage of ammonia (NH_3) and the purification of olefins. This thesis also presents an in-depth examination of the impact of host–guest interactions on the efficiency of gas storage and ability to achieve efficient separation. The ultimate goal is to utilise these findings in the design of improved materials for future applications in clean energy storage and gas purification.

Chapter 1 provides a comprehensive literature review focusing on two key areas: the economies of ammonia (NH_3) and light olefins (C_2H_4 and C_3H_6). The chapter explores the host−guest interactions and separation mechanisms involved in the storage of NH_3 and the purification of olefins using metal-organic frameworks (MOFs). It examines how these interactions and mechanisms influence the performance of MOFs in terms of NH_3 storage and olefin purification. The review aims to establish a solid foundation for understanding the current state of research in this field and identify potential areas for further investigation and improvement.

Chapter 2 provides an overview of the aims, objectives, and strategy of MOFs selection for ammonia adsorption and olefin purification. This chapter introduces a range of robust MOFs including Al-MOFs, Sc-MOFs, Zr-MOFs, In-MOFs and Cu-MOFs in these two areas. This chapter further provides a summary of the results from

the experiments conducted on these selected MOFs, which demonstrates the significant impact that pore size, shape, and functional groups can have on the efficiency of MOFs for ammonia adsorption and olefin purification, providing valuable insights into the properties of a wider range of MOFs and their potential applications for gas adsorption and separation. This thus leads to our works on the NH_3 adsorption in chapter 3 and 4, as well as on olefin purification in chapter 5.

Chapter 3 describes an efficient NH_3 adsorption in a robust MIL-160. The effects of functional groups (e.g., μ_2-OH), pore geometry and structural flexibility on the selected Al-based MOFs have been studied for NH_3 adsorption. MIL-160 shows high uptakes of NH_3 of 4.8 and 12.8 mmol g^{-1} at both low and high pressure (0.001 and 1.0 bar, respectively) at 298 K, owing to its suitable pore size, anchored μ_2-OH, and the O-heteroatom of the furan linker. Dynamic breakthrough experiments confirm its excellent ability to capture NH_3 with a dynamic uptake of 4.2 mmol g^{-1} at 1000 ppm. The study of host−guest interactions reveals the preferred adsorption domains of NH_3 molecules and an unusual distortion of the local structure of [AlO_6] moieties. Considering its high NH_3 affinity and uptakes, and high stability, MIL-160 has a great potential in practical application as a robust sorbent for NH_3.

Chapter 4 describes an exceptional NH_3 adsorption in a robust MFM-300(Sc). At 273 K and 1.0 bar, MFM-300(Sc) shows an exceptional NH_3 uptake of 19.5 mmol g^{-1}. *In situ* neutron powder diffraction (NPD), inelastic neutron scattering (INS), synchrotron infrared micro-spectroscopy (SRIR) and solid-state nuclear magnetic resonance (ssNMR) reveal the reversible host–guest and guest–guest hydrogen bond interactions between NH_3 and MFM-300(Sc). The moderate strength of the host–guest interaction

in MFM-300(Sc) leads to excellent adsorption reversibility and stability with full retention of the capacity over 90 cycles.

Chapter 5 describes the efficient purification of C_2H_4 and C_3H_6 from mixtures of C_2H_6/C_2H_4 and C_3H_4/C_3H_6 in MFM-300(In). Single-component adsorption isotherms reveal that MFM-300(In) has an unusually selective adsorption of C_2H_6 over C_2H_4, and a distinct binding affinity to C_3H_4 over C_3H_6. The breakthrough experiments confirmed the efficient separation of equimolar mixtures of C_2H_6/C_2H_4 and C_3H_4/C_3H_6, which results in a high productivity of 4.6 L/kg of C_2H_4 (purity >99.9%) and of 16.3 L/kg of C_3H_6 (purity >99.95%) at the outlet. The study of *in situ* NPD and *in situ* INS confirmed the stronger interactions of C_2H_6 and C_3H_4 over C_2H_4 and C_3H_6.

Chapter 6 summarises the results in this thesis and outlines an outlook for future research directions.

Declaration

Except where specific reference is made or contributions stated, no portion of the work referred to in this thesis has been submitted in support of an application for another degree or qualification of this or any other university or other institute of learning.

Signed by Lixia Guo

Copyright Statement

Acknowledgements

Firstly, I would like to thank Prof. Sihai Yang and Prof. Martin Schröder for offering remarkable opportunity to undertake my PhD program at the University of Manchester. I extend my deepest gratitude to Prof. Sihai Yang, who provided invaluable advice, guidance, and support during periods of my uncertainty and doubt. I have learnt a lot during the past four years, not only about doing better research, but also about being a better thinker. Thank you from the bottom of my heart.

Thank all group members for the daily help, support, and suggestions on the lab experience. I would like to express my thanks to Dr. Jiangnan Li, Dr. Xue Han, and Dr. Wanpeng Lu for their expert guidance and imparting their knowledge in isotherms and breakthrough experiments, which formed the foundation of my research. Special acknowledgement to Dr. Xue Han for her generous assistance in revising my manuscript for *Chem. Commun.,* **2022,** *58*, 5753−5756. Her insights and expertise have undoubtedly enriched the quality of this work. In particularly, I would like to thank Dr. Xi Chen who gave me a huge support during the first two years. Thank Dr. Jiangnan Li, Dr. Yujie Ma, Yinlin Chen, Dukula De Alwis Jayasinghe, and Xiangdi Zeng for the advice, discussion, and revision on my thesis.

I wish to express my deep appreciation to Dr. Daniel Lee and Joe Hurd for invaluable assistance with the collection and analysis of solid-state NMR data. Their insightful contributions to the data analysis and revision of manuscripts have undeniably augmented the quality of this work on ammonia adsorption.

Many thanks must go to ISIS Neutron, Diamond Light Source, and Oak Ridge National Laboratory for access to their facilities. The quality of my research has greatly benefited from the resources provided by these esteemed institutions.

Specifically, I would like to acknowledge the WISH team for the collection and analysis of neutron powder diffraction (NPD) data. Thanks to Dr. Pascal Manuel, Dr. Yujie Ma, Dr. Weiyao Li, Yinlin Chen, Dr. Jiangnan Li, Xiangdi Zeng, and Danielle Crawshaw contributed to the NPD data collection, their efforts are sincerely appreciated. Additionally, I am indebted to Dr. Ivan da Silva, Meng He, and Yinlin Chen for their help with the NPD data analysis.

My thanks also extend to the B22 team for the collection of *in-situ* synchrotron infrared spectroscopy (SRIR) data. I am grateful to Dr. Mark D. Frogley, Meredydd Kippax-Jones, Dr. Jiangnan Li, Xiangdi Zeng, and Dr. Wanpeng Lu for their contributions.

I would like to express my appreciation to Dr. Svemir Rudić, Dr. Yongqiang Cheng, and Dr. Xue Han for the inelastic neutron scattering (INS) data collection and their generous assistance with data analysis. The guidance and support of these experts were invaluable in understanding and interpreting the results.

Last but not least, I would like to thank the China Scholarship Council (CSC) and the University of Manchester for funding my PhD program. Moreover, this journey would not have been possible without the support and encouragement from my family and friends. I am forever grateful for their contribution to my personal and academic growth over the past four years.

The Author

Lixia Guo grew up in Zhoukou, Henan province, China. She completed her B.Sc. in Chemistry in 2016 from Shanghai Normal University, followed by a M.Sc. in Chemistry from Tongji University in 2019. Her consistent academic excellence was recognised through multiple achievements, including several Excellent Student Scholarships and National Excellent Student Scholarships. She also graduated as an Excellent Graduate from Tongji University in 2019. In the same year, she was awarded a scholarship by the China Scholarship Council (CSC), allowing her to begin her PhD program in 2019 under the supervision of Prof. Sihai Yang and Prof. Martin Schröder. Her research interests are centred in multidisciplinary areas of inorganic chemistry and materials chemistry, with a specific focus on porous metal–organic frameworks (MOFs) and for gas adsorption and separation. Currently, her research lies in ammonia storage and light hydrocarbon separation, with particular interest in separation of C_2 and C_3 molecules. During her PhD study, she has performed experiments at ISIS Neutron Facility for neutron powder diffraction experiments. Adding to her academic achievements, she has published three peer-reviewed research papers as first author during her PhD studies, with publications including *Chem. Commun.,* **2022,** *58*, 5753−5756; *Chem. Mater*. **2022,** *34*, 5698–5705; *Commun. Chem.,* **2023**, *6*, 55. In addition to her first-author contributions, she also collaborated and contributed as part of a team. Her participation as a co-author on at least two unpublished works shows her versatility as a research and her dedication in her field.

Author Contributions

Chapter 1, 2 & 5: *Introduction*

Written exclusively by LG.

Chapter 3: *Efficient capture and storage of ammonia in robust aluminium-based metal–organic frameworks*

Lixia Guo, Joseph Hurd, Meng He, Wanpeng Lu, Jiangnan Li, Danielle Crawshaw, Mengtian Fan, Sergei Sapchenko, Yinlin Chen, Xiangdi Zeng, Meredydd Kippax-Jones, Zhaodong Zhu, Wenyuan Huang, Pascal Manuel, Mark D. Frogley, Daniel Lee, Martin Schröder and Sihai Yang

L.G. and W.H. synthesised and characterised the MOF samples, measured and analysed adsorption isotherms and the breakthrough data. J.H. and D.L. collected and analysed the ssNMR data. M.H., J.L., D.C., M.F., S.S., P.M., Y.C. and L.G. collected and analysed the NPD data. W.L., X.Z., J.L., M.K.-J., M.D.F. and L.G. collected and analysed SRIR data. L.G and Z. Z collected the TPD data. M.S. and S.Y. directed and supervised the project. L.G., J.H., M.H., D.L., M.S. and S.Y prepared the manuscript.

Chapter 4: *High capacity ammonia adsorption in a robust metal–organic framework mediated by reversible host–guest interactions*

Lixia Guo, Xue Han, Yujie Ma, Jiangnan Li, Wanpeng Lu, Weiyao Li, Daniel Lee, Ivan da Silva, Yongqiang Cheng, Svemir Rudic, Pascal Manuel, Mark D. Frogley, Anibal J. Ramirez-Cuesta, Martin Schröder and Sihai Yang

L.G. synthesised and characterised the MOF samples, measured and analysed adsorption isotherms and the breakthrough data. Y. M., W. L., S. R., and P. M., collected the NPD data. I. S., refined the structure from the NPD data. L.G. analysed the structure from the NPD data. X.H., Y.C., and A.R.C., collected and analysed INS data. D. L. collected and analysed the ssNMR data. J.L., W. Lu and M. F. and L.G. collected and analysed the IR data. M.S. and S.Y. directed and supervised the project. L.G., X.H., D.L., M.S. and S.Y prepared the manuscript.

Chapter 5: *Direct visualisation of supramolecular binding and separation of light hydrocarbons in MFM-300(In)*

Lixia Guo, Mathew Savage, Joseph H. Carter, Xue Han, Ivan da Silva, Pascal Manuel, Svemir Rudic, Chiu C. Tang, Sihai Yang and Martin Schröder

M.S. and L. G. synthesised and characterised the MOF samples, measured adsorption isotherms. L.G. analysis the adsorption isotherms, collected and analysised the breakthrough data. J.H.C., P.M. and I.S. collected and refined the NPD data. L. G. analysed the structure from the NPD data. S.R. and C.T. collected, X. H. analysed the INS data. M.S. and S.Y. directed and supervised the project. L.G., M.S. and J.H.C., X.H., M.S. and S.Y prepared the manuscript. L.G., M.S. and S.Y revised the manuscript. L.G., M.S. and J.H.C. authors contribute equally to this work.

List of Works

1. **Guo, L.;** Han, X.; Ma, Y.; Li, J.; Lu, W.; Li, W.; Lee, D.; Silva, I.; Cheng, Y.; Rudic, S.; Manuel, P.; Manuel, P.; Frogley, M.; Cuesta, A.; Schröder, M. and Yang, S. High capacity ammonia adsorption in a robust metal–organic framework mediated by reversible host–guest interactions. *Chem. Commun.*, **2022,** *58*, 5753−5756. (IF = 6.605).

2. **Guo, L.;** Savage, M.; Carter, J.; Han, X.; Silva, I.; Manuel, P.; Rudic, S.; Tang, C.; Yang, S. and Schröder, M. Direct visualization of supramolecular binding and separation of light hydrocarbons in MFM-300(In). *Chem. Mater.* **2022,** *34*, 5698–5705. (IF = 10.508).

3. **Guo, L.;** Hurd, J.; He, M.; Lu, W.; Li, J.; Crawshaw, D.; Fan, M.; Sapchenko, S.; Chen, Y.; Zeng, X.; Jones, M.; Huang, W.; Zhu, Z.; Manuel, P.; Frogley, M.; Lee, D.; Schröder, M. and Yang, S. Efficient capture and storage of ammonia in robust aluminium-based metal–organic frameworks. *Commun. Chem.*, **2023**, *6*, 55. (IF=7.211).

4. Lu, W.; Chen, Y.; Wang, Z.; Chen, J.; **Guo, L.;** Ma, Y.; Li, W.; Li, J.; He, M.; Fan, M.; Sheveleva, A.; Tuna, F.; McInnes, E.; Frogley, M.; Chater, P.; Dejoie, C.; Schröder, M. and Yang, S. High ammonia adsorption in copper-carboxylate materials: host–guest interaction and crystalline-amorphous-crystalline phase transition. *To be submitted.*

5. Huang, W.; Mei, Q.; Xu, S.; An, B.; He, M.; Li, J.; Chen, Y.; Han, X.; Luo, T.; **Guo, L.;** Hurd, J.; Lee, D.; Tillotson, E.; Haigh, S.; Walton, A.; Day, S.; Natrajan, L.; M. Schröder, M. and Yang, S. Direct synthesis of N-formamides by integrating reductive amination of ketones and aldehydes and CO_2 fixation in a metal–organic framework. *Submitted.*

6 **Guo, L.;** Schröder, M. and Yang, S. The role of ligand functionalization and open metal sites in a copper-based metal–organic framework for reversed C_2H_6/C_2H_4 separation. *In preparation.*

7. **Guo, L.;** Schröder, M. and Yang, S. Efficient C_2H_2/CO_2 separation in a copper-carboxylate metal–organic framework. *In preparation.*

Chapter 1

Introduction

Chapter 1. Introduction

With the increasing exhaustion of fossil fuels reserves and rising concerns over global warming, there is a critical need to explore alternative clean energy carriers that can supplement the current fuel supplies.[1-3] This exploration is particularly essential in realising the ambitious goal of achieving net-zero carbon dioxide (CO_2) emissions by 2050.[3,4] Hydrogen (H_2) emerges as a promising green fuel due to its distinctive characteristics, including a high energy density, zero greenhouse gas emissions, and potential to be produced from renewable sources[2]. However, the production, distribution, and on-board storage of H_2 can be challenging and costly.[5] Methane (CH_4) is increasingly regarded as a potential hydrogen carrier due to its higher hydrogen-to-carbon ratio. Nevertheless, there is carbon emission during CH_4 combustion, making it a less ideal solution for contributing zero carbon emissions.[6] In comparison, ammonia (NH_3) is attracting attention as a potential transportable fuel and hydrogen carrier owing to its high volumetric hydrogen density (17.6 *wt*.% gravimetrically and 123 kg m^{-3} volumetrically, nearly double that of liquid H_2),[7,8] relatively low storage pressure requirements (10 bar)[9] and potential environmentally to fascinate zero carbon emissions.[2,5,10] Given these characteristics, NH_3 can play a crucial role in helping achieve a sustainable and carbon-neutral energy future.

Another critical strategy to help contribute to the goal of achieving net-zero CO_2 emissions by 2050 is through improvements in energy efficiency, which could substantially reduce overall energy consumption.[11] Ethylene (C_2H_4) and propylene (C_3H_6) are essential building blocks for the production of plastics and advanced chemicals, with the demand for C_2H_4 and C_3H_6 is estimated to increase threefold by 2050.[12-14] This indicates a significant growth in the use of these olefins, highlighting

the importance of efficient and sustainable production and purification processes. The purification of these olefins from their olefins/paraffins mixtures has been recently identified as "one of the seven purifications that can change the world".[10] However, the current methods for achieving high-purity C_2H_4 and C_3H_6 involve significant energy consumption, accounting for approximately 15% of total industrial energy consumption.[15] Given the high energy cost associated with the separation process, it is evident that the development of more energy-efficient processes for the purification of olefins represents a major priority within the industry. Research and development efforts in this area can greatly contribute to the goal of reduced energy consumption and net-zero CO_2 emissions.

1.1 Ammonia and olefins economy

1.1.1 Ammonia production

NH_3 production plays a vital role in global industry with estimated annual production of 200 million tonnes, making it the second most synthetically manufactured chemical after sulfuric acid (H_2SO_4) in the world.[7,9] The conventional and most common method for NH_3 production is the Haber–Bosch process, a technology that has been invented about 100 years ago and has seen multiple improvements since then.[16] The overall reaction of this process can be represented by the following equation:[8]

$$N_2 + 3\ H_2 \rightleftharpoons 2\ NH_3 \qquad \Delta H = -91.4\ \text{kJ mol}^{-1}$$

In this process (Figure 1.1), NH_3 is basically obtained by reacting nitrogen (N_2) (separated from the air by a separation unit process) with H_2 (often generated from the natural gas or coal) in the presence of an iron-based catalyst[17]. To increase the kinetics of the reaction, it is typically performed at elevated temperatures (300–550 °C) and high pressures (200–350 bar), giving approximately 15% conversion to NH_3[6-8]. The

Haber–Bosch process is responsible for approximately 85% of the total global production of NH_3. Despite its wide use, the Haber–Bosch process, including high energy consumption, high capital and operating costs, and significant greenhouse gas emissions.

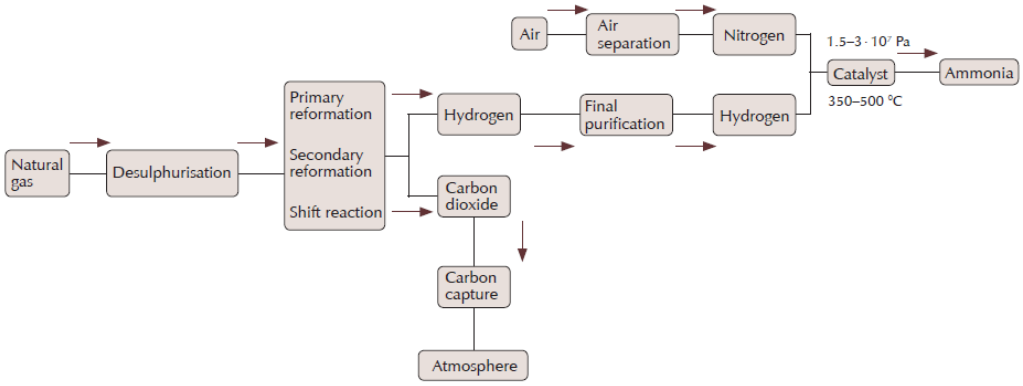

Figure 1.1. The current Haber–Bosch process for production of ammonia.[16]

The thermochemical cycle has emerged as a potential alternative method for NH_3 production, which comprises a two-step process: N_2 activation through reduction, followed by NH_3 formation through steam-hydrolysis.[18] Unlike the Haber–Bosch process, the thermochemical cycle can operate at atmospheric pressure without the use of a catalyst, eliminating the need for high-pressure equipment and thereby reducing the energy consumption and greenhouse gas emissions. However, this system requires very high operating temperatures, typically above 800 °C, which restricts the available heat sources and materials.[18] Moreover, the development of stable and efficient materials for both N_2 reduction and hydrolysis steps poses a significant challenge. Despite these challenges, this system shows great promise, and ongoing research is focused on improving its efficiency, scalability, and sustainability.

1.1.2 Ammonia storage

Despite its promising role as a potential energy carrier, the toxic and corrosive nature of NH_3 makes the high risk associated with its accidental release. NH_3 concentrations of 1700 ppm can be detrimental to both the environment and human health.[7,19,20] To facilitate safe transportation, NH_3 is commonly stored either in a liquefied state at atmospheric pressure at 240 K, or in pressurised vessels at approximately 10 bar at ambient temperature.[6,20,21] This method employs existing infrastructure, including pipelines, tankers, and ships.[6] However, this requires harsh operating conditions and comes with high energy costs, giving rise to challenges in its transportation, storage, and conversion. Consequently, reducing or eliminating the energy consumption associated with NH_3 storage is highly desirable.

In this regard, porous sorbents have been foreseen as prospective adsorbents for gas capture and storage following the discovery of their permanent porosities. These materials offer advantages over traditional energy-intensive gas storage technologies.[1,22] By adsorbing NH_3 within their porous frameworks, these materials can store quantities of NH_3 under milder conditions compared to traditional methods, potentially decreasing the energy cost and safety risks associated with storing and transporting NH_3.

1.1.3 Olefins production

C_2H_4 and C_3H_6, which belong to the class of unsaturated hydrocarbons featuring a single double bond, serve as essential building blocks for the production of polyethylene and polypropylene polymers, as well as many other industrial chemicals.[12-14] The annual production of C_2H_4 reached 201 million metric tons in

2020,[23] while C_3H_6 production exceeded 130 million metric tons in 2019.[24,25] Notably, production of C_2H_4 and C_3H_6 alone accounts for approximately 0.3% of global energy consumption,[10] underscoring the urgency of developing energy-efficient methods for their production and purification.

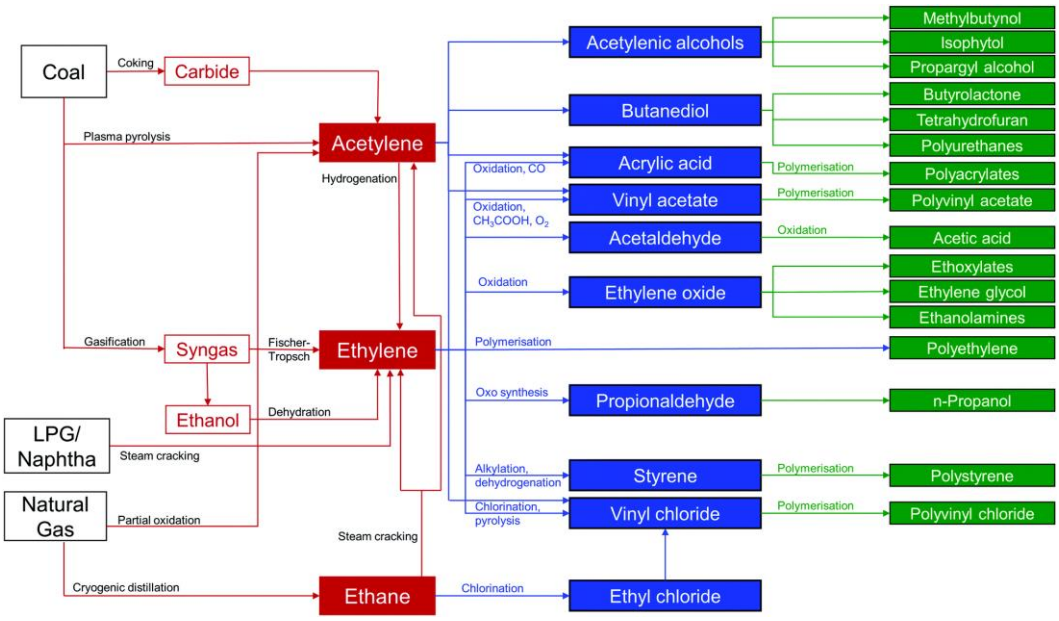

Figure 1.2. A schematic of industrial routes for the production of C_2 hydrocarbons and derived products.[31]

The primary production method for C_2H_4 relies on the steam cracking of naphtha and C_2H_6, which remains the dominant method employed in the petrochemical industry (Figure 1.2). During this process, it unavoidably produces C_2H_6 (5−9 %) and a small amount of acetylene (C_2H_2) as byproduct.[26-30] In this process, C_2H_6 acts as a diluent, extending the residence time within the reactor, which in turn reduces the production rate of C_2H_4. Furthermore, the escape of C_2H_6 during the polyethylene process can lead to emissions with potential detrimental effects on both the environment and human health. C_2H_2 is highly reactive and can deactivate the catalysts used in the polyethylene process, impacting the production quality of polyethylene. Additionally, when C_2H_2 comes into contact with metal catalysts or pipelines, it can form solid metal

acetylides. These solid can block fluid flow, potentially causing operational issues and even posing a risk of explosions.

C_3H_6 is primarily produced through steam cracking in petroleum refining or the cracking of propane (C_3H_8) (Figure 1.3). It is common for C_3H_6 accompanied by impurities such as C_3H_8 (0.2–4.0 %), and trace amount of propyne (C_3H_4) as undesirable by product.[32,33,36] C_3H_8 can interfere with propylene polymerization reactions, potentially affecting the quality of the final product. C_3H_4, on the other hand, can act as a catalyst poison, reducing the effectiveness of the catalysts and leading to a decrease in polymerization efficiency. Given these factors, it is crucial to purify C_2H_4 and C_3H_6 to a purity of >99.95% that is required to meet polymer grade specification.[34,35]

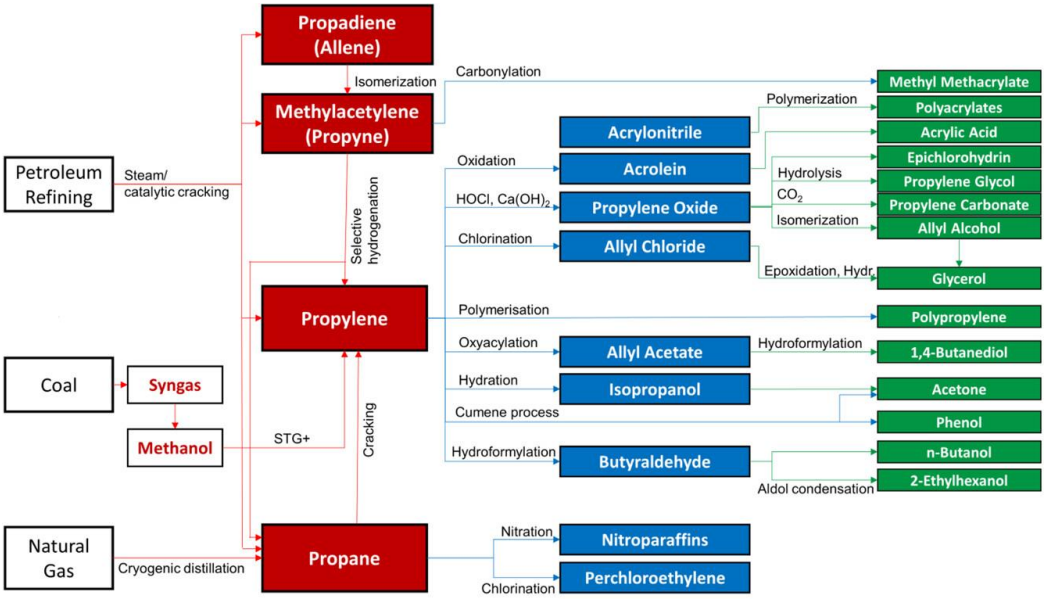

Figure 1.3. A schematic diagram that highlights industrial routes for production of C_3 hydrocarbons and derived products.[36]

1.1.4 Purification of olefin

The cryogenic distillation is a widely used process in industrial purification of C_2H_4 and C_3H_6 from their respective mixtures (Figure 1.4),[37,38] which operates by taking advantages of the different boiling temperatures of mixed gases (boiling point for C_2H_4: 169.4 K; C_2H_6: 184.5 K; C_3H_6: 225.4 K; C_3H_8: 231.1 K).[39,40] The process involves cooling of these mixed gases to their respective boiling points for vaporisation, subsequently separating them based on their boiling temperatures. Gases with lower boiling temperatures will vaporise first, allowing them to be separated from those with higher boiling temperatures.

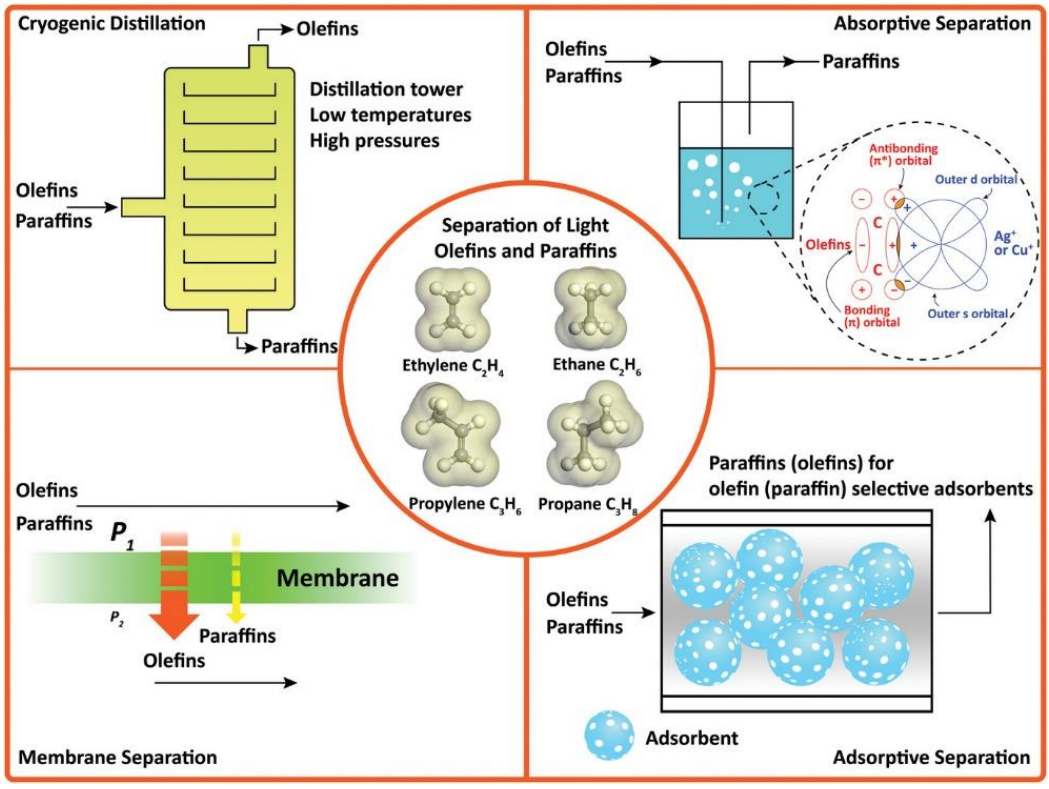

Figure 1.4. A schematic comparison of different processes of light olefin/paraffin separations.[38]

The distillation process generally necessitates multiple evaporation-condensation cycles under severe conditions, often operating within a temperature ranging from 180

to 583 K and pressure ranging from 7 to 28 bar.[41] Moreover, cryogenic distillation often requires the use of more than 100 distillation trays and reflux ratios as high as 20, making it an extremely energy-intensive process. Such techniques account for approximately 90–95% of all separations, and 10–15% of the global energy consumption.[10,42]

Furthermore, the cryogenic distillation process involves the use of liquid adsorbents that requires a complete separation process, including heating and cooling of the adsorbent to release the adsorbed gas. This additional step can lead to an increase in energy consumption, higher operating costs, reduced energy-efficient and significant carbon emissions. Given these factors, the need for alternative purification technologies that are more energy-efficient, cost-effective, and environmentally friendly is apparent. The pursuit and implementation of innovative and sustainable separation technologies have the potential to contribute towards achieving net-zero carbon emissions by 2050.

Physisorption-based purification methods using solid porous materials offer the potential to reduce the energy footprint associated with the purification processes, and have experienced an explosive growth (Figure 1.5).[13] These separation processes rely on differential adsorption capability of various components within the gas mixture by the adsorbent to achieve gas separation. A general process of adsorptive gas separation or purification includes passing the gas mixture through a column packed with adsorbents or fixed-bed adsorbents. This results in the production of a product enriched in the component that is more weakly adsorbed, followed by desorption of the strongly adsorbed component allowing the adsorbent to be reused. A desirable adsorbent for

this purpose should possess several key characteristics. These include high adsorption capacity and selectivity, good stability, as well as favourable adsorption kinetics and regenerability.

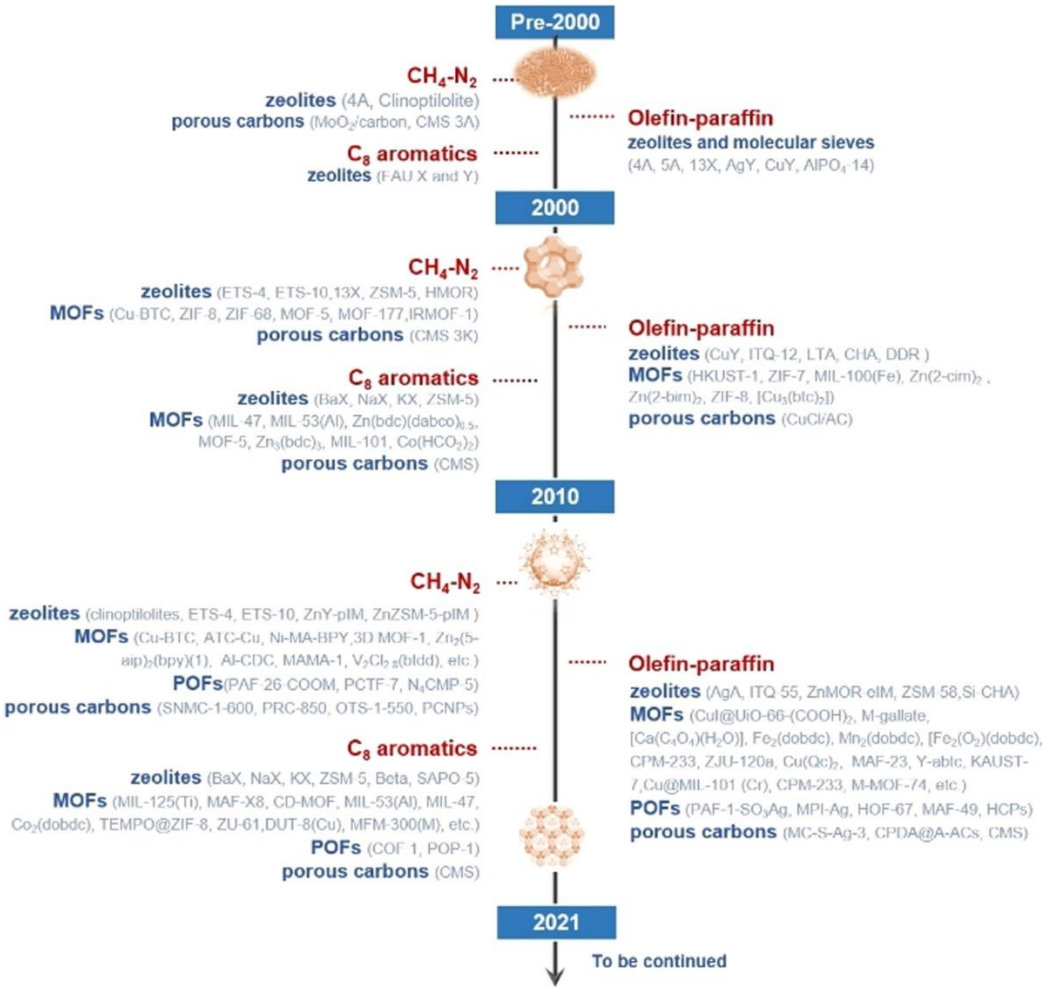

Figure 1.5. Timeline summarizing the trends in adsorptive hydrocarbon separation and purification with various porous materials over the latest three decades.[13]

1.2 Porous adsorbents

Conventional porous adsorbents, including activated carbons and zeolites, have been extensively utilised for various gas storage and separation applications, such as NH_3 storage and light hydrocarbons separation.[15,43] However, the restricted surface area and the challenge in tailoring the pore structure of carbon materials and zeolites often limit their gas storage and separation efficiency.[13] Moreover, achieving fine-tuning and

directed chemical manipulation of active sites in these materials at the atomic level can be challenging due to the lack of direct structural insights and limited structural diversity.

Metal–organic frameworks (MOFs), constructed from metal ions/clusters and organic ligands, have attracted significant attention as a rapidly expanding class of porous crystalline materials. Their appeal stems from their extraordinary properties, such as large porosity, crystallinity for structure determination, structural diversity, and tunable functionalities.[44] These versatile characteristics make MOFs as promising candidates to meet the specific requirements of various applications, ranging from gas adsorption,[2,45-47] separation,[42,48,49] catalysis,[50,51] to water harvesting,[52,53] and drug delivery,[54] *etc.*, highlighting the unique role that other inorganic materials cannot replicate.

The moieties, metal ions/clusters and organic ligands, can be rationally designed and functionalised, providing diverse active sites such as open metal sites (OMSs)[55] and functional groups (*e.g.*, hydroxyl group: –OH, carboxyl group: –COOH, amino group: –NH_2, *etc.*).[56] These groups are instrumental in enhancing specific interactions and distinguishing gases for gas adsorption and separation.[57] Besides, the high porosity and tunable pore sizes in MOFs offer exceptional potential for delivering high gas adsorption uptake and targeted gas separation by accommodating and/or excluding gases.

More importantly, the crystalline nature of MOFs provides a valuable platform for a better understanding of structure-properties relationships at the atomic level for further

development. The start-of-the-art characterization techniques have been developed to investigate host–guest interactions and elucidate the sorption and separation mechanisms of MOFs.[58,59] Techniques such as synchrotron powder X-ray diffraction (sPXRD),[60,61] *in-situ* neutron powder diffraction (NPD),[62] *in-situ* synchrotron infrared spectroscopy (SRIR),[63,64] and *in-situ* inelastic neutron scattering (INS)[61,65] have played a crucial role in providing detailed information about structural changes, host–guest interactions, and dynamic behaviour of gases within MOFs.

1.3 Ammonia adsorption in MOFs

MOF materials have gained huge interests in the field of NH_3 adsorption studies.[19,66] The ideal MOFs used as efficient adsorbents for NH_3 capture and storage should possess high affinity, high working capacity (i.e. NH_3 uptake, packing and storage density), easy recyclability and excellent stability towards NH_3.[19,64,67] This thesis engages with the design strategy, specifically focus on enhancing NH_3 uptakes and MOF stability.

1.3.1 MOFs with unsaturated metal sites

One effective strategy to improve NH_3 uptakes is the incorporation of open metal sites (OMSs) within the MOF frameworks.[68,69] The presence of an electron-deficient metal centre originating from OMSs can function as Lewis acidic sites, which enables them to exhibit a strong affinity towards basic NH_3 molecules. The relatively strong affinity between the OMSs and the guest molecules facilitates efficient gas capture and/or storage under low and/or high concentrations. An illustrative example of this proposition can be seen in a study conducted by Saha and Deng in 2010, which investigated NH_3 adsorption in two benchmark MOFs, MOF-5 and MOF-177.[68] These

MOFs demonstrated an NH_3 capacity of 12.1 mmol g^{-1} at 1.0 bar and 298 K. However, it was observed that both materials suffered a loss of crystallinity and porosity upon NH_3 exposure. This was evidenced by the disappearance of almost all Bragg peaks in the powder X-ray diffraction (PXRD) patterns and a reduction in the Brunauer–Emmett–Teller (BET) surface area.

While the strong coordination between NH_3 and OMSs can indeed enhance NH_3 adsorption capacity, it is important to consider the potential structural collapse or irreversible desorption that may arise from the formation of covalent bonds between OMSs and NH_3. Employing ligands with stronger donating ability for the metals, such as triazolate, could potentially improve the tolerance of the framework to NH_3 to a certain extent.[69] One example of this proposition is the study by Dincă *et al.* in 2016, where they reported the M_2Cl_2BTDD (BTDD = bis(1*H*-1,2,3-triazolo[4,5-b],[4′,5′-*i*])dibenzo[1,4]dioxin; M = Mn, Co, Ni and Cu) materials that utilize strong donor triazolate linkers to create a high density of open metal sites.[69] The M_2Cl_2BTDD analogues exhibited NH_3 uptakes of 15.47 mmol g^{-1} (Mn), 12.00 mmol g^{-1} (Co) and 12.02 mmol g^{-1} (Ni), respectively. In the case of Mn_2Cl_2BTDD material, despite the observed loss of porosity after NH_3 adsorption, the open metal sites responsible for binding NH_3 remained accessible. This indicated that a decrease in BET surface area does not predict a decline in NH_3 uptakes definitively. Rather, the strength of interaction between the material and NH_3 serves as a better predictor of the overall uptake. Moreover, M_2Cl_2BTDD materials exhibited greater stability towards NH_3 compared to MOF-5, displaying reversible NH_3 adsorption over at least three cycles. The strong donor nature of the triazolate linkers in M_2Cl_2BTDD materials is proposed

to effectively shield the metal sites from direct interaction with NH_3, contributing to the stability of M_2Cl_2BTDD towards NH_3.

In the pursuit of enhancing NH_3 capacity in MOFs without OMSs, researchers have explored the introduction of open active sites into defected MOFs. A recent study conducted by the Schröder and Yang group in 2021 reported an enhancement of NH_3 uptake in UiO-66-Cu, achieved through the decorating open Cu sites into UiO-66-defect.[70] The study revealed that UiO-66-defect, UiO-66-Cu^{I} and UiO-66-Cu^{II} exhibited comparable surface areas, ranging from 1111 to 1135 $m^2 g^{-1}$. However, UiO-66-Cu^{II} demonstrated a significant improvement of 43% in the NH_3 isothermal uptake of 16.9 mmol g^{-1} at 273 K and 1.0 bar, as compared to 11.8 mmol g^{-1} in UiO-66-defect (Figure 1.6). Furthermore, a 100% enhancement was observed in the dynamic NH_3 adsorption at 630 ppm and 298 K (from 2.07 mmol g^{-1} in UiO-66-defect to 4.15 mmol g^{-1} in UiO-66-Cu^{II}). The enhancements in NH_3 uptake observed in UiO-66-Cu^{II} highlighted the successful introduction of open Cu sites into the UiO-66-defect framework.

The presence of stronger host–guest interactions in UiO-66-Cu^{II}, as compared to UiO-66-defect and UiO-66-Cu^{I}, was consistent with the higher heat of adsorption (Q_{st}) calculated for UiO-66-Cu^{II} (55 kJ mol^{-1}) than UiO-66-defect and UiO-66-Cu^{I} (40 and 35 kJ mol^{-1}, respectively). A comprehensive analysis employing NPD, ssNMR, and IR spectroscopy revealed that the enhanced NH_3 uptake in UiO-66-Cu^{II} originated from the unique Cu(II) sites forming the {Cu(II)$\cdots NH_3$} interaction. A reversible change in geometry at Cu(II) from near-linear to trigonal coordination was observed. This was distinct from four and five-coordinated Cu(II) sites that can lead to

irreversible structural degradation upon desorption of NH_3. These findings highlighted the importance of designing and fine-tuning active sites within MOFs for achieving high-performing NH_3 adsorption while retaining the porosity of a given material.

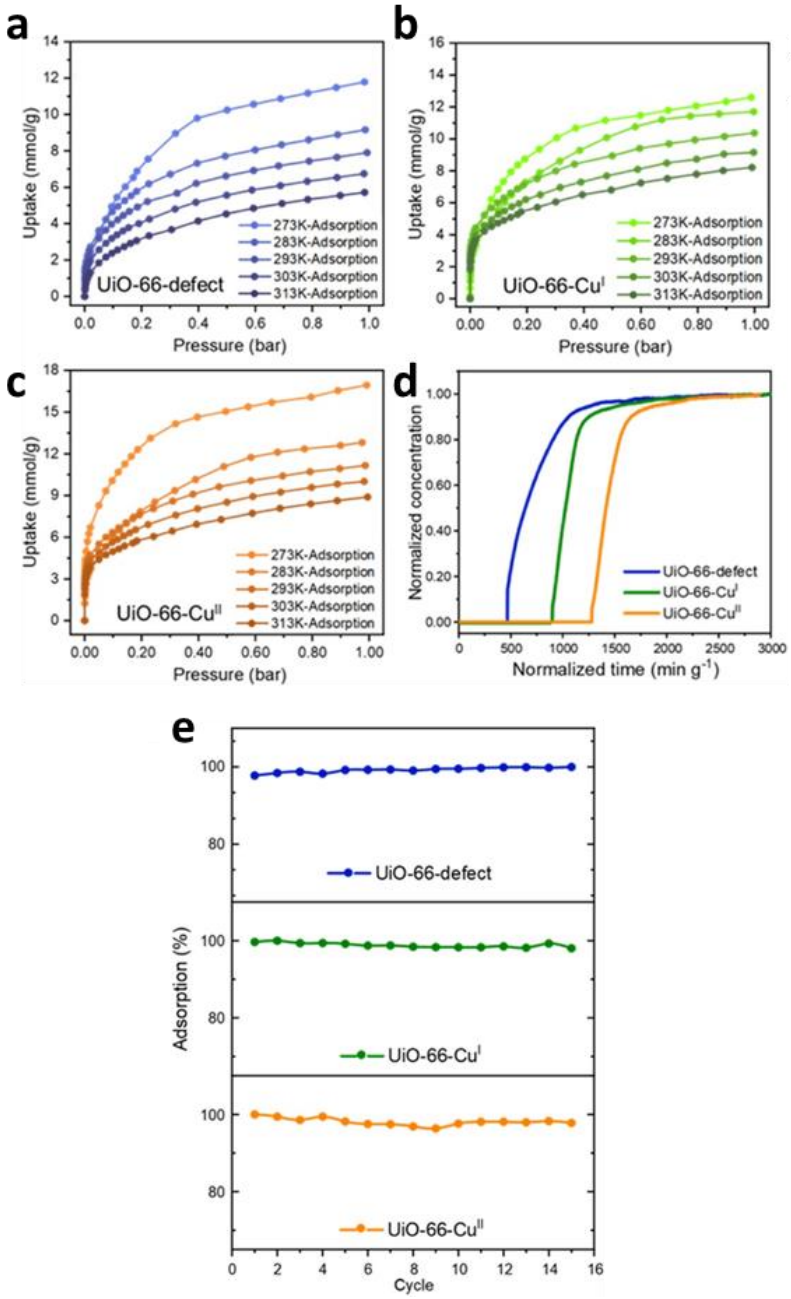

Figure 1.6. Adsorption isotherms for NH_3 in (a) UiO-66-defect, (b) UiO-66-Cu^{I}, and (c) UiO-66-Cu^{II} from 273 to 313 K. (d) Breakthrough curves at 298 K of NH_3 (630 ppm of NH_3 diluted in He) through a fixed-bed packed with UiO-66-defect, UiO-66-Cu^{I}, and UiO-66-Cu^{II}. (e) Cycles of pressure-swing sorption of NH_3 at 298 K between 0 and 0.15 bar in UiO-66-defect, UiO-66-Cu^{I}, and UiO-66-Cu^{II}.[70]

1.3.2 MOFs with functional groups

Grafting functional groups (*e.g.*, –OH, –COOH, heteroatom oxygen) onto the pore interiors is another efficient method to enhance NH_3 adsorption affinity and uptakes. These functional groups can introduce diverse interactions like hydrogen bonding, electrostatic interactions, and acid-base interactions, which are relatively weaker compared in comparison to OMSs.[61,71]

Schröder and Yang *etc.*, reported the utilisation of Brønsted acidic –OH and/or –COOH moieties in MFM-30X series (MFM = Manchester Framework Material, replacing NOTT = Nottingham University designation) as primary binding sites to promote the adsorption of NH_3.[61,64,72,73] For example, MFM-300(Al), featuring the bridging μ_2-OH groups at the four corners of its square-shaped channel, displayed an exceptional NH_3 packing density of 0.62 g cm^{-3} under near ambient conditions (with reference to liquid NH_3 of 0.68 g cm^{-3} at 240 K). It outperformed the start-of-the-art materials in terms of NH_3 packing density, reversibility and stability. *In situ* NPD for $1.5ND_3$/Al-loaded MFM-300(Al) identified three distinct binding sites (Figure 1.7). The adsorbed site I of ND_3 dominantly formed hydrogen bonding with the bridging μ_2–OH along with the channel. The short distance [μ_2–O<u>H</u>··· <u>N</u>D_3 = 1.76(2) Å] and the high Q_{st} (> 40 kJ mol^{-1}) indicated a strong binding mode being present between NH_3 and MFM-300(Al). The presence of site II and III contributed to an extensive hydrogen bonding network of ND_3 molecules along the 1D channel of the framework, which enhancing the adsorption and interaction of ND_3 within the material. *In situ* synchrotron IR micro-spectroscopy witnessed a rapid and reversible site-exchange between hydrogen (H) and deuterium (D), with no detectable structural degradation of the long-range order of the framework. This observation signifies the structural

integrity and stability of MFM-300(Al) during NH_3 adsorption and exchange processes.

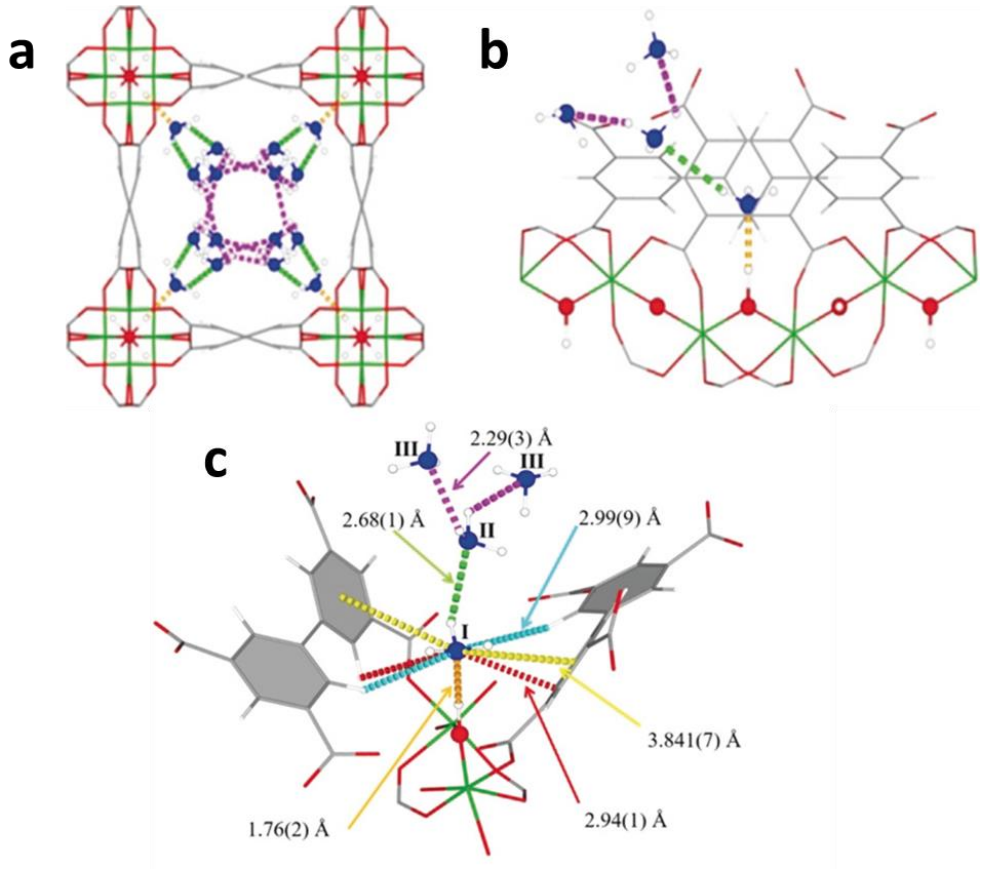

Figure 1.7. View of the structure of 1.5 ND_3/Al-loaded MFM-300(Al) determined by *in-situ* NPD studies.[64]

Moreover, the enhanced acidity of Brønsted acidic hydroxyl groups facilitates the formation of hydrogen bonds with NH_3, thus giving rise to stronger interaction and higher NH_3 uptake.[74] Farha *etc.*, reported three isoreticular porphyrin-based MOFs with one-dimensional metal (Al, Ga, and In) nodes and bridging −OH sites for NH_3 adsorption.[74] At 298 K and 1.0 bar, Al-PMOF, Ga-PMOF, and In-PMOF exhibited NH_3 adsorption uptakes of 7.67 mmol g^{-1}, 10.50 mmol g^{-1}, and 9.41 mmol g^{-1}, respectively. The isotherm curves for Ga-PMOF and In-PMOF indicated a more pronounced uptake in the low-pressure region (< 0.1 bar), whereas Al-PMOF showed nearly a linear uptake with increasing pressure. This suggested a stronger affinity of

NH_3 by Ga-PMOF and In-PMOF, resulting in a steeper and significant uptake at low pressures. Furthermore, the comparison of NH_3 adsorption between first and second cycles revealed that Ga-PMOF and In-PMOF retained a significant portion of the adsorbed NH_3, which were comparable to the calculated –OH group sites in the ideal MOF. This indicated that the NH_3 molecules adsorbed to –OH sites were not desorbed prior to the second cycle, suggesting a stronger interaction between NH_3 and –OH sites in Ga-PMOF and In-PMOF compared to Al-PMOF. The diffuse reflectance infrared Fourier transform spectroscopy (DRIFTS) analysis (Figure 1.8) provided the evidence supporting the impact of metal identity on the strength of the Brønsted acidic −OH sites in MOFs. Specifically, the results indicated that the acidity of −OH sites followed the trend of Al-PMOF > Ga-PMOF > In-PMOF, resulting in stronger interactions between NH_3 and the framework in Ga-PMOF and In-PMOF compared to Al-PMOF.

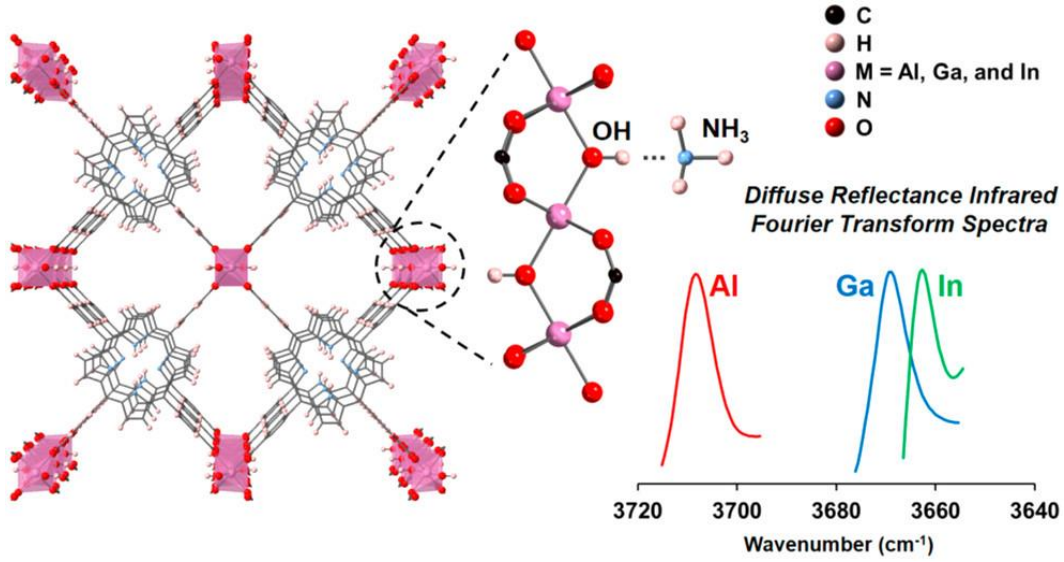

Figure 1.8. Structure and DRIFTS spectra of M-PMOF (M = Al, Ga, and In).

Furthermore, the strategy of increasing the number of active sites in the ligands was employed to construct multiple bonding sites with NH_3 in MOF-303(Al).[71] This approach resulted in MOF-303(Al) exhibited a high adsorption capacity of 19.7 mmol

g^{-1} at 298 K and 1.0 bar, along with fully reversible recycling for at least 20 cycles. The Mid-IR spectra (Figure 1.9a) showed that after NH_3 adsorption, a red shift of the peak at 1209 cm^{-1} corresponding to the N−H in-plane rocking of pyrazole-3,5-dicarboxylate ligand was observed, indicating the presence of strong hydrogen bonding interactions between NH_3 and the N−H site of the MOF. Additionally, a new peak appearing at 1194 cm^{-1} was assigned to the bending of three N–H groups of adsorbed NH_3 on the N–H site of the MOF. These observations confirmed the presence of hydrogen bonding interactions between NH_3 and MOF-303(Al). The far-infrared spectra (Figure 1.9b) revealed two new peaks at 100 and 77 cm^{-1}, which were assigned to the stretching vibration of hydrogen bonds between the N atom in NH_3 and the H atom in both N−H and μ_2-OH sites of MOF-303(Al). This indicated that the multiple adsorption sites in MOF-303(Al), including N−H, μ_2-OH and H−C, formed hydrogen bonding interactions with NH_3. These multiple interactions of MOF-303(Al) contributed to the superior capacity for highly efficient NH_3 storage application.

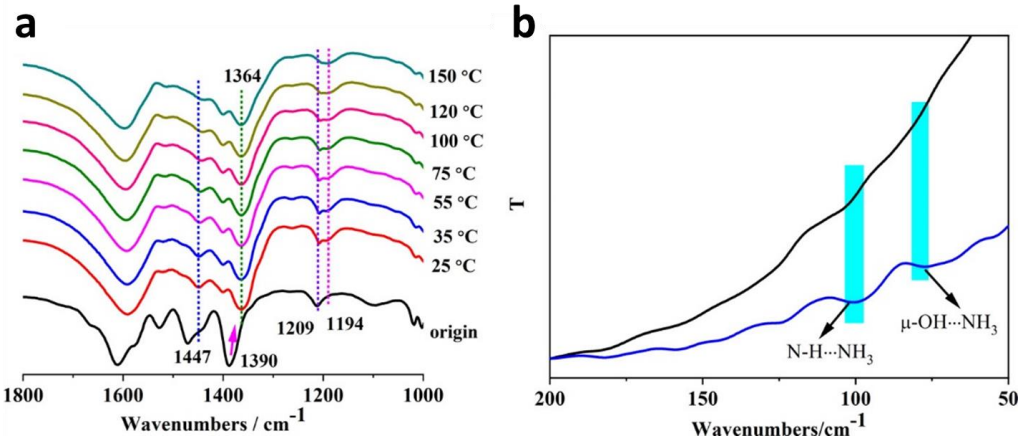

Figure 1.9. (a) Enlarged mid-IR spectra of MOF-303(Al) after NH_3 adsorption at different temperatures and normal pressure. (b) far-infrared spectra of MOF-303(Al) before (black line) and after (blue line) NH_3 adsorption.[71]

1.3.3 MOFs with confinement effect

The diverse range of pore sizes, shapes, and porosities exhibited by MOF materials plays a crucial role in enhancing their ability to adsorb NH_3. In 2018, Dincă *et al.* reported the synthesis of isoreticular analogues M_2Cl_2BBTA (M = Co, Ni, Cu; BBTA = 1H, 5H-benzo(1,2-d),(4,5-d') bistriazole), which exhibited exceptional static and dynamic NH_3 capacities.[75] Compared to the larger pore in M_2Cl_2BBTD materials,[69] the M_2Cl_2BBTA materials featured a smaller pore size and a higher density of open metal sites (Figure 1.10). The NH_3 sorption isotherms for activated M_2Cl_2BBTA (M = Co, Ni, Cu) at 298 K revealed steep uptakes at low absolute pressure. The total uptakes of NH_3 at 1.0 bar were recorded to be 17.95 mmol g^{-1}, 14.68 mmol g^{-1}, and 19.79 mmol g^{-1} for the Co, Ni, and Cu analogues, respectively. These uptake values for M_2Cl_2BBTA are considerably higher than for the larger pore M_2Cl_2BBTD materials. This could be attributed to the confinement effect within the smaller pores and the increased density of open metal sites in M_2Cl_2BBTA. Dynamic breakthrough experiments conducted with 5 ppm NH_3 demonstrated that Co_2Cl_2BBTA adsorbed a higher amount of NH_3 (6.24 mmol g^{-1}) compared to Co_2Cl_2BBTD (4.42 mmol g^{-1}). This corresponds to 1.08 and 1.00 molecules of NH_3 per open metal site, respectively. These results served as further evidence that reducing the pore size and increasing the density of open metal sites can result in a linear increase in the breakthrough performance.

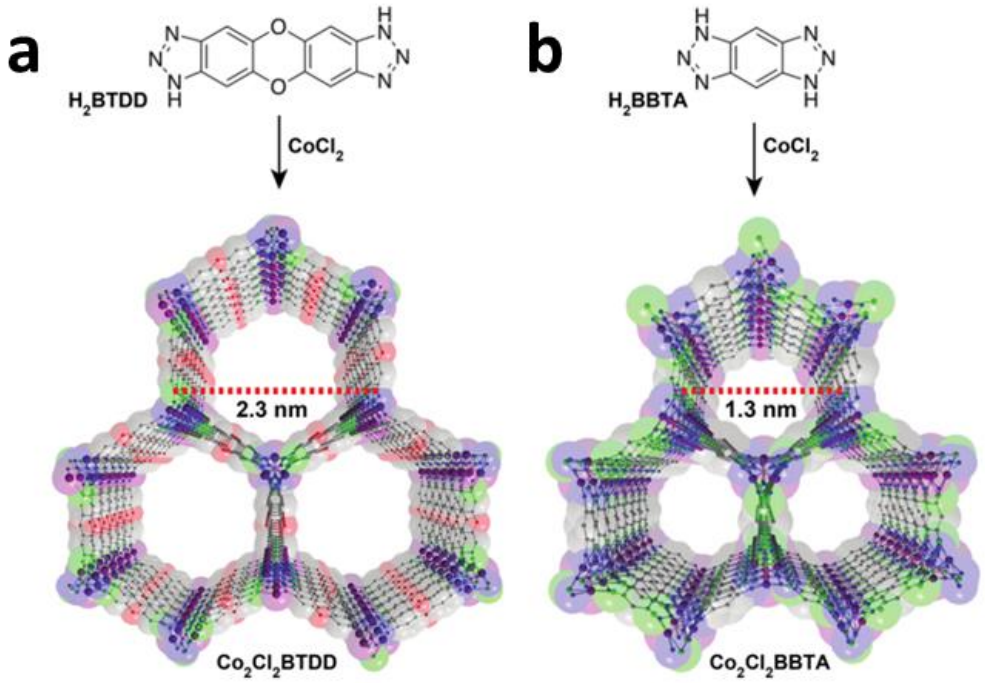

Figure 1.10. Synthesis and structure of (a) Co_2Cl_2BTDD and (b) Co_2Cl_2BBTA.[75]

1.4 Purification of olefin in MOFs

MOF materials can be meticulously designed to possess specified pore sizes and surface functionalities, enabling the selective adsorption and separation of gases based on their respective molecular size, shape and polarizability (Table 1.1).[36,39] The operative mechanisms for adsorption and separation embodied by MOFs can be of considerable complexity and are roughly classified into three major categories: molecular sieving, thermodynamic effects and kinetic effects.[41]

Table 1.1. The physical properties of light C_2 and C_3.[36,39]

Adsorbate molecules	Boiling point (K)	Kinetic diameter (Å)	Molecular size (Å^3)	Polarizability ($\times10^{-25}$ cm^3)
C_2H_2	188.40	3.3	3.3×3.3×5.7	33.3–39.3
C_2H_4	169.42	4.2	3.3×4.2×4.8	42.52
C_2H_6	184.55	4.4	3.8×4.1×4.8	44.3–44.7
C_3H_4	249.8	4.8	4.0×4.1×6.5	55.5
C_3H_6	225.46	4.7	4.2×5.3×6.4	62.6
C_3H_8	231.02	4.3–5.1	4.2×4.8×6.8	62.9–63.7

1.4.1 Selective adsorption based on molecular-sieving effect

The molecular-sieving effect refers to a selective adsorption process whereby certain molecules are prevented from entering the pores of an adsorbent, while others are permitted to enter the pores. Consequently, selective adsorption is achieved by the adsorbent material based on the size and shape of the adsorbates.

In the work documented by Chen *et al.*, the synthesis of M-gallate (M refers to Mg, Co, and Ni) MOFs was employed for selectively adsorbing C_2H_4 while blocking C_2H_6.[76] These materials are characterised by three-dimensionally (3D) interconnected zigzag channels and optimal aperture dimensions ranging from 3.47 to 3.69 Å. These dimensions precisely align with the minimal cross-section sizes of C_2H_4 (3.3×4.2×4.8 $Å^3$) and C_2H_6 (3.8×4.1×4.8 $Å^3$), thus allowing for high selectivity in favour of C_2H_4 over C_2H_6 (Figure 1.11). The Co-gallate, exhibiting a zigzag channel size of 3.69×4.95 $Å^2$, demonstrated an unprecedented ideal adsorbed solution theory (IAST) selectivity of 52 for C_2H_4 over C_2H_6, accompanied by an C_2H_4 uptake of 3.37 mmol g^{-1} at 298K and 1 bar. This performance significantly surpasses the performance of the benchmark MOF material, NOTT-300 (also named MFM-300).[80] Dynamic breakthrough experiments utilising an C_2H_4/C_2H_6 (50/50, *v*/*v*) mixture observed a complete separation. The adsorbed C_2H_4 molecules within the column can be readily desorbed by employing an inert gas, such as helium, or using the vacuum swing method after adsorption saturation. This process yielded high-purity C_2H_4, owing to the relatively weak interaction between C_2H_4 and Co-gallate.

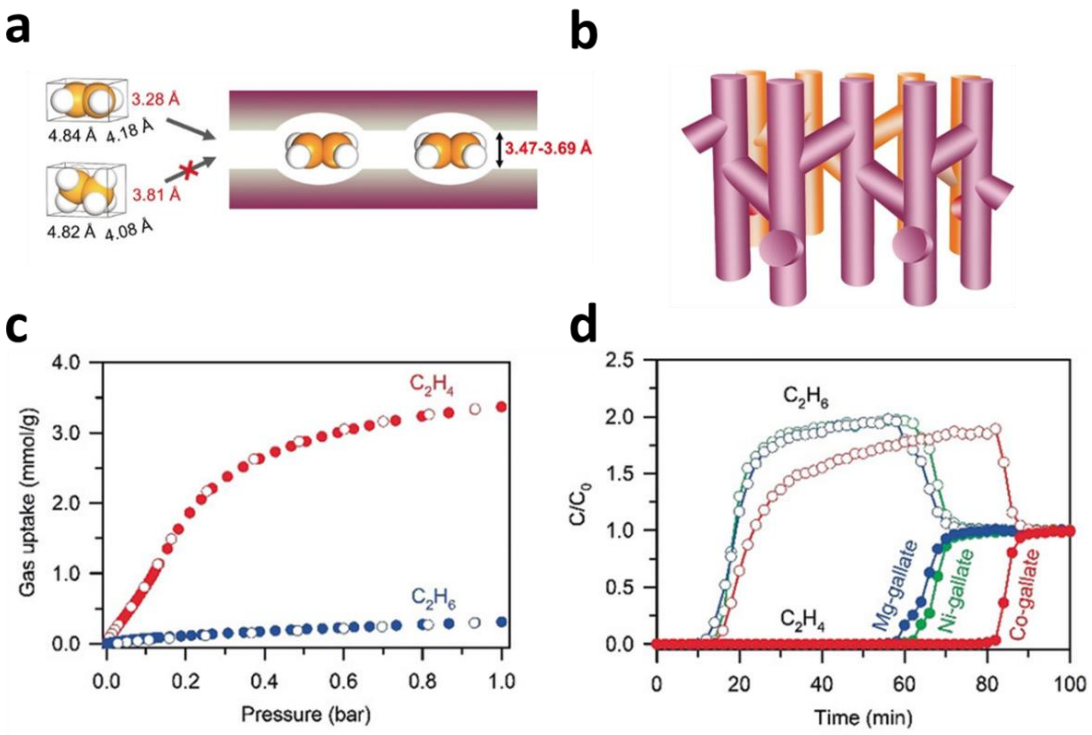

Figure 1.11. (a) Diagram of the fusiform branched channels. (b) Diagram of the zigzag channels. The zigzag channels in different layers are coloured by purple and orange, respectively. (c) Single-component adsorption isotherms of C_2H_4 (red) and C_2H_6 (blue) in Co-gallate at 298 K in the pressure range of 0–1.0 bar. (d) Experimental breakthrough curves of M-gallate for the equimolar C_2H_4/C_2H_6 mixture at 273 K and 1 bar with a constant flow rate of 0.5 mL min^{-1}.[76]

The separation of C_3H_6 and C_3H_8 molecules presents a more challenge compared to separation of C_2H_4 and C_2H_6, owing to greater similarities as the same alkyl part (i.e., the CH_3 group) are shared.[77] Li *et al*. have illustrated this complexity and has addressed it by conducting regulated separation of C_3H_6/C_3H_8 in a HIAM-301 (HIAM = Hoffmann Institute of Advanced Materials).[78] This was achieved by employing reticular chemistry to achieve a precisely distorted pore size (4.6 Å). The modified pore structure of HIAM-301 effectively excludes C_3H_8 whilst maintaining high selectivity (>150) and substantial capacity (~3.2 mmol g^{-1}) for C_3H_6 at 298 K and 1.0 bar (Figure 1.12). Column breakthrough experiments employing an equimolar mixture of C_3H_8/C_3H_6 exhibited a distinct separation in the HIAM-301 framework. From a feed

of C_3H_6/C_3H_8 = 95:5 (*v*/*v*), C_3H_6 with a purity of 99.6% was produced. This work highlighted the potential of carefully engineered MOFs such as HIAM-301 for the efficient and effective separation of gases with similar structural characteristics.

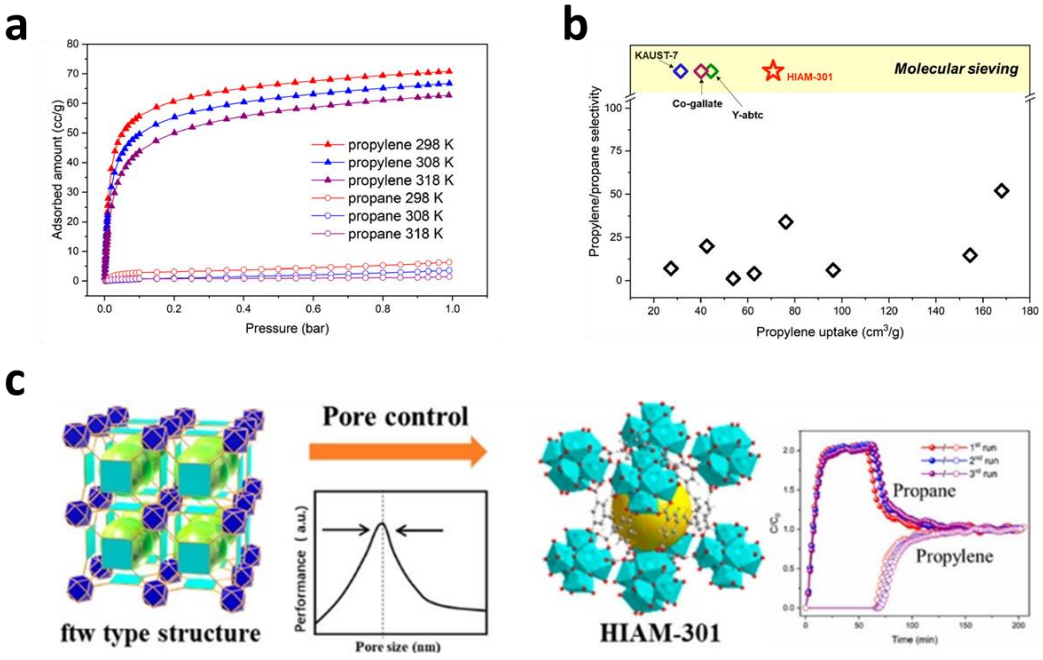

Figure 1.12 (a) Adsorption isotherms of C_3H_6 and C_3H_8 on HIAM-301. Desorption branches are omitted for clarity. (b) Comparison of C_3H_6/C_3H_8 IAST selectivity for an equimolar binary mixture and C_3H_6 gravimetric uptake (298 K and 1.0 bar) for different porous materials. (c) Structure and dynamic breakthrough curves of HIAM-301.[78]

1.4.2 Selective adsorption based on thermodynamic equilibrium

In cases where the pores of the adsorbent are sufficiently large to permit the passage of all component gases, the interaction between the adsorbate and the adsorbent becomes a crucial role in determining separation efficiency.[79] The strength of interaction can be modulated by designing MOFs with OMSs or by incorporating functional groups into the frameworks. One such example is the $[M_2(dobdc)]$ (M= Fe, Co, Mn). These materials can selectively adsorb unsaturated molecules such as C_2H_4 and C_3H_6 over saturated C_2H_6 and C_3H_8 by exploiting the π-complexation interactions between C=C bonds and open metal sites.[40] However, these strong binding interactions

necessitate considerable energy consumption for regeneration. Moreover, these materials often demonstrate rapid decline in activity when exposed to moisture. Conversely, a hydroxyl-functionalized porous MOF, NOTT-300 (also referred to as MFM-300),[80] has demonstrated exceptional structural stability under varied conditions, as well as high selectivity of 2.30 for C_2H_2/C_2H_4 and 48.7 for C_2H_4/C_2H_6 (Figure 1.13 b-c). Comprehensive characterization studies suggested that the –OH groups, aromatic C-H groups and phenyl rings present in NOTT-300 participate in weak additive, supramolecular interactions, preferential adsorbing unsaturated molecules such as C_2H_2 and C_2H_4. The moderate Q_{st} of 16–32 kJ mol^{-1} (C_2H_2 > C_2H_4 > C_2H_6) in NOTT-300 (Figure 1.13 d) confirmed that these relatively weak supramolecular bonding interactions are capable of selectively recognizing and binding guest molecules, thereby achieving high selectivity and uptake capacity simultaneously.

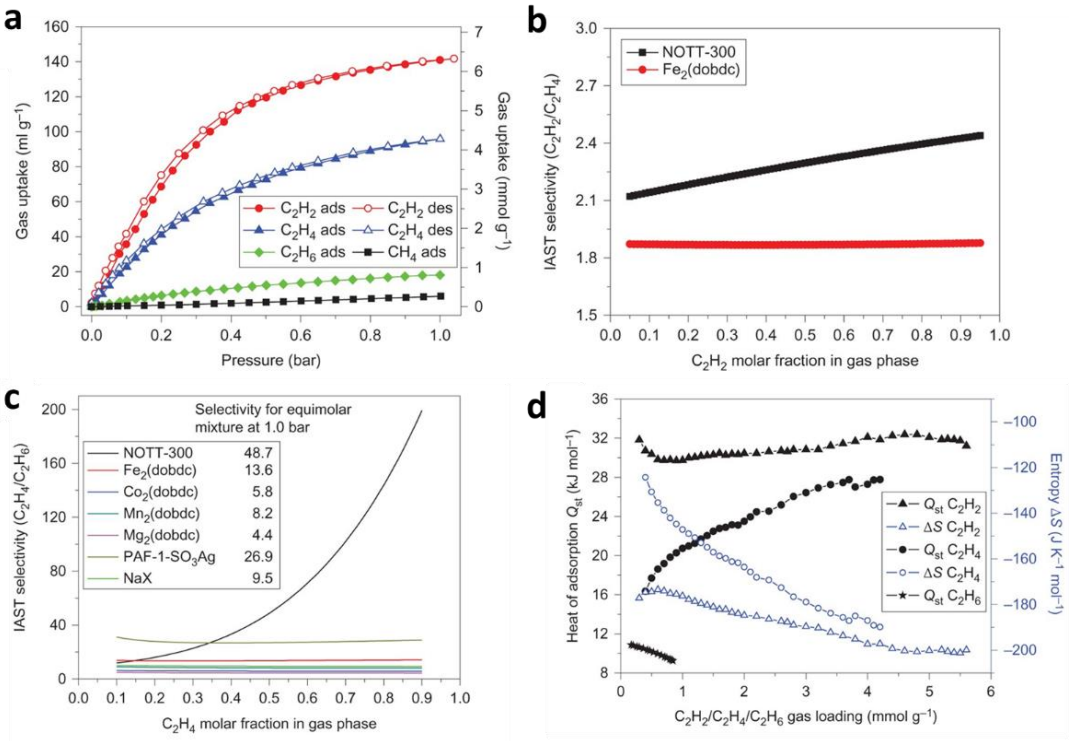

Figure 1.13. Hydrocarbon adsorption isotherms, selectivity data and heat of adsorption in NOTT-300.[80]

The incorporation of functional groups in MOFs can enhance gas uptakes and separation compared to its parent material.[30] For example, the amino−functionalized Tb-MOF-76(NH_2) demonstrated increased C_2H_6 and C_2H_4 uptakes as well as C_2H_6/C_2H_4 selectivity in comparison to Tb-MOF-76 (Figure 1.14). Furthermore, Tb-MOF-76(NH_2) exhibited a superior one-step separation performance for C_2H_6/C_2H_4 mixtures, achieving a high C_2H_4 purity (> 99.95%) and productivity of 17.66 L kg^{-1}, a significant increase from 7.53 L kg^{-1} exhibited by Tb-MOF-76. This improved outcome can be attributed to the suitable pore confinement and accessible $-NH_2$ groups on pore surfaces.[30]

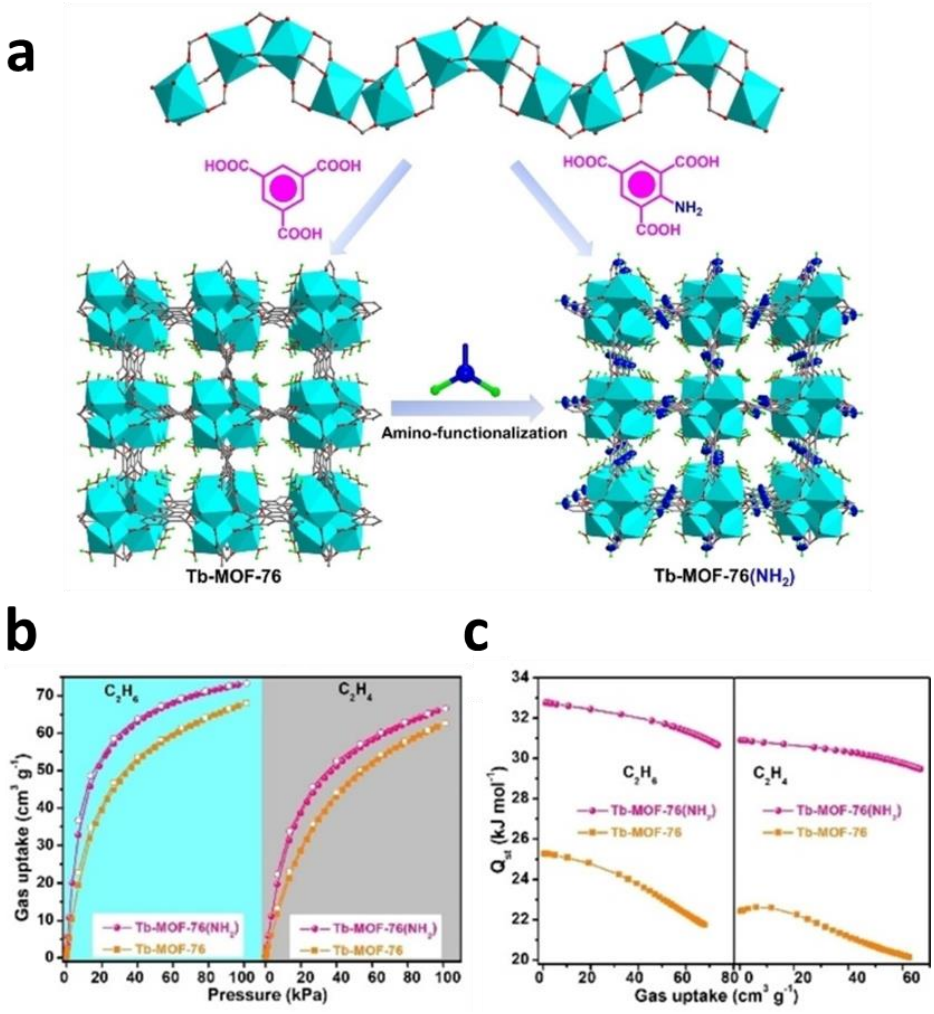

Figure 1.14 (a) Isostructural frameworks of Tb-MOF-76 and Tb-MOF-76(NH_2). (b) C_2H_4 and C_2H_6 sorption isotherms at 298 K; (c) Q_{st} plots of C_2H_4 and C_2H_6.[30]

The introduction of functional groups can even inverse the selectivity of its parent material due to alterations in host–guest interactions.[81] At present, most MOFs preferentially adsorb C_2H_4 and C_3H_6 in C_2H_4/C_2H_6 and C_3H_6/C_3H_8 mixtures. This preference arises either from π-complexation interactions leading to stronger host–guest interactions, or from molecule size sieving effects due to the relatively larger gas size of paraffins relative to olefins. Nevertheless, achieving pure C_2H_4 and C_3H_6 products that are preferentially adsorbed still necessitates an additional desorption step, which often requires high temperature or vacuum conditions. Therefore, designing paraffins-selective MOFs that preferentially adsorb C_2H_6 or C_3H_8 in the mixtures of C_2H_4/C_2H_6 and C_3H_6/C_3H_8 will facilitate a one-step greener purification process for olefins.

Li and Chen *et al.* reported the utilisation of an NH_2-functionalized UiO-67-$(NH_2)_2$ as an C_2H_2/C_2H_6-selective material, thereby enabling the efficient one-step production of polymer-grade C_2H_4 from ternary mixtures (Figure 1.15).[81] The authors emphasised that efficiently enhancing C_2H_2 adsorption could be achieved by introducing Lewis basic groups (such as amino or nitrogen sites) into C_2H_6-selective MOFs, thus allowing high C_2H_2/C_2H_4 and C_2H_6/C_2H_4 separation in a single adsorbent. In this study, UiO-67-$(NH_2)_2$ displayed a notably enhanced C_2H_2 and C_2H_6 adsorption capacities, with the uptake trend ordered as $C_2H_2 > C_2H_6 > C_2H_4$, which differs from the order of $C_2H_6 > C_2H_4 > C_2H_2$ found for UiO-67. Benchmark selectivities of 1/99 (*v*/*v*) C_2H_2/C_2H_4 (2.1) and 50/50 (*v*/*v*) C_2H_6/C_2H_4 (1.7) were reported, as well as exceptional performance for one-step C_2H_4 purification from a ternary mixture under ambient conditions in dynamic column breakthrough experiments.

Grand canonical Monte Carlo (GCMC) simulations illustrated that, in UiO-67, C_2H_6 molecule interacted with three phenyl rings from three linkers and four oxygen atoms from three carboxylic groups, thereby forming four C–H···π (H···π = 3.20–3.50 Å) and four C–H···O (H···O = 3.26−3.57 Å) interactions. Comparatively fewer C–H···π and C–H···O interactions were observed for C_2H_4 and C_2H_2 molecules. In contrast, when C_2H_6 was adsorbed on UiO-67-$(NH_2)_2$, the interactions encompassed not only C–H···π interactions and C–H···O interactions, but also three C−H···N (H···N= 3.50−4.25 Å) interactions between C_2H_6 and the $-NH_2$ groups. This led to much stronger binding strength than that exhibited by UiO-67. Additionally, three C−H···N (H···N = 3.83−4.80 Å) and three N−H···C (H···C = 4.29−4.74 Å) interactions was also observed in C_2H_2 adsorbed UiO-67-$(NH_2)_2$. Conversely, only two additional C−H···N (H···N = 3.48−3.98 Å) interactions were formed by the C_2H_4 molecule with $-NH_2$ groups in C_2H_4 adsorbed UiO-67-$(NH_2)_2$. The incorporation of $-NH_2$ groups facilitated stronger binding of the framework with C_2H_2 and C_2H_6 over with C_2H_4, thus leading to the higher binding energy for C_2H_2 and C_2H_6 than for C_2H_4 in UiO-67-$(NH_2)_2$.

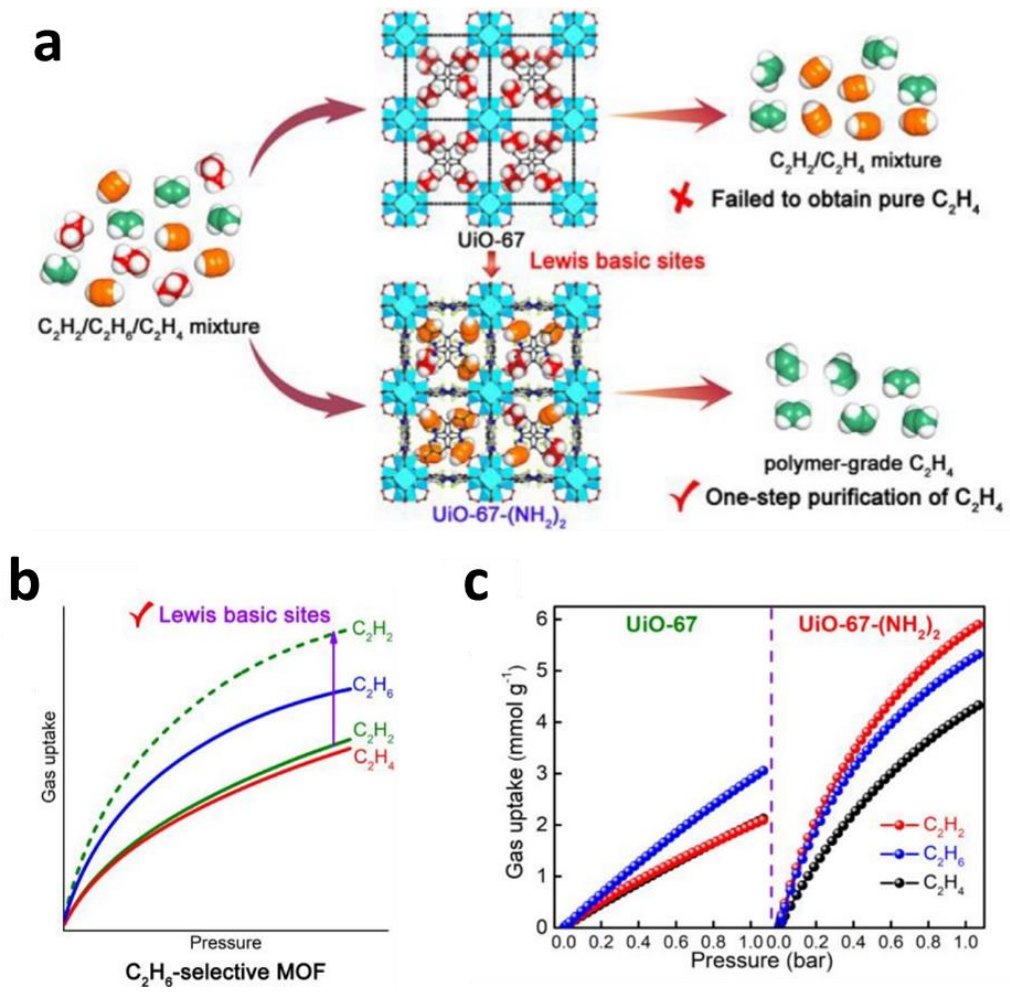

Figure 1.15 (a) Scheme of introduction of Lewis basic sites into UiO-67 to achieve one-step purification of C_2H_4. (b) Proposed strategy based on C_2H_6-selective MOFs for one-step C_2H_4 purification. (c) Gas adsorption isotherms of UiO-67 and UiO-67-$(NH_2)_2$ at 296 K.[81]

1.4.3 Selective adsorption based on kinetic effect

Kinetic effect-based separation utilising MOFs provides an effective method for selective separation of molecules with similar thermodynamic properties and sizes. This approach primarily relies on differential diffusion rates of these molecules into the pore system.[82] For example, ELM-12 (ELM = Elastic layer-structured metal–organic frameworks) showed a close equilibrium adsorption amount for both C_3H_6 (62 mg g^{-1}) and C_3H_8 (60 mg g^{-1}).[83] This is paired with comparable adsorption heat (C_3H_6: 30 kJ mol^{-1}; C_3H_8: 28 kJ mol^{-1}), low C_3H_6/C_3H_8 IAST selectivity (1.5), as well as

similar binding interactions (Figure 1.16a). These properties render ELM-12 less desirable for thermodynamic-based separation. Nevertheless, ELM-12 is equipped with optimally sized channels, featuring pore windows approximately 4.0 Å in wide (Figure 1.16b). This feature allows ELM-12 match better with C_3H_6 than C_3H_8, resulting in a considerably faster uptake of C_3H_6 than C_3H_8 (Figure 1.16c), and as a result, there is an extended breakthrough time interval, which provides clear separation of C_3H_6/C_3H_8 (Figure 1.16d).

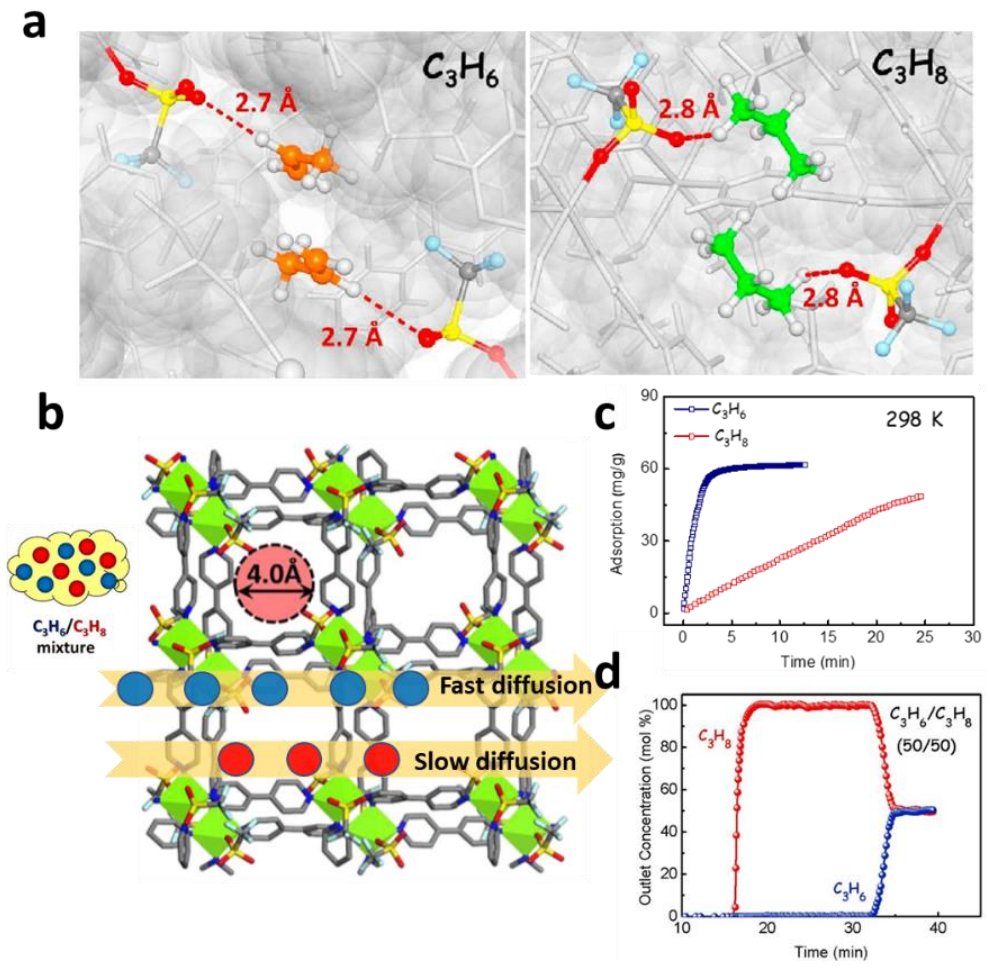

Figure 1.16. (a) DFT-calculated C_3H_6 and C_3H_8 locations in ELM-12. (b) Crystal structure of ELM-12. (c) Kinetic adsorption profiles of C_3H_6 and C_3H_8 for ELM-12 at 298 K, and (d) breakthrough cycling test for C_3H_6/C_3H_8 (50/50 v/v) mixture through ELM-12 material at 298 K and 1.01 bar.[83]

1.5 References

1. Schoedel, A.; Ji, Z.; Yaghi, O. The role of metal–organic frameworks in a carbon-neutral energy cycle. *Nat. Energy* **2016**, *1*, 16034.
2. Zhao, D.; Yuan, D.; Zhou, H. The current status of hydrogen storage in metal–organic frameworks. *Energ. Environ. Sci.* **2008**, *1*, 222−235.
3. Eisenberg, R.; Gray, H.; Crabtree, G. Addressing the challenge of carbon-free energy. *Proc. Natl. Acad. Sci.* **2020**, *117*, 12543−12549.
4. Deutch, J. Is net zero carbon 2050 possible? *Joule* **2020**, *4*, 2237−2240.
5 Crabtree, G.; Dresselhaus, M.; Buchanan, M. The hydrogen economy. *Phys. Today* **2004**, *57*, 39−44.
6 Klerke, A.; Christensen, C.; Nørskov, J.; Vegge, T. Ammonia for hydrogen storage: challenges and opportunities. *J. Mater. Chem.* **2008**, *18*, 2304−2310.
7. Ghavam, S.; Vahdati, M.; Wilson, I.; Styring, P. Sustainable ammonia production processes. *Front. Energy Res.* **2021**, *9*, 580808.
8. Demirhan, C.; Tso, W.; Powell, J.; Pistikopoulos, E. Sustainable ammonia production through process synthesis and global optimization. *AIChE J.* **2019**, *65*,1−23.
9. Han, X.; Yang, S.; Schröder, M. Metal–organic framework materials for production and distribution of ammonia. *J. Am. Chem. Soc.* **2023**, *145*, 1998−2012.
10. Sholl, D.; Lively, R. Seven chemical separations to change the world. *Nature* **2016**, *532*, 435−437.
11. Fankhauser, S.; Smith, S.; Allen, M.; Axelsson, K.; Hale, T.; Hepburn, C.; Kendall, J.; Khosla, R.; Lezaun, J.; Mitchell-Larson, E.; Obersteiner, M.; Rajamani, L.; Rickaby, R.; Seddon, N.; Wetzer, T. The meaning of net zero and how to get it right. *Nat. Clim. Change* **2021**, *12*, 15−21.
12. He, Y.; Krishna, R.; Chen, B. Metal–organic frameworks with potential for energy-efficient adsorptive separation of light hydrocarbons. *Energ. Environ. Sci.* **2012**, *5*, 9107−9120.
13. Wu, Y.; Weckhuysen, B. Separation and purification of hydrocarbons with porous materials. *Angew. Chem. Int. Ed.* **2021**, *60*, 18930−18949.
14. Yang, S.; Sun, F.; Krishna, R.; Zhang, Q.; Zhou, L.; Zhang, Y. ; Hu, T. Propane-trapping ultramicroporous metal–organic framework in the low-pressure area toward the purification of propylene. *Chem. Eng. J.* **2021**, *13*, 35990−35996.
15. Jia, T.; Gu, Y.; Li, F. Progress and potential of metal–organic frameworks (MOFs) for gas storage and separation: A review. *J. Environ. Chem. Eng.* **2022**, *10*, 108300.
16. Gezerman, A. A critical assessment of green ammonia production and ammonia production technologies. *Kem. Ind.* **2022**, *71*, 57−66.
17. Humphreys, J.; Lan, R.; Tao, S. Development and recent progress on ammonia synthesis catalysts for Haber–Bosch process. *Adv. Energy Sustainability Res.* **2020**, *2*, 2000043.
18. Juangsa, F.; Irhamna, A.; Aziz, M. Production of ammonia as potential hydrogen carrier: Review on thermochemical and electrochemical processes. *Int. J. Hydrogen Energ.* **2021**, *46*, 14455−14477.
19. Vikrant, K.; Kumar, V.; Kim, K.; Kukkar, D. Metal–organic frameworks (MOFs): potential and challenges for capture and abatement of ammonia. *J. Mater. Chem. A* **2017**, *5*, 22877−22896.
20. Afif, A.; Radenahmad, N.; Cheok, Q.; Shams, S.; Kim, J.; Azad, A. Ammonia-fed fuel cells: a comprehensive review. *Renew. Sust. Energ. Rev.* **2016**, *60*, 822−835.

21. MacFarlane, D.; Cherepanov, P.; Choi, J.; Suryanto, B.; Hodgetts, R.; Bakker, J.; Ferrero Vallana, F.; Simonov, A. A roadmap to the ammonia economy. *Joule* **2020**, *4*, 1186−1205.
22. Ma, S.; Zhou, H. Gas storage in porous metal–organic frameworks for clean energy applications. *Chem. Commun.* **2010**, *46*, 44−53.
23. Ding, Q.; Zhang, Z.; Liu, Y.; Chai, K.; Krishna, R.; Zhang, S. One-step ethylene purification from ternary mixtures in a metal–organic framework with customized pore chemistry and shape. *Angew. Chem. Int. Ed.* **2022**, *61*, e202208134.
24. Lv, L.; Song, G.; Zhao, X.; Chen, J. Environmental burdens of China's propylene manufacturing: comparative life-cycle assessment and scenario analysis. *Sci. Total. Environ.* **2021**, *799*, 149451.
25. Lee, C.; Bae, Y.; Jeong, N.; Farha, O.; Sarjeant, A.; Stern, C.; Nickias, P.; Snurr, R.; Hupp, J.; Nguyen, S. Kinetic separation of propene and propane in metal–organic frameworks: controlling diffusion rates in plate-shaped crystals via tuning of pore apertures and crystallite aspect ratios. *J. Am. Chem. Soc.* **2011**, *133*, 5228−5231.
26. Wang, Z.; Luo, H.; Wang, Y.; Xu, M.; He, C.; Liu, Q. Octanuclear cobalt(II) cluster-based metal–organic framework with caged structure exhibiting the selective adsorption of ethane over ethylene. *Inorg. Chem.* **2021**, *60*, 10596−10602.
27. Yang, S.; Sun, F.; Liu, P.; Li, L.; Krishna, R.; Zhang, Y.; Li, Q.; Zhou, L.; Hu, T. Efficient purification of ethylene from C_2 Hydrocarbons with an C_2H_6/C_2H_2-selective metal–organic framework. *ACS Appl. Mater. Interfaces* **2021**, *13*, 962−969.
28. Liu, P.; Wang, Y.; Chen, Y.; Yang, J.; Wang, X.; Li, L.; Li, J. Construction of saturated coordination titanium-based metal–organic framework for one-step C_2H_2/ C_2H_6/ C_2H_4 separation. *Sep. Purif. Technol.* **2021**, *276*, 119284.
29. Kang, M.; Kang, D.; Choe, J.; Kim, H.; Kim, D.; Park, H.; Hong, C. A robust hydrogen-bonded metal–organic framework with enhanced ethane uptake and selectivity. *Chem. Mater.* **2021**, *33*, 6193−6199.
30. Wang, G.; Krishna, R.; Li, Y.; Shi, W.; Hou, L.; Wang, Y.; Zhu, Z. Boosting ethane/ethylene separation by MOFs through the amino-functionalization of pores. *Angew. Chem. Int. Ed.* **2022**, *61*, e202213015.
31. Mukherjee, S.; Sensharma, D.; Chen, K.; Zaworotko, M. Crystal engineering of porous coordination networks to enable separation of C_2 hydrocarbons. *Chem. Commun.* **2020**, *56*, 10419−10441.
32. Christopher, C.; Dutta, A.; Farooq, S.; Karimi, I. Process synthesis and optimization of propylene/propane separation using vapor recompression and self-heat recuperation. *Ind. Eng. Chem. Res.* **2017**, *56*, 14557−14564.
33. Sadrameli, S. Thermal/catalytic cracking of hydrocarbons for the production of olefins: a state-of-the-art review I: thermal cracking review. *Fuel* **2015**, *140*, 102−115.
34. Yang, L.; Cui, X.; Yang, Q.; Qian, S.; Wu, H.; Bao, Z.; Zhang, Z.; Ren, Q.; Zhou, W.; Chen, B.; Xing, H. A single-molecule propyne trap: highly efficient removal of propyne from propylene with anion-pillared ultramicroporous materials. *Adv. Mater.* **2018**, *30*, 1705374.
35. McCue, A. J.; Guerrero-Ruiz, A.; Rodríguez-Ramos, I.; Anderson, J. Palladium sulphide – a highly selective catalyst for the gas phase hydrogenation of alkynes to alkenes. *J. Catal.* **2016**, *340*, 10−16.
36. Gao, M.; Song, B.; Sensharma, D.; Zaworotko, M. Crystal engineering of porous coordination networks for C_3 hydrocarbon separation. *SmartMat* **2020**, *2*, 38−55.

37. Lin, R.; Xiang, S.; Xing, H.; Zhou, W.; Chen, B. Exploration of porous metal–organic frameworks for gas separation and purification. *Coordin. Chem. Rev.* **2019**, *378*, 87−103.
38. Wang, Y.; Peh, S.; Zhao, D. Alternatives to cryogenic distillation: advanced porous materials in adsorptive light olefin/paraffin separations. *Small* **2019**, *15*, 1900058.
39. Li, J.; Kuppler, R.; Zhou, H. Selective gas adsorption and separation in metal–organic frameworks. *Chem. Soc. Rev.* **2009**, *38*, 1477−1504.
40. Geier, S.; Mason, J.; Bloch, E.; Queen, W.; Hudson, M.; Brown, C.; Long, J. Selective adsorption of ethylene over ethane and propylene over propane in the metal–organic frameworks M_2(dobdc) (M = Mg, Mn, Fe, Co, Ni, Zn). *Chem. Sci.* **2013**, *4*, 2054−2061.
41. Anwar, F.; Khaleel, M.; Wang, K.; Karanikolos, G. Selectivity tuning of adsorbents for ethane/ethylene separation: a review. *Ind. Eng. Chem. Res.* **2022**, *61*, 12269−12293.
42. Li, J.; Sculley, J.; Zhou, H. Metal–organic frameworks for separations. *Chem. Rev.* **2012**, *112*, 869−932.
43. Freund, R.; Zaremba, O.; Arnauts, G.; Ameloot, R.; Skorupskii, G.; Dinca, M.; Bavykina, A.; Gascon, J.; Ejsmont, A.; Goscianska, Kalmutzki, M.; Lächelt, U.; Ploetz, E.; Diercks, C.; Wuttke, S. The current status of MOF and COF applications. *Angew. Chem. Int. Ed.* **2021**, *60*, 23975−24001.
44. Zhou, H.; Long, J.; Yaghi, O. Introduction to metal–organic frameworks. *Chem. Rev.* **2012**, *112*, 673−674.
45. Zhang, X.; Maddock, J.; Nenoff, T.; Denecke, M.; Yang, S.; Schröder, M. Adsorption of iodine in metal–organic framework materials. *Chem. Soc. Rev.* **2022**, *51*, 3243−3262.
46. Sumida, K.; Rogow, D.; Mason, J.; McDonald, T.; Bloch, E.; Herm, Z.; Bae, T.; Long, J. Carbon dioxide capture in metal–organic frameworks. *Chem. Rev.* **2012**, *112*, 724−781.
47. Makal, T.; Li, J.; Lu, W.; Zhou, H. Methane storage in advanced porous materials. *Chem. Soc. Rev.* **2012**, *41*, 7761−7779.
48. Han, X.; Yang, S.; Schröder, M. Porous metal–organic frameworks as emerging sorbents for clean air. *Nat. Reviews Chem.* **2019**, *3*, 108−118.
49. Lin, R.; Xiang, S.; Zhou, W.; Chen, B. Microporous metal–organic framework materials for gas separation. *Chem* **2020**, *6*, 337−363.
50. Lee, J.; Farha, O.; Roberts, J.; Scheidt, K.; Nguyen, S.; Hupp, J. Metal–organic framework materials as catalysts. *Chem. Soc. Rev.* **2009**, *38*, 1450−1459.
51. Xiao, J.; Jiang, H. Metal–organic frameworks for photocatalysis and photothermal catalysis. *Acc Chem. Res.* **2019**, *52*, 356−366.
52. Kalmutzki, M.; Diercks, C.; Yaghi, O. Metal–organic frameworks for water harvesting from air. *Adv. Mater.* **2018**, *30*, 1704304.
53. Hanikel, N.; Pei, X.; Chheda, S.; Lyu, H.; Jeong, W.; Sauer, J.; Gagliardi, L.; Yaghi, O. Evolution of water structures in metal–organic frameworks for improved atmospheric water harvesting. *Science* **2021**, *374*, 454−459.
54. Sun, C.; Qin, C.; Wang, C.; Su, Z.; Wang, S.; Wang, X.; Yang, G.; Shao, K.; Lan, Y.; Wang, E. Chiral nanoporous metal–organic frameworks with high porosity as materials for drug delivery. *Adv. Mater.* **2011**, *23*, 5629−5632.
55. Kokcam-Demir, U.; Goldman, A.; Esrafili, L.; Gharib, M.; Morsali, A.; Weingart, O.; Janiak, C. Coordinatively unsaturated metal sites (open metal sites) in metal–organic frameworks: design and applications. *Chem. Soc. Rev.* **2020**, *49*, 2751−2798.

56. Paz, F.; Klinowski, J.; Vilela, S.; Tome, J.; Cavaleiro, J.; Rocha, J. Ligand design for functional metal–organic frameworks. *Chem. Soc. Rev.* **2012**, *41*, 1088−1110.
57. Sahoo, R.; Das, M. C. C_{2s}/C_1 hydrocarbon separation: The major step towards natural gas purification by metal–organic frameworks (MOFs). *Coordin. Chem. Rev.* **2021**, *442*, 213998.
58. Bon, V.; Brunner, E.; Pöppl, A.; Kaskel, S. Unraveling structure and dynamics in porous frameworks *via* advanced *in situ* characterization techniques. *Adv. Funct. Mater.* **2020**, *30*, 1907847.
59. Van Vleet, M.; Weng, T.; Li, X.; Schmidt, J. R. *In situ*, time-resolved, and mechanistic studies of metal–organic framework nucleation and growth. *Chem. Rev.* **2018**, *118*, 3681−3721.
60. Savage, M.; Cheng, Y.; Easun, T.; Eyley, J.; Argent, S.; Warren, M.; Lewis, W.; Murray, C.; Tang, C.; Frogley, M.; Cinque, G.; Sun, J.; Rudić, S.; Murden, R.; Benham, M.; Fitch, A.; Blake, A.; Ramirez-Cuesta, A.; Yang, S.; Schröder, M. Selective adsorption of sulfur dioxide in a robust metal–organic framework material. *Adv. Mater.* **2016**, *28*, 8705−8711.
61. Marsh, C.; Han, X.; Li, J.; Lu, Z.; Argent, S.; Silva, I.; Cheng, Y.; Daemen, L.; Ramirez-Cuesta, A.; Thompson, S.; Blake, A.; Yang, S.; Schröder, M. Exceptional packing density of ammonia in a dual-functionalized metal–organic framework. *J. Am. Chem. Soc.* **2021**, *143*, 6586−6592.
62. Savage, M.; Silva, I.; Johnson, M.; Carter, J.; Newby, R.; Suyetin, M.; Besley, E.; Manuel, P.; Rudic, S.; Fitch, A.; Murray, C.; David, W.; Yang, S.; Schröder, M. Observation of binding and rotation of methane and hydrogen within a functional metal–organic framework. *J. Am. Chem. Soc.* **2016**, *138*, 9119−9127.
63. Greenaway, A.; Gonzalez-Santiago, B.; Donaldson, P. M.; Frogley, M. D.; Cinque, G.; Sotelo, J.; Moggach, S.; Shiko, E.; Brandani, S.; Howe, R. F.; Wright, P. *In situ* synchrotron IR microspectroscopy of CO_2 adsorption on single crystals of the functionalized MOF $Sc_2(BDC\text{-}NH_2)_3$. *Angew. Chem. Int. Ed.* **2014**, *53*, 13483−13487.
64. Godfrey, H.; Silva, I.; Briggs, L.; Carter, J.; Morris, C.; Savage, M.; Easun, T.; Manuel, P.; Murray, C.; Tang, C.; Frogley, M.; Cinque, G.; Yang, S.; Schröder, M. Ammonia storage by reversible host–guest site exchange in a robust metal–organic framework. *Angew. Chem. Int. Ed.* **2018**, *57*, 14778−14781.
65. Easun, T.; Moreau, F.; Yan, Y.; Yang, S.; Schröder, M. Structural and dynamic studies of substrate binding in porous metal–organic frameworks. *Chem. Soc. Rev.* **2017**, *46*, 239−274.
66. Kang, D.; Ju, S.; Kim, D.; Kang, M.; Kim, H.; Hong, C. Emerging Porous Materials and Their Composites for NH_3 Gas Removal. *Adv. Sci.* **2020**, *7*, 2002142.
67. Chen, Z.; Wang, X.; Cao, R.; Idrees, K. B.; Liu, X.; Wasson, M. C.; Farha, O. Water-based synthesis of a stable iron-based metal–organic framework for capturing toxic gases. *ACS Mater. Letters* **2020**, *2*, 1129−1134.
68. Saha, D.; Deng, S. Ammonia adsorption and its effects on framework stability of MOF-5 and MOF-177. *J. Colloid. Interface Sci.* **2010**, *348*, 615−620.
69. Rieth, A.; Tulchinsky, Y.; Dinca, M. High and reversible ammonia uptake in mesoporous azolate metal–organic frameworks with open Mn, Co, and Ni Sites. *J. Am. Chem. Soc.* **2016**, *138*, 9401−9404.
70. Ma, Y.; Lu, W.; Han, X.; Chen, Y.; da Silva, I.; Lee, D.; Sheveleva, A. M.; Wang, Z.; Li, J.; Li, W.; Fan, M.; Xu, S.; Tuna, F.; McInnes, E.; Cheng, Y.; Rudić, S.; Manuel, P.; Frogley, M.; Ramirez-Cuesta, A.; Schröder, M.; Yang, S. Direct

observation of ammonia storage in UiO-66 incorporating Cu(II) binding sites. *J. Am. Chem. Soc.* **2022**, *144*, 8624−8632.

71. Wang, Z.; Li, Z.; Zhang, X.; Xia, Q.; Wang, H.; Wang, C.; Wang, Y.; He, H.; Zhao, Y.; Wang, J. Tailoring multiple sites of metal–organic frameworks for highly efficient and reversible ammonia adsorption. *ACS Appl. Mater. Interfaces* **2021**, *13*, 56025−56034.
72. Han, X.; Lu, W.; Chen, Y.; Silva, I.; Li, J.; Lin, L.; Li, W.; Sheveleva, A.; Godfrey, H.; Lu, Z.; Tuna, F.; McInnes, E.; Cheng, Y.; Daemen, L.; McPherson, L.; Teat, S.; Frogley, M.; Rudić, S.; Manuel, P.; Ramirez-Cuesta, A.; Yang, S.; Schröder, M. High ammonia adsorption in MFM-300 materials: dynamics and charge transfer in host–guest binding. *J. Am. Chem. Soc.* **2021**, *143*, 3153−3161.
73. Guo, L.; Han, X.; Ma, Y.; Li, J.; Lu, W.; Li, W.; Lee, D.; Silva, I.; Cheng, Y.; Rudic, S.; Manuel, P.; Frogley, M.; Ramirez-Cuesta, A.; Schröder, M.; Yang, S. High capacity ammonia adsorption in a robust metal–organic framework mediated by reversible host–guest interactions. *Chem. Commun.* **2022**, *58*, 5753−5756.
74. Moribe, S.; Chen, Z.; Alayoglu, S.; Syed, Z.; Islamoglu, T.; Farha, O. Ammonia capture within isoreticular metal–organic frameworks with rod secondary building units. *ACS Mater. Lett.* **2019**, *1*, 476−480.
75. Rieth, A.; Dinca, M. Controlled gas uptake in metal–organic frameworks with record ammonia sorption. *J. Am. Chem. Soc.* **2018**, *140*, 3461−3466.
76. Bao, Z.; Wang, J.; Zhang, Z.; Xing, H.; Yang, Q.; Yang, Y.; Wu, H.; Krishna, R.; Zhou, W.; Chen, B.; Ren, Q. Molecular sieving of ethane from ethylene through the molecular cross-section size differentiation in gallate-based metal–organic frameworks. *Angew. Chem. Int. Ed.* **2018**, *57*, 16020−16025.
77. Liang, B.; Zhang, X.; Xie, Y.; Lin, R. B.; Krishna, R.; Cui, H.; Li, Z.; Shi, Y.; Wu, H.; Zhou, W.; Chen, B. An ultramicroporous metal–organic framework for high sieving separation of propylene from propane. *J. Am. Chem. Soc.* **2020,** *142*, 17795−17801.
78. Yu, L.; Han, X.; Wang, H.; Ullah, S.; Xia, Q.; Li, W.; Li, J.; da Silva, I.; Manuel, P.; Rudic, S.; Cheng, Y.; Yang, S. Thonhauser, T.; Li, J. Pore distortion in a metal–organic framework for regulated separation of propane and propylene. *J. Am. Chem. Soc.* **2021**, *143*, 19300−19305.
79. Wang, H.; Luo, D.; Velasco, E.; Yu, L.; Li, J. Separation of alkane and alkene mixtures by metal–organic frameworks. *J. Mater. Chem. A* **2021**, *9* , 20874−20896.
80. Yang, S.; Ramirez-Cuesta, A.; Newby, R.; Garcia-Sakai, V.; Manuel, P.; Callear, S.; Campbell, S.; Tang, C.; Schröder, M. Supramolecular binding and separation of hydrocarbons within a functionalized porous metal–organic framework. *Nat. Chem.* **2014**, *7*, 121−129.
81. Gu, X. W.; Wang, J. X.; Wu, E.; Wu, H.; Zhou, W.; Qian, G.; Chen, B.; Li, B. Immobilization of Lewis basic sites into a stable ethane-selective mof enabling one-step separation of ethylene from a ternary mixture. *J. Am. Chem. Soc.* **2022**, *144*, 2614−2623.
82. Lyndon, R.; You, W.; Ma, Y.; Bacsa, J.; Gong, Y.; Stangland, E.; Walton, K.; Sholl, D.; Lively, R. Tuning the structures of metal–organic frameworks *via* a mixed-linker strategy for ethylene/ethane kinetic separation. *Chem. Mater.* **2020**, *32*, 3715−3722.
83. Li, L.; Lin, R.; Wang, X.; Zhou, W.; Jia, L.; Li, J.; Chen, B. Kinetic separation of propylene over propane in a microporous metal–organic framework. *Chem. Eng. J.* **2018**, *354*, 977−982.

[Blank page]

Chapter 2

MOFs selection and scoping

Chapter 2. MOFs selection and scoping

2.1 Aims of the thesis

The principal objective of this thesis is to enhance clean energy storage and improve separation efficiency, thereby contributing to reductions in energy consumption and zero carbon emission. In this respect, our focus is centred exploring promising MOF materials for efficient NH_3 storage and olefins purification. A key element of our research is studying the impact of host–guest interactions on the adsorption and separation processes within MOFs through a combined application of various techniques, including *in situ* neutron powder diffraction, solid-state nuclear magnetic resonance (ssNMR), *in situ* synchrotron Fourier transform infrared micro spectroscopy and *in situ* inelastic neutron scattering. The overarching aim is to utilise the insights garnered from these analyses to inform the design of improved materials for future applications.

2.2 Objectives of the thesis

The following objectives are included to achieve the aims of NH_3 adsorption and olefin purification, respectively:

The objectives of NH_3 adsorption

1. MOF selection with high stability.

2. Synthesis and characterisation of MOFs samples and stability tests towards the exposure to NH_3.

2. Studies of gas adsorption isotherms, thermodynamic parameters.

3. *In situ* crystallographic studies on the binding domains of adsorbed gas.

4. Spectroscopic studies of host guest binding dynamics.

The objectives of olefin purification

1. Synthesis and characterisation of MOF samples with suitable size and pore environment.

2. Studies of gas adsorption isotherms, thermodynamic parameters, kinetic parameters.

3. Analysis of gas selectivity and dynamic breakthrough separations.

4. *In situ* crystallographic studies on the binding domains of adsorbed gas.

5. Spectroscopic studies of host guest binding dynamics.

2.3 Strategy of MOFs selection

2.3.1 For NH_3 adsorption

One important consideration for NH_3 adsorption is the chemical stability of MOF materials. To construct chemically stable MOFs that could tolerate NH_3, one common deign strategy is to follow Pearson's hard/soft acid/base (HSAB) principle.[1] This involves using the high-oxidation-state metals such as Al^{3+}, Cr^{3+}, Sc^{3+}, and Zr^{4+} as metal sources to form strong coordination bonds with organic carboxylate ligands.[2] High oxidation state metals tend to form multi-metal clusters or metal chains with high connectivity, which leads to large specific surface areas and high porosities in the resulting MOF materials.[3] As a result, these MOFs are well-suited for NH_3 adsorption applications due to their high porosity and stability to NH_3.

Aluminium-MOFs (Al-MOFs) is one class of these robust materials for gas storage applications.[3,4] They have excellent physicochemical stability due to the strong Al–O bonds. Besides, aluminium is abundant in the earth, the affordability from a metal perspective makes Al-MOFs an attractive option when compared to other stable MOFs.[5] In addition, the aluminium element is lighter, leading to Al-MOFs with a

density lower than that of other MOFs, which is conductive to gas adsorption.[3,6] More importantly, Al-MOFs are less toxic than other chemically stable MOFs such as Cr-MOFs and Zr-MOFs, making Al-MOFs a more environmentally friendly option.[3]

Scandium-MOFs (Sc-MOFs) have shown great materials stability due to the strong coordination Sc–O bonds.[7] Sc(III) is the lightest of the rare earth elements and its coordination chemistry provides a range of possibilities, including coordination number of three to nine, with hexacoordinate being the most common. Sc exhibits distinct characteristics, characterised by an ionic radius of 0.745 Å (in its hexacoordinated Sc(III) form), surpassing that of any M(III) ions found in the 3d transition metals group. In addition, Sc(III) complexes exhibit stronger complexes than the lanthanides due to their smaller ionic size and greater polarising ability. Some Sc(III) complexes, due to the extreme electron deficiency of the Sc(III) ion, act as some of the strongest Lewis acids among any transitions metal complexes. However, despite recent work, the complex chemistry of Sc remains insufficiently investigated, likely as a result of the very high price of the metal due to its low abundance in the earth.[8]

Zirconium-MOFs (Zr-MOFs) have shown great potential in various applications due to their unique properties such as high surface areas, large pore volumes and excellent structure robustness.[9,10] The high symmetry and connectivity enable the Zr_6 cluster to serve as different types of nodes in the resulting networks *via* reducing the connectivity, making it compatible to form three-dimensional (3D) periodic frameworks with different linkers. They generally possess high chemical, thermal and water/moisture stability due to the presence of strong Zr–O bonds and robust multinuclear secondary

building units (SBUs, composed of Zr_6 clusters). Due to the high stability, they have been widely used in toxic and corrosive gases adsorption, including the adsorption of SO_2 and NO_2.[11,12]

2.3.1.1 Introduction to selected Al-MOFs

MIL-160, CAU-10(H), Al-fum, and MIL-53(Al). The pore environment (size, shape and chemical environment) of the pores within a porous framework could impact directly and control the adsorption of gas molecules. To achieve the efficient capture of NH_3 (kinetic diameter of *cca.* 3.7 Å), the promising way is either through fine-tuning the pore size or fabricating specific functional sites within the porous that could trap the NH_3 molecule in the pore. In this regard, MIL-160, which has a narrow pore channel size of 5.0 Å and exhibits high-density hydrogen-bonding nano-traps (μ_2-OH, heteroatom O of the linker) within the pore surfaces,[13] is a promising candidate to achieve the aforementioned mission. MIL-160 had already been examined thoroughly for various applications, such as C_2H_2/CO_2 separation, H_2O sorption, and SO_2 adsorption.[13-15] For example, in 2022, Ma *etc.*, reported that MIL-160 with the abundant hydrogen-bonding acceptors as nano traps selectively captures C_2H_2 to achieve the superior C_2H_2/CO_2 selectivity.[13] More importantly, MIL-160 can be synthesised in large quantities under green (aqueous) and mild conditions in a single step from readily commercially available compounds. These advantages of MIL-160 inspire us to study the capture of NH_3 in this material. To further demonstrate our hypothesis, four aluminium-based MOFs, named MIL-160, CAU-10(H),[16] Al-fum,[17] and MIL-53(Al)[18] incorporating distinct functional groups, pore size, and BET surface areas, were selected to study the impact of functional groups, pore size and structure robustness on the NH_3 uptakes.

Al-bttotb. $[Al_3(bttotb)_2(OH)_3](DMF)_{5.5}(H_2O)_3$, also called as Al-bttotb, was constructed by 4,4',4"-[benzene-1,3,5-triyl-tris(oxy)]tribenzoic acid (H_3bttotb) and AlO_6 polyhedra.[19,20] In its structure, each Al(III) centre is octahedrally coordinated to oxygen atoms from four carboxylates and two bridging hydroxyl anions, forming a 1D array of corner-sharing AlO_6 polyhedra. The 1D chains are further interconnected through $bttotb^{3-}$, forming a 3D network with two types of 1D channels with a square-shaped cross section (Figure 2.1 a). The desolvated framework reveals a BET surface area of 572 $m^2\ g^{-1}$, a pore volume of 0.22 $cm^3\ g^{-1}$ and a uniform pore size of 5.6 Å. This material has high thermal stability (stable upon prolonged heating at 350 °C) and excellent chemical stability after soaking in familiar organic solvents, acidic or alkaline solution and even in boiling water (Figure 2.1 b). The high stability, suitable pore size and possessed μ_2-OH of Al-bttotb encourage us to explore its adsorption properties toward NH_3, especially in the application of NH_3 capture.

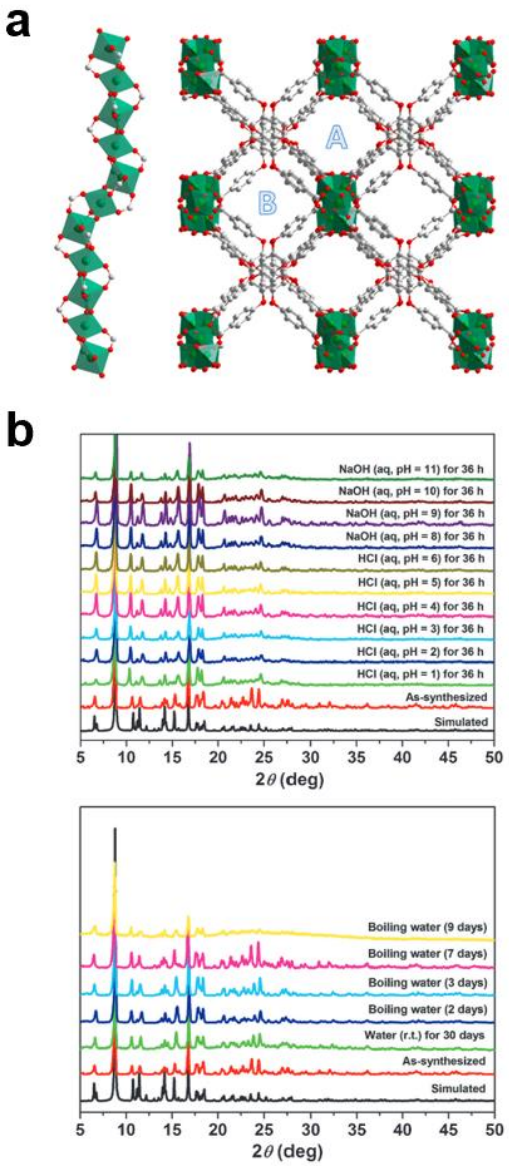

Figure 2.1. (a) Crystal structure of Al-bttotb. 1D array sharing AlO_6 polyhedra (left). 3D structure of Al-bttotb showing two types of channel (right). (b) PXRD patterns for Al-bttotb after treating in the water solutions of HCl or NaOH with different pH values, as well as after treating in water at room temperature and 100 ^{o}C for different durations.[19,20]

2.3.1.2 Introduction to selected Sc-MOFs

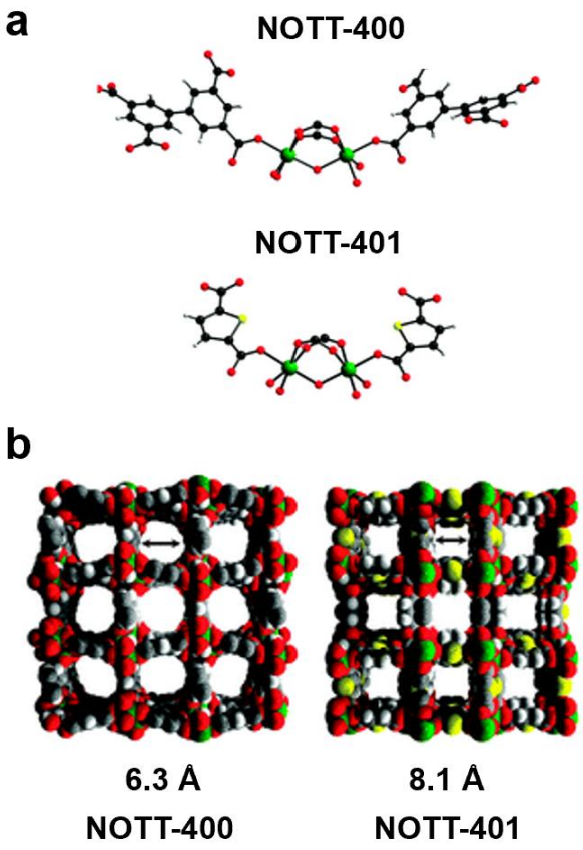

Figure 2.2 (a) Views of the co-ordination environment of binuclear Sc(III) centres with $BPTC^{4-}$ and TDA^{2-}. (b) Space-filling views of the structure of NOTT-400 along the b-axis showing 8.1 Å channels, and the structure of NOTT-401 along the c-axis showing the 6.3 Å channels (scandium: green; sulfur: yellow; oxygen: red; carbon: grey; hydrogen: small grey).[21]

MFM-300(Sc). MFM-300(Sc), previously denoted as NOTT-400,[21] shares isostructural characteristics with MFM-300(M) (M = Al, In, Fe, Cr). It adopts a chiral tetragonal space group $I4_122$ and features a binuclear [$Sc_2(\mu_2$-OH)]. The overall structure of MFM-300(Sc) exhibits an overall 3D framework structure with a channel size of 8.1 Å, and a high surface area of 1350 $m^2\ g^{-1}$. It also shows high chemical stability[7] and interesting properties for the adsorption of diverse toxic gases including H_2S[22] and SO_2,[23] as well as vapours including H_2O[24] and I_2.[25] For instance, MFM-300(Sc) demonstrated a notable SO_2 uptake of 9.4 mmol g^{-1} at 298 K and 1.0 bar,[23]

notably exceeding that of its Al- and In-based analogues owing to its larger pore volume and pore size. The retention of crystalline structure ensured remarkable reversibility and sustained host stability across numerous SO_2 adsorption/desorption cycles. Building upon these findings, we postulated that MFM-300(Sc) would exhibit substantial NH_3 uptake capacity due to its high stability, pore volume and pore size.

NOTT-401(Sc). NOTT-401(Sc)[21] is based on binuclear $[Sc_2(\mu_2\text{-OH})(O_2CR)_2]$ building blocks, connected with the linker TDA^{2-} (thiophene-2,5-dicarboxylic acid). The Sc(III) centre adopts a similar octahedral environment to NOTT-400, with four O-donors from four different thiophene carboxylate ligands and two μ_2-OH groups defining the co-ordination sphere. NOTT-401(Sc) exhibits a good thermal stability and a high BET surface area of 1514 $m^2\ g^{-1}$ with a channel size of 6.3 Å (Figure 2.2). With a narrower channel size and higher BET surface area and the same functional groups (μ_2-OH) incorporated in the frameworks compared to MFM-300(Sc), it suggests that NOTT-401(Sc) may have more host−guest hydrogen-bonding interactions with NH_3, which could lead to a better NH_3 capture and/or storage performance. Hence, we postulated that NOTT-401(Sc) would be a promising material for NH_3 adsorption. Further studies are needed to confirm these hypotheses and evaluate the practical applications of NOTT-401(Sc) as a NH_3 capture and/or storage material. We therefore selected MFM-300(Sc) and NOTT-401(Sc) for the studies of NH_3 adsorption.

2.3.1.3 Introduction to selected Zr-MOFs

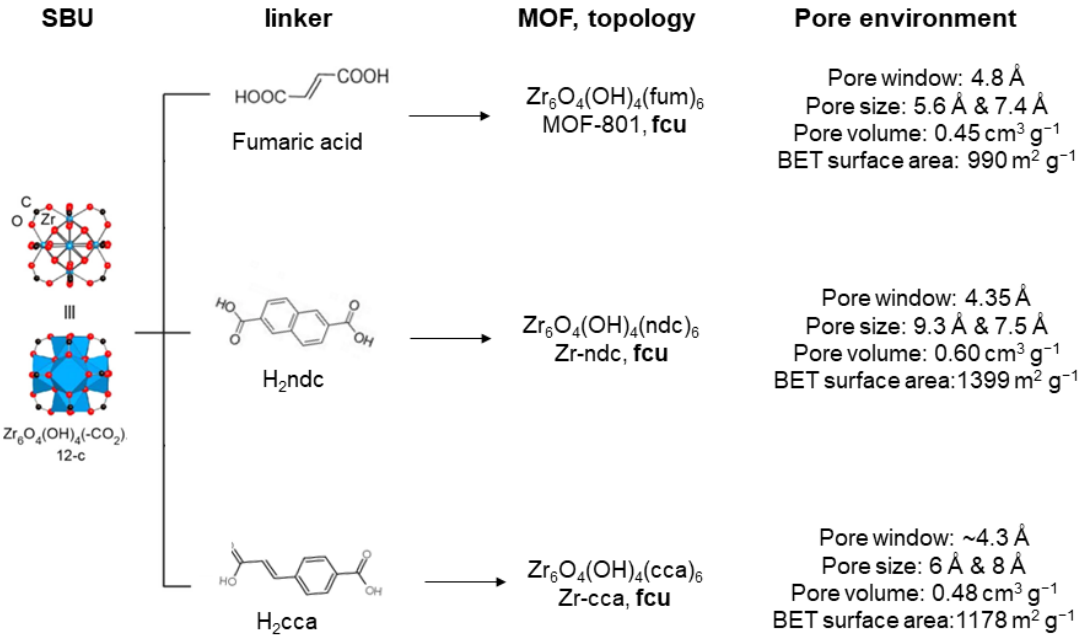

Figure 2.3. $Zr_6O_4(OH)_4$ secondary building units (SBUs) are connected with organic linkers to form MOFs of **fcu** topology.[26,29,30]

MOF-801. MOF-801 is a robust crystalline compound that shares the same face-centered cubic (fcc) topology as the UiO-66(Zr) framework, but with inorganic clusters connected by a smaller, nonlinear dicarboxylate linker, leading a pore size ranging from 7.4 to 5.6 to 4.8 Å with a BET surface area of 990 $m^2\ g^{-1}$ and total pore volumes of 0.45 $cm^3\ g^{-1}$ (Figure 2.3).[26] The relatively small pore size could be suitable to capture of small gas molecules. For example, MOF-801 has been reported to exhibit a remarkably steep H_2O adsorption isotherm at low relative pressure, which makes it a potential candidate for use as a water scavenger membrane or in a water harvesting device that captures H_2O from air in low relative humidity environments.[27] Additionally, MOF-801 has potential for green synthesis and facile shaping through direct monolith formation by a gel approach,[28] making it a promising material for various applications. Given

these properties, MOF-801 was considered and chosen as a prime candidate for the application of NH_3 capture.

Zr-ndc. Zr-ndc, also known as DUT-52(Zr), is constructed of $Zr_6O_4(OH)_4$ SBUs, which are interconnected by 12 disordered 2,6-ndc linkrs.[29] In Zr-ndc, the network incorporates octahedral and tetrahedral micropores with 9.3 Å and 7.5 Å in diameter (Van der Waals radii are taken into account). Each octahedral pore shares its triangular windows with 8 cages, which restricts pore accessibility to a diameter of 4.35 Å. The desolvated framework Zr-ndc exhibits a high surface area of 1399 $m^2\ g^{-1}$ and a pore volume of 0.60 $cm^3\ g^{-1}$. These narrow pore window and high porosities could make Zr-ndc a promising material for the application of either NH_3 capture or storage.

Zr-cca. $[Zr_6O_4(OH)_4(cca)_6]$ (Zr-cca),[30] which is assembled from $Zr_6O_4(OH)_4$ SBUs, and 4-carboxycinnamic acid (H_2cca), is isoreticular to the prototype UiO-66 but comprises a longer organic ligand. Two types of cages presented in Zr-cca, a tetrahedron with a pore size of∼6 Å and an octahedron with a pore size of∼8 Å, with the similar pore shape/size to Zr-ndc. Upon removal of solvent molecules initially residing inside the pores, Zr-cca exhibits permanent porosity with a BET surface area of 1178 $m^2\ g^{-1}$. Zr-cca also shows good thermal stability (stable up to 400°C) and high resistance to acidity over a wide pH range. Considering its suitable pore size, high BET surface and high thermal/chemical stability, Zr-cca is considered as a promising material for the application of either NH_3 capture or storage.

2.3.2 For olefin purification

As discussed in Chapter 1.4, the pore environment, including pore size and functionality, plays a crucial role in the separation of C_2H_6/C_2H_4 in MOF materials. The pore size of MOFs plays a critical role in determining the kinetic energy of the gas molecules when passing through the pores, which in turn affects their partitioning into the MOF pores. This directly impacts the selectivity and efficiency of the separation process. In addition to pore size, the functionalization of MOF materials with chemical groups such as $–NH_2$ or –OH can also influence the separation performance. Therefore, careful selection and design of MOF materials with appropriate pore characteristics is necessary to achieve optimal separation performance.

2.3.2.1 Introduction to selected In-MOFs

In Chapter 1.4.2, we discussed that a hydroxyl-functionalised MFM-300(Al) has a high selectivity of 48.7 for C_2H_4/C_2H_6 due to the anchoring of the –OH groups, aromatic C-H groups and phenyl rings present in the framework, which preferentially adsorb unsaturated molecules of C_2H_4. However, in the C_2H_4-selective MFM-300(Al) system, requiring an additional desorption step to release the adsorbed C_2H_4 molecules, leading to increased energy costs through the use of vacuum and/or heating. Therefore, our goal is to develop C_2H_6-selective adsorbents to directly produce polymer-grade C_2H_4 in one step by selectively retaining C_2H_6. A recent computational study reported that a small change in the diameter of the channel could induce a large effect on the selectivity of C_2H_4/C_2H_6 whilst maintaining the overall pore chemistry and structure.[31] The larger pores of MOFs may facilitate the diffusion of C_2H_4 away from C_2H_6, resulting in the efficient ethylene purification.

Despite the development of Al-MOFs, the largest number of the reported MOFs that are constructed with the group thirteen trivalent corresponds to indium MOFs (In-MOFs).[32] This comes from several advantages of In-MOFs, including the high stability in air and humid environments, the high crystallinity that allowed for structural tendencies and correlations within their synthesis parameters. Interestingly, MFM-300(In) exhibits identical pore chemistry but only differs slightly in pore diameter compared to MFM-300(Al) (6.8 Å and ~6.0 Å for MFM-300(In) and MFM-300(Al), respectively).[33] Given this knowledge, we expect any unusual observation of C_2H_4/C_2H_6 separation in MFM-300(In). Therefore, MFM-300(In) was chosen for further study on ethylene purification, and the experiments and corresponding discussion will be presented in Chapter 5 and Appendix III.

2.3.2.2 Introduction to selected Cu-MOFs

Despite the fact that tailoring pore size can influence the selectivity of C_2H_4/C_2H_6, the incorporation of open metal sites,[34] and polar functional group[35] can also enhance or reverse the selectivity of C_2H_4/C_2H_6 by strengthening the host–guest interactions in MOFs. Whilst many MOFs have been reported for their gas separation properties, it is often difficult to completely explain differences in performance owing to many variables such as porosity and pore geometry, functionality and presence of open metal sites. Therefore, thorough investigations of isoreticular series of MOFs are crucial to assist design-based approaches for developing promising materials for olefin purification.

Copper-based MOFs (Cu-MOFs) have attracted significant attention due to their unique properties and potential applications.[36] By selecting appropriate organic ligands and reaction conditions, Cu-MOFs with specific structures and properties can be easily synthesised.[37] These MOFs can be readily obtained as single crystals, allowing their characterization through techniques such as single crystal X-ray diffraction to gain insights into their detailed molecular and topological structures. In this regard, we aim to enhance the selectivity of C_2H_4/C_2H_6 by incorporating functional groups into a series of designed Cu-MOFs (MFM-126–128).

MFM-126–128 were designed by adapting the amide group, ethynyl bond and phenyl ring into isostructural structures, respectively (Figure 2.4 a).[38] All these three frameworks are constructed from Cu(II) cations bridged by four carboxylate groups from four independent linkers and capped by two pyrimidyl nitrogen donors to form elongated octahedral $[Cu_2(RCOO)_4(NR)_2]$ nodes. The capping of the $\{Cu_2\}$ paddlewheels at both axial positions results in the absence of any open Cu(II) sites, which affords an excellent platform to study the role of functional group on gas binding. Two types of cages were observed in these MOFs frameworks, the larger one cage A (Figure 2.4 b) is comprised of six ligands and six $[Cu_2(RCOO)_4(NR)_2]$ paddlewheel units forming a hexagonal bipyramid. The six $\{Cu_2\}$ units form the six equatorial vertices of this cage and the hexagonal window of the Kagomé lattice (Figure 2.4 e). Six pyrimidyl units form the apical vertices, whereby ligands form six of the twelve faces of the hexagonal bipyramid. The smaller cage B (Figure 2.4 c) is constructed from six ligands and six $\{Cu_2\}$ paddlewheels forming a ditrigonal scalenohedral cage, whereby two sets of three $\{Cu_2\}$ paddlewheels bridged by three linker isophthalate units form triangular windows of neighbouring Kagomé lattices. The overall structure

of these MOFs is comprised of discrete cages A and B, which are packed in an alternating manner (Figure 2.4 d), giving highly porous and robust 3D frameworks. By tailoring the functional groups into the three isostructural MOFs, this approach allows us to study the effect of functionality to rationalize the C_2H_4/C_2H_6 separation properties of these materials.

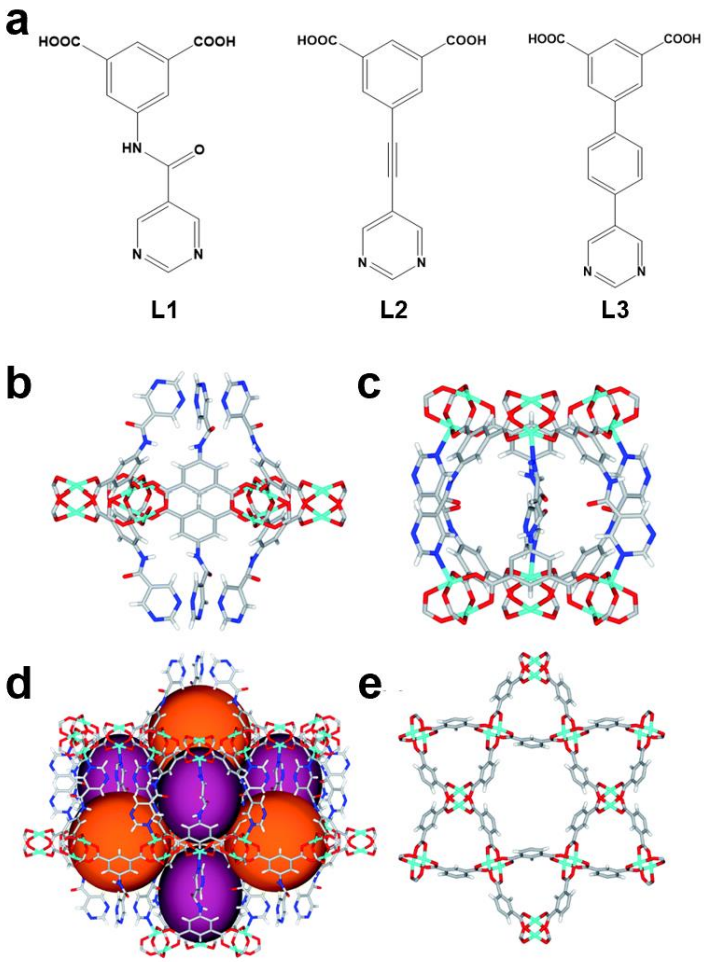

Figure 2.4. (a) Structures of linkers of L1 to L3 for MFM-126 to MFM-128. Views of crystal structure of MFM-126. (b) Cage A; (c) cage B. (d) View of the alternate packing of cages A (void space coloured orange) and B (void space coloured plum). (e) View along the c-axis of the Kagomé lattice in MFM-126. Colours: C, grey; H, white; O, red; N, blue; Cu, teal.[38]

2.4 Discussion

In this Chapter, we discussed the selected Al-MOFs, Sc-MOFs, and Zr-MOFs for NH_3 adsorption due to their robust structures and high porosities. In addition, In-MOFs, and Cu-MOFs were selected for C_2H_4/C_2H_6 separation based on their suitable pore size and surface functionalities. These materials include Al-MOFs—MIL-160, CAU-10(H), MIL-53(Al), Al-fum, Al-bttotb; Sc-MOFs—MFM-300(Sc), NOTT-401(Sc); Zr-MOFs—MOF-801, Zr-ndc and Zr-cca; In-MOFs—MFM-300(In); and Cu-MOFs—MFM-126, MFM-127, MFM-128.

2.4.1 NH_3 adsorption in selected MOFs

MIL-160, CAU-10(H), Al-fum, and MIL-53(Al). These four Al-MOFs were synthesised successfully and subsequently subjected to a stability test involving NH_3 dosing experiment. The acetone-exchanged MOF samples were then used for NH_3 isotherms measurements. MIL-160 exhibits both high uptakes at both low and high pressure at 298 K (4.8 and 12.8 mmol g^{-1} at 0.001 and 1.0 bar, respectively), as well as a high NH_3 packing density at 273 K (0.59 g cm^{-3}), comparable to that of liquid NH_3 at 240 K (0.68 g cm^{-3}). Additionally, at 298 K and 1.0 bar, the NH_3 uptakes follow the order of MIL-160 (12.8 mmol g^{-1}) > CAU-10-H (10.0 mmol g^{-1}) > Al-fum (8.9 mmol g^{-1}) > MIL-53(Al) (3.0 mmol g^{-1}). The detailed experiments, results and discussion will be presented in detail in Chapter 3 and Appendix II.

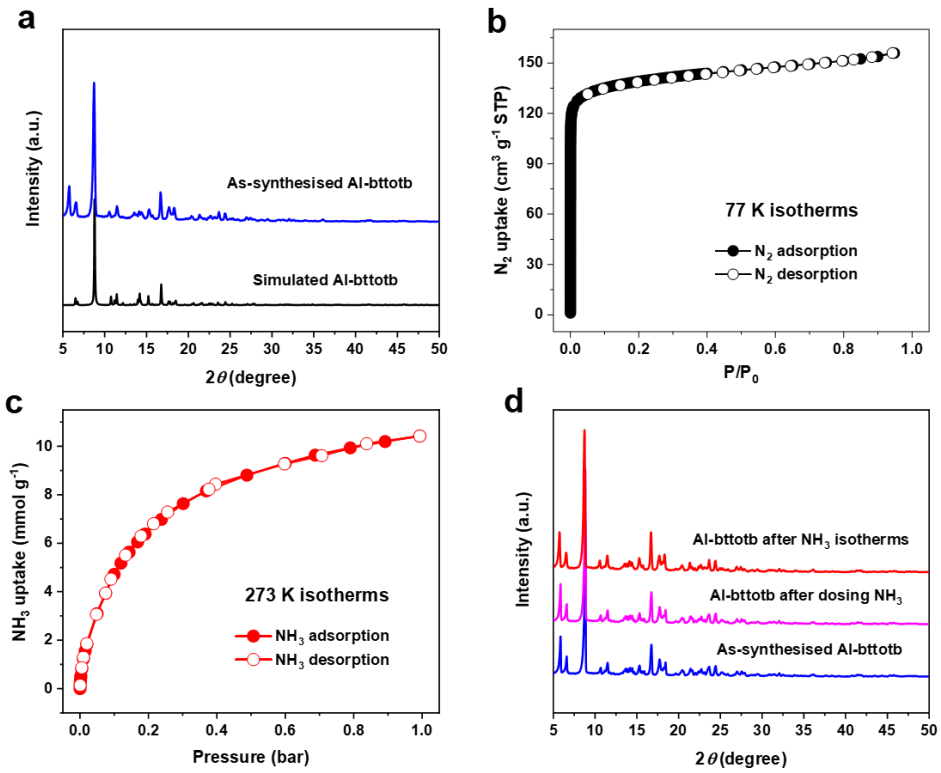

Figure 2.5. (a) PXRD patterns of simulated (black), as-synthesised (blue) sample for Al-bttotb. (b) Adsorption-desorption isotherms of N_2 at 77 K for Al-bttotb (solid: adsorption; open: desorption). (c) Adsorption-desorption isotherms of NH_3 at 273 K for Al-bttotb (solid: adsorption; open: desorption). (d) PXRD patterns of as-synthesised (blue), after dosing NH_3 for 1 day (magenta), after NH_3 adsorption isotherms (red) for Al-bttotb.

Al-bttotb. Al-bttotb was successfully synthesised and the purity of Al-bttotb was evaluated by PXRD patterns and nitrogen adsorption at 77 K (Figure 2.5 a-b). Subsequently, a stability test involving NH_3 dosing experiment was performed. Remarkably, it exhibited high stability towards NH_3, as evidenced by the retained crystalline structure after the NH_3 dosing experiment. Followed by this, methanol-exchanged Al-bttotb was utilised for isotherm measurements of NH_3 (Figure 2.5 c). The NH_3 isotherms measurements show that it has a NH_3 uptake of 10.5 mmol g^{-1} at 273 K under 1.0 bar. The moderate capacity of Al-bttotb towards NH_3 can be attributed to its relatively low surface area and small pore volume, which may thus limit the accessibility of NH_3 for adsorption.

MFM-300(Sc). MFM-300(Sc) was synthesised successfully and subsequently subjected to a stability test involving NH_3 dosing experiment. Remarkably, it exhibited remarkable stability towards NH_3, retaining both its crystalline structure and BET surface area even after a day-long NH_3 dosing experiment. Following this, the acetone-exchanged MFM-300(Sc) was utilised for isotherm measurements of NH_3. Impressively, it showcased an outstanding NH_3 uptake of 19.5 mmol g^{-1} at 273 K under 1.0 bar (Table 2.1). A comprehensive presentation of the experiments, results, and in-depth discussion can be found in Chapter 4 and Appendix III.

NOTT-401. The purity of NOTT-401 was evaluated by PXRD patterns and nitrogen adsorption at 77 K (Figure 2.6). The acetone-exchanged NOTT-401 was then subjected to a series of experiments to access its NH_3 stability and isotherms measurements under different pressures. The isotherm increases sharpy to 6.0 mmol g^{-1} at the low pressure of 30 mbar at 273 K, which could account for binding interactions between NH_3 and the functional groups (μ_2-OH) within the frameworks. The NH_3 uptake capacity of NOTT-401 remained moderate at 15.7 mmol g^{-1} under 1.0 bar at 273 K. This could be attributed to the relatively small pore volume of the material and the electron-donating hetero sulfur atom along the channel, limiting the accessibility of NH_3 for accommodation. However, it was noted that the crystallinity of the material remained unchanged after the NH_3 dosing experiments and isotherm measurements, indicating its high stability in handling NH_3.

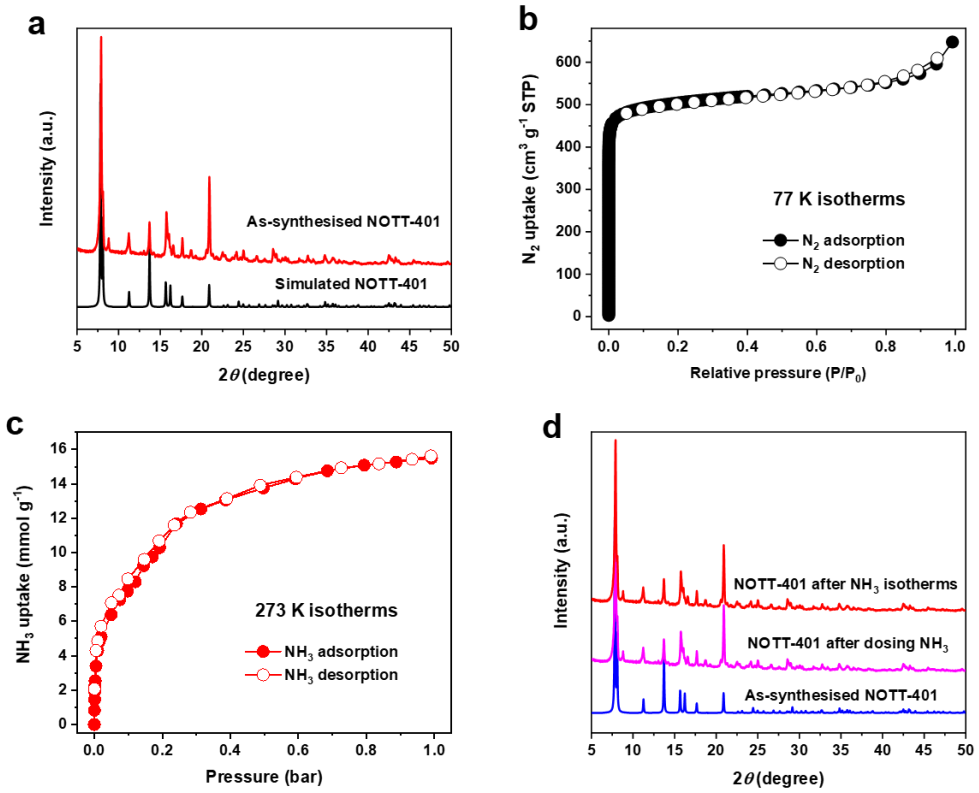

Figure 2.6. (a) PXRD patterns of simulated (black), as-synthesised (red) sample for NOTT-401. (b) Adsorption-desorption isotherms of N_2 at 77 K for pristine NOTT-401 (solid: adsorption; open: desorption). (c) Adsorption-desorption isotherms of NH_3 at 273 K for NOTT-401 (solid: adsorption; open: desorption). (d) PXRD patterns of as-synthesised (blue), after dosing NH_3 for 1 day (magenta), after NH_3 adsorption isotherms (red) for NOTT-401.

MOF-801, Zr-ndc and Zr-cca. The purity of MOF-801, Zr-ndc and Zr-cca was evaluated by PXRD patterns and nitrogen adsorption at 77 K (Figure 2.7-2.9). The acetone-exchanged MOFs samples was then used for NH_3 stability test and isotherms measurements under 1.0 bar. The crystallinity of these materials remained unchanged after the NH_3 isotherms measurements, indicating their high stability in handling NH_3. The NH_3 isotherms of these three MOFs under 1.0 bar at 273 K showed a moderate NH_3 uptake capacity of 10.7 mmol g^{-1}, 11.0 mmol g^{-1}, 11.5 mmol g^{-1} for MOF-801, Zr-ndc, and Zr-cca, respectively (Supplementary Table 2.1). All these three MOFs exhibit a sharp isotherm curve under low pressure, which could account for relatively strong binding interactions between NH_3 and the frameworks due to the functional

groups (μ_3-OH) and the small pore size. For Zr-ndc, it increases as a liner from 0.05 mbar to 1.0 bar, and far to reach its saturation point. This indicates that it could achieve much higher NH_3 uptakes at high pressures owing to its high BET surface area. The hysteresis phenomenon in the isotherm curves of Zr-cca is speculated to be due to the narrow pore size that limited the diffusion for the NH_3 desorption. The low NH_3 uptake capacities of these MOFs may be attributed to their relatively small pore size and pore volume, which limits the accessibility of NH_3. Although moderate NH_3 uptakes were obtained, further study could be put into investigating the relationships between the NH_3 uptakes and structure of these Zr-MOFs due to the robust structures considering the actual industrial applications.

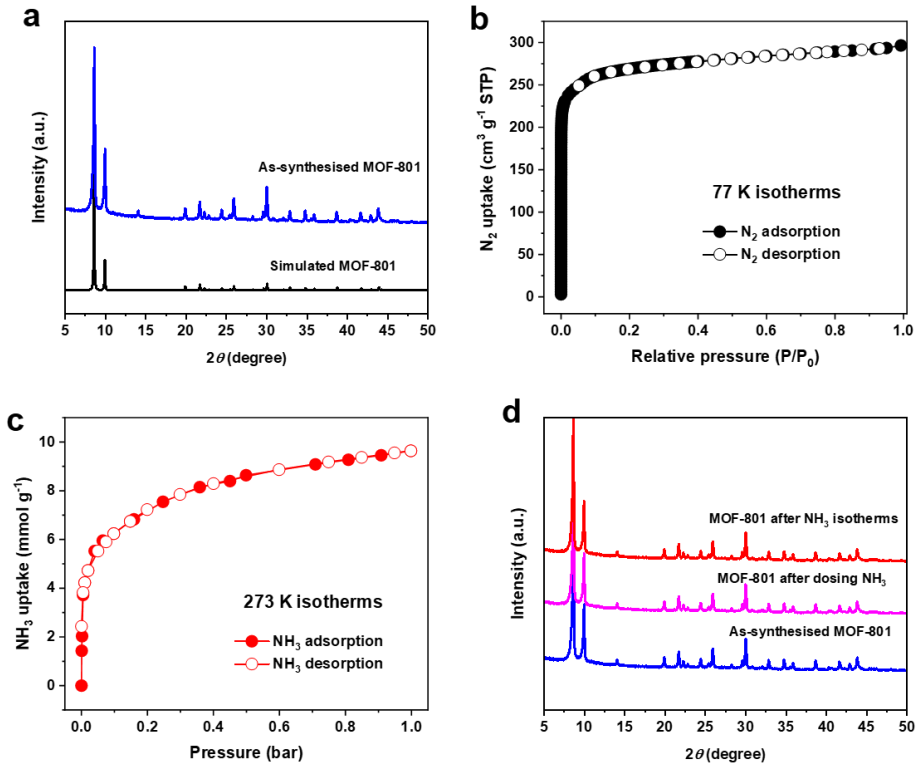

Figure 2.7. (a) PXRD patterns of simulated (black), as-synthesised (blue) sample for MOF-801. (b) Adsorption-desorption isotherms of N_2 at 77 K for pristine MOF-801 (solid: adsorption; open: desorption). (c) Adsorption-desorption isotherms of NH_3 at 273 K for MOF-801 (solid: adsorption; open: desorption). (d) PXRD patterns of as-synthesised (blue), after dosing NH_3 for 1 day (magenta), after NH_3 adsorption isotherms (red) for MOF-801.

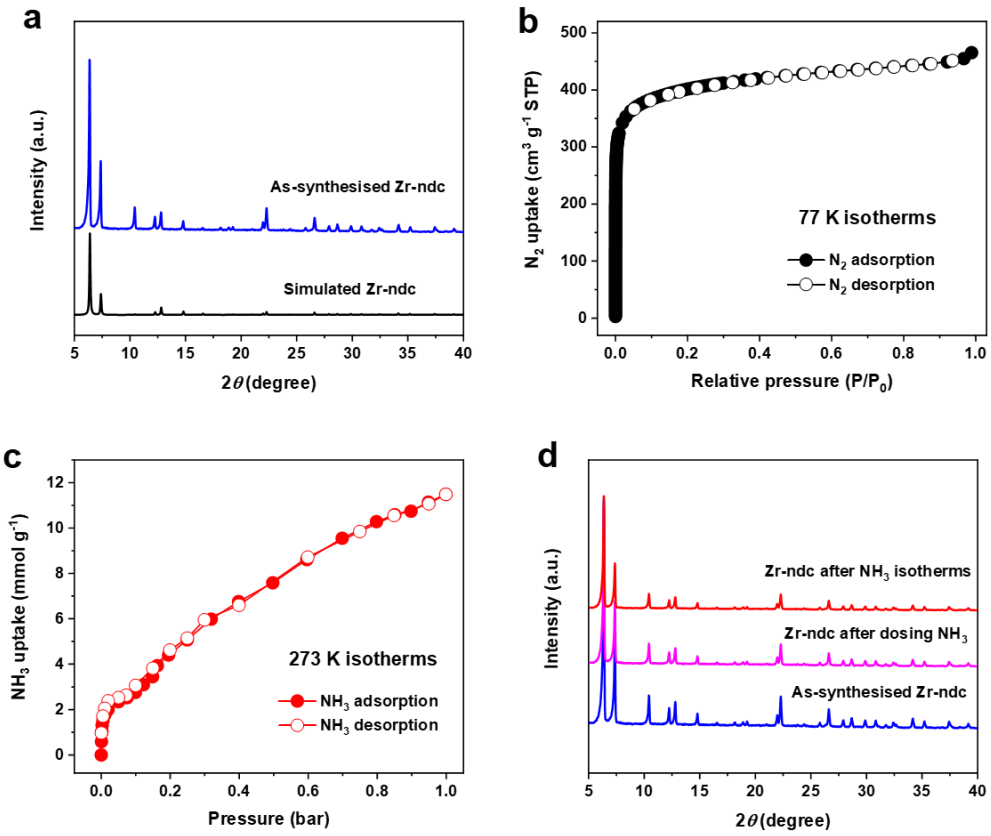

Figure 2.8. (a) PXRD patterns of simulated (black), as-synthesised (blue) sample for Zr-ndc. (b) Adsorption-desorption isotherms of N_2 at 77 K for pristine Zr-ndc (solid: adsorption; open: desorption). (c) Adsorption-desorption isotherms of NH_3 at 273 K for Zr-ndc (solid: adsorption; open: desorption). (d) PXRD patterns of as-synthesised (blue), after dosing NH_3 for 1 day (magenta), after NH_3 adsorption isotherms (red) for Zr-ndc.

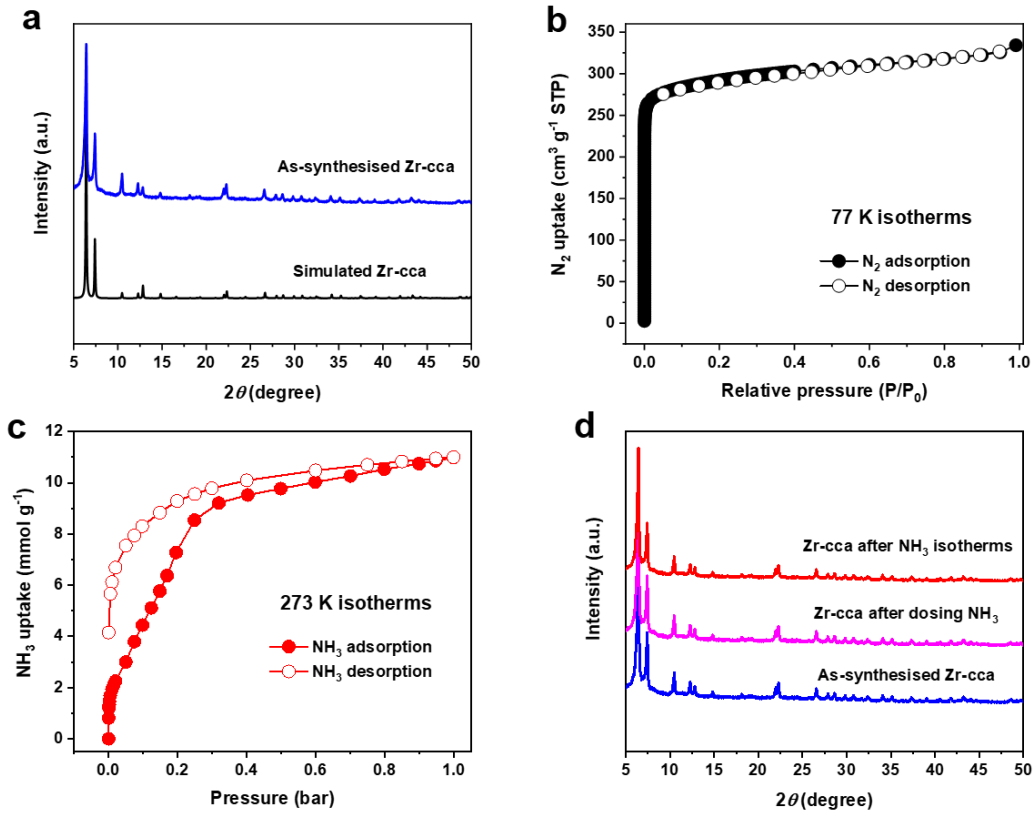

Figure 2.9. (a) PXRD patterns of simulated (black), as-synthesised (blue) sample for Zr-cca. (b) Adsorption-desorption isotherms of N_2 at 77 K for pristine MOF- Zr-cca (solid: adsorption; open: desorption). (c) Adsorption-desorption isotherms of NH_3 at 273 K for Zr-cca (solid: adsorption; open: desorption). (d) PXRD patterns of as-synthesised (blue), after dosing NH_3 for 1 day (magenta), after NH_3 adsorption isotherms (red) for Zr-cca.

2.4.2 Olefin purification in selected MOFs

MFM-300(In). The synthesis and basic characterisations of MFM-300(In) were conducted before applying for isotherms collection. Single-component adsorption isotherms revealed that MFM-300(In) has a distinct binding affinity to C_3H_4 over C_3H_6 and C_3H_8, and to C_2H_6 over C_2H_4 over a wide range of temperatures from 273 to 303 K. This suggests that MFM-300(In) has a good potential for the purification of C_2H_4 and C_3H_6. A comprehensive presentation of the experiments, results, and in-depth discussion can be found in Chapter 5 and Appendix IV.

MFM-126 and MFM-127. The adsorption isotherms for C_2H_4 and C_2H_6 in MFM-126 and MFM-127 at 293 K are presented in Figure 2.10. It was found that MFM-126 exhibits similar uptakes for C_2H_4 and C_2H_6 at 293 K under 1.0 bar, while MFM-127 observes selective adsorption of C_2H_6 over C_2H_4 at whole pressure range at 293 K. The ideal adsorbed solution theory (IAST) was utilised for calculating the adsorption selectivity for binary gas mixtures based on the single component sorption isotherms (Figure 2.11). The adsorption selectivity for equimolar C_2H_6 and C_2H_4 is 1.8 at 293 K and 1 bar, which is comparable to those of PCN-245(1.9),[39] IRMOF-8 (1.8),[40] $Ni(bdc)(ted)_{0.5}$ (2.0),[41] MUF-5 (1.96)[42] and PCN-250 (1.9).[43] The recorded selectivity of 9.4 is afforded by MAF-49,[44] but its separation performance is severely lowered by its very low C_2H_6 sorption capacity (1.72 mmol g^{-1}). Thus, MFM-127 with a high C_2H_4 sorption capacity, and moderate adsorption selectivity is a promising candidate for the separation of the C_2H_6/C_2H_4 mixture.

The observed differences in adsorption behaviour between MFM-126 and MFM-127 could be attributed to the presence of alkynyl groups in MFM-127, which may have stronger interactions with C_2H_6 than with C_2H_4. However, this hypothesis has not yet been confirmed experimentally, and further in-depth study, such as *in situ* neutron powder diffraction, heat of adsorption will be conducted to investigate the host−guest interactions between adsorbed gas molecules and the framework. Additionally, to study the impact of functional groups on the separation of C_2H_6/C_2H_4, MFM-128 will be synthesised for the single-component adsorption isotherms measurements.

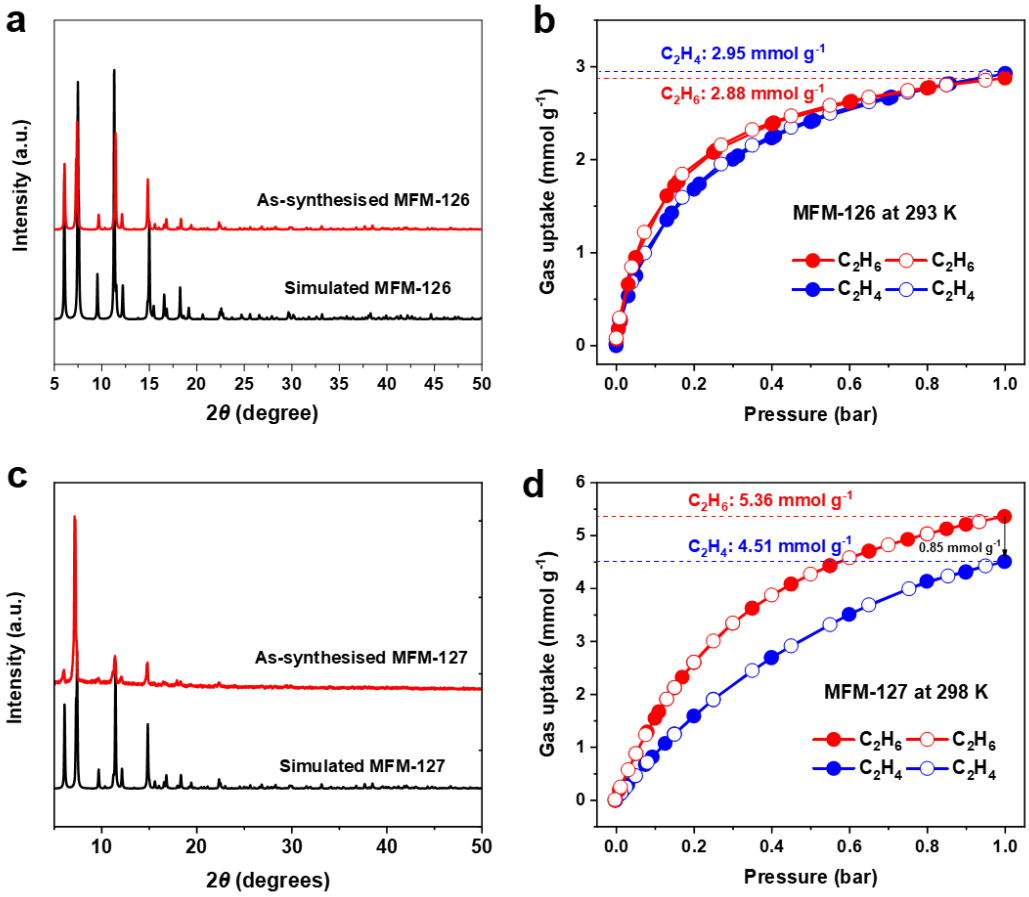

Figure 2.10. PXRD patterns of simulated (black), as-synthesised (red) sample for MFM-126 (a), and MFM-127 (c). Adsorption-desorption isotherms of C_2H_4 and C_2H_6 at 293 K for MFM-126 (b), and MFM-127 (d) (solid: adsorption; open: desorption).

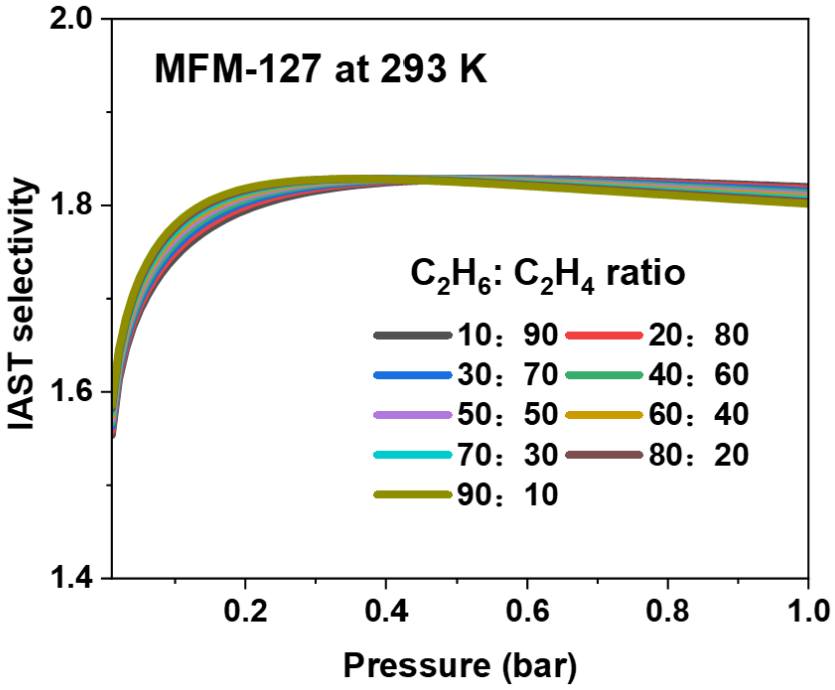

Figure 2.11. IAST selectivity of C_2H_4/C_2H_6 at 293 K for MFM-127.

2.4.3 Conclusions

In summary, this Chapter presents the strategy for selecting MOFs in the context of NH_3 adsorption and olefin purification. When it comes to NH_3 adsorption, the primary consideration is the chemical stability of the MOF materials. On the other hand, for efficient olefin purification, the focus shifts towards evaluating the pore environment. Consequently, a variety of MOFs including Al-MOFs, Sc-MOFs, Zr-MOFs, In-MOFs and Cu-MOFs were carefully chosen, synthesised, and subsequently applied in either NH_3 adsorption or olefin purification. Through the careful selection and analysis of various MOFs, this chapter provides valuable insights into the factors influencing NH_3 adsorption and highlights the importance of optimizing the pore environment for effective olefin purification. Ultimately, the results presented in Chapter 2 contribute to the ongoing development of MOFs as a promising class of materials for use in gas separation processes.

2.5 References

1. Ding, M.; Cai, X.; Jiang, H. Improving MOF stability: approaches and applications. *Chem. Sci.* **2019,** *10*, 10209−10230.
2. Devic, T.; Serre, C. High valence 3p and transition metal based MOFs. *Chem. Sci. Rev.* **2014,** *43*, 6097−6115.
3. Wang, B.; Zhang, X.; Huang, H.; Zhang, Z.; Yildirim, T.; Zhou, W.; Xiang, S.; Chen, B. A microporous aluminium-based metal-organic framework for high methane, hydrogen, and carbon dioxide storage. *Nano Res.* **2021**, *14*, 507–511.
4. Fan, W.; Wang, K.; Welton, C.; Feng, L.; Wang, X.; Liu, X.; Li, Y.; Kang, Z.; Zhou, H.; Wang, R.; Sun, D. Aluminium metal–organic frameworks: From structures to applications. *Coord. Chem. Rev.* **2023,** *489*, 215175.
5. Loiseau, T.; Volkringer, C.; Haouas, M.; Taulelle, F.; Férey, G. Crystal chemistry of aluminium carboxylates: from molecular species towards porous infinite three-dimensional networks. *C. R. Chimie.* **2015**, *18*, 1350−1369.
6. Si, X.; Jiao, C.; Li, F.; Zhang, J.; Wang, S.; Liu, S.; Li, Z.; Sun, L.; Xu, F.; Gabelica, Z.; Schick, C. High and selective CO_2 uptake, H_2 storage and methanol sensing on the amine-decorated 12-connected MOF CAU-1. *Energy Environ. Sci.* **2011**, *4*, 4522−4527.
7. Lopez-Cervantes, V. B.; Obeso, J. L.; Yanez-Aulestia, A.; Islas-Jacome, A.; Leyva, C.; Gonzalez-Zamora, E.; Sanchez-Gonzalez, E.; Ibarra, I. A. MFM-300(Sc): a chemically stable Sc(III)-based MOF material for multiple applications. *Chem. Commun.* **2023**, *59*, 10343.
8. Moeller, T.; Kremers, H. E. The basicity characteristics of scandium, yttrium, and the rare earth elements. *Chem. Rev.* **1945**, *37*, 97–159.
9. Bai, Y.; Dou, Y.; Xie, L.; Rutledge, W.; Li, J.; Zhou, H. Zr-based metal–organic frameworks: design, synthesis, structure, and applications. *Chem. Soc. Rev.*, **2016**, *45*, 2327−2367.
10. Li, J.; Huang, J.; Meng, Y.; Li, L.; Zhang, L.; Jiang, H. Zr- and Ti-based metal–organic frameworks: synthesis, structures and catalytic applications. *Chem. Commun.* **2023**, *59*, 2541−2559.
11. Carter, J.; Han, X.; Moreau, F.; Silva, I.; Nevin, A.; Godfrey, H.; Tang, C.; Yang, S.; Schröder, M. Exceptional adsorption and binding of sulfur dioxide in a robust zirconium-based metal–organic framework. *J. Am. Chem. Soc.*, **2018**, *140*, 15564–15567.
12. Li, J.; Wang, Z.; Chen, Y.; Cheng, Y.; Daemen, L.; Tuna, F.; Mclnnes, E.; Day, S.; Ramirez-Cuesta, A.; Schröder, M.; Yang, S. Synthesis of nitro compounds from nitrogen dioxide captured in a metal-organic framework. *J. Am. Chem. Soc.*, **2022**, *144*, 18967–18975.
13. Ye, Y.; Xian, S.; Cui, H.; Tan, K.; Gong, L.; Liang, B.; Pham, T.; Pandey, H.; Krishna, R.; Lan, P.; Forrest, K.; Space, B.; Thonhauser, T.; Li, J.; Ma, S. Metal–organic framework based hydrogen-bonding nanotrap for efficient acetylene storage and separation. *J. Am. Chem. Soc.* **2022**, *144*, 1681–1689.
14. Solovyeva, M.; Krivosheeva, I.; Gordeeva, L.; Aristov, Y. MIL-160 as an adsorbent for atmospheric water harvesting. *Energies* **2021**, *14*, 3586.
15. Brandt, P.; Nuhnen, A.; Lange, M.; Möllmer, J.; Weingart, O.; Janiak, C. Metal–organic frameworks with potential application for SO_2 separation and flue gas desulfurization. *ACS Appl. Mater. Interfaces* **2019**, *11*, 17350–17358.

16. Lenzen, D.; Bendix, P.; Reinsch, H.; Frohlich, D.; Kummer, H.; Mollers, M.; Hugenell, P.; Glaser, R.; Henninger, S.; Stock, N. Scalable green synthesis and full-scale test of the metal–organic framework CAU-10-H for use in adsorption-driven chillers. *Adv. Mater.* **2018,** *30*, 1705869.
17. Alvarez, E.; Guillou, N.; Martineau, C.; Bueken, B.; Van de Voorde, B.; Le Guillouzer, C.; Fabry, P.; Nouar, F.; Taulelle, F.; de Vos, D.; Chang, J.; Cho, K.; Ramsahye, N.; Devic, T.; Daturi, M.; Maurin, G.; Serre, C. The structure of the aluminium fumarate metal–organic framework A520. *Angew. Chem. Int. Ed.* **2015,** *127*, 3735−3739.
18. Boutin, A.; Coudert, F.; Springuel-Huet, M.; Neimark, A.; Férey, G.; Fuchs, A. The behavior of flexible MIL-53(Al) upon CH_4 and CO_2 adsorption. *J. Phys. Chem. C* **2010,** *114*, 22237−22244.
19. Yu, L.; Dong, X.; Gong, Q.; Acharya, S.; Lin, Y.; Wang, H.; Han, Y.; Thonhauser, T.; Li, J. Splitting mono-and dibranched alkane isomers by a robust aluminium-based metal–organic framework material with optimal pore dimensions. *J. Am. Chem. Soc.*, **2020,** *142*, 6925−6929.
20. Wang, Z.; Chen, M.; Liu, C.; Wang, X.; Zhao, H.; Du, M. A versatile Al^{III}-based metal–organic framework with high physicochemical stability. *Chem. Eur. J.*, **2015,** *21*, 17215−17219.
21. Ibarra, I.; Yang, S.; Lin, X.; Blake, A.; Rizkallah, P.; Nowell, H.; Allan, D. R.; Champness, N.; Hubberstey, P.; Schröder, M.; Highly porous and robust scandium-based metal–organic frameworks for hydrogen storage. *Chem. Commun.*, **2011**, *47*, 8304−8306.
22. Flores, J. G.; Zarate-Colın, J. A.; Sanchez-Gonźalez, E.; Valenzuela, J. R.; Gutíerrez-Alejandre, A.; Ramírez, J.; Jancik, V.; AguilarPliego, J.; Zorrilla, M. C.; Lara-García, H. A.; Gonźalez-Zamora, E.; Guzḿan-Gonźalez, G.; Gonźalez, I.; Maurin, G.; Ibarra, I. A. Partially reversible H_2S adsorption by MFM-300(Sc): formation of polysulfides. *ACS Appl. Mater. Interfaces,* **2020,** *12*, 18885–18892.
23. Źarate, J. A.; Śanchez-Gonźalez, E.; Williams, D. R.; GonźalezZamora, E.; Martis, V.; Martínez, A.; Balmaseda, J.; Maurin, G.; Ibarra, I. A. High and energy-efficient reversible SO_2 uptake by a robust Sc(III)-based MOF. *J. Mater. Chem. A*, **2019**, *7*, 15580–15584.
24. Álvarez, J. R.; Peralta, R. A.; Balmaseda, J.; Gonźalez-Zamora, E.; Ibarra, I. A. Water adsorption properties of a Sc(III) porous coordination polymer for CO_2 capture applications. *Inorg. Chem. Front.*, **2015**, *2*, 1080–1084.
25. Zhang, X.; Silva, I.; Godfrey, H. G. W.; Callear, S. K.; Sapchenko, S. A.; Cheng, Y.; Vitórica-Yreźabal, I.; Frogley, M. D.; Cinque, G.; Tang, C. C.; Giacobbe, C.; Dejoie, C.; Rudíc, S.; Ramirez-Cuesta, A. J.; Denecke, M. A.; Yang, S.; Schröder, M. Confinement of iodine molecules into triple-helical chains within robust metal–organic frameworks. *J. Am. Chem. Soc.*, **2017**, *139*, 16289–16296.
26. Lacomi, P.; Formalik, F.; Marreiros. J.; Shang, J.; Rogacka, J.; Mohmeyer, A.; Behrens, P.; Ameloot, R.; Kuchta, B.; Llewellyn, P. L. Role of structural defects in the adsorption and separation of C_3 hydrocarbons in Zr-fumarate-MOF (MOF-801). *Chem. Mater.*, **2019,** *31*, 20, 8413−8423.
27. Furukawa, H.; Gandara. F.; Zhang, Y.; Jiang, J.; Queen, W.; Hudson, M.; Yaghi, O. Water adsorption in porous metal–organic frameworks and related materials. *J. Am. Chem. Sci.*, **2014,** *136*, 11, 4369−4381.

28. He, Y.; Fu, T.; Wang, L.; Liu, J.; Liu, G.; Zhao, H. Self-assembly of MOF-801 into robust hierarchically porous monoliths for scale-up atmospheric water harvesting. *Chem. Eng. J.*, **2023,** *472*, 144786.
29. Bon, V.; Senkovska, I.; Weiss, M.; Kaskel, S. Tailoring of network dimensionality and porosity adjustment in Zr- and Hf-based MOFs. *CrystEngComm.*, **2013,** *15*, 9572−9577.
30. Wang, H.; Wang, Q.; Teat, S. J.; Olson, D.; Li, J. Synthesis, structure, and selective gas adsorption of a single-crystalline zirconium based microporous metal–organic framework. *Cryst. Growth Des.*, **2017,** *17*, 4, 2034−2040.
31. Xiang, H.; Fan, X.; Siperstein, F. R. Understanding ethane/ethylene adsorption selectivity in ethane-selective microporous materials. *Sep. Purif. Technol.* **2020,** *241*, 116635.
32. Aguirre-Díaz, L.; Reinares-Fisac, D.; Iglesias, M.; Gutiérrez-Puebla, E.; Gándara, F.; Snejko, N.; Monge, M. Group 13th metal-organic frameworks and their role in heterogeneous catalysis. *Coord. Chem. Rev.*, **2017**, *335*, 1–27.
33. Savage, M.; Cheng, Y.; Easun, T.; Eyley, J.; Argent, S.; Warren, M.; Lewis, W.; Murray, C.; Tang, C.; Frogley, M.; Cinque, G.; Sun, J.; Rudic, S.; Murden, R.; Benham, M.; Fitch, A.; Blake, A.; Ramirez-Cuesta, A.; Yang, S.; Schröder, M. Selective adsorption of sulfur dioxide in a robust metal–organic framework material. *Adv. Mater.* **2016**, *28*, 8705–8711.
34. Geier, S.; Mason, J.; Bloch, E.; Queen, W.; Hudson, M.; Brown, C.; Long, J. Selective adsorption of ethylene over ethane and propylene over propane in the metal–organic frameworks M_2(dobdc) (M = Mg, Mn, Fe, Co, Ni, Zn). *Chem. Sci.* **2013**, *4*, 2054–2061.
35. Gu, X. W.; Wang, J. X.; Wu, E.; Wu, H.; Zhou, W.; Qian, G.; Chen, B.; Li, B. Immobilization of Lewis basic sites into a stable ethane-selective MOF enabling one-step separation of ethylene from a ternary mixture. *J. Am. Chem. Soc.* **2022**, *144*, 2614−2623.
36. Duan, X.; Cai, J.; Yu, J.; Wu, C.; Cui, Y.; Yang, Y.; Qian, G. Three-dimensional copper (II) metal–organic framework with open metal sites and anthracene nucleus for highly selective C_2H_2/CH_4 and C_2H_2/CO_2 gas separation at room temperature. *Microporous Mesoporous Mater.* **2013**, *181*, 99−104.
37. Duong, T.; Sapchenko, S.; Silva, I.; Godfrey, H.; Cheng, Y.; Daemen, L.; Manuel, P.; Ramirez-Cuesta, A.; Yang, S.; Schröder, M. Optimal binding of acetylene to a nitro-decorated metal–organic framework. *J. Am. Chem. Soc.* **2018**, *140*, 16006–16009.
38. Humby, J.; Benson, O.; Smith, G.; Argent, S.; Silva, I.; Cheng, Y.; Rudic, S.; Manuel, P.; Frogley, M.; Clique, G.; Saunders, L.; Yrezabal, I.; Whitehead, G.; Easun, T.; Lewis, W.; Blake, A.; Cuesta, A.; Yang, S.; Schröder, M. Host–guest selectivity in a series of isoreticular metal–organic frameworks: observation of acetylene-to-alkyne and carbon dioxide-to-amide interactions. *Chem. Sci.*, **2019,** *10*, 1098−1106.
39. Lv, D.; Shi, R.; Chen, Y.; Wu, Y.; Wu, H.; Xi, H.; Xia, Q.; Li, Z., Selective adsorption of ethane over ethylene in PCN-245: impacts of interpenetrated adsorbent. *ACS Appl. Mater. Interfaces* **2018**, *10*, 8366–8373.
40. Pires, J.; Pinto, M. L.; Saini, V. K., Ethane selective IRMOF-8 and its significance in ethane-ethylene separation by adsorption. *ACS Appl. Mater. Interfaces* **2014**, *6*, 12093–12099.

41. Liang, W.; Xu, F.; Zhou, X.; Xiao, J.; Xia, Q.; Li, Y.; Li, Z., Ethane selective adsorbent Ni(Bdc)(Ted)$_{0.5}$ with high uptake and its significance in adsorption separation of ethane and ethylene. *Chem. Eng. J.* **2016**, *148*, 275–281.
42. Qazvini, O. T.; Babarao, R.; Shi, Z. L.; Zhang, Y. B.; Telfer, S. G., A robust ethane-trapping metal-organic framework with a high capacity for ethylene purification. *J. Am. Chem. Soc.* **2019**, *141*, 5014–5020.
43. Chen, Y.; Qiao, Z.; Wu, H.; Lv, D.; Shi, R.; Xia, Q.; Zhou, J.; Li, Z., An ethane-trapping MOF PCN-250 for highly selective adsorption of ethane over ethylene. *Chem. Eng. J.* **2018**, *175*, 110–117.
44. Liao, P.; Zhang, W.; Zhang, J.; Chen, X. Efficient purification of ethene by an ethane-trapping metal-organic framework. *Nat. Commun.* **2015**, *6*, 8697.

Chapter 3

Efficient capture and storage of ammonia in robust aluminium-based metal–organic frameworks

Chapter 3. Efficient capture and storage of ammonia in robust aluminium-based metal–organic frameworks

Manuscript

Lixia Guo,[1] Joseph Hurd,[2] Meng He,[1] Wanpeng Lu,[1] Jiangnan Li,[1] Danielle Crawshaw,[1] Mengtian Fan,[1] Sergei Sapchenko,[1] Yinlin Chen,[1] Xiangdi Zeng,[1] Meredydd Kippax-Jones,[1,4] Wenyuan Huang,[1] Zhaodong Zhu,[1] Pascal Manuel,[3] Mark D. Frogley,[4] Daniel Lee,[2] Martin Schröder[1]* and Sihai Yang[1]*

1. Department of Chemistry, University of Manchester, Manchester, M13 9PL (UK) M.Schröder@manchester.ac.uk; Sihai.Yang@manchester.ac.uk
2. Department of Chemical Engineering, University of Manchester, Manchester, M13 9PL (UK)
3. ISIS Facility, STFC Rutherford Appleton Laboratory, Chilton, Oxfordshire, OX11 0QX (UK)
4. Diamond Light Source, Harwell Science and Innovation Campus, Oxfordshire, OX11 0DE (UK)

Published: *Commun. Chem.*, **2023**, *6*, 55.

DOI: 10.1038/s42004-023-00850-4.

3.1 Abstract

The development of stable sorbent materials to deliver reversible adsorption of ammonia (NH_3) is a challenging task. Here, we report the efficient capture and storage of NH_3 in a series of robust microporous aluminium-based metal–organic framework materials, namely MIL-160, CAU-10-H, Al-fum, and MIL-53(Al). In particular, MIL-160 shows high uptakes of NH_3 of 4.8 and 12.8 mmol g^{-1} at both low and high pressure (0.001 and 1.0 bar, respectively) at 298 K. The combination of *in situ* neutron powder diffraction, synchrotron infrared micro-spectroscopy and solid-state nuclear magnetic resonance spectroscopy reveals the preferred adsorption domains of NH_3 molecules in MIL-160, with H/D site-exchange between the host and guest and an unusual distortion of the local structure of [AlO_6] moieties being observed. Dynamic breakthrough experiments confirm the excellent ability of MIL-160 to capture NH_3 with a dynamic uptake of 4.2 mmol g^{-1} at 1000 ppm. The combination of high porosity, pore aperture size and multiple binding sites promotes the significant binding affinity and capacity for NH_3 in MIL-160, which makes it a promising candidate for practical applications.

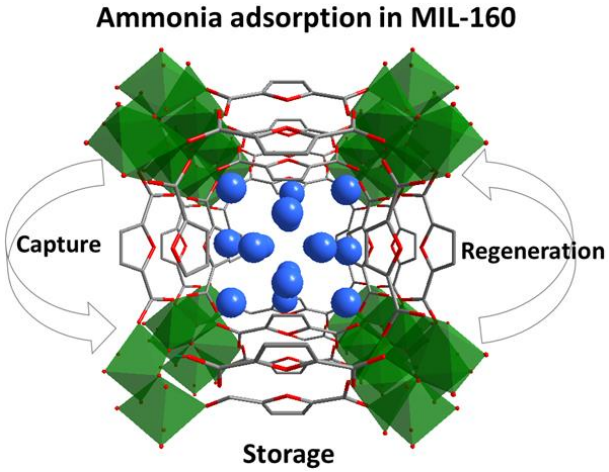

Graphical Abstract 3.1. Efficient capture and storage of ammonia in MIL-160.

3.2 Introduction

Ammonia (NH_3) is an essential feedstock for agriculture and industry and is currently being produced at a scale of approximately 180 million tonnes annually.[1] Moreover, the high density of H_2 (17.7 *wt.*% gravimetrically and 123 kg m^{-3} volumetrically) within NH_3 make the latter an attractive surrogate H_2 storage medium.[2] However, because of its toxic and corrosive nature, exposure to NH_3 is detrimental to the environment and health,[3] and thus porous sorbents that are capable of removing trace NH_3 and exhibit high NH_3 uptakes are of great interest for air remediation and NH_3 storage.[4,5] The adsorbents must display high affinity to NH_3 to allow adsorption at low pressures and/or low concentrations.[6] Conventional materials such as activated carbons[7] and organic polymers,[8] usually suffer from low adsorption affinity, poor stability and/or low uptakes for NH_3 adsorption. Therefore, it is an important but challenging task to design new materials with simultaneously high affinity, uptake, and stability for adsorption of NH_3.

Metal–organic frameworks (MOFs) have emerged as excellent adsorbents for NH_3 that surpass the performance of conventional sorbents owing to their high porosity and tuneable structure.[9] MOFs with varying pore size and functional groups have been explored, and the optimisation of pore environment is key to improve the adsorption of NH_3. For example, the μ_2-OH moieties in MFM-300(M) (M = Al, Fe, V, Cr, In, Sc),[2,10,11] and –COOH and μ_2-OH groups in MFM-303(Al)[12] can act as the primary binding sites to promote the adsorption of NH_3. MOFs incorporating unsaturated metal sites can also exhibit strong adsorption of NH_3 at low pressure owing to the strong host–guest interactions, but they often show severe structural degradation upon desorption.[13-16] Al-based MOFs received much interest in adsorption of corrosive

gases due to their high chemical stability and inexpensive synthesis at large scale. Nevertheless, their performance for adsorption of NH_3 has only been investigated to date in exceptional cases,[10,12,17] and robust Al-MOFs showing high uptakes of NH_3 at both low and high pressures are yet to be developed.

Herein, we report the study of NH_3 adsorption in four Al-MOFs, namely, MIL-160,[18] CAU-10-H,[19] Al-fum,[20] and MIL-53(Al),[21] incorporating distinct functional groups and structures. Specifically, the microporosity, abundant functional groups within the pores, and stability of MIL-160 make it promising for the study of capture and storage of NH_3, promoted by strong host–guest interactions and confinement effects. At 298 K, MIL-160 shows high uptakes of NH_3 of 4.8 and 12.8 mmol g^{-1} at 0.001 and 1.0 bar, respectively. Dynamic breakthrough experiments confirm the excellent capability of MIL-160 for NH_3 capture at low concentration (1000 ppm) with a high dynamic uptake of 4.2 mmol g^{-1}, consistent with the high observed isosteric heats of adsorption (45-63 kJ mol^{-1}). The strong binding of NH_3 molecules to the μ_2-OH groups and the heteroatom of the furan linker was directly visualised at crystallographic resolution *via* a combination of *in situ* neutron powder diffraction (NPD), synchrotron infrared micro-spectroscopy (SRIR) and solid-state nuclear magnetic resonance (ssNMR) spectroscopy. The host–guest interactions also impact the local structure of the MOF upon NH_3 binding, leading to distortions of [AlO_6] moieties, representing the first example of such an observation in a MOF studied by ^{27}Al ssNMR. This work demonstrates the promising potential of robust Al-based MOFs for high and reversible adsorption of NH_3.

3.3 Results and discussions

3.3.1 Materials and characterisation

The size, shape and chemical environment of the pores within a porous framework impact directly and control the adsorption of gas molecules. MIL-160,[18] CAU-10-H,[19] Al-fum[20] and MIL-53(Al)[21] were selected to investigate the effects of pore geometry, binding sites and the rigidity of framework on adsorption of NH_3 (Figure 3.1). In each of these four materials, the Al(III) centre is bound by six O atoms from two hydroxyl and four carboxylate groups to give an [AlO_6] octahedral geometry. The frameworks in MIL-160 and CAU-10-H contain 4-fold helical chains comprised of corner-sharing [$AlO_4(OH)_2$] octahedral moieties linked through *cis*-μ_2-OH bridges and bent linkers H_2fdc (2,5-furandicarboxylic acid) and *m*-H_2bdc (isophthalic acid), respectively. The "wine-rack" structures of MIL-160 and CAU-10-H give rise to square-shaped 1D channels of 5–6 Å diameter running along the *c* axis (Figure 3.1). By altering the linkers (from bent to linear), a distinct type of framework is formed for the isostructural Al-fum and MIL-53(Al) comprising of chains of *trans*-corner-sharing [AlO_6] octahedra linked with H_2fum (fumaric acid) and *p*-H_2bdc (terephthalic acid) ligands, respectively, to form 1D rhomb-shaped channels. MIL-53(Al) can reveal the impact of framework flexibility on NH_3 adsorption, while MIL-160, decorated with both μ_2-OH groups and heteroatom oxygen centres in the pore, affords additional active sites. Importantly, the synthesis of MIL-160 is compatible with industrial requirements using water as the solvent and a biomass-derived organic linker. We hypothesised that the π-electrons of the furan rings and narrow micropores of MIL-160 would contribute to strong surface electrostatic interactions that would be beneficial for adsorption of NH_3.

The phase purity of all bulk materials was confirmed by powder X-ray diffraction (PXRD) (Supplementary Figure 3.1). CAU-10-H shows a PXRD pattern that is nearly identical to that of MIL-160 due to the same *yfm* topology.[18, 19] The PXRD pattern of as-synthesised Al-fum show a broad peak at ca. 20 degrees, which is consistent with reported work.[20] The thermal stability of these Al-MOFs was evaluated by thermogravimetric analysis (TGA) (Supplementary Figure 3.2). In air, these Al-MOFs show thermal decomposition at 350 °C. The permanent micro-porosities of these Al-MOFs were evaluated by N_2 isotherms at 77 K, and all four MOFs exhibit a fully reversible type-I adsorption profile (Supplementary Figure 3.3−3.6) with Brunauer−Emmett−Teller (BET) surface areas of 1000, 680, 1050, and 955 $m^2 g^{-1}$ for desolvated MIL-160, CAU-10-H, Al-fum and MIL-53(Al), respectively. These results are consistent with those previously reported for these materials.[18-21] The pore size distributions (PSD) were assessed according to the Horvath−Kawazoe cylinder model (Supplementary Figure 3.3−3.6). All MOFs display narrow PSDs with main distribution centred at 5.5 Å (MIL-160), 6.0 Å (CAU-10-H), 6.0 Å (Al-fum) and 7.0/7.7 Å [MIL-53(Al)], consistent with the pore size determined from the crystal structure.

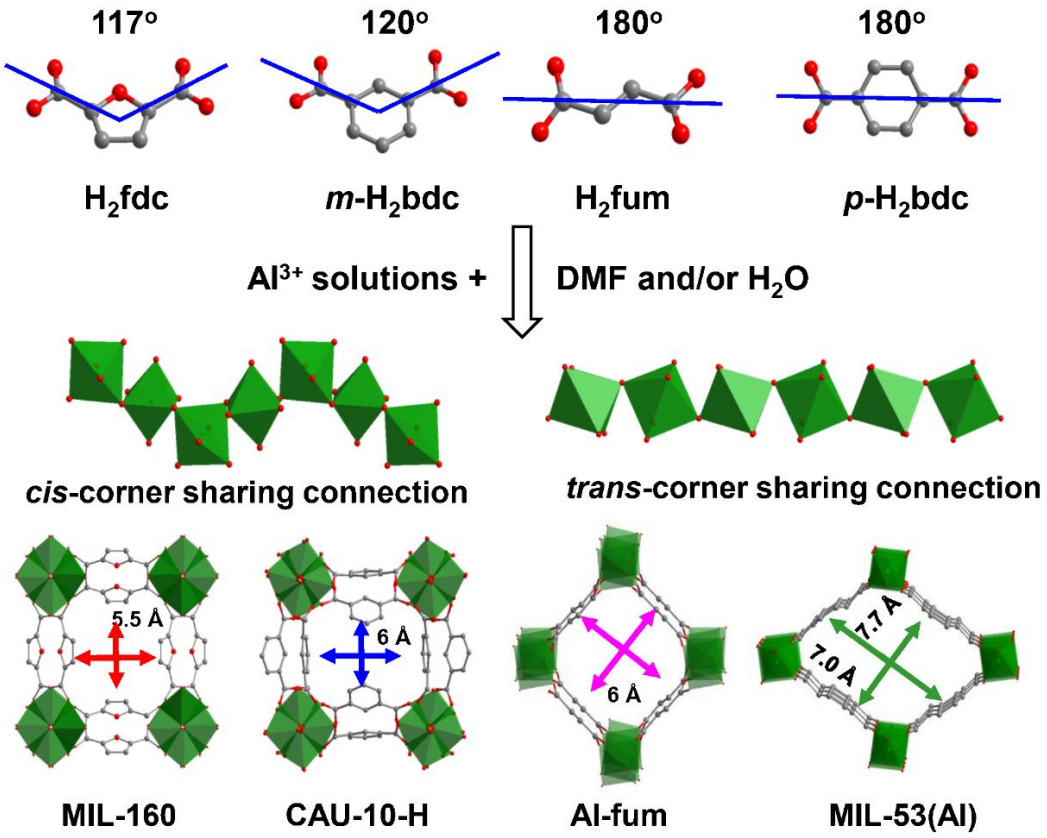

Figure 3.1. Schematic illustration. Schematic illustration of selected linkers, the self-assembly processes through *cis*- and/or *trans*-μ_2-OH connected [AlO_6] octahedral and the resulting MOFs.

3.3.2 Gas adsorption isotherms and breakthrough experiments

Adsorption−desorption isotherms at 298 K and 0.001/1.0 bar show NH_3 uptake of 4.8/12.8, 1.4/10.0, 0.47/9.0, and 0.07/3.0 mmol g^{-1} for MIL-160, CAU-10-H, Al-fum, and MIL-53(Al), respectively (Figure 3.2a). The higher uptake of NH_3 in CAU-10-H compared with Al-fum and MIL-53(Al) suggests, not unexpectedly, that the surface area is not a direct indicator for NH_3 adsorption. Instead, the synergetic effect of pore geometry, rigidness of framework, and binding sites (e.g., μ_2-OH) in the framework plays an important role in the total adsorption capacity.[8] With abundant π-electrons of the furan rings, high-density hydrogen-bonding nanotraps[22] and narrow micropores, MIL-160 exhibits the highest uptake of NH_3 among these four MOFs of 4.8/12.8 mmol

g^{-1} (at 298 K) and 6.9/15.5 mmol g^{-1} (at 273 K) at 0.001/1.0 bar (Figure 3.2 b). The uptake of NH_3 at low pressures in MIL-160 exceeds those of best-behaving materials, such as MFM-300(Sc)[2] (2.0 mmol g^{-1} at 0.001 bar at 273 K) and MFM-303(Al)[12] [6.0 and 8.3 mmol g^{-1} at 0.002 bar and 273 K for MFM-303(Al) and MIL-160, respectively], indicating its excellent potential for capture of NH_3 at low concentrations.

The ability of MIL-160, CAU-10-H, Al-fum and MIL-53(Al) to capture NH_3 at 1000 ppm (diluted in He) was evaluated by dynamic breakthrough experiments at 298 K, and dynamic capacities were calculated to be 4.2, 1.3, 0.4 and 0.15 mmol g^{-1}, respectively (Figure 3.2c and Supplementary Table 2.1). These values are consistent with the static, low-pressure capacities obtained from the isotherms at 298 K at 0.001 bar (4.8, 1.5, 0.5 and 0.17 mmol g^{-1}). The high dynamic uptake for MIL-160 suggests the presence of strong interactions between NH_3 and framework. The isosteric heats of adsorption (Q_{st}) of MIL-160 increases from 45 kJ mol^{-1} to 63 kJ mol^{-1} with increasing loading of NH_3 (Figure 3.2d and Supplementary Figure 3.7), higher than that of MFM-303(Al) (61.5 kJ mol^{-1})[12] and UiO-66-Cu^{II} (25−55 kJ mol^{-1})[16] (Supplementary Table 2.2), consistent with the presence of strong host–guest interactions and the observed high uptakes at low pressures. The NH_3-temperature programmed desorption (TPD) plot for MIL-160 shows that the absorbed NH_3 could be removed at around 200 °C (Supplementary Figure 3.8), further confirming the strong host–guest interactions between NH_3 and MIL-160. In addition, a more negative entropy of adsorption (ΔS) was observed in MIL-160 compared with other reported MOFs,[10,12,16] suggesting a higher degree of order of adsorbed NH_3 molecules within the framework.

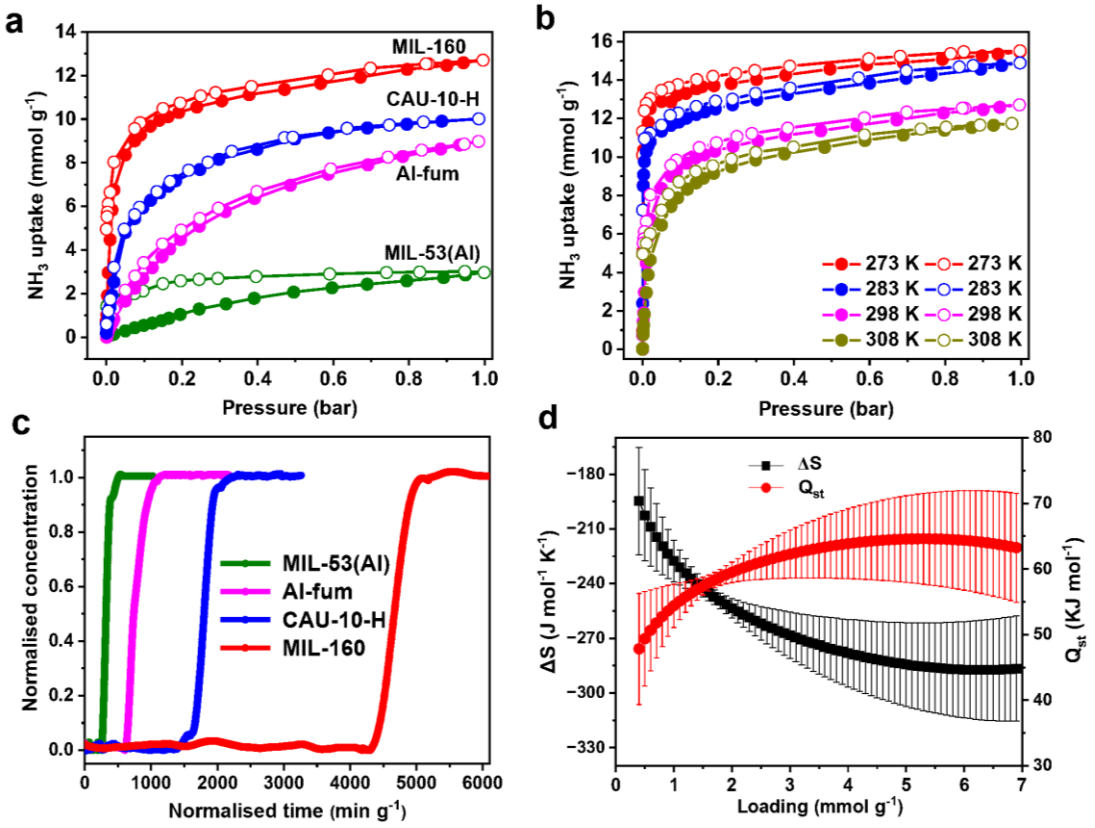

Figure 3.2. Adsorption and thermodynamics data. (a) Adsorption-desorption isotherms for four Al-MOFs at 298 K (red: MIL-160; blue: CAU-10-H; magenta: Al-fum; olive: MIL-53(Al); solid: adsorption; open: desorption). (b) Adsorption-desorption isotherms for MIL-160 at 273−308 K (red: 273 K; blue: 283 K; magenta: 298 K; dark yellow: 308 K; solid: adsorption; open: desorption). (c) Dynamic breakthrough plots for NH_3 (1000 ppm diluted in He) with an inlet gas flow rate of 25 mL min^{-1} through a fixed-bed packed with (olive) MIL-53(Al), (magenta) Al-fum, (blue) CAU-10-H and (red) MIL-160 samples at 298 K. (d) Plots for isosteric heats of adsorption (Q_{st}) and entropies of adsorption (ΔS) (red: Q_{st}; black: ΔS). The error bars were derived by least-squares linear fitting from four isotherms at different temperatures.

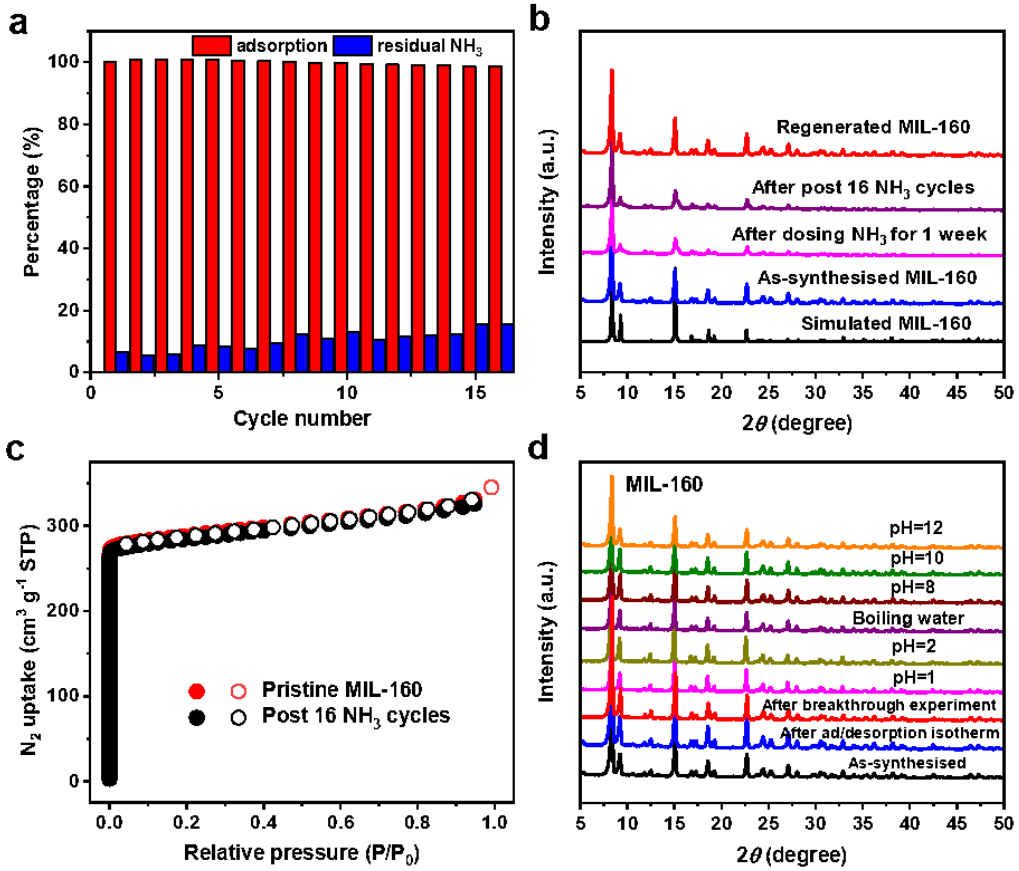

Figure 3.3. Stability data of MIL-160. (a) 16 cycles of NH_3 adsorption-desorption at 298 K between 0 and 0.2 bar in MIL-160 (pressure-swing conditions) (red bars represents the uptake capacity and blue bars indicate the residual NH_3 in the pore upon pressure swing desorption). (b) PXRD patterns of simulated (black), as-synthesised (blue), after dosing NH_3 for 1 week (magenta), after 16 cycles of NH_3 adsorption (purple) and regenerated sample (red) for MIL-160. (c) Adsorption-desorption isotherms of N_2 at 77 K for pristine MIL-160 (red) and sample regenerated after 16 cycles of NH_3 adsorption (black) (solid: adsorption; open: desorption). (d) PXRD patterns of MIL-160 for as-synthesised (black), after NH_3 ad/desorption isotherms (blue), breakthrough experiments (red), and samples soaked in solutions with pH = 1 (magenta), 2 (dark yellow), 8 (wine), 10 (olive), 12 (orange) and in boiling water (purple) for 12 h.

3.3.3 Regeneration and stability test

MIL-160 also shows a high packing density of NH_3 of 0.59 g cm^{-3} at 273 K, comparable to that of liquid NH_3 (0.68 g cm^{-3}) at 240 K[16] and that of top-performing MOFs (Supplementary Table 2.3), suggesting MIL-160 is an efficient system for NH_3

storage. Moreover, MIL-160 shows high stability with retention of the NH_3 capacity during the cyclic adsorption-desorption for at least 16 cycles at 298 K (Figure 3.3a). The PXRD patterns of MIL-160 after cycling experiment (Figure 3.3b) show that the Bragg peak at low angle broadens and decreases slightly in intensity, which could be attributed to the distortion of the framework with residual NH_3 trapped in the pore, as revealed by ssNMR results (*vide infra*). Residual NH_3 can be fully removed by heating at 453 K under dynamic vacuum, and a complete regeneration of the structure (Figure 3.3b) with full retention of the porosity (Figure 3.3c) is achieved, thus confirming the excellent regenerability of MIL-160 for NH_3 storage. MIL-160 also exhibits excellent chemical robustness on adsorption and desorption of NH_3 and in breakthrough experiments, as well as boiling water, acidic and alkaline solutions (Figure 3.3d). In contrast, CAU-10-H, Al-fum and MIL-53(Al) undergo structural degradation upon some of these treatments (Supplementary Figure 3.9).

3.3.4 Studies of the preferred binding sites and supramolecular interactions

3.3.4.1 Determination of the binding sites for adsorbed ND_3

In situ NPD was applied to determine the binding sites of ND_3 in MIL-160 (Figure 3.4, Supplementary Figure 3.11–3.13 and Supplementary Table 2.4−2.8). Rietveld refinement of the NPD data of ND_3-loaded MIL-160 [MIL-160·$(ND_3)_{0.4}$] reveals two binding sites, denoted as I and II (Figure 3.4a and 3.4b). Site I (0.202 ND_3/Al) exhibits direct binding interactions to the μ_2-OH groups in the pore [μ_2-OH···ND_3= 2.36(2) Å], with additional hydrogen bonding [ND_3···O_{ligand}= 2.20(1) Å] and [ND_3···H−C_{ligand} = 2.11(2) Å] and intermolecular interactions with site II [ND_3···ND_3 = 2.82(3) Å]. Electrostatic interactions between adsorbed ND_3 molecules and the furan rings are also observed [ND_3···C=C = 2.99(4) Å]. Site II (0.220 ND_3/Al) is stabilised by hydrogen bonding [ND_3···O_{ligand} = 3.17(2) Å] to the oxygen centre in the furan ring and

intermolecular interactions with site I [$ND_3 \cdots ND_3$ = 2.82(3) Å]. Three binding sites were observed at higher loading of ND_3 in [MIL-160·$(ND_3)_{1.5}$] (Figure 3.4c and 3.4d); ND_3(I) (0.956 ND_3/Al) is also stabilised by hydrogen bonding [μ_2-OH$\cdots ND_3$ = 2.31(2) Å; $ND_3 \cdots O_{ligand}$ = 2.32(4) Å; $ND_3 \cdots$H–C = 2.53(2) Å], supplemented by electrostatic interactions to the furan rings [$ND_3 \cdots$C=C = 3.60(4) Å] as well as intermolecular interactions between site I and site II/site III [$ND_3 \cdots ND_3$ = 4.11(2) and 3.79(4) Å]. Site II (0.358 ND_3/Al) exhibits hydrogen bonding to the furan ligand [$ND_3 \cdots O_{ligand}$= 2.94(2) Å], together with guest–guest interactions with site I [$ND_3 \cdots ND_3$ = 4.11(2) Å]. The NH_3 molecules at site III (0.188 ND_3/Al) are stabilised by intermolecular interactions to site I [$ND_3 \cdots ND_3$ = 3.79(4) Å], which is comparable to the distance of NH_3–NH_3 in solid ammonia,[23] suggesting high NH_3 packing density in MIL-160. Interestingly, in [MIL-160·$(ND_3)_{1.5}$] the hydroxyl groups showed H/D exchange with ND_3 molecules at site I in the pore, further confirming the formation of direct host–guest hydrogen bond.[10] The multiple binding sites and efficient packing of NH_3 molecules suggest strong host–guest and guest–guest interactions in the framework, consistent with the high value observed for Q_{st} (45–63 kJ mol^{-1}) for NH_3 in MIL-160.

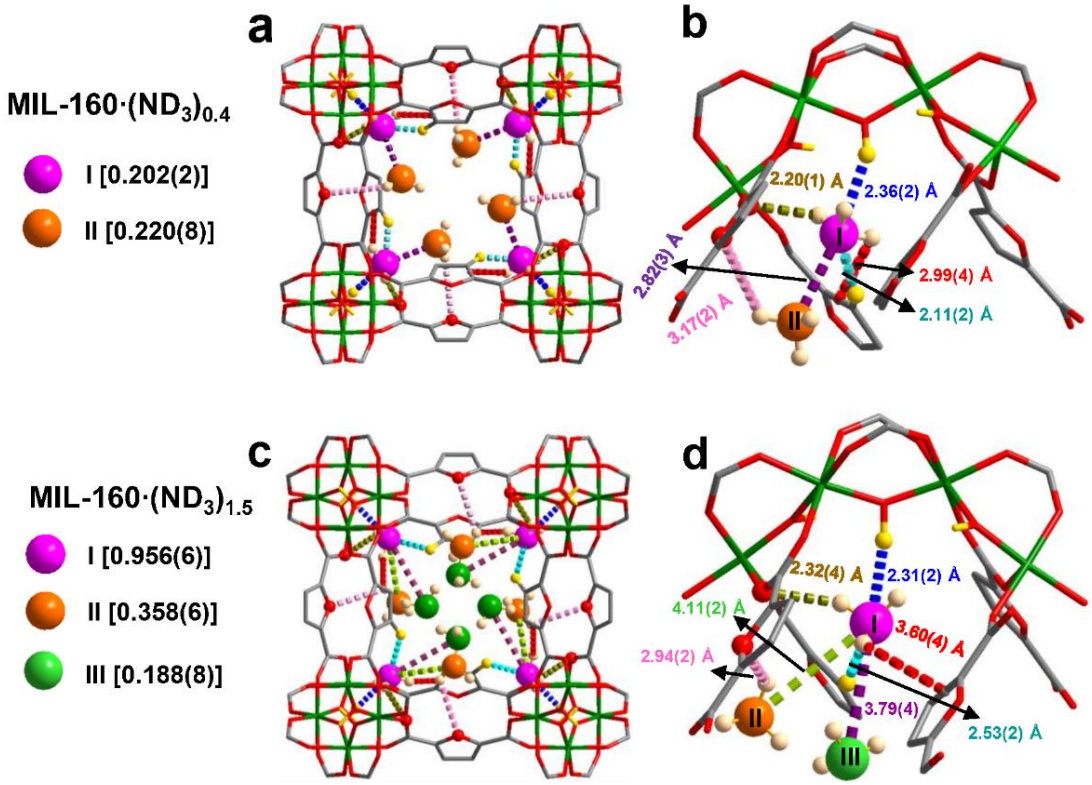

Figure 3.4. *In situ* NPD analysis. Views of the host–guest interactions in ND_3-loaded MIL-160 determined by *in situ* NPD at 10 K. The occupancy of each site has been converted into ND_3 per Al for clarity. (a) Views of ND_3 in MIL-160·$(ND_3)_{0.4}$ along the *c*-axis and (b) detailed views of host–guest interactions between MIL-160 and ND_3 (Site I: pink, Site II: orange); (c) Views of ND_3 in MIL-160·$(ND_3)_{1.5}$ along the *c*-axis and (d) detailed views of host–guest interactions between MIL-160 and ND_3 (Site I: pink; Site II: orange; Site III: green).

3.3.4.2 Analysis of NH_3 adsorption in MIL-160 by ssNMR spectroscopy

The impact of adsorption of NH_3 on the framework of MIL-160 was investigated with ssNMR spectroscopy to interrogate any local atomic-scale structural changes.[18,24] The ^1H NMR spectra clearly shows the expected presence and absence of NH_3 upon loading and removal of the substrate (Supplementary Figure 3.14). Interestingly, after full NH_3 equilibration, an additional NH_3 peak is observed at higher ^1H chemical shift, indicating strong hydrogen bonding and host–guest and guest–guest interactions; this agrees with the NPD analysis (*vide supra*). Distortions to the environment at the [AlO_6] moieties upon NH_3 uptake are probed using ^{27}Al NMR. The corresponding spectra

(Figure 3.5a) confirm that the octahedral symmetry is reduced (through an increased C_Q) with partial loading of NH_3. Notably, a component related to a distribution of environments begins to appear. Upon equilibration of NH_3 within MIL-160, octahedral moieties of [AlO_6] distorted as the ^{27}Al NMR spectrum displays a line shape characteristic of amorphous octahedral environments, whereas long-range order remained as suggested by PXRD pattern (Figure 3.3b). Upon regeneration, the crystalline structure of [AlO_6] moieties are recovered. This ^{27}Al NMR data suggests that notable framework distortion occurs upon NH_3 loading, and this may be attributed to structural "breathing" and/or to adsorption of guest molecules to metal sites,[25] as observed for MIL-53(Al).[26] Breathing has already been shown for MIL-160 when hydrated (i.e., with hydrogen-bonded guest molecules)[27] and this can be linked to changes in observed ^{27}Al NMR parameters.[18] Therefore, it is reasonable to suggest that breathing also occurs for MIL-160(Al) to facilitate uptake of NH_3, but this results in a re-distribution of [AlO_6] geometries locally, which is distinct to the conventional structural phase transition as observed in MIL-53(Al) (Supplementary Figure 3.1d).

As suggested above, the primary adsorption sites fill rapidly (Supplementary Figure 3.10) and are difficult to regenerate completely with moderate heating at 150 ºC (Supplementary Figure 3.8), as the presence of trace NH_3 is still shown in the corresponding ^{1}H NMR spectrum (Supplementary Figure 3.15). A ^{1}H-^{13}C heteronuclear dipolar correlation NMR spectrum (Supplementary Figure 3.16) confirms that the NH_3 protons are in close proximity to the carboxylate carbons, indicating their location near the pore corners (Figure 3.4) and the hydrogen-bonding of NH_3 to the framework, confirming the results from the NPD (*vide supra*). The strongly bound NH_3 required further heating treatment (up to 250 ºC) for its complete

removal. This treatment caused minor structural degradation of the MOF, as shown through the presence of new peaks in the corresponding ^{13}C and ^{1}H NMR spectrum (Figure 3.5b and Supplementary Figure 3.17). This degradation is due to the heat treatment alone and not the presence of NH_3 during heating and the NMR chemical shifts of some of these new peaks ($\delta\{^{13}C\}$ ~ 170 ppm (Figure 3.5) and $\delta\{^{1}H\}$ ~ 10 ppm (Supplementary Figure 3.14) suggest that the regenerated structure contains a small amount of carboxylic acid terminating groups. The amount of this structural degradation has been estimated (using a ratio of the acid ^{13}C peak to the carboxylate ^{13}C peak: 1:8) to ~13% of the structure with the retention of porosity and NH_3 capacity (Figure 3.3a and 3.3c). Nevertheless, the overall high capture and storage capacity are remained for regenerated MIL-160.

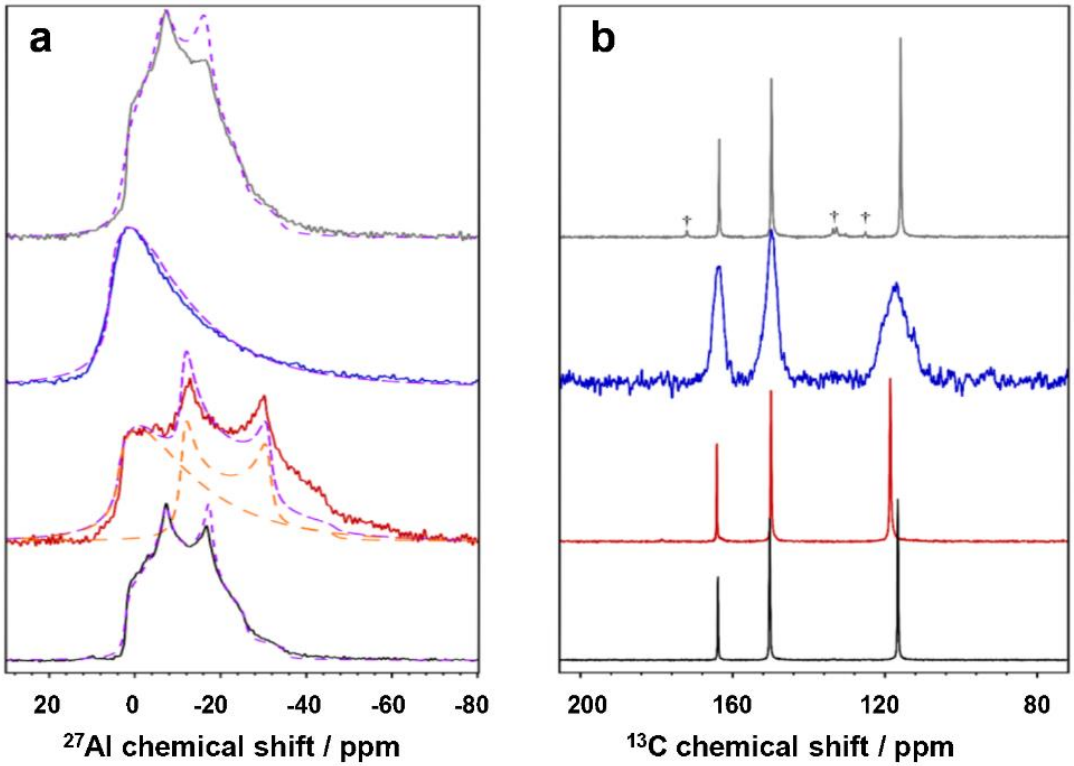

Figure 3.5. Solid-state NMR spectra. (a) ^{27}Al direct excitation and (b) {^{1}H-}^{13}C cross-polarization MAS NMR spectra of treated MIL-160 samples: pristine (black curve), partial ammonia adsorption (red curve), ammonia saturation after 1 week sealed in a rotor (blue curve) and after active desorption (250 ºC for 12 hours under dynamic vacuum) (grey curve). Daggers denote peaks arising due to structural decomposition. Simulated ^{27}Al NMR spectra (purple dashed lines) were produced using the following non-zero parameters: MIL-160 C_Q = 5.2 MHz, η_Q = 0.4, δ_{iso} = 3.8 ppm, NH_3-MIL-160' C_Q = 4.8 MHz, δ_{iso} = 4.0 ppm (Gaussian Isotropic Distribution Model) and C_Q = 5.5 MHz, η_Q = 0, δ_{iso} = -5.4 ppm, NH_3-MIL-160 C_Q = 4.8 MHz, δ_{iso} = 6.0 ppm, NH_3-MIL-160_{250} C_Q = 5.2 MHz, η_Q = 0.46, δ_{iso} = 4.0 ppm.

3.3.4.3 In situ spectroscopic analysis of host–guest binding dynamics

The binding dynamics of MIL-160 upon loading of NH_3 were further investigated by *in situ* synchrotron infrared (SRIR) micro-spectroscopy (Figure 3.6). The SRIR spectra (Figure 3.6a) of desolvated MIL-160 sample is consistent with the literature data.[28] Upon introduction of 1% NH_3, disappearance of the O–H stretching band at 3686 cm^{-1} was observed (Figure 3.6b), further confirming the strong host–guest interaction between NH_3 molecules and the framework. The band at 1655 cm^{-1} is assigned to the

asymmetric stretching vibrations of the carboxylate groups. Upon loading with NH_3 (1−100%), the peak shows red shifts to 1644 cm^{-1} (Δ = 11 cm^{-1}) (Figure 3.6c). The characteristic band at 1574 cm^{-1} is assigned to the C=C bond stretching mode, and the peak at 780 cm^{-1} to the out-of-plane deformation vibrations of C−H bonds in the furan rings. On dosing with NH_3, the red shift (Δ = 7 cm^{-1}) of the peak at 1574 cm^{-1} reflects the presence of NH_3···C=C interactions (Figure 3.6d). The peaks in the range of 1000−1250 cm^{-1} can be attributed to the asymmetric and symmetric stretching vibrations of the C−O−C in the furan rings. Specifically, the peak at 1243 cm^{-1} shows a red shift and broadens, while the band at 1013 cm^{-1} both reduces in intensity and broadens as NH_3 loading increases (Figure 3.6e). The emergence of a new band at 1101 cm^{-1} can be assigned to the N−H wagging upon NH_3 adsorption. When the loading of NH_3 increases to 40%, the peak broadens indicative of a more complex binding environment, consistent with the NPD data (*vide supra).* These results are consistent with the interactions of ND_3···O_{ligand}. Furthermore, the blue shift of the C–H deformation band to 785 cm^{-1} (Δ = 5 cm^{-1}) is observed, again consistent with the presence of interactions between NH_3 and furan rings (Figure 3.6f). Upon regeneration, the entire spectrum of the framework returns to that of the original activated material, confirming the high structural robustness of MIL-160.

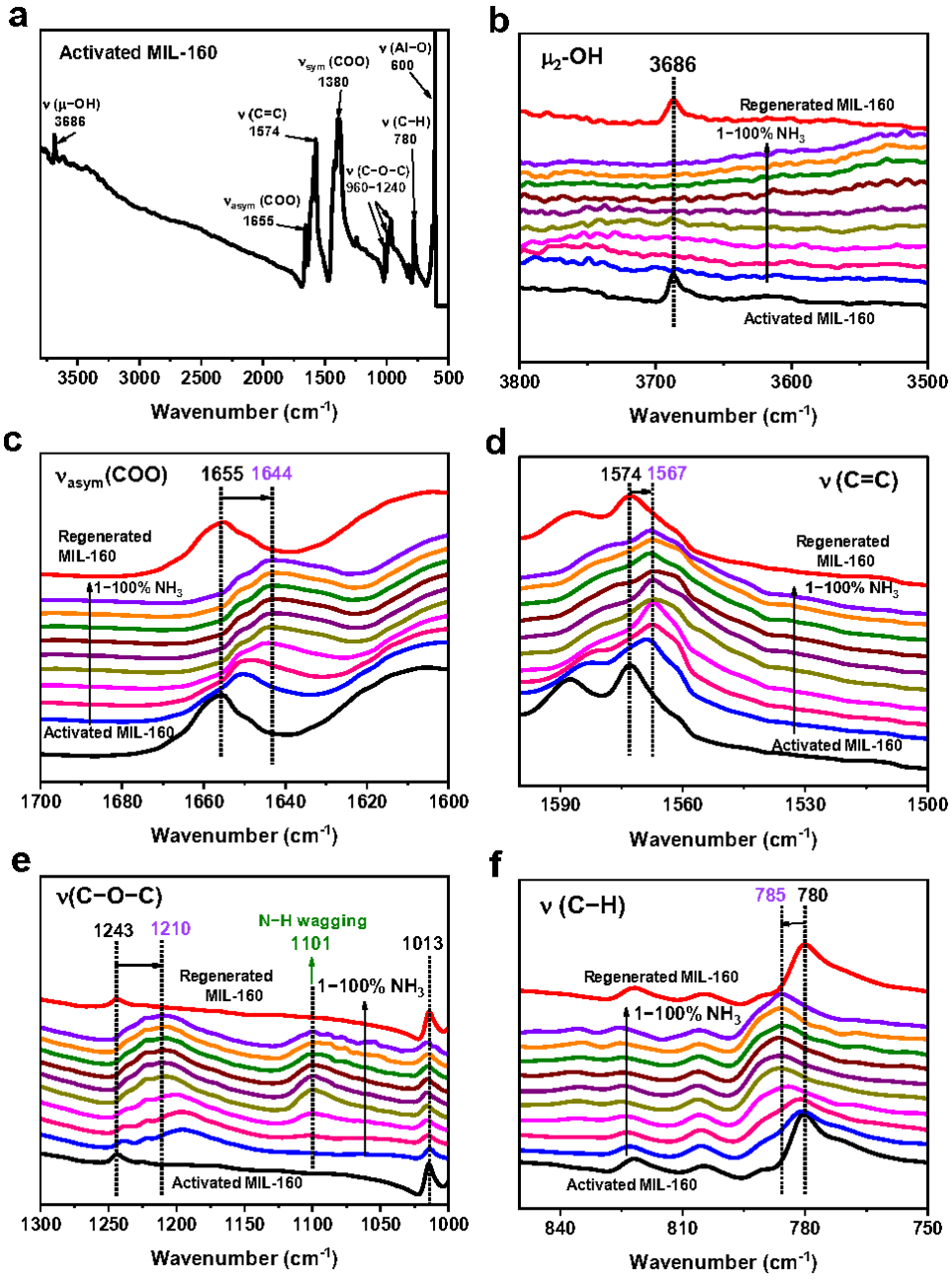

Figure 3.6. *In situ* synchrotron IR spectra. (a) *In situ* synchrotron IR spectra for activated MIL-160; *In situ* synchrotron IR spectra for MIL-160 as a function of adsorption of NH_3 (diluted in dry N_2) and after regeneration under a dry N_2 flow at 10 mL min^{-1} at 423 K for 2 h: (b) 3800-3500 cm^{-1}, (c) 1700-1600 cm^{-1}, (d) 1600-1500 cm^{-1}, (e) 1300-1000 cm^{-1}, (f) 850-750 cm^{-1}. Activated MIL-160 (black), 1% NH_3-loaded MIL-160 (blue), 2% NH_3-loaded MIL-160 (pink), 5% NH_3-loaded MIL-160 (magenta), 10% NH_3-loaded MIL-160 (dark yellow), 20% NH_3-loaded MIL-160 (purple), 40% NH_3-loaded MIL-160 (wine), 60% NH_3-loaded MIL-160 (olive), 80% NH_3-loaded MIL-160 (orange), 100% NH_3-loaded MIL-160 (violet), regenerated MIL-160 (red).

3.4 Conclusions

We report the crucial effects of functional groups (e.g., μ_2-OH), pore geometry and structural flexibility on the development of Al-based MOF materials for efficient capture and storage of NH_3. At 298 K and 1.0 bar, NH_3 uptakes follow the order of MIL-160 (12.8 mmol g^{-1}) > CAU-10-H (10.0 mmol g^{-1}) > Al-fum (8.9 mmol g^{-1}) > MIL-53(Al) (3.0 mmol g^{-1}). The suitable pore size, anchored μ_2-OH, and the O-heteroatom of the furan linker within the channel of MIL-160 enable strong interactions with NH_3 molecules, thus promoting the excellent adsorption of NH_3 at both low and high pressure. The *in-situ* NPD, synchrotron IR and ssNMR spectroscopy reveal the adsorption mechanism and interaction with μ_2-OH groups in the pores and distortion of the [AlO_6] moieties upon NH_3 uptake. Considering the advantages of the high NH_3 affinity and uptakes, and high stability, MIL-160 has a great potential in practical application as a robust sorbent for NH_3.

3.5 References

1. Gezerman, A.O. A critical assessment of green ammonia production and ammonia production technologies. *Kem. Ind.* **2022,** *71*, 57−66.
2. Guo, L.; Han, X.; Ma, Y.; Li, J.; Lu, W.; Li, W.; Lee, D.; Silva, I.; Cheng, Y.; Rudic, S.; Manuel, P.; Frogley, M.; Cuesta, A.; Schröder, M.; Yang, S. High capacity ammonia adsorption in a robust metal–organic framework mediated by reversible host–guest interactions. *Chem. Commun.,* **2022,** *58*, 5753−5756.
3. Martínez-Ahumada, E.; Díaz-Ramírez, M. L.; Velásquez-Hernández, M. d. J.; Jancik, V.; Ibarra, I. A. Capture of toxic gases in MOFs: SO_2, H_2S, NH_3 and NO_x. *Chem. Sci.* **2021,** *12*, 6772−6799.
4. Kang, D. W.; Ju, S. E.; Kim, D. W.; Kang, M.; Kim, H.; Hong, C. S. Emerging porous materials and their composites for NH_3 gas removal. *Adv. Sci.* **2020,** *7*, 2002142.
5. Chen, Y.; Zhang, X.; Ma, K.; Chen, Z.; Wang, X.; Knapp, J.; Alayoglu, S.; Wang, F.; Xia, Q.; Li, Z.; Islamoglu, T.;, Farha, O. K. Zirconium-based metal–organic framework with 9-connected nodes for ammonia capture. *ACS Appl. Nano Mater.* **2019,** *2*, 6098−6102.
6. Kim, D. W.; Kang, D. W.; Kang, M.; Lee, J. H.; Choe, J. H.; Chae, Y. S.; Choi, D. S.; Yun, H.; Hong, C. S. High ammonia uptake of a metal–organic framework adsorbent in a wide pressure range. *Angew. Chem. Int. Ed.* **2020,** *59*, 22531−22536.

7. Qajar, A.; Peer, M.; Andalibi, M. R.; Rajagopalan, R.; Foley, H. C. Enhanced ammonia adsorption on functionalized nanoporous carbons. *Micropor. Mesopor. Mat.* **2015,** *218*, 15−23.
8. Doonan, C. J.; Tranchemontagne, D. J.; Glover, T. G.; Hunt, J. R.; Yaghi, O. M. Exceptional ammonia uptake by a covalent organic framework. *Nat. Chem.* **2010,** *2*, 235–238.
9. Islamoglu, T.; Chen, Z.; Wasson, M. C.; Buru, C. T.; Kirlikovali, K. O.; Afrin, U.; Mian, M. R.; Farha, O. K. Metal–organic frameworks against toxic chemicals. *Chem. Rev.* **2020,** *120*, 8130−8160.
10. Godfrey, H.; Silva, I., Briggs, L.; Carter, J. H.; Morris, C. G.; Savage, M.; Easun, T. L.; Manuel, P.; Murray, C. A., Tang, C. C.; Frogley, M. D.; Cinque, G.; Yang, S.; Schröder, M. Ammonia storage by reversible host–guest site exchange in a robust metal–organic framework. *Angew. Chem. Int. Ed.* **2018,** *130*, 14994−14997.
11. Han, X.; Lu, W.; Chen, Y.; Silva, I.; Li, J.; Lin, L.; Li, W.; Sheveleva, A.; Godfrey, H.; Lu, Z.; Tuna, F.; McInnes, E.; Cheng, Y.; Daemen, L.; McPherson, L.; Teat, S.; Frogley, M.; Rudic, S.; Manuel, P.; Ramirez-Cuesta, A.; Yang, S.; Schröder, M. High ammonia adsorption in MFM-300 materials: dynamics and charge transfer in host–guest binding. *J. Am. Chem. Soc.* **2021,** *143*, 3153−3161.
12. Marsh, C.; Han, X.; Li, J.; Lu, Z.; Argent, S.; Silva, I.; Cheng, Y.; Daemen, L.; Ramirez-Cuesta, A.; Thompson, S.; Blake, A.; Yang, S.; Schröder, M. Exceptional packing density of ammonia in a dual-functionalized metal–organic framework. *J. Am. Chem. Soc.* **2021,** *143*, 6586−6592.
13. Liu, J.; Lu, Z.; Chen, Z.; Rimoldi, M.; Howarth, A.; Chen, H.; Alayoglu, S.; Snurr, R.; Farha, O.; Hupp, J. Ammonia capture within zirconium metal–organic frameworks: reversible and irreversible uptake. *ACS Appl. Mater. Interfaces* **2021,** *13*, 20081−20093.
14. Saha, D.; Deng, S. Ammonia adsorption and its effects on framework stability of MOF-5 and MOF-177. *J. Colloid. Interf. Sci.* **2010,** *348*, 615−620.
15. Kim, D.; Kang, D.; Kang, M.; Choi, D.; Yun, H.; Kim, S.; Lee, S.; Lee, J.; Hong, C. High gravimetric and volumetric ammonia capacities in robust metal–organic frameworks prepared via double post synthetic modification. *J. Am. Chem. Soc.* **2022,** *144*, 9672−9683.
16. Ma, Y.; Lu, W.; Han, X.; Chen, Y.; Silva, I.; Lee, D.; Sheveleva, A.; Wang, Z.; Li, J.; Li, W.; Fan, M.; Xu, S.; Tuna, F.; McInnes, E.; Cheng, Y.; Rudic, S.; Manuel, P.; Frogley, M.; Cuesta, A.; Schröder, M.; Yang, S. Direct observation of ammonia storage in UiO-66 incorporating Cu(II) binding sites. *J. Am. Chem. Soc.* **2022,** *144*, 8624–8632.
17. Wang, Z.; Li, Z.; Zhang, X.; Xia, Q.; Wang, H.; Wang, C.; Wang, Y.; He, H.; Zhao, Y.; Wang, J. Tailoring multiple sites of metal–organic frameworks for highly efficient and reversible ammonia adsorption. *ACS Appl. Mater. Interfaces* **2021,** *13*, 56025−56034.
18. Cadiau, A.; Lee, J.; Damasceno Borges, D.; Fabry, P.; Devic, T.; Wharmby, M. T.; Martineau, C.; Foucher, D.; Taulelle, F.; Jun, C.; Hwang, Y.; Stock, N.; De Lange, M.; Kapteijn, F.; Gascon, J.; Maurin, G.; Chang, J.; Serre, C. Design of hydrophilic metal organic framework water adsorbents for heat reallocation. *Adv. Mater.* **2015,** *27*, 4775−4780.
19. Lenzen, D.; Bendix, P.; Reinsch, H.; Frohlich, D.; Kummer, H.; Mollers, M.; Hugenell, P.; Glaser, R.; Henninger, S.; Stock, N. Scalable green synthesis and

full-scale test of the metal–organic framework CAU-10-H for use in adsorption-driven chillers. *Adv. Mater.* **2018,** *30*, 1705869.
20. Alvarez, E.; Guillou, N.; Martineau, C.; Bueken, B.; Van de Voorde, B.; Le Guillouzer, C.; Fabry, P.; Nouar, F.; Taulelle, F.; de Vos, D.; Chang, J.; Cho, K.; Ramsahye, N.; Devic, T.; Daturi, M.; Maurin, G.; Serre, C. The structure of the aluminium fumarate metal–organic framework A520. *Angew. Chem. Int. Ed.* **2015,** *127*, 3735−3739.
21. Boutin, A.; Coudert, F.; Springuel-Huet, M.; Neimark, A.; Férey, G.; Fuchs, A. The behavior of flexible MIL-53(Al) upon CH_4 and CO_2 adsorption. *J. Phys. Chem. C* **2010,** *114*, 22237−22244.
22. Ye, Y.; Xian, S.; Cui, H.; Tan, K.; Gong, L.; Liang, B.; Pham, T.; Pandey, H.; Krishna, R.; Lan, P.; Forrest, K.; Space, B.; Thonhauser, T.; Li, J.; Ma, S. Metal−organic framework based hydrogen-bonding nanotrap for efficient acetylene storage and separation. *J. Am. Chem. Soc.* **2022,** *144*, 1681–1689.
23. Brunner, E.; Rauche, M. Solid-state NMR spectroscopy: an advancing tool to analyse the structure and properties of metal–organic frameworks. *Chem. Sci.* **2020,** *11*, 4297−4304.
24. Cho, H.; Deng, H.; Miyasaka, K.; Dong, Z.; Cho, M.; Neimark, A.; Kang, J.; Yaghi, O.; Terasaki, O. Extra adsorption and adsorbate super lattice formation in metal–organic frameworks. *Nature*, **2015,** *527*, 503−507.
25. Khudozhitkov, A.; Arzumanov, S.; Toktarev, A.; Cherepanova, S.; Gabrienko, A.; Kolokolov, D.; Stepanov, A. Dissecting the effects of water guest adsorption and framework breathing on the $AlO_4(OH)_2$ centres of metal–organic framework MIL-53(Al) by solid state NMR and structural analysis. *Phys. Chem. Chem. Phys.* **2021,** *23*, 18925–18929.
26. Wahiduzzaman, M.; Lenzen, D.; Maurin, G.; Stock, N.; Wharmby, M. Rietveld refinement of MIL-160 and its structural flexibility upon H_2O and N_2 adsorption. *Eur. J. Inorg. Chem*. **2018,** *32*, 3626–3632.
27. Solovyeva, M.; Krivosheeva, I.; Gordeeva, L.; Aristov, Yuri. MIL-160 as an adsorbent for atmospheric water harvesting. *Energies*, **2021,** *14*, 3586.
28. Massiot, D.; Fayon, F.; Capron, M.; King, I.; Calve, S.; Alonso, B.; Durand, J.; Bujoli, B.; Gan, Z.; Hoatson, G. Modelling one- and two-dimensional solid-state NMR spectra. *Magn. Reson. Chem*. **2002,** *40*, 70–76.

3.6 Additional information

Author information. Correspondence and requests for materials should be addressed to M.S. (M.Schröder@manchester.ac.uk) and S.Y. (Sihai.Yang@manchester.ac.uk).

Conflicts of interest. The authors declare no competing interest.

Acknowledgements. We thank EPSRC (EP/I011870, EP/V056409), Royal Society, and University of Manchester funding. This project has received funding from the European Research Council (ERC) under the European Union's Horizon 2020 research and innovation programme (grant agreement No 742401, *NANOCHEM*). We are grateful to ISIS facility and Diamond Light Source for access to Beamlines WISH

and B22, respectively. L.G., M.H. and W.H. thank the China Scholarship Council (CSC) for funding.

Supporting information. The supporting information of this paper is listed in Appendix I.

[Blank page]

Chapter 4

High capacity ammonia adsorption in a robust metal–organic framework mediated by reversible host–guest interactions

Chapter 4: High capacity ammonia adsorption in a robust metal–organic framework mediated by reversible host–guest interactions

Manuscript

Lixia Guo,[1] Xue Han,[1] Yujie Ma,[1] Jiangnan Li,[1] Wanpeng Lu,[1] Weiyao Li,[1] Daniel Lee,[2] Ivan da Silva,[3] Yongqiang Cheng,[4] Svemir Rudić,[3] Pascal Manuel,[3] Mark D. Frogley,[5] Anibal J. Ramirez-Cuesta,[4] Martin Schröder*[1] and Sihai Yang*[1]

1. Department of Chemistry, University of Manchester, Manchester, M13 9PL, UK.

* M.Schröder@manchester.ac.uk; Sihai.Yang@manchester.ac.uk

2. Department of Chemical Engineering and Analytical Science, University of Manchester, Manchester, M13 9PL, UK

3. ISIS Facility, STFC Rutherford Appleton Laboratory, Oxfordshire, OX11 0QX, UK

4. Neutron Scattering Division, Neutron Sciences Directorate, Oak Ridge National Laboratory, Oak Ridge, TN 37831, USA

5. Diamond Light Source, Harwell Science and Innovation Campus, Oxfordshire, OX11 0DE, UK

Published: *Chem. Commun.*, **2022**, *58*, 5753−5756.

DOI: 10.1039/D2CC01197B.

4.1 Abstract

To understand the exceptional adsorption of ammonia (NH_3) in MFM-300(Sc) (19.5 mmol g^{-1} at 273 K and 1 bar without hysteresis), we report a systematic investigation of the mechanism of adsorption by a combination of *in situ* neutron powder diffraction, inelastic neutron scattering, synchrotron infrared micro spectroscopy, and solid-state ^{45}Sc NMR spectroscopy. These complementary techniques reveal the formation of reversible host–guest supramolecular interactions, which explains directly the observed excellent reversibility of this material over 90 adsorption–desorption cycles.

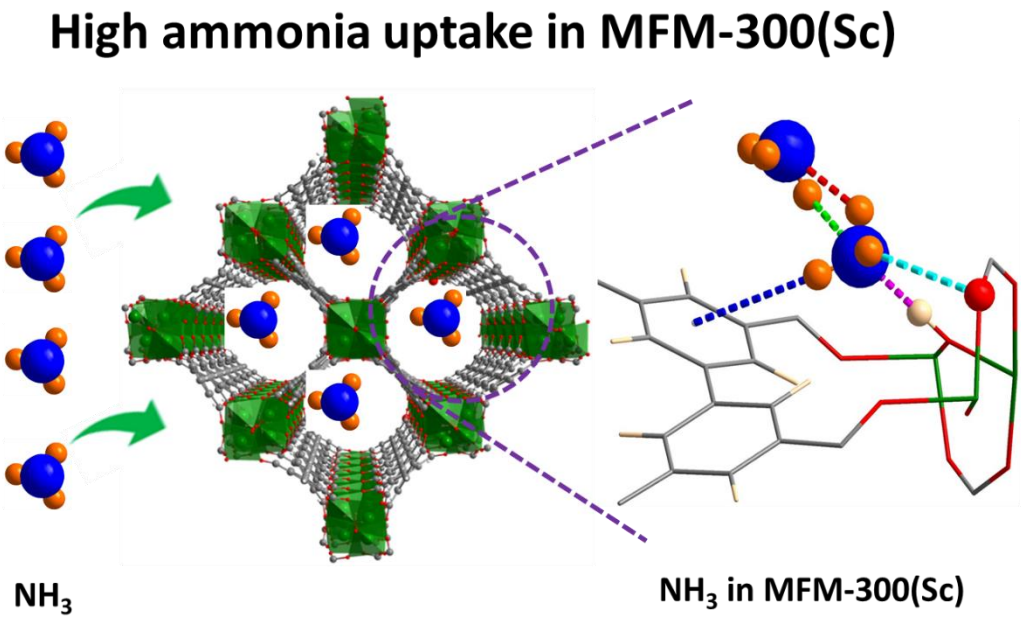

Graphical Abstract 4.1. High ammonia storage in a robust Scandium-MOF

4.2 Introduction

Annual global production of ammonia (NH_3) is around 170 million tonnes reflecting its role as a major feedstock for agriculture and industry.[1] The high hydrogen content (17.8 *wt.*%) and hydrogen volume density (105 kg m^{-3}) of NH_3 make it a desirable carbon-free hydrogen carrier, and NH_3 is therefore regarded as a surrogate for the H_2

economy. However, the corrosive and toxic nature of NH_3 makes the development of stable storage materials with high and reversible uptakes extremely challenging. Conventional sorbent materials such as zeolites,[2] activated carbons,[3] and organic polymers[4] have been investigated for the storage of NH_3 but show low and often irreversible uptakes. Metal–organic framework (MOFs) materials have been postulated as promising candidates for gas storage due to their high surface areas and versatile pore structures.[5] As opposed to conventional adsorbents, the affinities of MOF materials to a target gas can be tailored by grafting the pore interior with functional groups to anchor the gas through coordination, hydrogen bonding, electrostatic interactions, acid- base interactions or $\pi\cdots\pi$ stacking.[5-7] A large number of MOFs with functional groups (*e.g.* –COOH,[8] –OH[9]) and open metal sites[10] have been reported to impart enhanced affinity to gas molecules. Several state-of-the-art MOFs, such as MOF-177,[11] M_2Cl_2BBTA [BBTA = 1*H*,5*H*-benzo(1,2-d:4,5-*d'*)bistriazole; M = Co, Mn],[12] $M_2Cl_2(BTDD)$ {BTDD = bis(1*H*-1,2,3-triazolo[4,5-b],[4′,5′-*i*])dibenzo[1,4]dioxin); M = Mn, Co, Ni and Cu}[13] as well as MFM-300(M) (M = Al, Fe, V, Cr, In)[6,14] have been investigated for NH_3 adsorption. However, due to the reactive and corrosive nature of NH_3, many MOF systems showed structural degradation and/or significant loss of uptake after consecutive cycles owing to irreversible host–guest binding. So far, only a very limited number of MOFs exhibit reversible NH_3 sorption over multiple cycles.[6,8,13-16] Unravelling the molecular details on the host–guest interactions are of critical importance if new efficient ammonia storage systems are to be developed. This is however highly challenging, not least because hydrogen atoms are invisible in X-ray diffraction experiments and NH_3 molecules can act as a rapid rotor even in solid state.

The mechanism of adsorption of NH_3 in MFM-300(Sc) was examined systematically using gas isotherms, breakthrough experiments, *in situ* solid-state nuclear magnetic resonance (ssNMR) spectroscopy, synchrotron infrared microspectroscopy, neutron powder diffraction (NPD) and inelastic neutron scattering (INS) techniques, coupled with DFT modelling. Distinct new insights have been gained into the mechanism of adsorption compared with a recent report based on theoretical and infrared spectroscopic studies of this system.[17] Importantly, we found the exceptional NH_3 uptake (19.5 mmol g^{-1} at 273 K and 1 bar) by MFM-300(Sc) was mediated by reversible host–guest and guest–guest hydrogen bond interactions. The moderate strength of the host–guest interaction in MFM-300(Sc) leads to excellent adsorption reversibility and stability with full retention of the capacity over 90 cycles.

4.3 Results and discussions

4.3.1 MFM-300(Sc)

MFM-300(Sc) shows a three-dimensional framework containing $[ScO_4(OH)_2]$ octahedra which are connected *via* the *cis*-μ_2-OH groups into infinite chains, and further coordinated by the $BPTC^{4-}$ ligand (H_4BPTC = biphenyl-3,3,5,5-tetracarboxylic acid) (Supplementary Figure 4.1).[18] Desolvated MFM-300(Sc) shows a Brunauer–Emmett–Teller (BET) surface area of 1390 $m^2\ g^{-1}$ and a pore volume of 0.48 $cm^3\ g^{-1}$ (Supplementary Figure 4.2). MFM-300(Sc) exhibits high thermal stability up to 500 °C under N_2 (Supplementary Figure 4.3) and high chemical stability in aqueous solutions of pH of 7–12 as well as in various organic solvents (Supplementary Figure 4.4).

4.3.2 Isotherms analysis and breakthrough experiment

Adsorption isotherms of NH_3 for MFM-300(Sc) were measured at 273–313 K, where an exceptional uptake of 19.5 mmol g^{-1} was recorded at 273 K and 1.0 bar (Figure 1a), reducing to 13.5 mmol g^{-1} at 298 K. MFM-300(Sc) shows the highest NH_3 uptake among the MFM-300(M) family[6,14] primarily due to its large pore size and pore volume allowing the accommodation of additional NH_3 molecules in the pore. MFM-300(Sc) shows an NH_3 uptake of 13.5 mmol g^{-1} at 298 K and 1.0 bar, comparing favourably with state-of-the-art materials (Figure 4.1d and Supplementary Table 6). The uptake of NH_3 in MFM-300(Sc) between 273 and 313 K decreases gradually with increasing temperature, consistent with an exothermic adsorption mechanism.[19] The isosteric heat of adsorption (Q_{st}) for NH_3 in MFM-300(Sc) decreases from 60 to 30 kJ mol^{-1} with increasing loading of NH_3 from 1 to 10 mmol g^{-1} (Supplementary Figure 4.7), confirming the presence of moderate adsorbate–adsorbent binding interaction. The repeated isotherm of NH_3 at 273 K using regenerated MFM-300(Sc) shows no loss in capacity with full retention of its porosity (Supplementary Figure 4.6). 90 consecutive cycles of adsorption–desorption were conducted at 298 K and confirmed excellent reversibility and stability of adsorption (Figure 4.1b), with retention of the crystal structure of MFM-300(Sc) as confirmed by powder X-ray diffraction (PXRD) (Supplementary Figure 4.5). The ability of MFM-300(Sc) to capture NH_3 at low concentrations (1000 ppm) was confirmed by dynamic breakthrough experiments at 298 K with a dynamic uptake of 1.65 mmol g^{-1}, consistent with that measured by isotherms (1.74 mmol g^{-1} at 10 mbar, equivalent to 1000 ppm; Figure 4.1c). With an exceptional adsorption capacity and excellent regenerability, MFM-300(Sc) represents a promising candidate for applications in NH_3 storage and transport.

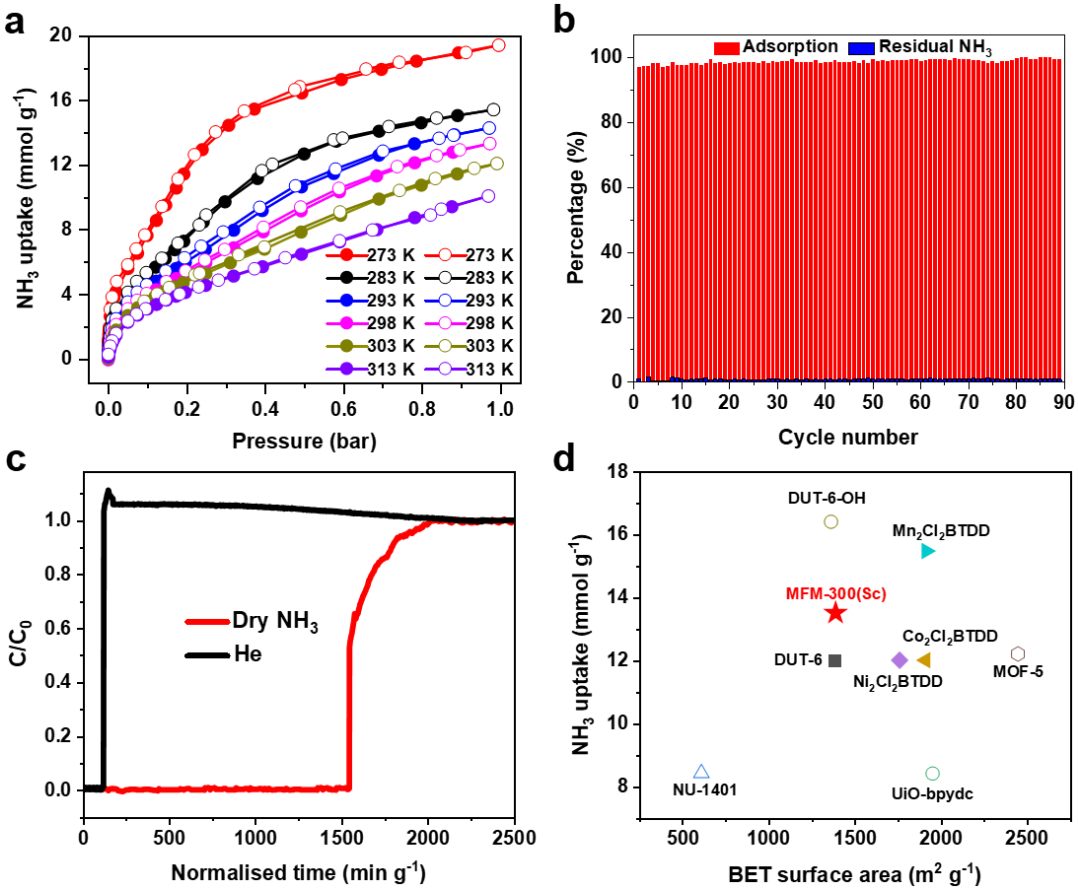

Figure 4.1. Isotherms and breakthrough data. (a) Adsorption isotherms for NH_3 in MFM-300(Sc) at 273 K (red), 283 K (black), 293 K (blue), 298 K (magenta), 303 K (dark yellow) and 313 K (violet) (adsorption: solid symbols; desorption: open symbols). (b) 90 cycles of adsorption-desorption of NH_3 in MFM-300(Sc) under pressure-swing conditions. (c) Dynamic breakthrough curve for NH_3 (1000 ppm diluted in He) with an inlet gas flow rate of 25 mL min^{-1} through a fixed-bed packed with MFM-300(Sc) at 298 K and 1.0 bar (Dry NH_3: red; He: black). (d) Comparison of NH_3 uptake at 1 bar under 298 K for selected materials plotted against their surface areas (solid symbols: reversible sorption; hollow symbols: irreversible sorption; full details are given in the supplementary information).

4.3.3 Studies on host–guest interactions

4.3.3.1 *In situ* neutron powder diffraction

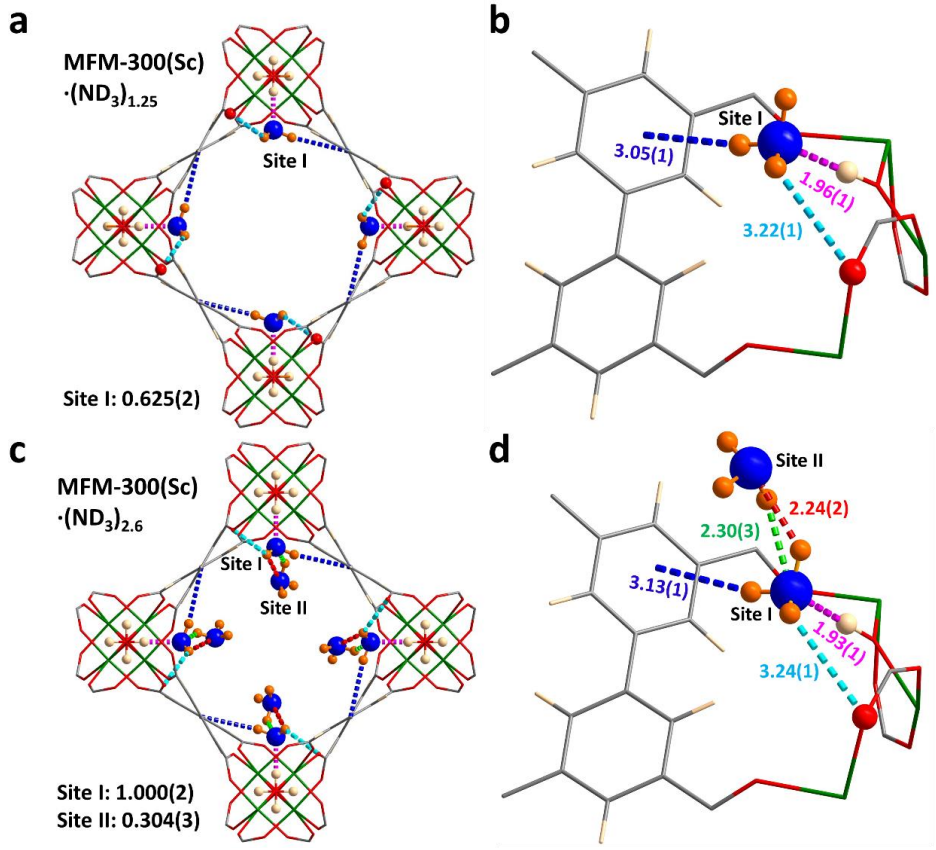

Figure 4.2 *In situ* NPD analysis. Views of binding sites for ND_3 in MFM-300(Sc) determined by NPD at 10 K (Sc: green; C: grey; O: red; H: light yellow; D: orange; N: blue). The occupancy of each site has been converted into ND_3/Sc for clarity. (a, c) Views along the *c*-axis showing packing of the guest molecules of NH_3 in MFM-300(Sc)·$(ND_3)_{1.25}$ and MFM-300(Sc)·$(ND_3)_{2.6}$, respectively. (b, d) Detailed views of host–guest interactions between MFM-300(Sc) and adsorbed molecules of ND_3.

In situ NPD data of MFM-300(Sc) as a function of ND_3 loading were collected and Rietveld refinements revealed the preferential binding sites for ND_3 (Figure 4.2). Interestingly, the NH_3-induced rearrangement of metal–ligand (Sc–O) bonds via insertion of NH_3 molecules into the MOF upon ND_3 binding as predicted by a DFT study[17] was not observed here. For MFM-300(Sc)·$(ND_3)_{1.25}$, $\{[Sc_2(L)(OD_{0.6}H_{0.4})_2]\cdot(ND_{2.05}H_{0.95})_{1.25}\}$, only one binding site was found, interacting

primarily with the bridging μ_2-OH groups at the four corners of its square-shaped channel [O_{bridge}–H···ND_3 = 1.96(1) Å] (Figure 4.2a and b). At the higher loading of MFM-300(Sc)·$(ND_3)_{2.6}$, {[Sc_2(L)$(OD_{0.75}H_{0.25})_2$]·$(ND_{2.42}H_{0.58})_{2.6}$}, two distinct binding sites were identified (Figure 4.2c and d). Site I is fully occupied by ND_3 molecules (1 ND_3/Sc), with hydrogen bonding between the μ_2-OH groups and the ND_3 molecule [O_{bridge}–H···ND_3 = 1.93(1) Å]. This is complemented by additional electrostatic interactions [ND_3···aromatic rings = 3.13(1) Å], and hydrogen bonding [ND_3···O_{ligand} = 3.24(1) Å]. Site II (0.3 ND_3/Sc) exhibited hydrogen bonding with the ND_3 at site I [2.30(3) Å and 2.24(2) Å], propagating along the 1D channel to form a cooperative $\{ND_3\}_\infty$ network. Similar to other MFM-300 analogues,[6,14] hydrogen/deuterium site exchange was also observed between the adsorbed ND_3 molecules and the μ_2-OH group for MFM-300(Sc).

4.3.3.2 Solid-state nuclear magnetic resonance

The analysis of the NPD data was entirely consistent with information from solid-state NMR spectroscopy. Upon loading MFM-300(Sc) with NH_3, only slight structural modifications were observed, and the crystalline nature of the framework was retained. ^{45}Sc magic angle spinning (MAS) NMR spectroscopy confirmed that the geometry around the Sc(III) centre was not notably distorted by interaction with NH_3, with the μ_2-OH groups (Supplementary Figure 4.11a) and {1H-}^{13}C CPMAS NMR spectra showing that the carboxyl resonance from the linker is unaffected upon NH_3 loading (i.e. minimal metal site distortion). However, the resonances assigned to the aromatic carbons do shift, reflecting an interaction of the rings with the guest molecules (Supplementary Figure 4.11b). The interaction of NH_3 with the MOF was also investigated using 2D ^{1}H-^{45}Sc dipolar correlation (HETCOR) NMR spectroscopy

(Figure 4.3). The spectrum of pristine MFM-300(Sc) (Figure 4.3a) shows clear cross peaks between aromatic protons (from the linker), as well as from hydroxyl protons (μ_2-OH groups), with the Sc(III) site, demonstrating a close proximity between these atomic environments. The corresponding spectrum of NH_3-loaded MFM-300(Sc) is substantially different. Whilst cross peaks with aromatic protons unchanged, cross peaks with μ_2-OH groups have moved to higher chemical shifts, indicating the presence of hydrogen bonding, and a new weak cross peak is observed and assigned to pore-confined NH_3 protons.

4.3.3.3 *In situ* synchrotron infrared microspectroscopy

In situ synchrotron FTIR microspectra were recorded at 298 K (Figure 4.3e and 3.3f). The characteristic O–H stretching mode of the μ_2-OH group is observed at 3678 cm^{-1}, which reduces in intensity and broadens upon loading of NH_3. The band at 3404 cm^{-1} is assigned to the N–H stretching of NH_3, and this exhibits a red shift to 3390 cm^{-1}.[6,14] The bands at 1614 and 1440 cm^{-1}, assigned to $\nu_{as}(COO^-)$ and $\nu_s(COO^-)$, respectively,[20] show small red shifts upon adsorption of NH_3 (Δ = 4–7 cm^{-1}), consistent with interaction between NH_3 and carboxylate groups. The bands between 3800 and 1400 cm^{-1} for the local framework remain unchanged upon re-activation, confirming the high structural stability of MFM-300(Sc). Thus, the ssNMR and FTIR studies verify that NH_3 is hydrogen-bonded to the μ_2-OH groups via the lone pair of electrons on nitrogen, fully consistent with the NPD analysis.

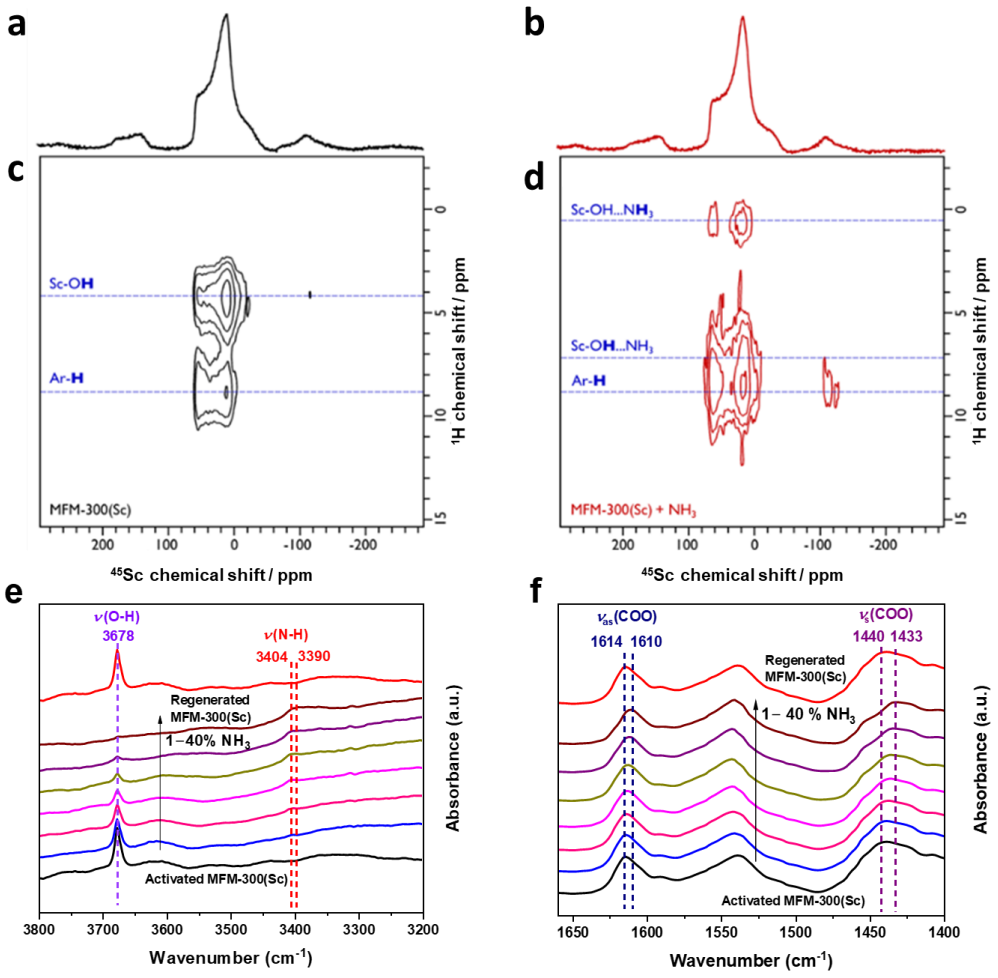

Figure 4.3. ssNMR and *in situ* FTIR spectra analysis. ^{1}H-^{45}Sc Heteronuclear dipolar correlation spectroscopy (HETCOR) MAS NMR spectra of (a, c) pristine and (b, d) NH_3-loaded MFM-300(Sc), with corresponding ^{45}Sc MAS NMR spectra (top). The spectra were recorded at 9.4 T using a MAS frequency of 12 kHz. The dashed blue lines highlight correlations between the Sc(III) site and various proton environments. *In situ* FTIR spectra of MFM-300(Sc) as a function of NH_3 loading (diluted in dry N_2) and re-activated under a flow of dry N_2 at 100 mL min^{-1} at 298 K for 2 h: (e) 3800−3200 cm^{-1}, (f) 1650−1400 cm^{-1}. Activated MFM-300(Sc) (black), 1% NH_3-loaded MFM-300(Sc) (blue), 2% NH_3-loaded MFM-300(Sc) (blue), 5% NH_3-loaded MFM-300(Sc) (pink), 10% NH_3-loaded MFM-300(Sc) (magenta), 20% NH_3-loaded MFM-300(Sc) (dark yellow), 40% NH_3-loaded MFM-300(Sc) (purple), and regenerated MFM-300(Sc) (red).

4.3.3.4 Inelastic neutron scattering

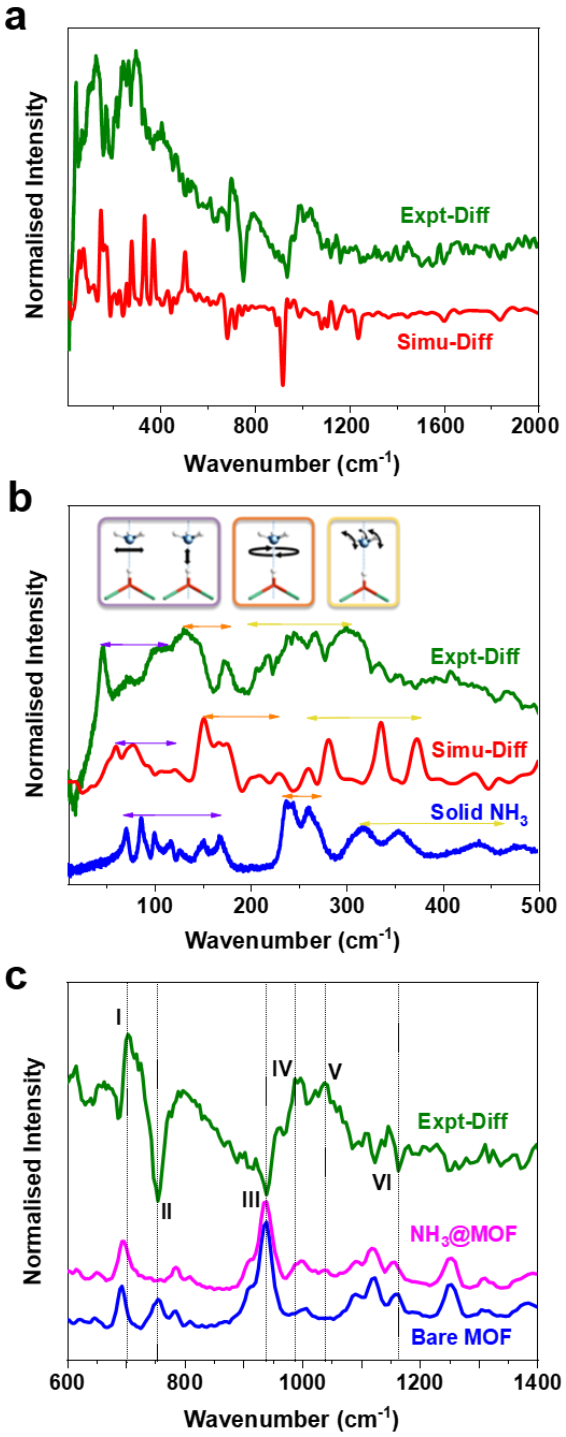

Figure 4.4. Dynamic studies by INS. (a) Experimental and simulated INS difference spectra of the adsorbed NH_3 within MFM-300(Sc), denoted as Expt-Diff (olive) and Simu-Diff (red), respectively. (b) Comparison of the INS spectra of adsorbed NH_3 of Expt-Diff (olive) and Simu-Diff (red) with solid NH_3 (blue). (c) Experimental INS spectra of bare MFM-300(Sc) (blue), NH_3-loaded MFM-300(Sc) (magenta) and the difference spectrum at the higher energy region (olive).

INS spectra of bare and NH_3-loaded MFM-300(Sc) were also collected (Supplementary Figure 4.12) and simulated using DFT calculations based upon the structural models derived from NPD analyses (Supplementary Figure 4.13). The difference spectra (Figure 4.4a), which were obtained by subtracting the spectrum of the bare MOF from that of the NH_3-loaded MOF, show the vibrational features of both the adsorbed NH_3 molecules and the changes for the MOF host. The peaks in the low energy region (Figure 4.4b) are primarily due to the vibrational modes of adsorbed NH_3 molecules, with a small contribution due to changes in the lattice modes of the framework. The agreement between experimental and simulated spectra in terms of the overall profile allows unambiguous assignment of all major peaks. Specifically, the bands between 45 and 116 cm^{-1} are assigned to the translational motion of the NH_3, which includes the vibration of NH_3 molecules perpendicular to and along the molecular C_3 axis and the hybrid of these modes. Peaks at 132 and 172 cm^{-1} are due to rotational motion of the NH_3 around its C_3 axis. Bands between 207 and 334 cm^{-1} are assigned to the rocking modes of the NH_3. Compared to the spectrum of NH_3 in the solid state, where each NH_3 forms a 3D hydrogen bonding network with 6 adjacent NH_3 molecules, bands in all regions for the adsorbed NH_3 shift to lower energy and exhibit more broad features, indicating more dynamic environment for the adsorbed NH_3. The features in the higher energy region mainly reflect the modes of the framework (Figure 4.4c). Features I and III are due to the broadening of the peaks at 692 and 934 cm^{-1} for bare MFM-300(Sc), and are assigned to the C–H rocking out of the C_6 plane, in-phase and anti-phase, respectively. Feature VI at higher frequency between 1090 and 1163 cm^{-1} shows reduced intensity upon adsorption of NH_3, and is assigned to the H_{ring} rocking within the C_6 plane. Features II and IV originate from a significant blue shift of the peak at 754 cm^{-1} in the spectrum of bare MFM-300(Sc) to

987 cm^{-1} in the spectrum of NH_3-loaded MFM-300(Sc). This is assigned to the rocking of μ_2-OH within the Sc–O–Sc plane. Interestingly, the features involving the motions of H_{ring} show only broadening and a decrease in intensities, while the features involving the motion of the μ_2-OH experience changes in energy. This indicates a stronger interaction between NH_3 and the μ_2-OH than with H_{ring} centres. Feature V in the difference spectrum is due to the umbrella motion of adsorbed NH_3. Thus, the combined INS and DFT study has visualised directly the host–guest binding dynamics, consistent with the reversible and high adsorption of NH_3 in MFM-300(Sc).

4.4 Conclusions

In summary, MFM-300(Sc) comprised of metal-oxide chains with bridging –OH groups show exceptional adsorption capacity (19.5 mmol g^{-1} at 273 K and 1 bar) and regenerability for NH_3. *In situ* NPD analysis, ^{45}Sc ssNMR spectroscopy, synchrotron FTIR and INS/DFT studies have unambiguously visualised the binding interactions and dynamics of NH_3 within the pores of MFM-300(Sc). This in-depth understanding of the structure–function relationship with these host–guest systems will enable the rational design of potential materials with desired properties.

4.5 References

1. E. Martínez-Ahumada, M. L. Díaz-Ramírez, M. d. J. Velásquez-Hernández, V. Jancik and I. A. Ibarra, Capture of toxic gases in MOFs: SO_2, H_2S, NH_3 and NO_x. *Chem. Sci.*, **2021**, *12*, 6772–6799.
2. MacFarlane, D.; Cherepanov, P.; Choi, J.; Suryanto, B.; Hodgetts, R.; Bakker, J.; Vallana, F.; and Simonov, A. A Roadmap to the Ammonia Economy. *Joule* **2020**, *4*, 1186–1205.
3. Li, H.; Wang, K.; Sun, Y.; Lollar, C.; Li, J.; Zhou, H. Recent advances in gas storage and separation using metal–organic frameworks. *Mater. Today* **2018**, *21*, 108–121.

4. Dietrich, M.; Rauch, D.; Simon, U.; Porch, A.; Moos, R. Ammonia storage studies on H-ZSM-5 zeolites by microwave cavity perturbation: correlation of dielectric properties with ammonia storage. *J. Sensors* **2015**, *4*, 263–269.
5. Mirajkar, S.; Rao, B.; Eapen, M.; Shiralkar, V. Sorption of ammonia in cation-exchanged omega zeolite and gallium analogue. *J. Phys. Chem. B* **2001**, *105*, 4356–4367.
6. Zeng, T.; Huang, H.; Kobayashi, N.; Li, J. Performance of an activated carbon-ammonia adsorption refrigeration system. *Nat. Resources* **2017**, *08*, 611–631.
7. Doonan, C.; Tranchemontagne, D.; Glover, T.; Hunt, J.; Yaghi, O. Exceptional ammonia uptake by a covalent organic framework. *Nat. Chem.* **2010**, *2*, 235–238.
8. Demir, H.; Walton, K.; Sholl, D. Computational screening of functionalized UiO-66 materials for selective contaminant removal from air. *J. Phys. Chem. C* **2017**, *121*, 20396–20406.
9. Han, X.; Lu, W.; Chen, Y.; Silva, I.; Li, J.; Lin, L.; Li, W.; Sheveleva, A.; Godfrey, H.; Lu, Z.; Tuna, F.; McInnes, E.; Cheng, Y.; Daemen, L.; McPherson, L.; Teat, S.; Frogley, M.; Rudic, S.; Manuel, P.; Ramirez-Cuesta, A.; Yang, S.; Schröder, M. High ammonia adsorption in MFM-300 materials: dynamics and charge transfer in host–guest binding. *J. Am. Chem. Soc.* **2021**, *143*, 3153–3161.
10. Nguyen, T.; Harreschou, I.; Lee, J.; Stylianou, K.; Stephan, D. A recyclable metal–organic framework for ammonia vapour adsorption. *Chem. Commun.* **2020**, *56*, 9600–9603.
11. Marsh, C.; Han, X.; Li, J.; Lu, Z.; Argent, S.; Silva, I.; Cheng, Y.; Daemen, L.; Ramirez-Cuesta, A.; Thompson, S.; Blake, A.; Yang, S.; Schröder, M. Exceptional packing density of ammonia in a dual-functionalized metal–organic framework. *J. Am. Chem. Soc.* **2021,** *143*, 6586–6592.
12. Yang, S.; Sun, J.; Ramirez-Cuesta, A.; Callear, S.; David, W.; Anderson, D.; Newby, R.; Blake, A.; Parker, J.; Tang, C.; Schröder, M. Selectivity and direct visualization of carbon dioxide and sulfur dioxide in a decorated porous host. *Nat. Chem.* **2012**, *4*, 887–894.
13. Smith, G.; Eyley, J.; Han, X.; Zhang, X.; Li, J.; Jacques, N.; Godfrey, H.; Argent, S.; McPherson, L.; Teat, S.; Cheng, Y.; Frogley, M.; Cinque, G.; Day, S.; Tang, C.; Easun, T.; Rudic, S.; Cuesta, A.; Yang, S.; Schröder, M. Reversible coordinative binding and separation of sulfur dioxide in a robust metal–organic framework with open copper sites. *Nat. Mater.* **2019**, *18*, 1358–1365.
14. Saha, D.; Deng, S. Ammonia adsorption and its effects on framework stability of MOF-5 and MOF-177. *J. Colloid. Interf. Sci.* **2010**, *348*, 615–620.
15. Rieth, A.; Dincă, M. Controlled gas uptake in metal–organic frameworks with record ammonia sorption. *J. Am. Chem. Soc.* **2018**, *140*, 3461–3466.
16. Rieth, A.; Tulchinsky, Y.; Dincă, M. High and reversible ammonia uptake in mesoporous azolate metal–organic frameworks with open Mn, Co, and Ni sites. *J. Am. Chem. Soc.* **2016**, *138*, 9401–9404.
17. Godfrey, H.; Silva, I.; Briggs, L.; Carter, J.; Morris, C.; Savage, M.; Easun, T.; Manuel, P.; Murray, C.; Tang, C.; Frogley, M.; Cinque, G.; Yang, S.; Schröder, M. Ammonia storage by reversible host–guest site exchange in a robust metal–organic framework. *Angew. Chem. Int. Edit.* **2018**, *57*, 14778–14781.
18. Chen, Y.; Zhang, F.; Wang, Y.; Yang, C.; Yang, J.; Li, J. Recyclable ammonia uptake of a MIL series of metal–organic frameworks with high structural stability. *Micropor. Mesopor. Mat.* **2018**, *258*, 170–177.

19. Kim, D.; Kang, D.; Kang, M.; Lee, J.; Choe, J.; Chae, Y.; Choi, D.; Yun, H.; Hong, C. High ammonia uptake of a metal–organic framework adsorbent in a wide pressure range. *Angew. Chem. Int. Ed.* **2020**, *132*, 22720–22725.
20. Lyu, P.; Wright, A.; Olvera, A.; Mileo, P.; Zárate, J.; Ahumada, E.; Martis, V.; Williams, D.; Dincă, M.; Ibarra, I.; Maurin, G. Ammonia capture *via* an unconventional reversible guest–induced metal–linker bond dynamics in a highly stable metal–organic framework. *Chem, Mater.* **2021**, *33*, 6186–6192.
21. Zhang, X.; Silva, I.; Godfrey, H.; Callear, S.; Sapchenko, S.; Cheng, Y.; Vitorica-Yrezabal, I.; Frogley, M.; Cinque, G.; Tang, C.; Giacobbe, C.; Dejoie, C.; Rudic, S.; Ramirez-Cuesta, A.; Denecke, M.; Yang, S.; Schröder, M. Confinement of iodine molecules into triple-helical chains within robust metal–organic frameworks. *J. Am. Chem. Soc.* **2017**, *139*, 16289–16296.
22. Yang, S.; Liu, L.; Sun, J.; Thomas, K.; Davies, A.; George, M.; Blake, A.; Hill, A.; Fitch, A.; Tang, C.; Schröder, M. Irreversible network transformation in a dynamic porous host catalyzed by sulfur dioxide. *J. Am. Chem. Soc.* **2013**, *135*, 4954–4957.
23. Hadjiivanov, K.; Panayotov, D.; Mihaylov, M.; Ivanova, E.; Chakarova, K.; Andonova, S.; Drenchev, N. Power of infrared and raman spectroscopies to characterize metal–organic frameworks and investigate their interaction with guest molecules. *Chem. Rev.* **2021**, *121*, 1286–1424.

4.6 Additional information

Author information. Correspondence and requests for materials should be addressed to M.S. (M.Schröder@manchester.ac.uk) and S.Y. (Sihai.Yang@manchester.ac.uk).

Conflicts of interest. The authors declare no competing interest.

Acknowledgements. We thank EPSRC (grant EP/I011870), The Royal Society, and University of Manchester for funding. This project has received funding from the European Research Council (ERC) under the European Union's Horizon 2020 research and innovation programme (grant agreement No 742401, NANOCHEM). We are grateful to STFC/ISIS facility for access to Beamlines TOSCA and WISH. We thank Diamond Light Source for access to Beamline B22. LG and YM thank the China Scholarship Council (CSC) for funding. The computing resources were made available through the VirtuES and the ICE-MAN projects, funded by Laboratory Directed Research and Development program and Compute and Data Environment for Science (CADES) at ORNL.

Supporting information. The supporting information of this paper is listed in Appendix II.

Chapter 5

Direct visualisation of supramolecular binding and separation of light hydrocarbons in MFM-300(In)

Chapter 5: Direct visualisation of supramolecular binding and separation of light hydrocarbons in MFM-300(In)

Manuscript

Lixia Guo,[1§] Mathew Savage,[1§] Joseph H. Carter,[1,2§] Xue Han,[1] Ivan da Silva,[3] Pascal Manuel,[3] Svemir Rudic[3], Chiu C. Tang,[2] Sihai Yang[1*] and Martin Schröder[1*]

1. Department of Chemistry, University of Manchester, Manchester, M13 9PL (UK)
Sihai.Yang@manchester.ac.uk; M.Schröder@manchester.ac.uk

2. Diamond Light Source, Harwell Science and Innovation Campus, Didcot OX11 0DE (UK)

3. ISIS Facility, STFC Rutherford Appleton Laboratory, Chilton, Oxfordshire, OX11 0QX (UK)

§ These authors contribute equally to this work.

Published: *Chem. Mater.* **2022**, *34*, 5698–5705.

DOI: 10.1021/acs.chemmater.2c01097.

5.1 Abstract

The purification of light olefins is one of the most important chemical separations globally and consumes large amounts of energy. Porous materials have the capability to improve the efficiency of this process by acting as solid, regenerable adsorbents. However, to develop translational systems, the underlying mechanisms of adsorption in porous materials must be fully understood. Herein, we report the adsorption and dynamic separation of C_2 and C_3 hydrocarbons in the metal–organic framework MFM-300(In), which exhibits excellent performance in the separation of mixtures of ethane/ethylene and propyne/propylene. Unusually selective adsorption of ethane over ethylene at low pressure is observed, resulting in selective retention of ethane from a mixture of ethylene/ethane, thus demonstrating its potential for a one-step purification of ethylene (purity > 99.9%). *In situ* neutron powder diffraction and inelastic neutron scattering reveal the preferred adsorption domains and host–guest binding dynamics of adsorption of C_2 and C_3 hydrocarbons in MFM-300(In).

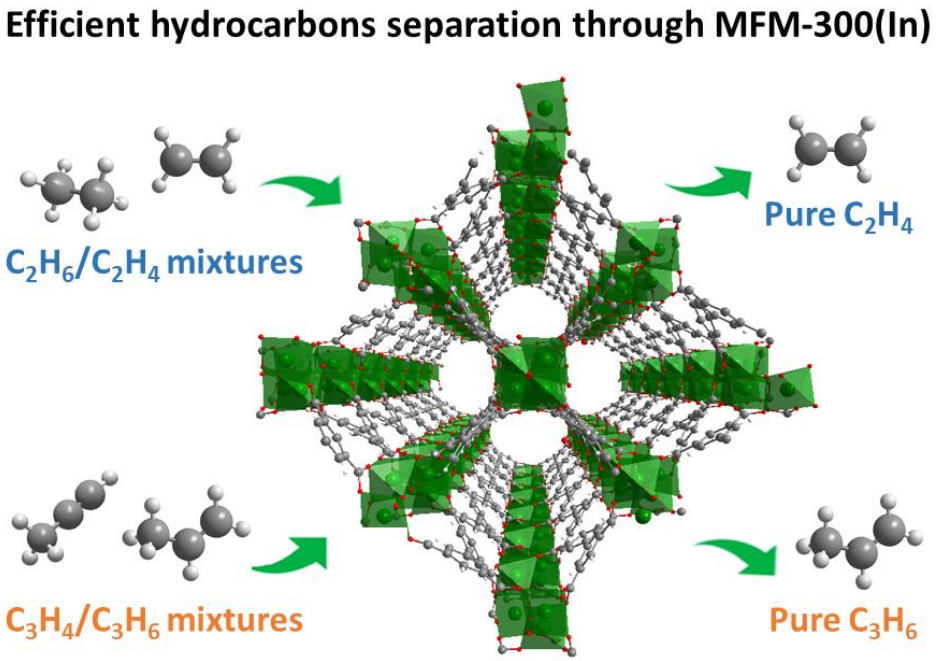

Graphical Abstract 5.1. Efficient light hydrocarbons separation through MFM-300(In).

5.2 Introduction

Light olefins, primarily ethylene (C_2H_4) and propylene (C_3H_6), are the cornerstone of petrochemical industries for the production of polymers and various fine chemicals.[1] Current global ethylene and propylene production is around 200 million tons per year.[1] These short chain alkenes are produced typically by the steam cracking of feedstocks derived from crude oil, such as naphtha, which is a liquid mixture of short and medium, typically comprising C_5–C_{12} chain hydrocarbons.[2–3] Steam cracking of naphtha produces a mixture of products, which must be separated prior to use. Most commonly post-cracking separation is performed using cryogenic distillation operating at high pressure and low temperature (as low as −160 ˚C). This is thus an incredibly energy intensive process, consuming around a third of the overall energy used in the process of ethylene production.[3] The development of energy-efficient alternatives to cryogenic distillation can effectively reduce energy consumption as well as emissions.[4] A possible strategy involves the use of porous materials to adsorb selectively a single component from gas mixtures (*e.g.*, alkynes and alkanes) while allowing other components to pass though. The binding of gas molecules in these materials is based often upon multiple, weak, long-range supramolecular interactions, which facilitate the removal of adsorbed species and regeneration of sorbents *via* either temperature swing or pressure swing desorption. This can operate potentially at ambient conditions and thus carries a relatively low energy penalty. Several porous adsorbents have been proposed for this application such as ion exchange resins,[5] zeolites[6–7] and, most notably, metal–organic framework (MOF) materials.[4,8–11]

Over the past two decades, MOFs have been studied widely for their applications in gas separations.[12] The ability to tune the pore size and the chemical environment of

MOFs makes them excellent candidates for separating molecules with similar physical properties, such as light hydrocarbons. Several MOF materials have been proposed for application in hydrocarbon separation. These utilise different strategies including the use of open metal sites,[13–15] specific gate opening effects,[16–18] and kinetic size exclusion.[19–23] Recently, an interesting computational study on the effects of pore size on the selectivity of ethane/ethylene has been reported.[24] It was found that for a given adsorbent, separation could be controlled by altering the size of the pore along one-dimension whilst maintaining the overall pore chemistry and structure. The purification of olefins from C_2 or C_3 hydrocarbon streams is considered one of the most challenging and important processes in the petrochemical industry. For the production of polymer-grade C_2H_4 from C_2H_4-selective adsorbents, an additional desorption step for the release of adsorbed C_2H_4 molecules is required, which adds additional energy costs *via* the application of vacuum and/or heating.[25] In contrast, C_2H_6-selective adsorbents have clear advantages in the practical separation of C_2H_6/C_2H_4 owing to the direct production of polymer-grade C_2H_4 in one step by selectively retention of C_2H_6.[4,26] However, C_2H_6-selective adsorbents are far less common than C_2H_4-selective materials.[9,23,27–28]

Porous materials incorporating unsaturated metal sites (typically transition metals) can afford unique electrostatic binding sites for C_2H_4 or C_3H_6 *via* π-complexation.[14,28] Although these materials show strong host–guest interactions accompanied by a high adsorption enthalpy compared with MOFs without open metal sites.[20,29] these materials often show limited stability, especially when exposed to humid conditions. In this context, the MFM-300 series of MOF materials[29–31] represents a useful practical example to examine the adsorption of hydrocarbons. The MFM-300 series is a group

of isostructural MOFs which are comprised of biphenyl-3,3′,5,5′-tetracarboxylate (L^{4-}) linkers connected to $[M(\mu_2\text{-}OH)_2]_\infty$ chains in a wine-rack mode. This family of MOFs differs from other MOF materials, which have been reported for separations of light hydrocarbon, in that they utilise hydroxyl groups as the primary binding site of adsorbed gas molecules. This may be advantageous over the reported method of relatively strong binding to open metal sites[14,32] in that the binding energy for guest–hydroxyl interactions are significantly lower, thus making MFM-300 materials more readily regenerable and less susceptible to poisoning by moisture.

Here, we report the adsorption and breakthrough separation of C_2 and C_3 hydrocarbons in MFM-300(In), which exhibits an unusual selective adsorption of ethane at low pressure that is distinct from that observed for MFM-300(Al).[29] We also describe the direct visualisation of the supramolecular binding of C_2 and C_3 hydrocarbons within the pore by a combination of *in situ* neutron powder diffraction (NPD) and inelastic neutron scattering (INS) experiments. The breakthrough experiments confirmed the efficient separation of equimolar mixtures of C_2H_6/C_2H_4 and C_3H_4/C_3H_6 by MFM-300(In) to produce high-purity ethylene and propylene (purity >99.9%) at room temperature.

5.3 Results and discussions

5.3.1 MFM-300(In)

MFM-300(In) was synthesised by following our previously reported method[33] (see Experimental section for details). MFM-300(In) is comprised of one-dimensional (1D) $[In(OH)_2O_4]_\infty$ chains bridged by tetracarboxylate ligands L^{4-} to afford a porous framework structure with 1D channels decorated with *cis*-μ_2-OH groups (Figure 5.1a).

The powder X-ray diffraction (PXRD) pattern and thermogravimetric curves confirm the high phase purity and thermal stability (Supplementary Figure 5.2-5.3). Using N_2 sorption isotherm data at 77 K, desolvated MFM-300(In) is found to display a Brunauer–Emmett–Teller (BET) surface area of 1030 $m^2\ g^{-1}$, a pore volume of 0.43 $cm^3\ g^{-1}$ with a pore size distribution centred at 6.8 Å (Supplementary Figure 5.4).

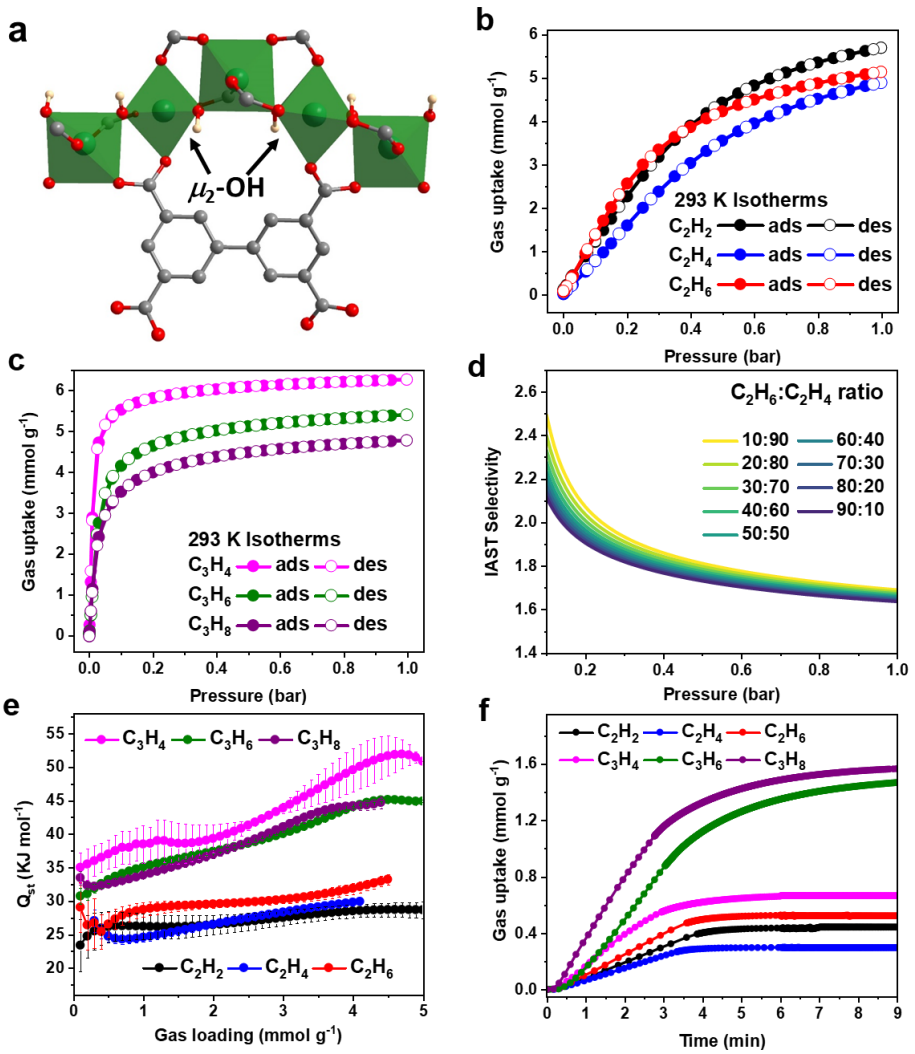

Figure 5.1. Structure and adsorption data. (a) View of infinite chain of $[InO_4(OH)_2]_\infty$ linked by tetracarboxylate ligands (In: green; C: grey; O: red; H: light yellow; hydrogen atoms on the ligands are omitted for clarity). Single-component adsorption isotherms for (b) C_2 and (c) C_3 hydrocarbons in MFM-300(In) at 293 K. (d) Analysis of IAST selectivity of C_2H_6/C_2H_4 for MFM-300(In) at 293 K and 1 bar. (e) Isosteric heats of adsorption (Q_{st}) for C_2 and C_3 hydrocarbons in MFM-300(In). (f) Adsorption kinetics of C_2 and C_3 hydrocarbons of MFM-300(In) at 293 K (30-70 mbar). C_2H_2 (black), C_2H_4 (blue), C_2H_6 (red), C_3H_4 (magenta), C_3H_6 (olive) and C_3H_8 (purple).

5.3.2 Analysis of gas adsorption isotherms

C_2 and C_3 hydrocarbons show fully reversible uptake in MFM-300(In) with type I isotherms being observed between 195 and 303 K (Figure 5.1b-c, Supplementary Figure 5.5-5.12). Single-component adsorption isotherms reveal that MFM-300(In) has a distinct binding affinity to C_3H_4 over C_3H_6 and C_3H_8, and to C_2H_6 over C_2H_4 over a wide range of temperatures from 273 to 303 K. The uptake of C_3 hydrocarbons exhibits steep adsorption isotherms at low pressure, with C_3H_4, C_3H_6 and C_3H_8 reaching 73 to 87% of their total adsorption capacity at 1 bar at a pressure of 100 mbar; it is notable that these isotherms reach a plateau at 400 mbar at 293 K. The total adsorption capacity of these gases at 1 bar and 293 K follows the degree of unsaturation of the gas, with C_3H_4, C_3H_6 and C_3H_8 reaching 6.3, 5.4 and 4.8 mmol g^{-1} respectively, comparable with the highest values reported for MOF materials in the literature.[34,35]

The C_2 hydrocarbons exhibit less steep adsorption profiles than the C_3 analogues, reaching only 16 to 49% of their total capacity at 1 bar at 100 mbar at 293 K. Interestingly, the uptake at low pressure of the C_2 hydrocarbons does not follow the degree of unsaturation as is observed in the isostructural MFM-300(Al).[29] Furthermore, analysis of the isotherms by ideal adsorbed solution theory (IAST) indicates that there is a distinct reversal of the selectivities of ethane and ethylene so that MFM-300(In) exhibits selectivity towards ethane at 293 K (Figure 5.1d) similar to that observed in MFM-300(V^{III}).[36] This is an unusual observation considering that the In(III), V(III) and Al(III) analogues of MFM-300 have identical pore chemistry and only differ in that MFM-300(In) and MFM-300(V^{III}) have a slightly larger pore diameter than MFM-300(Al).[29,33,36] As the uptakes of ethylene in MFM-300(M) (M =

In, V^{III} and Al) are similar (4.9, 6.0 and 4.3 mmol g^{-1}, respectively), this phenomenon can be explained by MFM-300(In) having a greater affinity for ethane, which has a much greater uptake in the In(III) and V(III) analogues (5.1 and 7.1 mmol g^{-1}) compared to Al(III) (~0.8 mmol g^{-1}) at 293 K and 1 bar. Interestingly, a recent computational study reported that a small change in the diameter of the channel was able to induce a large effect on the selectivity of ethane/ethylene.[24] This may shed light on the observed reversal of selectivity between the ethylene-selective MFM-300(Al) and the ethane-selective MFM-300(In), as the former has a smaller pore compared to latter (~6.0 and 6.8 Å, respectively, determined by analysis of N_2 isotherms at 77 K).

The isosteric enthalpy (Q_{st}) and entropy (ΔS) of adsorption as a function of gas uptake were determined by fitting of the van't Hoff equation to the adsorption isotherms measured for each gas (Figure 5.1e and Supplementary Figure 5.13-5.14). The initial value of Q_{st} for C_2H_2 is around 25 kJ mol^{-1} and the change is relatively steady throughout the uptake process. The value of Q_{st} for C_2H_6 at near-zero coverage is 30 kJ mol^{-1}, higher than that for both C_2H_4 and C_2H_2 over the entire range of loading, suggesting that MFM-300(In) exhibits a stronger binding affinity for C_2H_6 than C_2H_4 and C_2H_2. At the same time, Q_{st} for C_2H_6 increases continuously from 25 to 33 kJ mol^{-1} as the increase of gas loading from 0.1 to 4.0 mmol g^{-1}, demonstrating the presence of strong adsorbate−adsorbate intermolecular interactions at high surface coverage, reflecting potential cooperative binding. Similar behaviour has been observed in other porous sorbents.[4,37–39] The value of Q_{st} for C_2H_6 in MFM-300(In) are significantly higher than that for MFM-300(Al) reflecting the larger pores in the former due to the larger metal center and associated lattice parameters. This allows additional C_2H_6 molecules to be located at optimal sites within the pore of MFM-

300(In) *via* intermolecular interactions. The values of Q_{st} for C_2H_6 in MFM-300(In) are comparable with other reported C_2H_6-selective MOFs.[4,26] The adsorption enthalpy for C_3 hydrocarbons (30–36 kJ mol^{-1}) is relatively high at low loading compared with C_2 hydrocarbons, and C_3H_4 shows higher value for Q_{st} compared with C_3H_6 and C_3H_8, confirming strong binding affinity of MFM-300(In) for C_3H_4. The adsorption kinetics for substrate uptake have been measured for MFM-300(In) (Figure 5.1f), and all gases exhibit rapid diffusion to reach adsorption equilibrium within 10 mins. MFM-300(In) shows more rapid diffusion of C_2H_6 than C_2H_2 and C_2H_4, implying a kinetic selectivity for C_2H_6 over C_2H_4 and C_2H_2, which is beneficial to their separation under dynamic conditions. The high capacity and strong binding affinity of MFM-300(In) for C_3H_4 and C_2H_6, as well as the rapid adsorption kinetics, suggest potential for the purification of mixtures of C_3H_4/C_3H_6 and C_2H_4/C_2H_6 by selective adsorption of C_3H_4 and C_2H_6, respectively.

5.3.3 Breakthrough experiments

The promising static adsorption data encouraged us to assess further the separation performance of MFM-300(In) under dynamic flow conditions. Firstly, single-component gas breakthrough experiments were conducted to evaluate the dynamic gas adsorption (Figure 5.2 and Supplementary Figure 5.1). The dynamic adsorption capacities for each component were calculated by integrating the breakthrough curves to give dynamic uptakes of 1.4 mmol g^{-1} (C_2H_2), 1.0 mmol g^{-1} (C_2H_4), 1.6 mmol g^{-1} (C_2H_6), 4.4 mmol g^{-1} (C_3H_4), 3.5 mmol g^{-1} (C_3H_6), and 3.1 mmol g^{-1} (C_3H_8) upon saturation. These values are consistent with those obtained from static isotherm experiments.

To evaluate the feasibility of separation of C_2 and C_3 binary mixtures using a fixed-bed packed with MFM-300(In), breakthrough experiments for equimolar mixtures of C_2H_2/C_2H_4, C_2H_2/C_2H_6, C_2H_6/C_2H_4, C_3H_4/C_3H_6, C_3H_4/C_3H_8, and C_3H_6/C_3H_8 were performed at 293 K and 1.0 atm. Clear separation of mixtures of C_2H_4/C_2H_6 and C_3H_6/C_3H_4 was obtained (Figure 5.2). In the separation of C_2H_6/C_2H_4, the breakthrough of C_2H_4 was observed at 6 min g^{-1}, while the retention time of C_2H_6 was 15 min g^{-1}, consistent with the analysis of unusual adsorption selectivity and high Q_{st} for C_2H_6. It is especially challenging to develop C_2H_6-selective adsorbents to enable one-step purification of C_2H_4 due to the common co-adsorption of C_2H_4 and C_2H_6.[27] The profile of the breakthrough curves (Figure 5.2c) indicates[40] strong competitive sorption of C_2H_6 over C_2H_4 in MFM-300(In), further confirming the high efficiency of MFM-300(In) for practical C_2H_6/C_2H_4 separation. In the case of C_3H_4/C_3H_6, the breakthrough curves indicate the sharp breakthrough of both gases with retention time of 35 min g^{-1} and 48 min g^{-1} for C_3H_6 and C_3H_4, respectively. The apparent interval in the breakthrough time between C_3H_4 and C_3H_6 suggests that MFM-300(In) is effective for the separation of C_3H_4/C_3H_6, again consistent with the analysis of adsorption selectivity and thermodynamic data. The separation of mixtures of C_2H_6/C_2H_4 and C_3H_4/C_3H_6 by MFM-300(In) yields a productivity of 4.6 L kg^{-1} of C_2H_4 (purity >99.9%) and of 16.3 L kg^{-1} of C_3H_6 (purity >99.95%) at the outlet. The productivity of ethylene of MFM-300(In) is comparable with reported ethane-selective MOFs, such as IRMOF-8 (2.5 L kg^{-1})[41], $Cu(Qc)_2$ (4.3 L kg^{-1})[42], and PCN-245 (5.8 L kg^{-1})[43] (Supplementary Table 4.3). Thus, the efficient purification of C_2H_6/C_2H_4 and C_3H_4/C_3H_6 to produce polymer-grade olefins under the above conditions has been achieved by MFM-300(In).

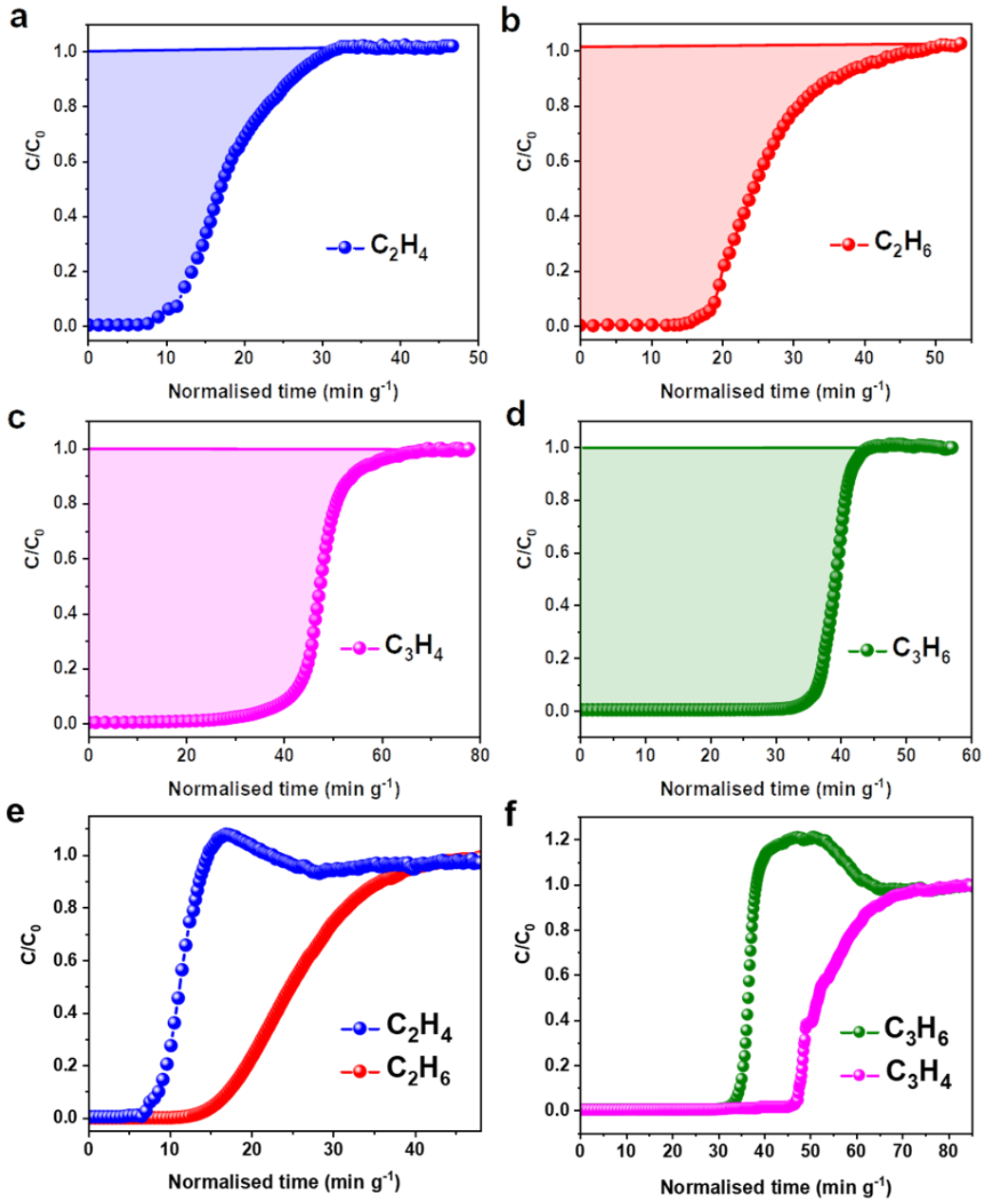

Figure 5.2. Breakthrough curves. Dynamic breakthrough plots for single-component (a) C_2H_4, (b) C_2H_6, (d) C_3H_4, and (e) C_3H_6 with an inlet target gas flow rate of 2.0 mL min^{-1} diluted in He (total flow rate: 20 mL min^{-1}). Dynamic breakthrough plots for equimolar mixtures of (c) C_2H_6/C_2H_4 and (f) C_3H_4/C_3H_6 with an inlet gas flow rate of 2.0 mL min^{-1}/2.0 mL min^{-1} diluted in He (total flow rate: 20 mL min^{-1}) through a fixed-bed packed with MFM-300(In) at 293 K. C_2H_4 (blue), C_2H_6 (red), C_3H_4 (magenta), and C_3H_6 (olive).

5.3.4 Studies of the preferred binding sites and supramolecular interactions

5.3.4.1 *In situ* neutron powder diffraction

In situ NPD data of MFM-300(In) as a function of gas loading with C_2D_2, C_2D_4, C_2D_6, C_3D_4, C_3D_6 or C_3D_8 were refined by the Rietveld method to determine the preferred binding domains for adsorbed gas molecules within the pore. The refinements reveal two similar binding sites for all of the C_2 hydrocarbons (Figure 5.3), comparable to those observed in MFM-300(Al). Site I occupies a position adjacent to the bridging hydroxyl of the framework. Both unsaturated molecules show an OH···π interaction, with acetylene having a reduced $H_{OH}\cdots C_2$ distance of 2.52(1) Å compared to 3.85(1) Å for ethylene, consistent with the increased polarizability of acetylene. For acetylene, this interaction is supplemented by π···π interactions between the guest molecules and the adjacent phenyl groups of the linker at distances of 3.83(1) and 4.04(1) Å. Ethylene does not have π-orbitals facing the phenyl groups of the linker so instead exhibits electrostatic interactions between the D-centers of the ethylene and the π-system of the phenyl group at distances of between 2.92(1) and 4.40(1) Å. In contrast, ethane does not exhibit a perpendicular interaction with the bridging hydroxyl of the MOF. Instead, it displays a O-H···C-D hydrogen interactions supplemented by interactions with the phenyl groups at distances of between 2.65(2) and 4.18(2) Å. This mode of binding is also observed in the structure of ethane-loaded MFM-300(Al), which has a longer $C_{C2D6}\cdots O_{OH}$ distance of 3.82(1) Å compared to 3.22(2) Å in the In(III) analogue. This shorter interaction distance in the MFM-300(In) suggests that the improved adsorption of ethane in MFM-300(In) is due to the presence of stronger intermolecular interactions between adsorbed ethane molecules, consistent with the Q_{st} values for ethane in MFM-300(In) over MFM-300(Al). The stronger Van der Waals interactions in MFM-300(In) are likely due to the slightly larger pore size allowing the ethane

molecules to orient themselves in a more favourable position compared to in MFM-300(Al).

Binding domains of the C_3 hydrocarbons were also determined (Figure 5.3d-f and Supplementary Figure 5.25-5.27). A single binding site was found for propyne involving interaction with the hydroxyl group of the framework and the methyl group with a H_{OH}-C_{C3D4} distance of 3.26(6) Å. Two binding sites were found for both propylene and propane. The primary binding site displays an interaction between the methyl group of the gas molecule with the hydroxyl group of the MOF with $H_{OH}\cdots C_{C3Dx}$ distances of 3.37(1) Å for propylene and of 2.72(2) Å for propane, respectively. The secondary binding sites for both propylene and propane lie more centrally in the pores of MFM-300(In). The π-orbitals of propylene site II interact with the methylene D-centres of site I *via* a T-shaped interaction at a $H_{C3H6(I)}$-$C_{C3H6(II)}$ distance of 1.91(2) Å. Site II of propane interacts with site I via Van der Waals interactions between the D-centres of the respective methyl groups at distances of 2.92 (2) to 3.19(2) Å.

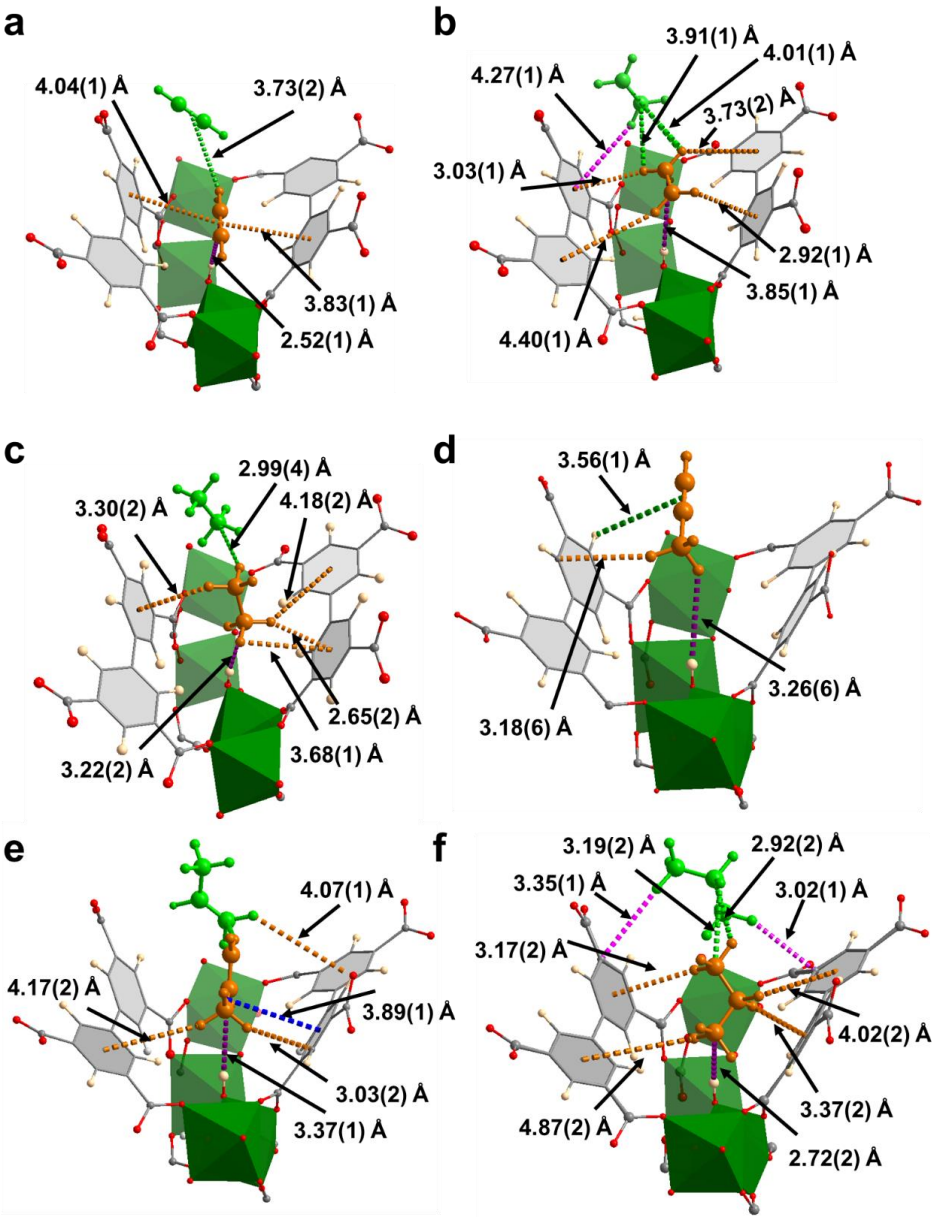

Figure 5.3. *In situ* NPD analysis. Binding sites (site I, orange; site II, green) of (a) acetylene, (b) ethylene, (c) ethane, (d) propyne, (e) propylene and (f) propane in MFM-300(In) obtained from NPD refinements (In: green; C: grey; O: red; H: light yellow; the $[InO_4(OH)_2]$ moiety is shown in green octahedron). The e.s.d. values of the bond distances are typically within 0.05 Å.

5.3.4.2 In situ inelastic neutron scattering

The INS spectra have been collected for MFM-300(In) as a function of gas loading (Figure 5.4 and Supplementary Figure 5.28-5.30). For the C_2H_2-loaded material, the

peaks in the difference spectra at around 80 and 95 meV are assigned to asymmetric and symmetric C–H vibrational modes of adsorbed C_2H_2, respectively. The peak at around 115 meV is assigned to the bending and out-of-plane wagging of the four aromatic C–H groups on two benzene rings adjacent to each C_2H_2 molecule (Figure 5.4a). The spectrum of ethylene-loaded MFM-300(In) reveals a broad peak at low energy transfer (below 25 meV), which is characteristic of almost free rotational motion around the C=C axis. A peak is observed at around 100 meV assigned to the in-plane rocking mode of $-CH_2$[34] in both the difference spectrum and that of the solid ethylene. In the spectra for ethane-loaded MFM-300(In), a broad peak is observed below 25 meV, corresponding the almost free rotational mode around the C–C axis. Two peaks are also observed in the difference spectra which align with peaks in the spectrum of solid ethane. A peak at 37 meV is assigned to the $–CH_3$ torsion, whereas the peak at 101 meV can be assigned to the CH_3 rocking motion.[33] The relatively high intensity of the $–CH_3$ rotational mode compared to that observed in MFM-300(Al) indicates that the larger pore of MFM-300(In) and the shorter $H_{OH}\cdots C_2D_6$ distance provides a greater degree of free rotation of the ethane molecule at site I, thus decreasing the entropic penalty for adsorption and driving further uptake of ethane in MFM-300(In) compared to MFM-300(Al).

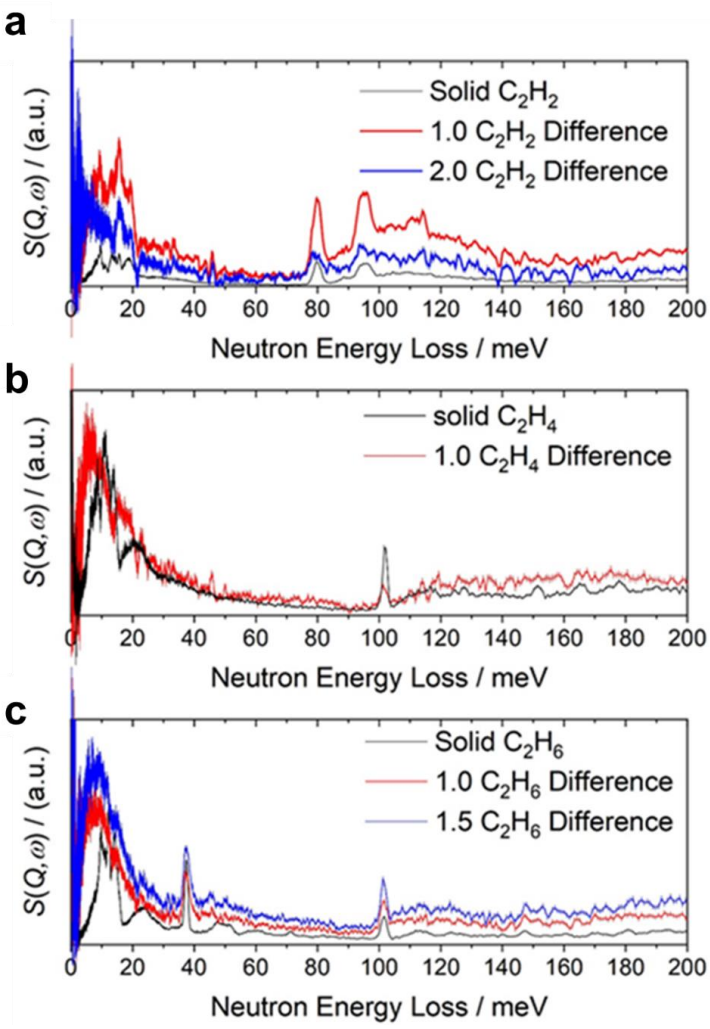

Figure 5.4. *In situ* INS studies. Comparison of the INS spectra of bare MFM-300(In) and MFM-300(In) loaded with (a) C_2D_2 (black: solid C_2H_2; red: 1.0 C_2H_2 difference; blue: 2.0 C_2H_2 difference), (b) C_2D_4 (black: solid C_2H_4; red: 1.0 C_2H_2 difference), and (c) C_2D_6 (black: solid C_2H_6; red: 1.0 C_2H_6 difference; blue: 1.5 C_2H_6 difference). For comparison, INS spectra of the condensed gas in the solid state are also included.

5.4 Conclusions

An understanding of the detailed effect that pore size has on the selectivity of ethane/ethylene is important to the design of improved materials for the separation of light hydrocarbons. The MFM-300 materials provide a useful platform to investigate changes in pore size while maintaining identical pore chemistry. This study has shown that the MFM-300(In) with slightly larger pores exhibits the opposite IAST selectivity

of ethane/ethylene to MFM-300(Al). Analysis of Q_{st} of these two gases along with NPD studies have revealed that the reason for the reversal is that the slightly larger pores of MFM-300(In) allow ethane to sit in a more favourable position which allows for a greater degree of host–guest and guest–guest interactions, thus increasing the overall uptake. MFM-300(In) exhibits excellent separation of mixtures of C_2H_6/C_2H_4 and C_3H_4/C_3H_6 as demonstrated by dynamic breakthrough experiments, allowing the production of polymer-grade C_2H_4 and C_3H_6 (purity >99.9%) in a one-step approach. The understanding on the structure-property relationship will inform the design of future efficient sorbent materials for important separations of gas mixtures.

5.5 References

1. Sholl, D.; Lively, R. Seven chemical separations to change the world. *Nature* **2016,** *532*, 435–437.
2. Blay, V.; Louis, B.; Miravalles, R.; Yokoi, T.; Peccatiello, K.; Clough, M.; Yilmaz, B. Engineering zeolites for catalytic cracking to light olefins. *ACS Catal.* **2017,** *7*, 6542–6566.
3. Ren, T.; Patel, M.; Blok, K. Olefins from conventional and heavy feedstocks: energy use in steam cracking and alternative processes. *Energy* **2006,** *31*, 425–451.
4. Geng, S.; Lin, E.; Li, X.; Liu, W.; Wang, T.; Wang, Z.; Sensharma, D.; Darwish, S.; Andaloussi, Y. H.; Pham, T.; Cheng, P.; Zaworotko, M. J.; Chen, Y.; Zhang, Z. Scalable room-temperature synthesis of highly robust ethane-selective metal–organic frameworks for efficient ethylene purification. *J. Am. Chem. Soc.* **2021,** *143*, 8654–8660.
5. Yang, R.; Kikkinides, E. New sorbents for olefin/paraffin separations by adsorption via π-complexation. *AIChE J.* **1995,** *41*, 509–517.
6. Bereciartua, P.; Cantin, A.; Corma, A.; Jorda, J.; Palomino, M.; Rey, F.; Valencia, S.; Corcoran, E.; W, Jr.; Kortunov, P.; Ravikovitch, P. I.; Burton, A.; Yoon, C.; Wang, Y.; Paur, C.; Guzman, J.; Bishop, A.; Casty, G. Control of zeolite framework flexibility and pore topology for separation of ethane and ethylene. *Science* **2017,** *358*, 1068–1071.
7. Aguado, S.; Bergeret, G.; Daniel, C.; Farrusseng, D. Absolute molecular sieve separation of ethylene/ethane mixtures with silver zeolite A. *J. Am. Chem. Soc.* **2012,** *134*, 14635–14637.
8. Li, L.; Lin, R.; Krishna, R.; Li, H.; Xiang, S.; Wu, H.; Li, J.; Zhou, W.; Chen, B. Ethane/ethylene separation in a metal–organic framework with iron-peroxo sites. *Science* **2018,** *362*, 443–446.
9. Li, J.; Han, X.; Kang, X.; Chen, Y.; Xu, S.; Smith, G. L.; Tillotson, E.; Cheng, Y.; McCormick McPherson, L. J.; Teat, S.; Rudic, S.; Ramirez-Cuesta, A.;

Haigh, S. J.; Schröder, M.; Yang, S. Purification of propylene and ethylene by a robust metal–organic framework mediated by host–guest interactions. *Angew. Chem. Int. Ed.* **2021,** *60*, 15541–15547.

10. Kang, M.; Kang, D.; Choe, J.; Kim, H.; Kim, D.; Park, H.; Hong, C. A robust hydrogen-bonded metal–organic framework with enhanced ethane uptake and selectivity. *Chem.Mater.* **2021,** *33*, 6193–6199.
11. Shen, J.; He, X.; Ke, T.; Krishna, R.; van Baten, J. M.; Chen, R.; Bao, Z.; Xing, H.; Dinca, M.; Zhang, Z.; Yang, Q.; Ren, Q. Simultaneous interlayer and intralayer space control in two-dimensional metal–organic frameworks for acetylene/ethylene separation. *Nat. Commun.* **2020,** *11*, 6259.
12. Zhao, X.; Wang, Y.; Li, D.; Bu, X.; Feng, P. Metal–organic frameworks for separation. *Adv. Mater.* **2018,** *30*, 1705189.
13. Abedini, H.; Asgari, M.; Watt Coull, M.; Shariati, A.; Reza Khosravi-Nikou, M. Efficient production of polymer-grade propylene from the propane/propylene binary mixture using Cu-MOF-74 framework. *Sep. Purif. Technol.* **2021,** *276*, 119284.
14. Bachman, J.; Kapelewski, M.; Reed, D.; Gonzalez, M.; Long, J. M_2(m-dobdc) (M = Mn, Fe, Co, Ni) Metal–organic frameworks as highly selective, high-capacity adsorbents for olefin/paraffin separations. *J. Am. Chem. Soc.* **2017,** *139*, 15363–15370.
15. Kim, A.; Yoon, T.; Kim, E.; Yoon, J.; Kim, S.; Yoon, J.; Hwang, Y.; Chang, J.; Bae, Y. Facile loading of Cu(I) in MIL-100(Fe) through redox-active Fe(II) sites and remarkable propylene/propane separation performance. *Chem. Eng. J.* **2018,** *331*, 777–784.
16. Wang, X.; Krishna, R.; Li, L.; Wang, B.; He, T.; Zhang, Y.; Li, J.; Li, J. Guest-dependent pressure induced gate-opening effect enables effective separation of propene and propane in a flexible MOF. *Chem. Eng. J.* **2018,** *346*, 489–496.
17. Sen, S.; Hosono, N.; Zheng, J.; Kusaka, S.; Matsuda, R.; Sakaki, S.; Kitagawa, S. Cooperative bond scission in a soft porous crystal enables discriminatory gate opening for ethylene over ethane. *J. Am. Chem. Soc.* **2017,** *139*, 18313–18321.
18. Chen, Y.; Qiao, Z.; Lv, D.; Duan, C.; Sun, X.; Wu, H.; Shi, R.; Xia, Q.; Li, Z. Efficient adsorptive separation of C_3H_6 over C_3H_8 on flexible and thermoresponsive CPL-1. *Chem. Eng. J.* **2017,** *328*, 360–367.
19. Li, L.; Lin, R.; Wang, X.; Zhou, W.; Jia, L.; Li, J.; Chen, B. Kinetic separation of propylene over propane in a microporous metal–organic framework. *Chem. Eng. J.* **2018,** *354*, 977–982.
20. Zeng, H.; Xie, M.; Wang, T.; Wei, R. J.; Xie, X. J.; Zhao, Y.; Lu, W.; Li, D. Orthogonal-array dynamic molecular sieving of propylene/propane mixtures. *Nature* **2021,** *595*, 542–548.
21. Hong, A.; Yang, H.; Li, T.; Wang, Y.; Wang, Y.; Jia, X.; Zhou, A.; Kusumoputro, E.; Li, J.; Bu, X.; Feng, P. Pore-space partition and optimization for propane-selective high-performance propane/propylene separation. *ACS Appl. Mater. Interfaces* **2021,** *13*, 52160–52166.
22. Peng, J.; Wang, H.; Olson, D. H.; Li, Z.; Li, J. Efficient kinetic separation of propene and propane using two microporous metal–organic frameworks. *Chem. Commun.* **2017,** *53*, 9332–9335.
23. Lin, R.; Li, L.; Zhou, H.; Wu, H.; He, C.; Li, S.; Krishna, R.; Li, J.; Zhou, W.; Chen, B. Molecular sieving of ethylene from ethane using a rigid metal–organic framework. *Nat. Mater.* **2018,** *17*, 1128–1133.

24. Xiang, H.; Fan, X.; Siperstein, F. R. Understanding ethane/ethylene adsorption selectivity in ethane-selective microporous materials. *Sep. Purif. Technol.* **2020,** *241*, 116635.
25. Wang, Y.; Hao, C.; Fan, W.; Fu, M.; Wang, X.; Wang, Z.; Zhu, L.; Li, Y.; Lu, X.; Dai, F.; Kang, Z.; Wang, R.; Guo, W.; Hu, S.; Sun, D., One-step ethylene purification from an acetylene/ethylene/ethane ternary mixture by cyclopentadiene cobalt-functionalized metal–organic frameworks. *Angew. Chem. Int. Ed.* **2021,** *60*, 11350–11358.
26. Wang, S.; Wang, F.; Dong, Y.; Shivanna, M.; Dong, Q.; Mu, X.; Duan, J.; Yang, Q.; Zaworotko, M.; Yang, Q. Reversed C_2H_6/C_2H_4 separation in interpenetrated diamondoid coordination networks with enhanced host–guest interaction. *Sep. Purif. Technol.* **2021,** *276*, 119385.
27. Chang, Y.; Huang, H.; Zhu, H.; Zhao, Y.; Wang, L.; Sun, Y.; Zhong, C., Robust carbazole-based covalent triazine frameworks with defective ultra-micropore structure for efficient ethane-selective ethane-ethylene separation. *Chem. Eng. J.* **2022,** *427*, 131726.
28. Geier, S.; Mason, J.; Bloch, E.; Queen, W.; Hudson, M.; Brown, C.; Long, J. Selective adsorption of ethylene over ethane and propylene over propane in the metal–organic frameworks M_2(Dobdc) (M = Mg, Mn, Fe, Co, Ni, Zn). *Chem. Sci.* **2013,** *4*, 2054–2061.
29. Yang, S.; Ramirez-Cuesta, A.; Newby, R.; Garcia-Sakai, V.; Manuel, P.; Callear, S.; Campbell, S.; Tang, C.; Schröder, M. Supramolecular binding and separation of hydrocarbons within a functionalized porous metal–organic framework. *Nat. Chem.* **2015,** *7*, 121–129.
30. Krap, C.; Newby, R.; Dhakshinamoorthy, A.; Garcia, H.; Cebula, I.; Easun, T. L.; Savage, M.; Eyley, J.; Gao, S.; Blake, A.; Lewis, W.; Beton, P.; Warren, M.; Allan, D.; Frogley, M.; Tang, C.; Cinque, G.; Yang, S.; Schröder, M. Enhancement of CO_2 adsorption and catalytic properties by Fe-doping of [$Ga_2(OH)_2$(L)] (H_4L = Biphenyl-3,3',5,5'-tetracarboxylic Acid), MFM-300(Ga_2). *Inorg. Chem.* **2016,** *55*, 1076–1088.
31. Zhang, X.; Silva, I.; Godfrey, H.; Callear, S.; Sapchenko, S.; Cheng, Y.; Vitorica-Yrezabal, I.; Frogley, M.; Cinque, G.; Tang, C.; Giacobbe, C.; Dejoie, C.; Rudic, S.; Ramirez-Cuesta, A.; Denecke, M.; Yang, S.; Schröder, M. Confinement of iodine molecules into triple-helical chains within robust metal–organic frameworks. *J. Am. Chem. Soc.* **2017,** *139*, 16289–16296.
32. Bae, Y.; Lee, C.; Kim, K.; Farha, O.; Nickias, P.; Hupp, J.; Nguyen, S.; Snurr, R. High propene/propane selectivity in isostructural metal–organic frameworks with high densities of open metal sites. *Angew. Chem. Int. Ed.* **2012,** *124*, 1893–1896.
33. Savage, M.; Cheng, Y.; Easun, T.; Eyley, J.; Argent, S.; Warren, M.; Lewis, W.; Murray, C.; Tang, C.; Frogley, M.; Cinque, G.; Sun, J.; Rudic, S.; Murden, R.; Benham, M.; Fitch, A.; Blake, A.; Ramirez-Cuesta, A.; Yang, S.; Schröder, M. Selective adsorption of sulfur dioxide in a robust metal–organic framework material. *Adv. Mater.* **2016,** *28*, 8705–8711.
34. Yang, S.; Sun, F.; Krishna, R.; Zhang, Q.; Zhou, L.; Zhang, Y.; Hu, T. Propane-trapping ultramicroporous metal–organic framework in the low-pressure area toward the purification of propylene. *ACS Appl. Mater. Interfaces* **2021,** *13*, 35990–35996.
35. Liang, B.; Zhang, X.; Xie, Y.; Lin, R.; Krishna, R.; Cui, H.; Li, Z.; Shi, Y.; Wu, H.; Zhou, W.; Chen, B. An ultra-microporous metal–organic framework

for high sieving separation of propylene from propane. *J. Am. Chem. Soc.* **2020,** *142*, 17795–17801.
36. Lu, Z.; Godfrey, H.; Silva, I.; Cheng, Y.; Savage, M.; Manuel, P.; Rudic, S.; Ramirez-Cuesta, A.; Yang, S.; Schröder, M. Direct observation of supramolecular binding of light hydrocarbons in Vanadium(III) and (IV) metal–organic framework materials. *Chem. Sci.* **2018,** *9*, 3401–3408.
37. Liao, P.; Zhang, W.; Zhang, J.; Chen, X. Efficient purification of ethene by an ethane-trapping metal–organic framework. *Nat. Commun.* **2015,** *6*, 8697.
38. Qazvini, O.; Babarao, R.; Shi, Z.; Zhang, Y.; Telfer, S. A robust ethane-trapping metal–organic framework with a high capacity for ethylene purification. *J. Am. Chem. Soc.* **2019,** *141*, 5014–5020.
39. Zhu, B.; Cao, J.; Mukherjee, S.; Pham, T.; Zhang, T.; Wang, T.; Jiang, X.; Forrest, K. A.; Zaworotko, M.; Chen, K. Pore engineering for one-step ethylene purification from a three-component hydrocarbon mixture. *J. Am. Chem. Soc.* **2021,** *143*, 1485–1492.
40. Yang, L.; Cui, X.; Ding, Q.; Wang, Q.; Jin, A.; Ge, L.; Xing, H. Polycatenated molecular cage-based propane trap for propylene purification with recorded selectivity. *ACS Appl. Mater. Interfaces* **2020,** *12*, 2525–2530.
41. Pires, J.; Pinto, M.; Saini, V. K. Ethane selective IRMOF-8 and its significance in ethane-ethylene separation by adsorption. *ACS Appl. Mater. Interfaces* **2014,** *6*, 12093–12099.
42. Lin, R.; Wu, H.; Li, L.; Tang, X. L.; Li, Z.; Gao, J.; Cui, H.; Zhou, W.; Chen, B. Boosting ethane/ethylene separation within isoreticular ultramicroporous metal–organic frameworks. *J. Am. Chem. Soc.* **2018,** *140*, 12940–12946.
43. Lv, D.; Shi, R.; Chen, Y.; Wu, Y.; Wu, H.; Xi, H.; Xia, Q.; Li, Z. Selective adsorption of ethane over ethylene in pcn-245: impacts of interpenetrated adsorbent. *ACS Appl. Mater. Interfaces* **2018,** *10*, 8366–8373.

4.6 Additional information

Author information. Correspondence and requests for materials should be addressed to M.S. (M.Schröder@manchester.ac.uk) and S.Y. (Sihai.Yang@manchester.ac.uk).

Conflicts of interest. The authors declare no competing interest.

Acknowledgements. We thank EPSRC (EP/I011870, EP/V056409), the Royal Society, Diamond Light Source, and the University of Manchester for funding. This project has received funding from the European Research Council (ERC) under the European Union's Horizon 2020 research and innovation program (grant agreement no 742401, NANOCHEM). We are grateful to ISIS/STFC for access to the Beamlines WISH and TOSCA.

Supporting information. The supporting information of this paper is listed in Appendix III.

[Blank page]

Chapter 6

Conclusions and Outlook

Chapter 6: Conclusions and Outlook

6.1 Conclusions

This thesis outlines two distinct strategies aimed at achieving the ambitious goal of net zero carbon emissions by 2050. These strategies include exploring alternative gas fuels as a substitute for fossil fuels and decreasing energy consumption in industry. Consequently, the focus leads to an investigation of NH_3 storage and olefin purification within porous MOFs, taking advantage of their high surface area, tuneable pore size and designable functionality.

Several key factors affecting the uptake of NH_3 were identified by analysing the isotherms for NH_3 in these MOFs. These factors include the pore size and shape, the presence of functional groups within the channels, as well as the porosities of the MOFs. It was observed that these variables had a significant impact on the adsorption capacity of NH_3. For instance, MOFs with larger pore sizes and pore volume tend to exhibit higher NH_3 uptake due to increased accessibility. The presence of specific functional groups within the channel of MOFs can enhance the affinity for NH_3 molecules. In addition, the pore size and functionality play a crucial role in the separation of C_2H_4/C_2H_6 in MOF materials, leading to improve or reverse the selectivity of C_2H_4/C_2H_6 by enhancing the host–guest interactions in MOFs. By understanding the interplay between pore size, functionalisation, and gas adsorption, researchers can tailor the properties of MOFs to suit specific separation requirements. This can lead to the development of highly efficient and selective separation processes for a variety of industrial applications.

Herein, a series of MOF materials, encompassing MIL-160, CAU-10(H), MIL-53(Al), Al-fum, Al-bttotb; MFM-300(Sc), NOTT-401(Sc); MOF-801, Zr-ndc, Zr-cca; MFM-300(In); and MFM-126, MFM-127, MFM-128, have been selected for studying the impact of host–guest interactions on NH_3 adsorption and light hydrocarbon separation. MIL-160, adorned with abundant functional groups (*e.g.*, μ_2-OH, heteroatom), along with a suitable pore size, and the potential for large- scale synthesis through environmentally friendly methods, was identified as a promising robust material for efficient capture and storage of NH_3 at high packing density. MFM-300(Sc) demonstrated an exceptional NH_3 uptake at 298 K and 1.0 bar, showed reversible adsorption of NH_3 over at least 90 cycles, and exhibited good reversibility without the need for energy-intensive processes. This characteristic makes it a feasible material for NH_3 storage. MFM-300(In) displayed a reversed and efficient C_2H_6/C_2H_4 separation with polymer-grand C_2H_4 produced in a one-step green route.

Besides their outstanding performance, the impact of host–guest interactions on efficient storage of NH_3 and purification of C_2H_4 and C_3H_6 is also elucidated at atomic level by combining several technologies. Our studies have uncovered that the pore-aperture size and the presence of functional groups are the key parameter for efficient storage of NH_3 and separation of light hydrocarbons. The experimental evidence confirms that the presence of functional groups and/or pore size in MOFs (i) enhances the affinity of MOFs towards polar molecules, thereby confirming a thermodynamically governed adsorption, and/or (ii) modulates the size and shape of the pore aperture for more efficient kinetic-driven adsorption. These results are critical in paving the way for efficient performance in gas adsorption and separation.

6.2 Outlook

Although MOFs have seen extensive exploration in the applications of gas adsorption and separation, there is still a long way to achieve decent storage or separation performance. One of the principal challenges that persist is enhancing the gas uptake while simultaneously achieving the molecular recognition of mixed gases by meticulously tailoring the chemical environment of the internal pores and channels in MOFs. An ideal adsorbent should also account for other important factors, such as water/moisture stability, cycling performance, regeneration cost, production scale.

Future directions for adsorption of NH_3 and separation of light hydrocarbons within MOF materials will likely focus on the following aspects:

1. Exploring the cracking of NH_3 to N_2 and H_2 for further use is in high demand, as the toxicity and vapour pressure of liquid NH_3 make it undesirable for direct use in mobile applications.
2. Since is impractical and unnecessary experimentally test each existing and hypothetical MOF for adsorption and separation, computer-assisted screening of MOF materials can serve as an efficient approach to identify suitable candidates for experimental investigation. This approach could entail screening suitable materials based on a stable MOF structure platform, investigating the interaction between functional groups and gases through simulation calculations, and predicting their impact on the gas storage and separation performance. Such predictions could then guide the functional modification of materials in subsequent experiments.
3. There is still vast potential for the discovery of new MOF materials with tailored structures, functionalities and pore size for specific gas adsorption and

separation applications. In addition, it is critical to develop aqueous and solvent-free synthesis methods using relatively cheap ligands and metal salts, to achieve large-scale production for MOF materials to make them more commercially viable.

4. The stability of most MOFs is still interior compared to other porous materials such as zeolites, mesoporous silica, and porous carbons. More investigations are required to increase MOF stability in the presence of moisture and other contaminants, which can degrade their performance over time. For NH_3 adsorption, more cycling experiments or long-term stability test, and wet ammonia breakthrough experiments should also be conducted, while more cycling breakthrough experiments for hydrocarbon separation. These investigations are paramount to understanding the resilience of MOF materials.

In conclusion, the future of MOFs in gas storage and separation lies in their continued optimization and the exploration of new materials, alongside rigorous testing for long-term stability and practical application scenarios.

Appendix I: Supporting information for Chapter 2

Supporting Information

1. Experimental Section

2. Supplementary Tables

3. Supplementary References

1. Experimental Section

Synthesis of H_3bttotb linker. The ligand synthesis was modified according to the reported work.[1] To a round-bottomed flask equipped with a dean-stark trap were charged phloroglucinol (0.63 g, 5.0 mmol), *p*-fluorobenzonitrile (1.91 g, 15.8 mmol), and K_2CO_3 (3.11 g, 22.5 mmol). Then N-Methylpyrrolidone, NMP (10 mL) and toluene (10 mL) were added into the flask under N_2. The reaction mixture was stirred at 150 ^oC for 2 h. After removal of toluene, the reaction temperature was increased to 180 ^oC and continued for 16 h. After cooling down to room temperature, the mixture was poured into water and acidified with 1 M HCl (aq). The resulting precipitate was collected and charged in a round bottomed flask containing KOH (13 g, 0.2 mol), H_2O (50 mL), and ethanol (50 mL), and the mixture was refluxed overnight. After removal of ethanol by distillation, the mixture was cooled to room temperature and poured into water and acidified with concentrated HCl (aq). The resulting precipitate was collected and recrystallized from ethanol and water (1/1, v/v) to yield white powder (yield: 1.42 g, 60%). ^{1}H NMR (400 MHz, DMSO-d_6, δ, ppm): 7.96 (d, J = 9.0 Hz, 6 H), 7.16 (d, J = 8.7 Hz, 6 H), 6 64 (s, 6 H).

Synthesis of Al-bttotb MOF.[2] Typically, a mixture of $Al(NO_3)_3{\cdot}9H_2O$ (80 mg, 0.21 mmol) and H_3bttotb (50 mg, 0.10 mmol), DMF/formic acid (8/4 mL) was stirred at room temperature for 30 minutes before being transferred to a 23 mL Teflon bomb. The bomb was placed at an oven preset at 150 °C for 5 days. After gradually cooling down to room temperature, colourless crystals were obtained and washed with fresh DMF solvent (yield: 67 mg, 65% based on $Al(NO_3)_3{\cdot}9H_2O$). The methanol-exchanged material was prepared by suspending the as-synthesised sample in an excess of methanol for 1 week with frequent exchange of solvent.

Synthesis of NOTT-401(Sc).[3] The mixture of scandium triflate (57 mg, 0.116 mmol), thiophene-2,6-dicarboxylic acid, H_2TDA, (10 mg, 0.058 mmol), THF (4.0 mL), DMF (3.0 mL), H_2O (1.0 mL) and HCl (36.5%, 2 drops) was transferred and sealed in a pressure tube. The pressure tube was then put in an oil bath preset at 90 ºC for 72 h. The tube was cooled to room temperature and then the colourless crystalline product was separated by filtration, washed with fresh DMF (5.00 mL) with three times and dried in air (yield: 10 mg, 70%, based on ligand). The acetone-exchanged sample was prepared by suspending the as-synthesised sample in an excess of acetone for 1 week with frequent exchange of solvent.

Synthesis of MOF-801.[4] Fumaric acid (58 mg, 0.5 mmol) and $ZrOCl_2 \cdot 8H_2O$ (160 mg, 0.5 mmol) were dissolved in a solvent mixture of DMF/formic acid (10 mL/3.5 mL) in a 20 mL screw-capped jar, which was heated at 130°C for 6 h. After cooling down, white precipitate was washed three times with 20 mL of fresh DMF and dried in air (yield: 89 mg, 79%, based on ligand). The sample was immersed in 20 mL of acetone for 3 days, during which time the acetone was replaced three times per day. The solid was then dried at 150°C under vacuum for 24 h to yield activated sample.

Synthesis of Zr-ndc.[5] $ZrCl_4$ (230 mg, 1.03 mmol), 2,6-naphthalenedicarboxylic acid (2,6-H_2ndc, 216 mg, 1.0 mmol) was dissolved in 20 mL DMF by sonication for 5 minutes. Followed by this, acetic acid (3 mL) were added and the mixture was sonicated for additional 15 minutes. The resulting solution was distributed among 6 Pyrex tubes (~4 mL in each one) and placed into the oven at 120 °C for 24 hours. The reaction was cooled to room temperature, and the white crystalline product was washed with fresh DMF and collected through filtration. (yield: 220 mg, 70% based

on ligand). The dried sample and then the solvent was exchanged with ethanol 3 times during 3 days.

Synthesis of Zr-cca.[6] Typically, $ZrOCl_2 \cdot 8H_2O$ (64.4 mg, 0.2 mmol) and benzoic acid (800 mg, 6.5 mmol) were ultrasonically dissolved in DMF (10 mL) in a 20 mL glass vial. 4-carboxycinnamic acid (H_2cca, 38.4 mg, 0.2 mmol) was subsequently added to the solution and was then sonicated for 5 minutes before being placed in an oven. After heating at 120°C for 3 days, the reaction was cooled to room temperature. Colorless crystals were obtained through filtration. (yield: 45 mg, 75% based on ligand). The sample was immersed in 100 mL of acetone for 3 days, during which time the acetone was replaced three times per day. The solid was then dried at 150°C under vacuum for 24 h to yield activated sample. The phase purity was confirmed by powder X-ray diffraction and porosity characterization.

Synthesis of MFM-126.[7] 5-(pyrimidine-5-carboxamido) isophthalic acid (10 mg, 0.04 mmol) and $Cu(NO_3)_{2.3}H_2O$ (20 mg, 0.08 mmol) were dissolved in DMF (4 mL) in a pressure tube and HCl (2M, 0.1 mL) was added to the mixture. The tube was tightly capped and heated in an oil bath at 80 ^oC for 18 h to afford hexagonal green plates which were washed with DMF and filtered and dried to yield MFM-126 (yield: 6.0 mg, 34% based on the ligand). The sample was immersed in 50 mL of acetone for 3 days, during which time the acetone was replaced three times per day. The solid was then dried at 120°C under vacuum for 24 h to yield activated sample.

Synthesis of MFM-127.[7] 5-(pyrimidin-5-yl) isophthalic acid (10 mg, 0.04 mmol) and $Cu(NO_3)_{2.3}H_2O$ (20 mg, 0.08 mmol) were dissolved in DMF (4 mL) and EtOH (1 mL) in a pressure tube and HCl (2M, 0.1 mL) was added to the mixture. The tube was tightly capped and heated in the oven at 80 ^oC for 24 h to afford green crystals which were washed with DMF, filtered off, rinsed with acetone, and dried to give MFM-127 (yield: 8 mg, 52% based on ligand). The sample was immersed in 50 mL of acetone for 3 days, during which time the acetone was replaced three times per day. The solid was then dried at 120°C under vacuum for 24 h to yield activated sample.

2. Supplementary Tables

Supplementary Table 2.1. Summary of the NH_3 isothermal uptakes, dynamic dry NH_3 breakthrough capacities, enthalpy of adsorption (Q_{st}) and (ΔS) in selected MOF materials.

MOF	NH_3 isothermal uptake at 1 bar (mmol g^{-1})	Measure condition	NH_3 dynamic capacity (mmol g^{-1})	Q_{st} (kJ mol^{-1})	ΔS (J mol^{-1} K^{-1})
Ni-acrylate[8]	13.1 (298 K)	1.0 mbar, 298 K	1.97	n/a	n/a
Ni_acryl_TMA[8]	23.5 (298 K)	1.0 mbar, 298 K	4.11	n/a	n/a
Ni_acryl_TGA[8]	17.4 (298 K)	1.0 mbar, 298 K	3.09	n/a	n/a
Mn_2Cl_2BTDD[9]	15.5 (298 K)	n/a	n/a	20-45	n/a
Co_2Cl_2BTDD[9,10]	12.0 (298 K)	1.0 mbar, 298 K	4.78	35-75	n/a
Ni_2Cl_2BTDD[9]	12.0 (298 K)	1.0 mbar, 298 K	3.36	50-120	n/a
Cu_2Cl_2BBTA[10]	19.8 (298 K)	1.0 mbar, 298 K	7.52	n/a	n/a
Co_2Cl_2BBTA[10]	17.9 (298 K)	1.0 mbar, 298 K	8.56	n/a	n/a
Mn_2(dobpdc)[11]	13.3 (298 K)	0.36 mbar, 298 K	4.77	n/a	n/a
Co_2(dobpdc)[11]	13.3 (298 K)	0.54 mbar, 298 K	4.72	n/a	n/a
Ni_2(dobpdc)[11]	20.8 (298 K)	0.58 mbar, 298 K	5.16	n/a	n/a
Mg_2(dobpdc)[11]	23.9 (298 K)	0.57 mbar, 298 K	8.25	n/a	n/a
Zn_2(dobpdc)[11]	15.2 (298 K)	0.42 mbar, 298 K	4.98	n/a	n/a
Fe-MIL-101-SO_3H[12]	17.8 (298 K)	0.51 mbar, 298 K	3.52	n/a	n/a
MOF-177[13]	12.2 (298 K)	0.99 mbar, 298 K	2.47	18	n/a
MOF-5[13]	12.2 (298 K)	0.99 mbar, 298 K	0.35	n/a	n/a
UiO-66-X (X=defect)[14]	11.8 (273 K)	0.63 mbar, 298 K	2.07	15−40	-(230−130)
UiO-66-X ($X=Cu^{I}$)[14]	12.6 (273 K)	0.63 mbar, 298 K	3.07	5−40	-(180 −20)
UiO-66-X ($X=Cu^{II}$)[14]	16.9 (273 K)	0.63 mbar, 298 K	4.15	25−55	-(250 −130)
MOF-303[15]	19.7 (298 K)	0.5 mbar, 298 K	2.2	n/a	n/a
MFM-303(Al)[16]	9.0 (293 K)	0.83 mbar, 298 K	2.9	61.5	n/a
MFM-300(Al)[17,18]	15.7 (273 K)	n/a	n/a	30−50	-(240−135)
MFM-300(Fe)[18]	15.6 (273 K)	1.0 mbar, 298 K	0.6	35−40	-(215−175)
MFM-300(Cr)[18]	14.0 (273 K)	1.0 mbar, 298 K	1.1	35−65	-(290−210)
MFM-300(V^{III})[18]	16.1 (273 K)	1.0 mbar, 298 K	1.9	35−45	-(215−150)
MFM-300(V^{IV})[18]	17.3 (273 K)	1.0 mbar, 298 K	1.0	30−60	-(240−180)
MIL-160	12.8 (298 K)	1.0 mbar, 298 K	4.2	45−63	-(285−195)
Our work	15.5 (273 K)				

CAU-10-H **Our work**	10.0 (298 K)	1.0 mbar, 298 K	1.3	n/a	n/a
Al-fum **Our work**	8.9 (298 K)	1.0 mbar, 298 K	0.4	n/a n/a	n/a
MIL-53(Al)	3.0 (298 K)	1.0 mbar, 298 K	0.15	n/a	n/a
MFM-300(Sc) **Our work**	13.1 (298 K) 19.5 (273 K)	1.0 mbar, 298 K	1.65	30−60	-(250−200)
NOTT-401(Sc) **Our work**	15.7 (273 K)	n/a	n/a	n/a	n/a
Al-bttotb **Our work**	10.5 (273 K)	n/a	n/a	n/a	n/a
MOF-801 **Our work**	10.7 (273 K)	n/a	n/a	n/a	n/a
Zr-ndc **Our work**	11.0 (273 K)	n/a	n/a	n/a	n/a
Zr-cca **Our work**	11.5 (273 K)	n/a	n/a	n/a	n/a

Supplementary Table 2.2. Comparison of separation performance for several reported MOFs.

MOF	**Temperature (K)**	**Uptake (mmol g^{-1}) at 1 bar**		**uptake ratio C_2H_6/C_2H_4**	**IAST Selectivity (C_2H_6/C_2H_4 = 50/50**	**C_2H_4 Productivity (L/kg)**
		C_2H_6	C_2H_4			
TJT-100[19]	299 K	~3.66	3.4	1.1	1.2	n/a
IRMOF-8[20]	298 K	2.16	1.25	1.7	1.8	2.5
MUF-15[21]	293 K	4.69	4.15	1.1	1.96	14
$Cu(Qc)_2$[22]	298 K	1.85	0.78	2.4	3.4	4.3
$Ni(bdc)(ted)_{0.5}$[23]	298 K	5.0	3.4	1.5	2	n/a
PCN-245[24]	298 K	3.27	2.39	1.4	1.9	5.8
$Fe_2(O_2)dobdc$[25]	298 K	3.45	2.68	1.3	4.4	19.3
ZIF-4[26]	293 K	2.3	2.2	1.0	1.7	n/a
ZIF-8[27]	293 K	2.54	1.5	1.7	1.8	n/a
NKMOF-14-PZ[28]	298 K	5.63	3.44	1.6	1.89	n/a
NKMOF-14-PD[28]	298 K	5.34	3.39	1.6	7.96	n/a
PCN-250[29]	298 K	5.21	4.22	1.2	1.9	10
Tb-MOF-76[30]	298 K	3.0	2.8	1.2	1.1	2.88
Tb-MOF-76(NH_2)[30]	298 K	3.3	3.0	1.9	1.1	7.53
Zn(ad)(int)[31]	298 K	2.3	2.2	1.0	2.4	n/a
[Zn-(BDC)(H_2BPZ)]·4H_2O[32]	298 K	3.6	3.3	1.0	2.2	n/a
Zn-FBA[33]	298 K	1.25	1.14	1.1	3.0	n/a
JNU-2[34]	298 K	4.19	3.62	1.2	1.6	21.2
HOF-76a[35]	296 K	2.95	1.67	1.76	2.0	7.2
ZJU-HOF-1[36]	298 K	4.9	4.0	1.2	2.25	21.9
MAF-49[37]	298 K	1.79	1.79	**1**	4.9	n/a
UiO-67-(NH_2)$_2$[38]	296 K	5.32	4.32	1.2	1.7	/
MFM-300(Al)[39]	293 K	0.85	4.28	**0.2**	C_2H_6/C_2H_4 =48.7	n/a
MFM-300(In) Our work	**293 K**	**5.1**	**4.9**	**1.0**	**1.7**	**4.6**
MFM-126 Our work	**293 K**	2.88	2.95	0.98	n/a	n/a
MFM-127 Our work	293 K	5.36	4.51	1.2	1.8	n/a

3. Supplementary References

1. Matsumoto, K.; Higashihara, T.; Ueda, M. Star-shaped sulfonated block copoly(ether ketone)s as proton exchange membranes. *Macromolecules* **2008**, *41*, 7560–7565.
2. Yu, L.; Dong, X.; Gong, Q.; Acharya, S.; Lin, Y.; Wang, H.; Han, Y.; Thonhauser, T.; Li, J. Splitting mono-and dibranched alkane isomers by a robust aluminium-based metal–organic framework material with optimal pore dimensions. *J. Am. Chem. Soc.*, **2020,** *142*, 6925−6929.
3. Ibarra, I.; Yang, S.; Lin, X.; Blake, A.; Rizkallah, P.; Nowell, H.; Allan, D. R.; Champness, N.; Hubberstey, P.; Schröder, M.; Highly porous and robust scandium-based metal–organic frameworks for hydrogen storage. *Chem. Commun.*, **2011**, *47*, 8304−8306.
4. Lacomi, P.; Formalik, F.; Marreiros. J.; Shang, J.; Rogacka, J.; Mohmeyer, A.; Behrens, P.; Ameloot, R.; Kuchta, B.; Llewellyn, P. L. Role of structural defects in the adsorption and separation of C_3 hydrocarbons in Zr-fumarate-MOF (MOF-801). *Chem. Mater.*, **2019,** *31*, 20, 8413−8423.
5. Bon, V.; Senkovska, I.; Weiss, M.; Kaskel, S. Tailoring of network dimensionality and porosity adjustment in Zr- and Hf-based MOFs. *CrystEngComm.*, **2013,** *15*, 9572−9577.
6. Wang, H.; Wang, Q.; Teat, S. J.; Olson, D.; Li, J. Synthesis, structure, and selective gas adsorption of a single-crystalline zirconium based microporous metal–organic framework. *Cryst. Growth Des.*, **2017,** *17*, 4, 2034−2040.
7. Humby, J.; Benson, O.; Smith, G.; Argent, S.; Silva, I.; Cheng, Y.; Rudic, S.; Manuel, P.; Frogley, M.; Clique, G.; Saunders, L.; Yrezabal, I.; Whitehead, G.; Easun, T.; Lewis, W.; Blake, A.; Cuesta, A.; Yang, S.; Schröder, M. Host–guest selectivity in a series of isoreticular metal–organic frameworks: observation of acetylene-to-alkyne and carbon dioxide-to-amide interactions. *Chem. Sci.*, **2019,** *10*, 1098−1106.
8. Kim, D.; Kang, D.; Kang, M.; Choi, D.; Yun, H.; Kim, S.; Lee, S.; Lee, J.; Hong, C. High gravimetric and volumetric ammonia capacities in robust metal–organic frameworks prepared via double postsynthetic modification. *J. Am. Chem. Soc.* **2022,** *144*, 9672−9683.
9. Rieth, A.; Tulchinsky, Y.; Dincă, M. High and reversible ammonia uptake in mesoporous azolate metal–organic frameworks with open Mn, Co, and Ni sites. *J. Am. Chem. Soc*. **2016,** *138*, 9401–9404.
10. Rieth, A.; Dinca, M. Controlled gas uptake in metal–organic frameworks with record ammonia sorption. *J. Am. Chem. Soc.* **2018**, *140*, 3461–3466.
11. Kim, D.; Kang, D.; Kang, M.; Lee, J.; Choe, J.; Chae, Y.; Choi, D.; Yun, H.; Hong, C. High ammonia uptake of a metal–organic framework adsorbent in a wide pressure range. *Angew. Chem. Int. Ed.* **2020**, *132*, 22720–22725.
12. Humbeck, J.; McDonald, T.; Jing, X.; Wiers, B.; Zhu, G.; Long, J. Ammonia capture in porous organic polymers densely functionalized with Brønsted acid groups. *J. Am. Chem. Soc.* **2014**, *136*, 2432–2440.
13. Saha, D.; Deng, S. Ammonia adsorption and its effects on framework stability of MOF-5 and MOF-177. *J. Colloid. Interf. Sci.* **2010**, *348*, 615–620.
14. Ma, Y.; Lu, W.; Han, X.; Chen, Y.; Silva, I.; Lee, D.; Sheveleva, A.; Wang, Z.; Li, J.; Li, W.; Fan, M.; Xu, S.; Tuna, F.; McInnes, E.; Cheng, Y.; Rudic, S.;

Manuel, P.; Frogley, M.; Cuesta, A.; Schröder, M.; Yang, S. Direct observation of ammonia storage in UiO-66 incorporating Cu(II) binding sites. *J. Am. Chem. Soc.* **2022,** *144*, 8624–8632.

15. Wang, Z.; Li, Z.; Zhang, X.; Xia, Q.; Wang, H.; Wang, C.; Wang, Y.; He, H.; Zhao, Y.; Wang, J. Tailoring multiple sites of metal–organic frameworks for highly efficient and reversible ammonia adsorption. *ACS Appl. Mater. Interfaces* **2021,** *13*, 56025−56034.
16. Marsh, C.; Han, X.; Li, J.; Lu, Z.; Argent, S.; Silva, I.; Cheng, Y.; Daemen, L. L.; Cuesta, A.; Thompson, S.; Blake, A.; Yang, S.; Schröder, M. Exceptional packing density of ammonia in a dual-functionalized metal–organic framework. *J. Am. Chem. Soc.* **2021**, *143*, 6586–6592.
17. Godfrey, H.; Silva, I.; Briggs, L.; Carter, J.; Morris, C.; Savage, M.; Easun, T.; Manuel, P.; Murray, C.; Tang, C.; Frogley, M.; Cinque, G.; Yang, S.; Schröder, M. Ammonia storage by reversible host–guest site exchange in a robust metal–organic framework. *Angew. Chem. Int. Ed.* **2018**, *57*, 14778–14781.
18. Han, X.; Lu, W.; Chen, Y.; Silva, I.; Li, J.; Lin, L.; Li, W.; Sheveleva, A.; Godfrey, H.; Lu, Z.; Tuna, F.; McInnes, E.; Cheng, Y.; Daemen, L.; McPherson, L.; Teat, S.; Frogley, M.; Rudic, S.; Manuel, P.; Cuesta, A.; Yang, S.; Schröder, M. High ammonia adsorption in MFM-300 materials: dynamics and charge transfer in host–guest binding. *J. Am. Chem. Soc.* **2021**, *143*, 3153–3161.
19. Hao, H. G.; Zhao, Y. F.; Chen, D. M.; Yu, J. M.; Tan, K.; Ma, S.; Chabal, Y.; Zhang, Z. M.; Dou, J. M.; Xiao, Z. H.; Day, G.; Zhou, H. C.; Lu, T. B., Simultaneous Trapping of C_2H_2 and C_2H_6 from a Ternary Mixture of $C_2H_2/C_2H_4/C_2H_6$ in a Robust Metal–Organic Framework for the Purification of C_2H_4. *Angew. Chem. Int. Edit.* **2018**, *130*, 16299–16303.
20. Pires, J.; Pinto, M. L.; Saini, V. K., Ethane Selective IRMOF-8 and its Significance in Ethane-Ethylene Separation by Adsorption. *ACS Appl. Mater. Interfaces* **2014**, *6*, 12093–12099.
21. Qazvini, O. T.; Babarao, R.; Shi, Z. L.; Zhang, Y. B.; Telfer, S. G., A Robust Ethane-Trapping Metal-Organic Framework with a High Capacity for Ethylene Purification. *J. Am. Chem. Soc.* **2019**, *141*, 5014–5020.
22. Lin, R. B.; Wu, H.; Li, L.; Tang, X. L.; Li, Z.; Gao, J.; Cui, H.; Zhou, W.; Chen, B., Boosting Ethane/Ethylene Separation within Isoreticular Ultramicroporous Metal-Organic Frameworks. *J. Am. Chem. Soc.* **2018**, *140*, 12940–12946.
23. Liang, W.; Xu, F.; Zhou, X.; Xiao, J.; Xia, Q.; Li, Y.; Li, Z., Ethane Selective Adsorbent $Ni(Bdc)(Ted)_{0.5}$ with High Uptake and Its Significance in Adsorption Separation of Ethane and Ethylene. *Chem. Eng. J.* **2016**, *148*, 275–281.
24. Lv, D.; Shi, R.; Chen, Y.; Wu, Y.; Wu, H.; Xi, H.; Xia, Q.; Li, Z., Selective Adsorption of Ethane over Ethylene in PCN-245: Impacts of Interpenetrated Adsorbent. *ACS Appl. Mater. Interfaces* **2018**, *10*, 8366–8373.
25. Li, L.; Lin, R. B.; Krishna, R.; Li, H.; Xiang, S.; Wu, H.; Li, J.; Zhou, W.; Chen, B., Ethane/Ethylene Separation in a Metal-Organic Framework with Iron-peroxo Sites. *Science* **2018**, *362*, 443–446.
26. Hartmann, M.; Bohme, U.; Hovestadt, M.; Paula, C., Adsorptive Separation of Olefin/Paraffin Mixtures with ZIF-4. *Langmuir* **2015**, *31*, 12382–12389.
27. Bohme, U.; Barth, B.; Paula, C.; Kuhnt, A.; Schwieger, W.; Mundstock, A.; Caro, J.; Hartmann, M., Ethene/Ethane and Propene/Propane Separation via The Olefin and Paraffin Selective Metal-Organic Framework Adsorbents CPO-27 And ZIF-8. *Langmuir* **2013**, *29*, 8592–600.

28. Liu, W.; Geng, S.; Li, N.; Wang, S.; Jia, S.; Jin, F.; Wang, T.; Forrest, K.; Pham, T.; Cheng, P.; Chen, Y.; Ma, J.; Zhang, Z. Highly robust microporous metal-organic frameworks for efficient ethylene purification under dry and humid conditions. *Angew. Chem. Int. Edit.* **2022**, *62*, e202217662.
29. Chen, Y.; Qiao, Z.; Wu, H.; Lv, D.; Shi, R.; Xia, Q.; Zhou, J.; Li, Z., An Ethane-Trapping MOF PCN-250 for Highly Selective Adsorption of Ethane over Ethylene. *Chem. Eng. J.* **2018**, *175*, 110–117.
30. Wang, G.; Krishna, R.; Li, Y.; Shi, W.; Hou, L.; Wang, Y.; Zhu, Z. Boosting ethane/ethylene separation by MOFs through the amino-functionalization of pores. *Angew. Chem. Int. Ed.* **2022**, *61*, e202213015.
31. Ding, Q.; Zhang, Z.; Liu, Y.; Chai, K.; Krishna, R.; Zhang, S. one-step ethylene purification from ternary mixtures in a metal–organic framework with customized pore chemistry and shape. *Angew. Chem. Int. Ed.* **2022**, *134*, e202208134.
32. Wang, G. D.; Li, Y. Z.; Shi, W. J.; Hou, L.; Wang, Y. Y.; Zhu, Z. One-step C_2H_4 purification from ternary $C_2H_6/C_2H_4/C_2H_2$ mixtures by a robust metal–organic framework with customized pore environment. *Angew. Chem. Int. Ed.* **2022**, *61*, e202205427.
33. Yang, L.; Yan, L.; Niu, W.; Feng, Y.; Fu, Q.; Zhang, S.; Zhang, Y.; Li, L.; Gu, X.; Dai, P.; Liu, D.; Zheng, Q.; Zhao, X. (2022). Adsorption in reversed order of C_2 hydrocarbons on an ultramicroporous fluorinated metal-organic Framework. *Angew. Chem. Int. Ed.* **2022**, *61*, e202204046.
34. Zeng, H.; Xie, X. J.; Xie, M.; Huang, Y. L.; Luo, D.; Wang, T.; Zhao, Y.; Lu, W.; Li, D., Cage-Interconnected Metal-Organic Framework with Tailored Apertures for Efficient C_2H_6/C_2H_4 Separation under Humid Conditions. *J. Am. Chem. Soc.* **2019**, *141*, 20390–20396.
35. Zhang, X.; Li, L.; Wang, J. X.; Wen, H. M.; Krishna, R.; Wu, H.; Zhou, W.; Chen, Z.; Li, B.; Qian, G.; Chen, B. Selective ethane/ethylene separation in a robust microporous hydrogen-bonded organic framework. *J. Am. Chem. Soc.* **2019**, *142*, 633–640.
36. Zhang, X.; Wang, J.; Li, L.; Pei, J.; Krishna, R.; Wu, H.; Zhou, W.; Qian, G.; Chen, B.; Li, B. A rod-packing hydrogen-bonded organic framework with suitable pore confinement for benchmark ethane/ethylene separation. *Angew. Chem. Int. Edit.* **2021**, *60*, 10304–10310.
37. Liao, P.; Zhang, W.; Zhang, J.; Chen, X. Efficient purification of ethene by an ethane-trapping metal-organic framework. *Nat. Commun.* **2015**, *6*, 8697.
38. Gu, X. W.; Wang, J. X.; Wu, E.; Wu, H.; Zhou, W.; Qian, G.; Chen, B.; Li, B. Immobilization of Lewis basic sites into a stable ethane-selective MOF enabling one-step separation of ethylene from a ternary mixture. *J. Am. Chem. Soc.* **2022**, *144*, 2614−2623.
39. Yang, S.; Ramirez-Cuesta, A.; Newby, R.; Garcia-Sakai, V.; Manuel, P.; Callear, S.; Campbell, S.; Tang, C.; Schröder, M. Supramolecular binding and separation of hydrocarbons within a functionalized porous metal–organic framework. *Nat. Chem.* **2014**, *7*, 121−129.

Appendix II: Supporting information for Chapter 3

Supporting Information

1. Experimental Section

2. Powder X-ray Diffraction

3. Thermo-Gravimetric Analysis

4. Characterisation of Porosity

5. Analysis and Derivation of the Isosteric Heats of Adsorption

6. Ammonia Temperature-Programmed Desorption

7. Stability Test

8. Kinetic Analysis

9. Neutron Powder Diffraction

10. Solid-state Nuclear Magnetic Resonance Spectroscopy

11. Supplementary Tables

12. Supplementary References

1. Experimental Section

Synthesis of Al-MOFs

MIL-160, CAU-10-H, Al-fum, and MIL-53(Al) were synthesised according to reported methods with small modifications.[18–21] MIL-160 was prepared by reaction of NaOH (0.08 g, 2.0 mmol), H_2fdc (0.15 g, 1.0 mmol), H_2O (15 mL) and $AlCl_3 \cdot 6H_2O$ (0.24 g, 1.0 mmol) under reflux at 378 K for 12 h. The product was collected by filtration and washed with DMF and H_2O, and then exchanged 3 days with acetone.

CAU-10-H was prepared by reaction of $Al_2(SO_4)_3 \cdot 18H_2O$ (0.4 g, 0.6 mmol), *m*-H_2bdc (0.1 g, 0.6 mmol), H_2O (4 mL) and DMF (1 mL) in a Teflon-lined stainless-steel autoclave (408 K, 12 h). The product was collected by filtration and washed with DMF and H_2O, and then exchanged for 3 days with acetone.

Al-fum was prepared by reaction of $Al_2(SO_4)_3 \cdot 18H_2O$ (0.4 g, 0.6 mmol), NaOH (0.15 g, 3.6 mmol) and H_2fum (0.14 g, 1.2 mmol) in H_2O (10 mL) with sonication for 5 min. The solution was transferred into a 38 mL pressure tube which was heated at 363 K for 2 h. The product was collected by filtration, washed with H_2O, and then exchanged 3 days with acetone.

MIL-53(Al) was prepared by reaction of $Al(NO_3)_3 \cdot 9H_2O$ (1.31 g, 3.5 mmol), *p*-H_2bdc (0.29 g, 1.7 mmol) and H_2O (15 mL) in a Teflon-lined stainless-steel autoclave at 483 K for 3 days. After cooling, the product was collected by filtration and washed with H_2O. The dried white powder was then calcined in a muffle-furnace with the air flow at 603 K for 3 days to remove the incorporated *p*-H_2bdc from the pores, and then stored under acetone.

General characterisation

Powder X-ray diffraction patterns were collected using a Philips X'pert X-ray diffractometer (40 kV and 30 mA) using Cu Kα radiation (λ = 1.5406 Å). The pore size, and surface areas were obtained from N_2 isotherms recorded on a 3-flex (Micrometrics) instrument at 77 K. Thermogravimetric analysis was conducted on a TA Instrument Q600 under air flow of 100 mL min^{-1}.

Ammonia temperature-programmed desorption (TPD)

Temperature-programmed desorption of ammonia (NH_3-TPD) with a Quantachrome Autosorb-1 equipped with a thermal conductivity detector (TCD) was performed to assess the affinity of NH_3 in MIL-160 framework. Typically, 80 mg of sample was pre-treated in a helium stream (30 mL min^{-1}) at 150 ^oC for 10 h. The adsorption of NH_3 was carried out at 50 ^oC for 1 h. The sample was flushed with helium at 100 ^oC for 2 h to remove physisorbed NH_3 from the sample surface. The TPD profile was recorded at a heating rate of 10 ^oC min^{-1} from 100 to 300 ^oC.

Gas adsorption and breakthrough experiments

Measurements of static adsorption isotherms (0−1.0 bar) for NH_3 were undertaken on an IGA gravimetric sorption analyser (Hiden Isochema, Warrington, UK) under ultra-high vacuum with the temperature controlled using a programmed water bath. Research-grade NH_3 was purchased from BOC and used as received. Acetone exchanged samples were loaded into the IGA system and degassed at 423 K and 1×10^{-6} mbar for 10 h to give a desolvated material of typical mass ca. 30 mg. For the cycling experiments, the pressure of NH_3 was increased from vacuum (1×10^{-8} mbar) to 0.2 bar and the uptake recorded. The pressure was then reduced to regenerate the

sample without heating. Dynamic breakthrough experiments were conducted on a Hiden Isochema IGA-003 with ABR attachments and a Hiden Analytical mass spectrometer by using a fixed-bed tube packed with 750 mg of powder. The sample was heated at 423 K under a flow of dry He for 12 h for activation, and then cooled to 298 K. The dynamic breakthrough experiments were collected at a concentration of 1000 ppm NH_3 (diluted in He) at the total flow rate of 25 mL min^{-1}. The concentration of NH_3 in the outlet was determined by mass spectrometry and compared with the inlet concentration C_0, where C/C_0 = 1 indicates complete breakthrough. The MIL-160 sample framework density is 1.1 g cm^{-3}, occupied a volume of 0.68 mL (assuming 100% purity and no framework collapse), leading the dead volume is determined to be 4.32 mL.

To determine the dynamic adsorption capacity, the uptake of each component (n_m) was calculated based on the breakthrough curves by the following equation:

$$V_m = \frac{\int_0^t v_{gas\ out}\,\mathrm{d}t - V_{dead}}{W_{MOF}} \qquad (1)$$

$$n_m = \frac{PV_m}{\mathrm{R}T} \qquad (2)$$

where $v_{\text{gas out}}$ is the flow rate of the target gas with the unit of mL min^{-1}, V_{dead} is the dead volume of the system (mL), W represents the mass of sample packed in the breakthrough bed (g). t is the retention time for the specific gas (min), P is pressure (kpa), R is the gas constant, and T is the measurement temperature (K).

***In situ* neutron powder diffraction experiments.**

Neutron powder diffraction (NPD) experiments for ND_3-loaded MIL-160 were undertaken on the WISH diffractometer at the ISIS Facility at Rutherford Appleton Laboratory (UK). The instrument has a solid methane moderator providing a high flux

of cold neutrons with a large bandwidth, transported to the sample via an elliptical guide. The divergence jaws of the WISH system allow tuning of the resolution according to the need of the experiment; in this case, it was setup in high resolution mode. The WISH detectors are 1 m long, 8 mm diameter pixelated ^{3}He tubes positioned at 2.2 m from the sample and arranged on a cylindrical locus covering a 2θ scattering angle of 10−170°. To reduce the background from the sample environment, WISH was equipped with an oscillating radial collimator that defines a cylinder of radius of approximately 22 mm diameter at 90^{o} scattering angle. The sample of desolvated MIL-160 was loaded into a cylindrical vanadium sample container with an indium vacuum seal connected to a gas handling system. The sample was degassed at 1×10^{-7} mbar and at 373 K for 12 h with He flushing to remove any remaining trace of guest molecules. The sample was dosed with ND_3 using the volumetric method after being warmed to room temperature (298 K) to ensure that the gas was well dispersed. A certain amount of ND_3 was dosed into the vanadium holder containing MIL-160. The ratio of ND_3 to the MOF was calculated through the difference on the partial pressure of the ND_3 in the buffer container (500 mL) before and after dosing, based on the equation $PV = nRT$, where the T is 298 K, R is the gas constant, V is the dead volume of the system (mL). Data collection for desolvated MIL-160 and two subsequent loadings of ND_3 (0.4 and 1.5 ND_3 molecules per metal site) were performed while the temperature was controlled using a He cryostat (10 ± 0.2 K).

Rietveld structural refinements were carried out on the NPD data using Bruker-AXS Topas (V5.0). The structure of desolvated MIL-160 was established based on the reported crystallographic structure and subsequently refined against the NPD pattern for activated MIL-160.[18] Soft restraints were applied on bond lengths and bond angles within the furan rings and carboxylates to keep the molecule integrity. Isotropic

displacement parameters (U_{iso}) were used for all non-H atoms, where the riding model was used for the hydrogen's displacement parameters. Upon loading of ND_3, obvious changes on peak intensity were observed indicating the successful adsorption of molecule in the bare framework. The ND_3 molecule was modelled as rigid body with fixed bond lengths and angles from DFT-optimised molecule geometry (B3LYP-D_3, 6-31G**, Gaussian09). The position of the primary ND_3 molecule was extracted from the difference Fourier map. The initial positions of other loaded ND_3 were guessed from simulated annealing via the Auto_T macro in TOPAS for molecules placed in general positions, where precise locations were obtained by subsequent refinement. Two binding sites were located with a total occupancy reaching 0.4 ND_3 per Al atom for the low-loading sample. An additional adsorption site filling the pore was obtained from the NPD pattern of high-loading sample with a total occupancy around 1.5 ND_3 per metal atom.

For the low-loading sample, no positional restraint was applied, while the fractional *x* coordinate of the N atom of site III ND_3 in the high loading structure was found to vibrate closely around a special position and was consequently fixed. All translations and rotations of ND_3 molecules were freed with no restraints allowing precise atomic positions of D of ND_3 to be determined. Isotropic displacement parameters were used for all N atoms, where the parameter for hydrogen was defined similarly with a riding model. Refining the H of the hydroxy group (−OH) on the framework as a combination of −OH and −OD in the high loading structure gave lower R-factors than purely −OH. This indicated the presence of H–D exchange between active framework hydroxyl groups and site I ND_3 molecules as the result of strong host–guest interactions. This exchange is apparent in the refinement of NPD data

owing to the significant difference of neutron scattering length (b_c, in fm) of proton (H, -3.74) and deuterion (D, 6.67).

In NH_3 loaded MOF frameworks, various binding interactions including hydrogen bonding, electrostatic interactions, and intermolecular interactions can occur, contributing to the overall stability of the system. Hydrogen bonding (X–H···Y) involves the interaction between a hydrogen atom bonded to an electronegative atom (X) and a lone pair or electronegative atom (Y). In the case of NH_3-loaded MIL-160 framework, this could occur when a NH_3 (N–H) and interacts with a suitable electron donor atom (Y) such as N, O, or C atom present in the system. The typical range for hydrogen bond distances is 1.5 to 3 Å, a longer hydron bond distance usually means the weaker hydrogen bonding.

Electrostatic interactions are long-range interactions that arise from the attraction or repulsion between charges. These interactions occur between the positive charges on the adsorbed gas molecules and the negative charges on the ligand rings within the MOF framework. In general, the bond distances involved in electrostatic interactions are typically longer than those hydrogen bonding discussed above.

Additionally, intermolecular interactions between the adsorbed gas molecules themselves can occur within the MIL160 frameworks. These interactions involve the physical proximity of the adsorbed gas molecules and can include Van der Waals forces, dipole-dipole interactions, or other weak intermolecular forces. The distance of this interaction is typically ranging from approximately 2 to 4 Å. These interactions contribute to the stability and structure of the loaded system. Overall, the combination of these binding interactions contributes to the stability and structure of the NH_3 loaded MOF framework.

Solid-state nuclear magnetic resonance experiments.

A 400 MHz Bruker Advance III spectrometer (9.4 T) was used at ambient temperature with a 4 mm HFX probe and a MAS frequency of 12 kHz. Samples were activated (423 K for 10 h under dynamic vacuum) and packed into 4 mm outer diameter zirconia

rotors under inert conditions. The various sample treatments were applied to the sample *in situ* in the rotor. Spectral simulations and fitting were performed in the solid lineshape analysis (SOLA) module v2.2.4 in Bruker TopSpin v4.0.9 for crystalline models and in DMFit[29] for Gaussian isotropic distribution models. ^{1}H and ^{13}C chemical shifts are given with respect to TMS (0 ppm) and ^{27}Al chemical shifts are referenced to a 1.1 mol/kg $Al(NO_3)_3$ in D_2O solution. More information on specific experimental details may be found in the supporting information.

***In situ* synchrotron infrared micro-spectroscopy experiments.**

In situ synchrotron infrared micro-spectroscopy experiments were carried out at multimode infrared imaging and micro spectroscopy (MIRIAM) beamline at the Diamond Light Source, UK. Measurements were performed using a Bruker Vertex 80V FTIR equipped with a mid-infrared LN_2-cooled MCT (Mercury Cadmium Telluride) detector and the Diamond Light Source synchrotron as an IR source. Spectra were collected in the range 4000−400 cm^{-1} and aperture size at the sample of approximately 20 × 20 μm. A microcrystalline powder of MIL-160 was scattered onto a 0.5 mm thick ZnSe infrared window and placed within a Linkam FTIR 600 gas-tight sample cell equipped with 0.5 mm thick ZnSe windows, a heating stage and gas inlet and outlet. Ultrapure N_2 and anhydrous NH_3 gases were used as supplied from the cylinder. The gases were dosed volumetrically to the sample cell using mass flow controllers, and the total flow rate was maintained at 100 mL min^{-1} for all experiments. The exhaust from the cell was directly vented to an extraction system and the total pressure in the cell was therefore 1.0 bar for all experiments. The sample was desolvated under a flow of dry N_2 at 100 mL min^{-1} and 423 K for 5 h, and was then cooled to 298 K under a continuous flow of N_2. Dry NH_3 was then dosed as a function

of partial pressure, maintaining a total flow of 100 mL min^{-1} with N_2 as a balance gas. The MOF sample was then regenerated with a flow of dry N_2.

2. Powder X-ray Diffraction

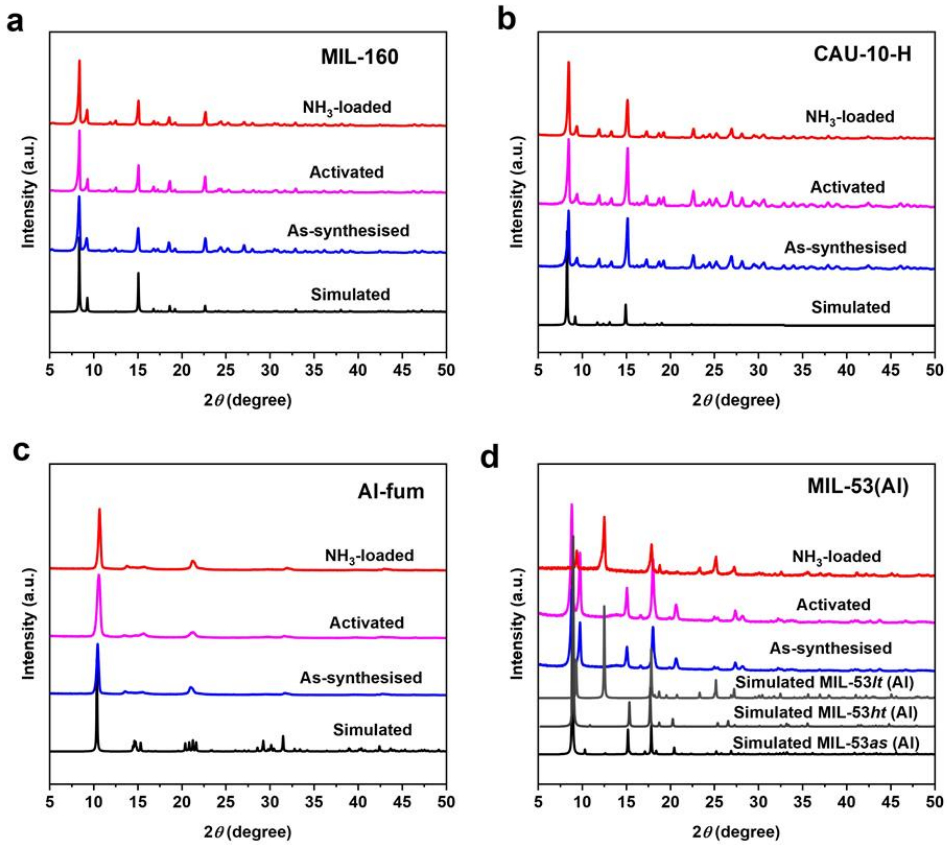

Supplementary Figure 3.1. PXRD patterns of simulated (black), as-synthesised (blue), activated (magenta) and NH_3-loaded (red) samples of (a) MIL-160, (b) CAU-10-H, (c) Al-fum and (d) MIL-53(Al).[1] MIL-53*as* (Al) is the form occupied by free terephthalic acid ligand; MIL-53*ht* (Al) is the calcined form with empty channels; MIL-53*lt* (Al) is the room temperature form with water molecule in the channels.

3. Thermogravimetric Analysis

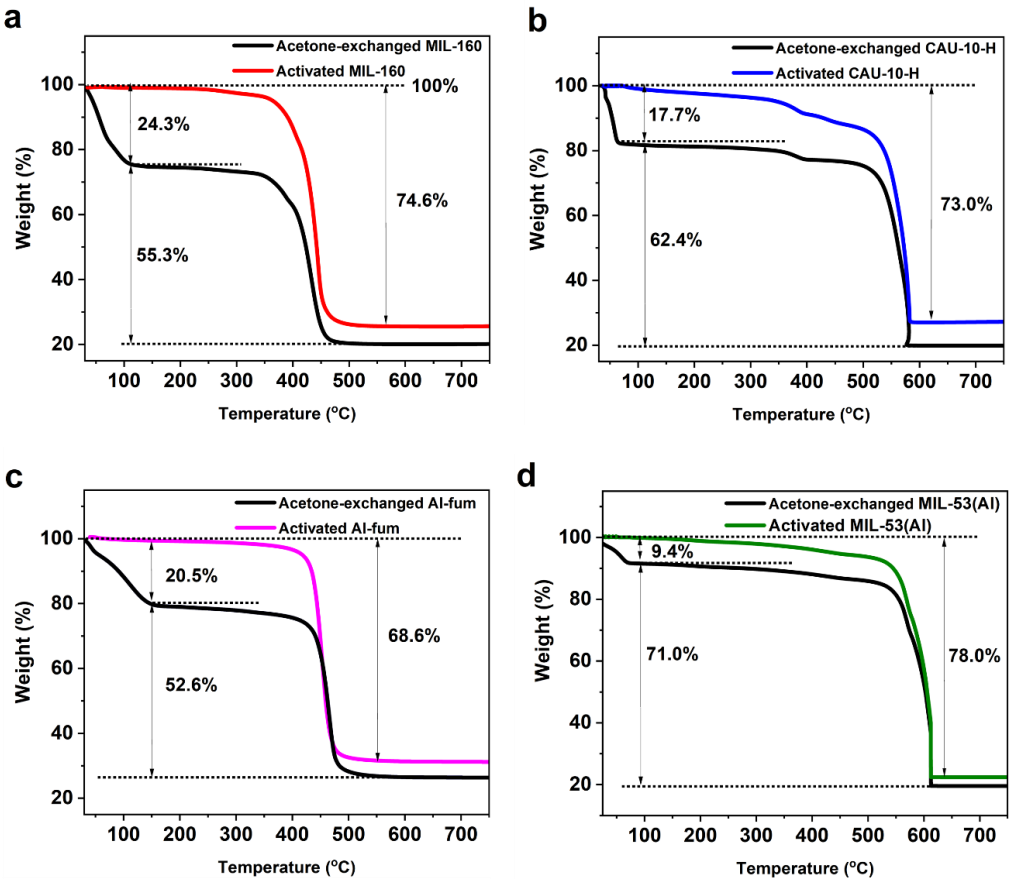

Supplementary Figure 3.2. TGA curves of acetone-exchanged and activated samples for (a) MIL-160, (b) CAU-10-H, (c) Al-fum and (d) MIL-53(Al) measured under an air flow (black: activated sample; red: activated MIL-160; blue: activated CAU-10-H; magenta: activated Al-fum; olive: activated MIL-53(Al)).

4. Characterisation of Porosity

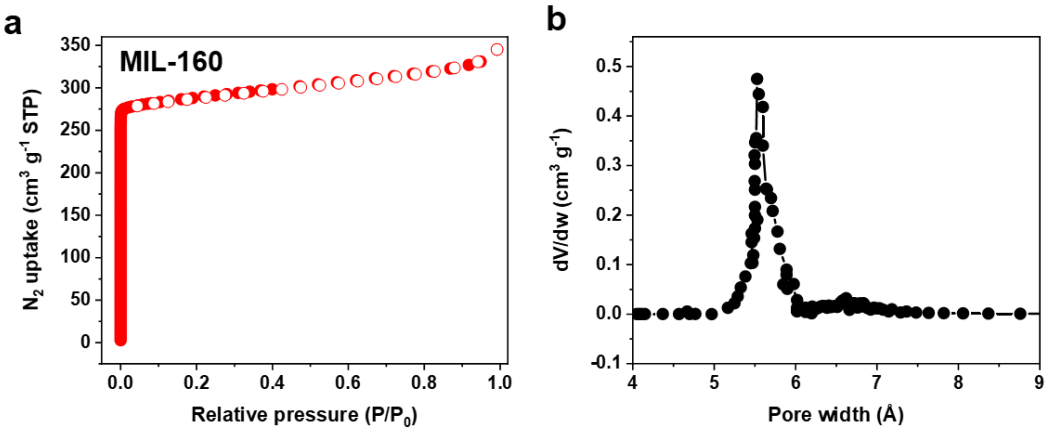

Supplementary Figure 3.3. (a) N_2 adsorption and desorption isotherms at 77 K (solid symbols: adsorption; hollow symbols: desorption) and (b) micropore size distribution for MIL-160.

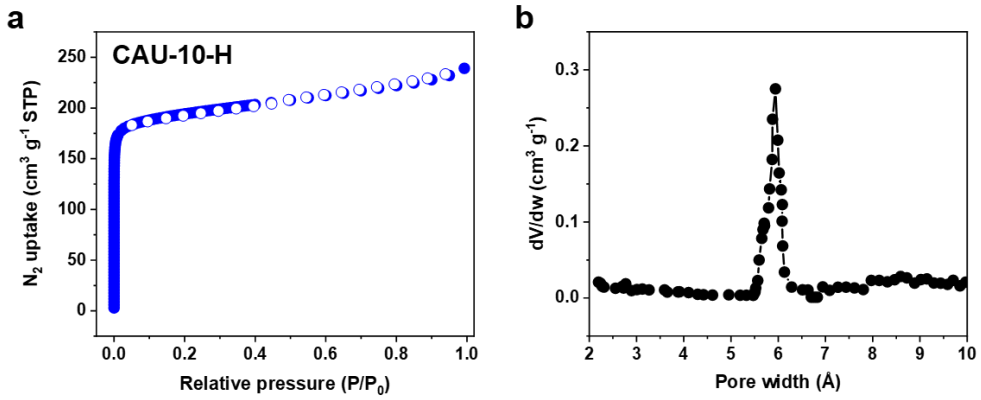

Supplementary Figure 3.4. (a) N_2 adsorption and desorption isotherms at 77 K (solid symbols: adsorption; hollow symbols: desorption) and (b) micropore size distribution for CAU-10-H.

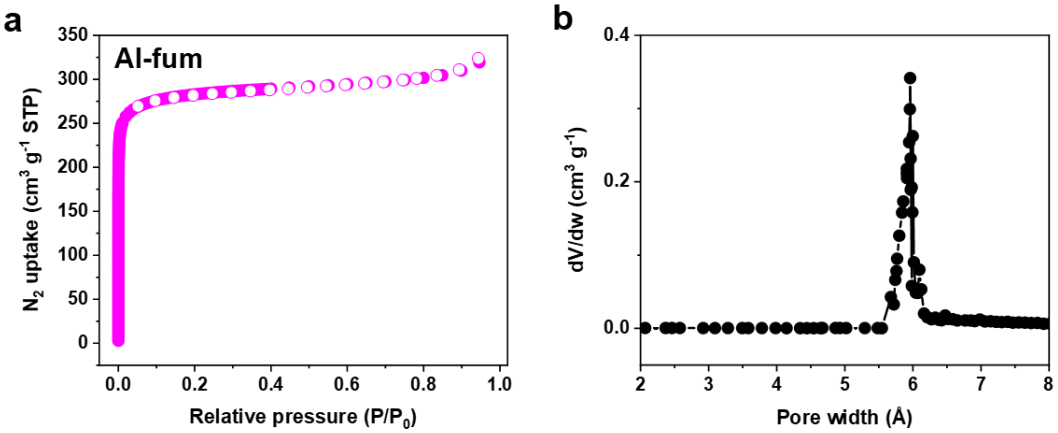

Supplementary Figure 3.5. (a) N_2 adsorption and desorption isotherms at 77 K (solid symbols: adsorption; hollow symbols: desorption) and (b) micropore size distribution for Al-fum.

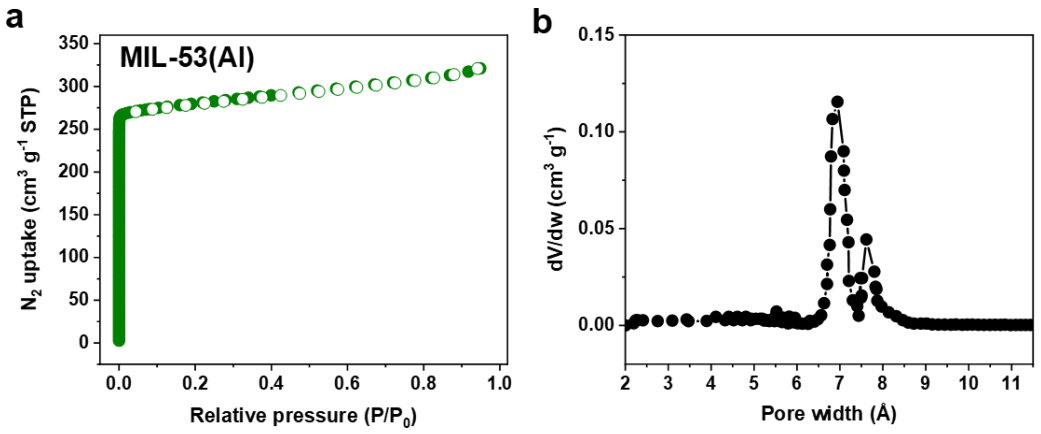

Supplementary Figure 3.6. (a) N_2 adsorption and desorption isotherms at 77 K (solid symbols: adsorption; hollow symbols: desorption) and (b) micropore size distribution for MIL-53(Al).

5. Analysis and Derivation of the Isosteric Heats of Adsorption

The isosteric enthalpies (ΔH_n) and entropies of adsorption (ΔS_n) were calculated as a function of NH_3 (n) from the isotherms that were measured over a range of temperatures (273–308 K) using the Clausius−Clapyeron equation (1).

$$\ln(P)_n = \frac{\Delta H_n}{RT} - \frac{\Delta S_n}{R} \qquad (1)$$

where p is pressure in Pa, T is the temperature, and R is the ideal gas constant. A graph of ln(p) versus 1/T at constant loading allows the differential enthalpy and entropy of adsorption and the isosteric enthalpy of adsorption (Q_{st}, n) to be determined.

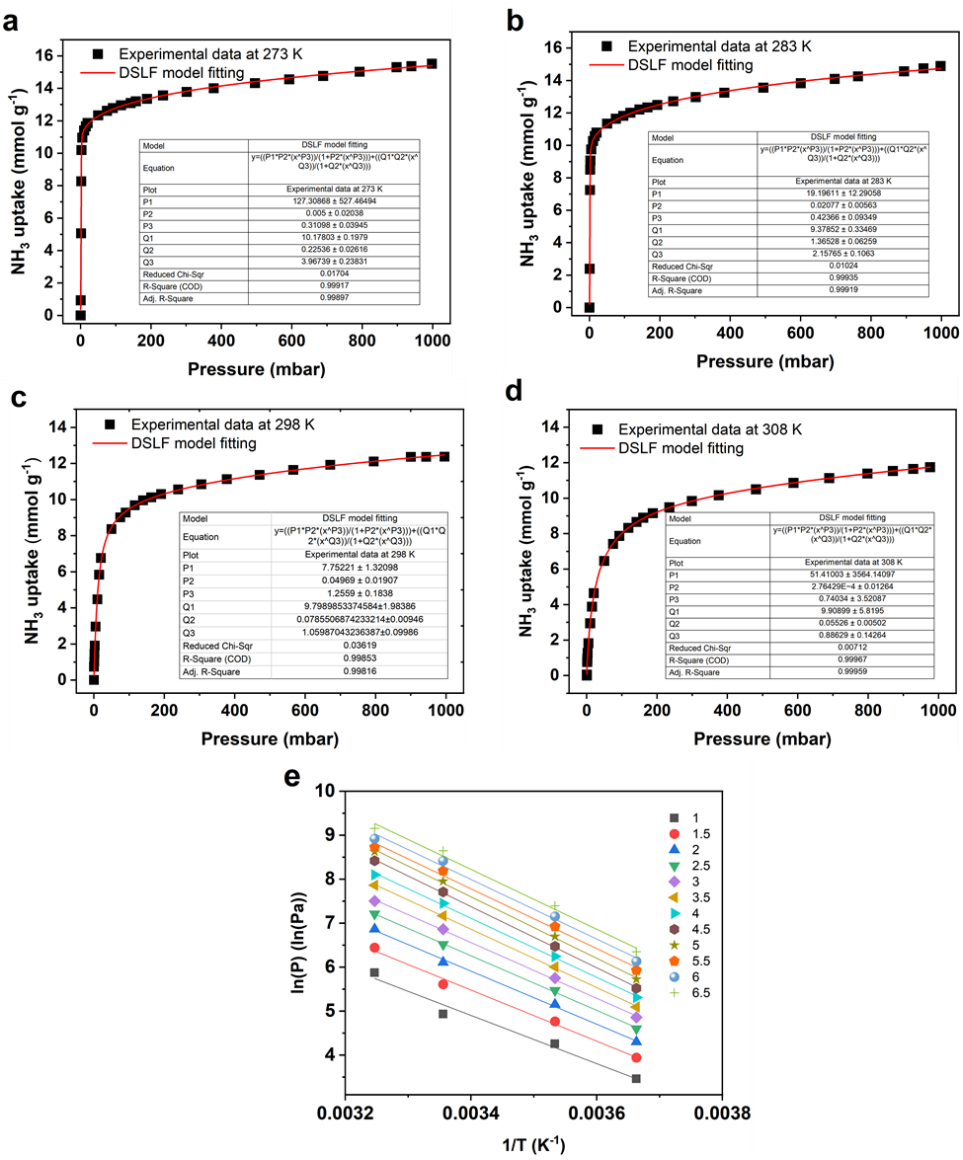

Supplementary Figure 3.7. (a-d) Fitting of isotherm by Dual-Site Langmuir Freundlich (DSLF) model for NH_3-loaded MIL-160 at 273, 283, 298 and 308 K up to 1.0 bar. (e) van't Hoff linear fittings.

6. Ammonia temperature-programmed desorption

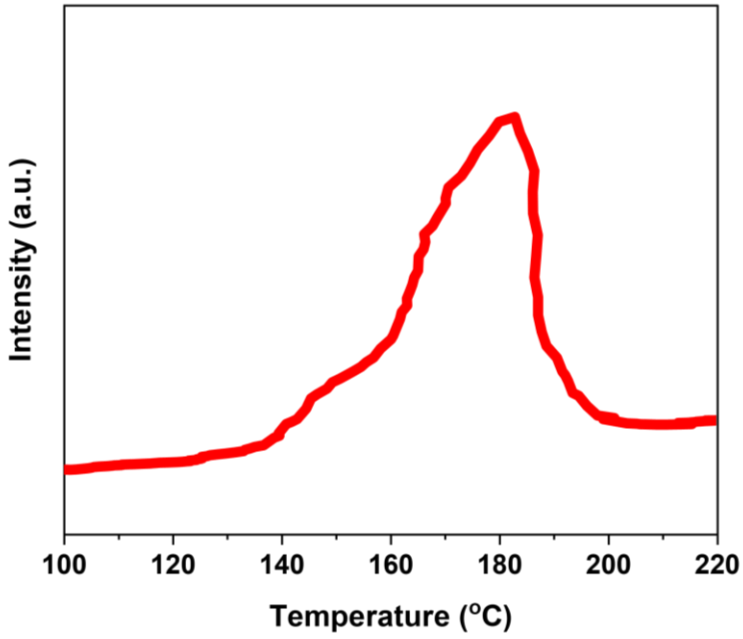

Supplementary Figure 3.8. NH_3-temperature programmed desorption (TPD) curve for MIL-160.

7. Stability Test

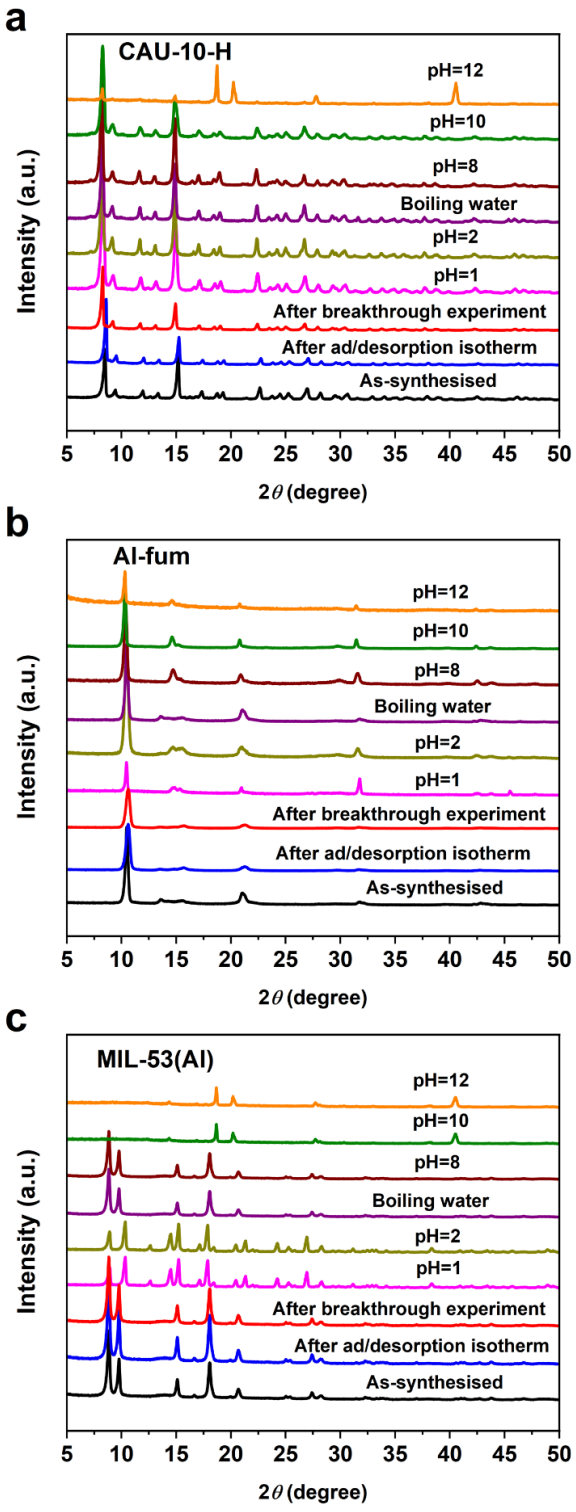

Supplementary Figure 3.9. PXRD patterns of (a) CAU-10-H, (b) Al-fum and (c) MIL-53 (Al) for as-synthesised samples and samples after NH_3 isotherms and dynamic breakthrough experiments and samples after soaked in solutions with pH=1, 2, 8, 10, 12 and in boiling water for 12 h.

8. Kinetic analysis

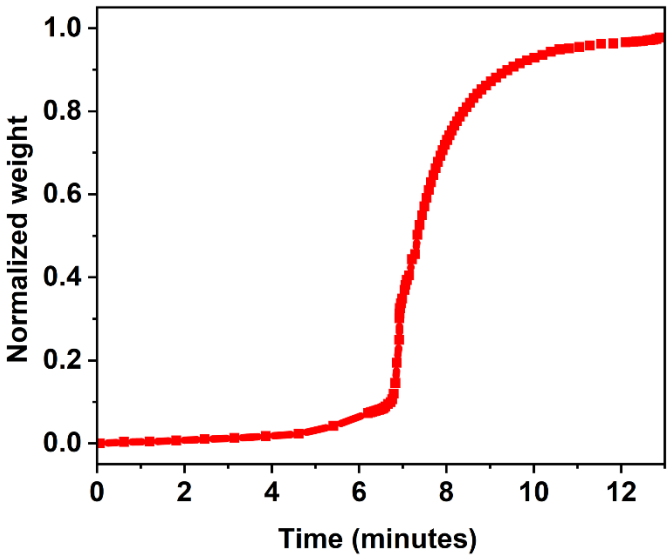

Supplementary Figure 3.10. Adsorption kinetics of NH_3 in MIL-160 from 1.9 to 3.0 mbar at 298 K.

9. Neutron Powder Diffraction

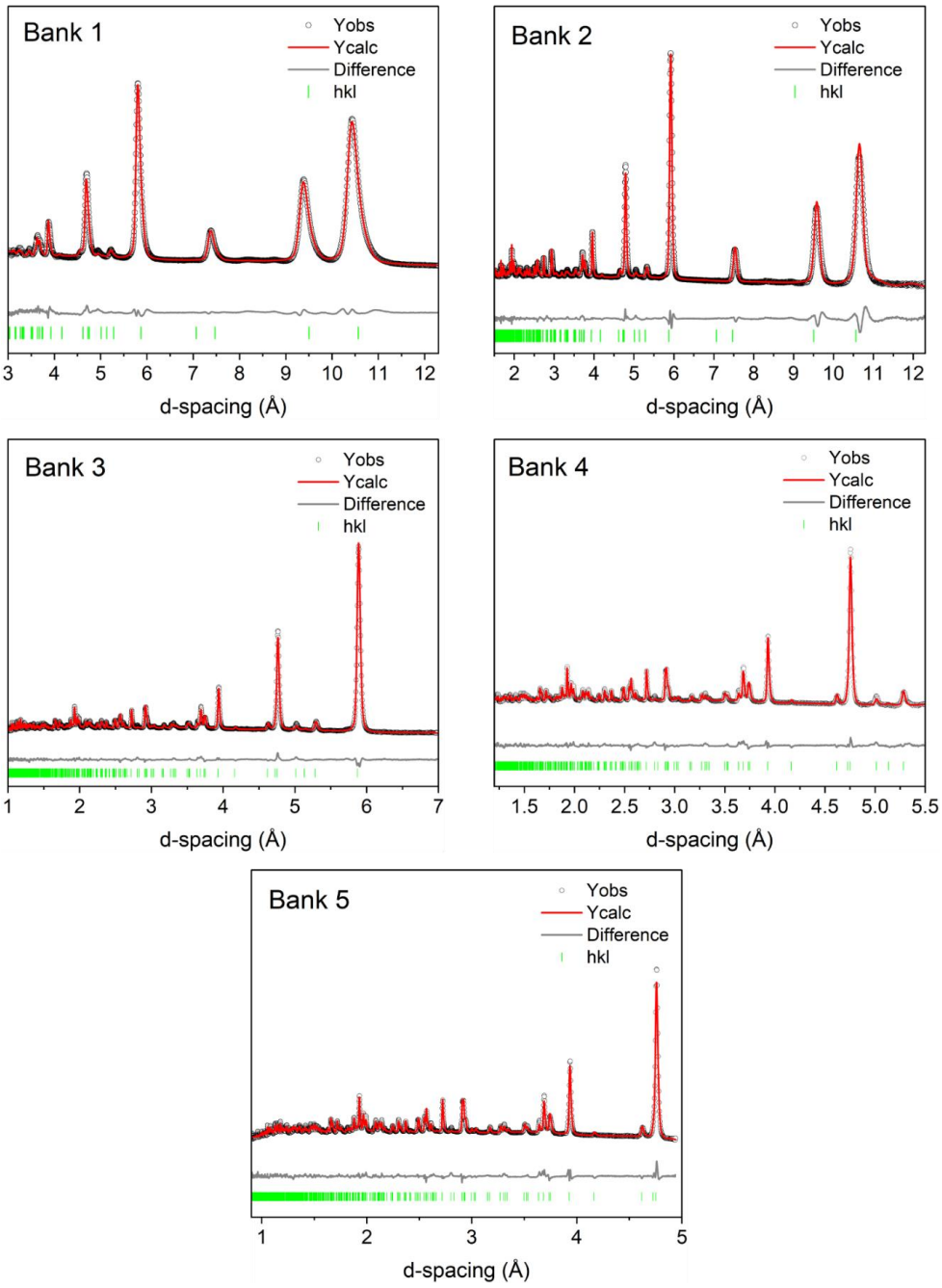

Supplementary Figure 3.11. Rietveld refinement patterns of the NPD data of bare MIL-160 from bank 1 to 5.

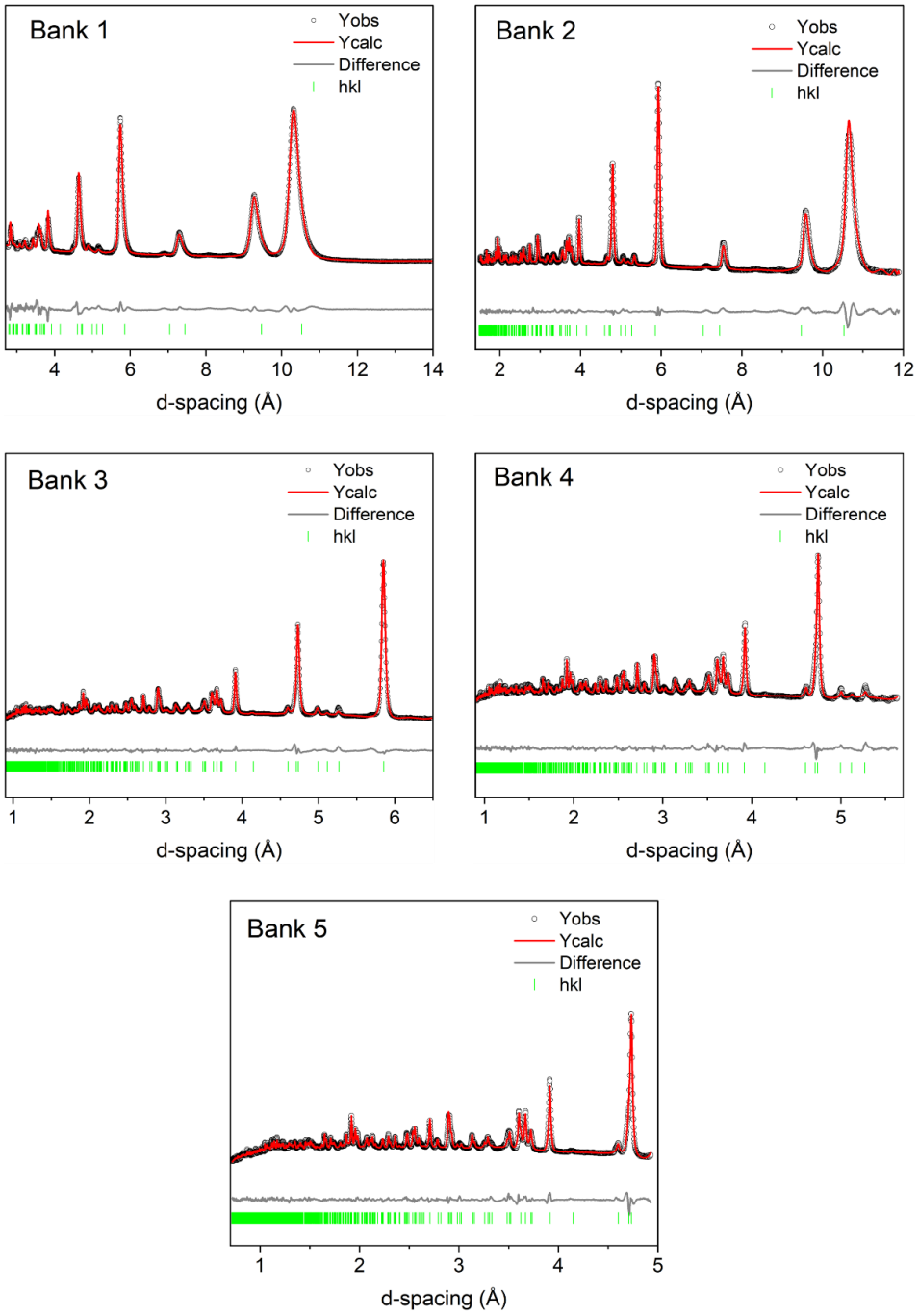

Supplementary Figure 3.12. Rietveld refinement patterns of the NPD data of MIL-160·$(ND_3)_{0.4}$ from bank 1 to 5. Due to excessively dosed ND_3 and rapid cooling, trace amount of solid ammonia with cubic structure[2] was identified through Pawley refinement and related peaks were treated as anomalous background in the Rietveld refinement.

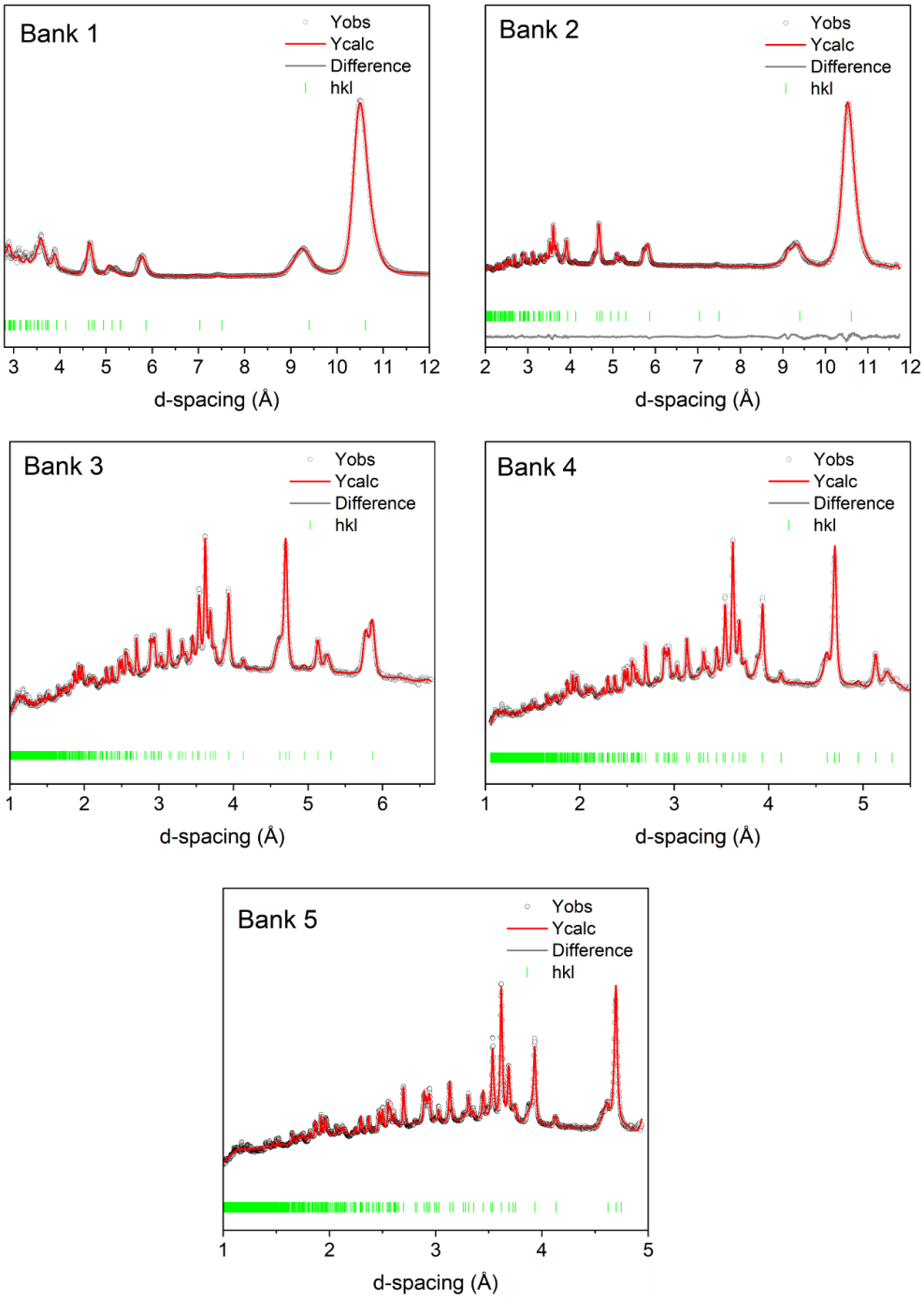

Supplementary Figure 3.13. Neutron powder diffraction and Rietveld fit profiles of MIL-160· $(ND_3)_{1.5}$ from bank 1 to 5. Due to excessively dosed ND_3 and presence of trace moisture in the pipeline, a series of ammonia monohydrate[3-6] was identified via Pawley refinement and related peaks were treated as anomalous background in Rietveld refinement.

10. Solid-state Nuclear Magnetic Resonance Spectroscopy

Solid-state NMR spectra were recorded using a Bruker 9.4 T (400 MHz ^{1}H Larmor frequency) AVANCE III spectrometer equipped with a 4 mm HFX MAS probe. Experiments were acquired at ambient temperature using a MAS frequency of 12 kHz and the number of scans varied from 16 (for ^{1}H NMR) through 128 (for ^{27}Al NMR) to 2048 (for {^{1}H-}^{13}C cross-polarisation (CP)). **^{1}**H pulses of 100 kHz were used for all experiments and for SPINAL-64 heteronuclear decoupling[19] during ^{13}C and ^{27}Al acquisition.

For the ^{27}Al direct excitation experiments a hard ($\nu_{rf} \approx 70$ kHz) ^{27}Al 0.5 μs pulse was used. For the {^{1}H-}^{13}C CPMAS experiments, 2 ms CP mixing time was employed using a ramped (70-100%) transfer pulse on the ^{1}H channel with 73 kHz maximum amplitude to match a square ^{13}C spin-lock pulse of 50 kHz.

Samples were packed into 4.0 mm o.d. zirconia rotors, treated, and then sealed with a Kel-F rotor cap. The treatments included activation (10 hours at 150 ºC under dynamic vacuum) [MIL-160], as-prepared partial loading with NH_3 (30 mins) [NH_3-MIL-160-*ap*], equilibration with NH_3 (after 1 week in ambient storage) [NH_3-MIL-160-*aw*], desorption at 150 ºC (10 hours under dynamic vacuum) [NH_3-MIL-160_{150}], desorption at 250 ºC (10 hours under dynamic vacuum) [NH_3-MIL-160_{250}], and activated pristine MIL-160 heated to 250 ºC (10 hours under dynamic vacuum) [MIL-160_{250}].

Spectral simulations were performed in the solid lineshape analysis (SOLA) module v2.2.4 in Bruker TopSpin v4.0.9 and using Dmfit[20] for a Gaussian Isotropic Model to represent the distribution in isotropic chemical shift and quadrupolar parameters. The ^{1}H and ^{13}C NMR chemical shifts were referenced to neat TMS externally, and the ^{27}Al chemical shifts were referenced externally to 1.1 mol/kg $Al(NO_3)_3$ in D_2O.

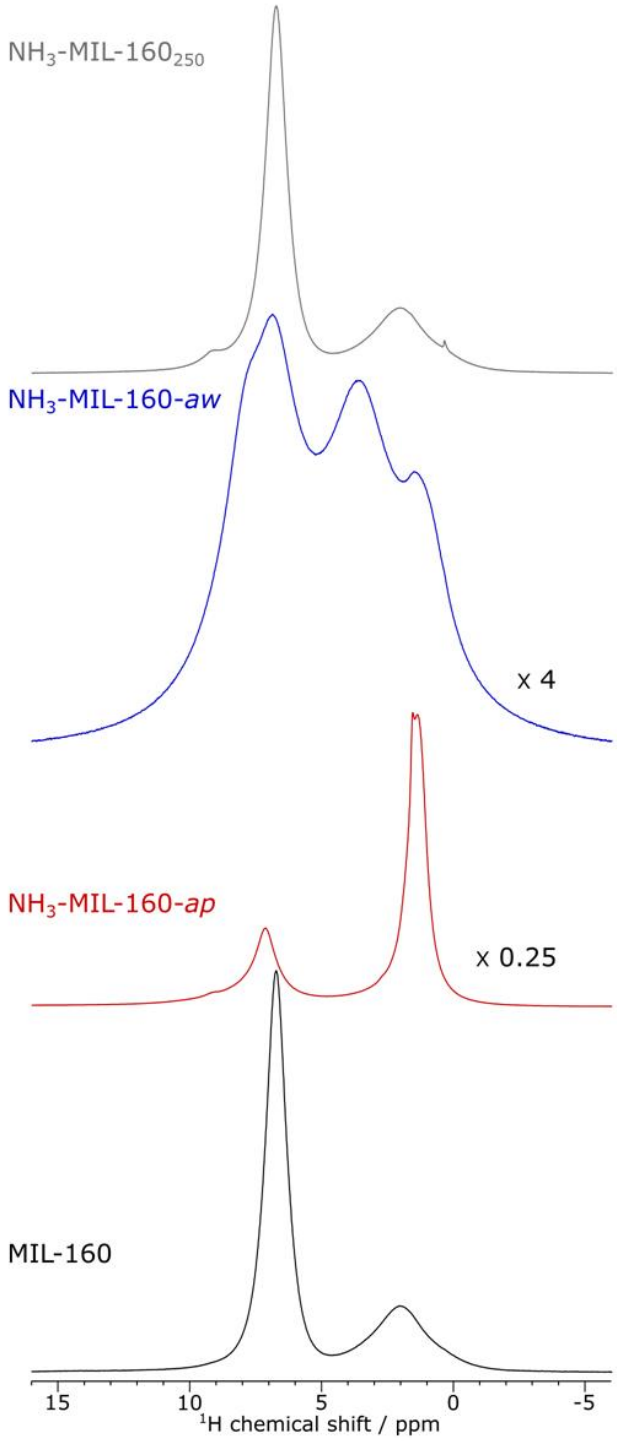

Supplementary Figure 3.14. ^{1}H Hahn-echo MAS NMR spectra of the MIL-160 samples. 1 rotor period was used as the delay either side of the π-pulse for the Hahn-echo. NH_3-MIL-160-*ap* is the MIL-160 sample as-prepared after NH_3 dosing, NH_3-MIL-160-*aw* is this dosed sample after one week of ambient storage, and NH_3-MIL-160_{250} is this latter sample after heating to 250 °C.

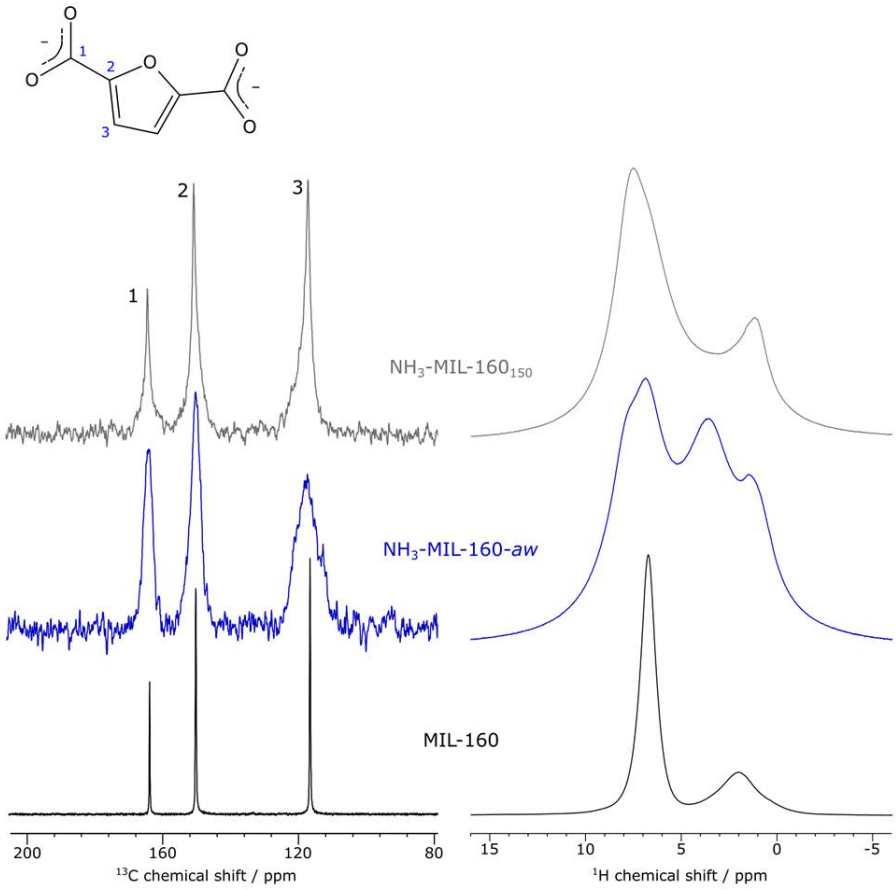

Supplementary Figure 3.15. {^{1}H-}^{13}C CPMAS (left) and ^{1}H Hahn-echo MAS (right) NMR spectra of select MIL-160 samples. 1 rotor period was used as the delay either side of the π-pulse for the Hahn-echo. The ^{1}H Hahn-echo MAS NMR spectra of MIL-160 and NH_3-MIL-160-*aw* are reproduced from Supplementary Figure 14 for comparison. After loading with NH_3, subsequent desorption at 150 ºC does not fully regenerate the MOF structure.

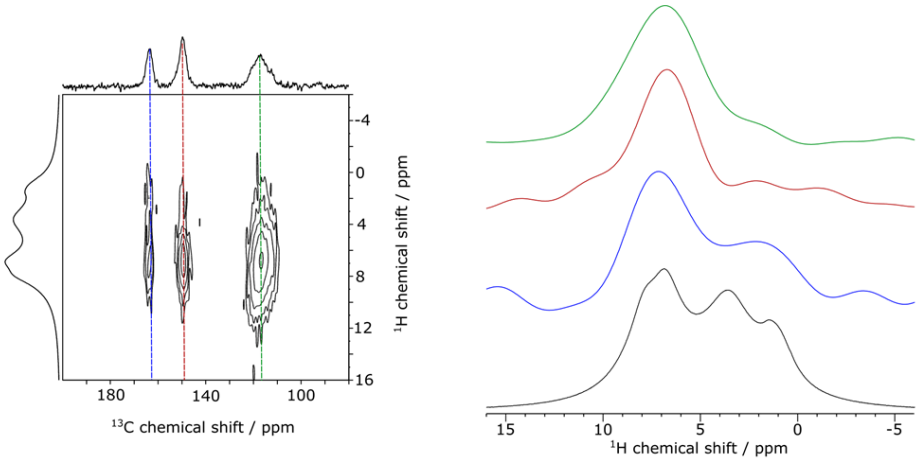

Supplementary Figure 3.16. ^{1}H-^{13}C heteronuclear dipolar correlation spectrum (left) of NH_3-MIL-160-*aw* and corresponding cross-sectional slices (right) taken at the positions indicated by the coloured dashed lines. The ^{1}H Hahn-echo MAS NMR spectrum for this sample is also reproduced (right, black) for comparison.

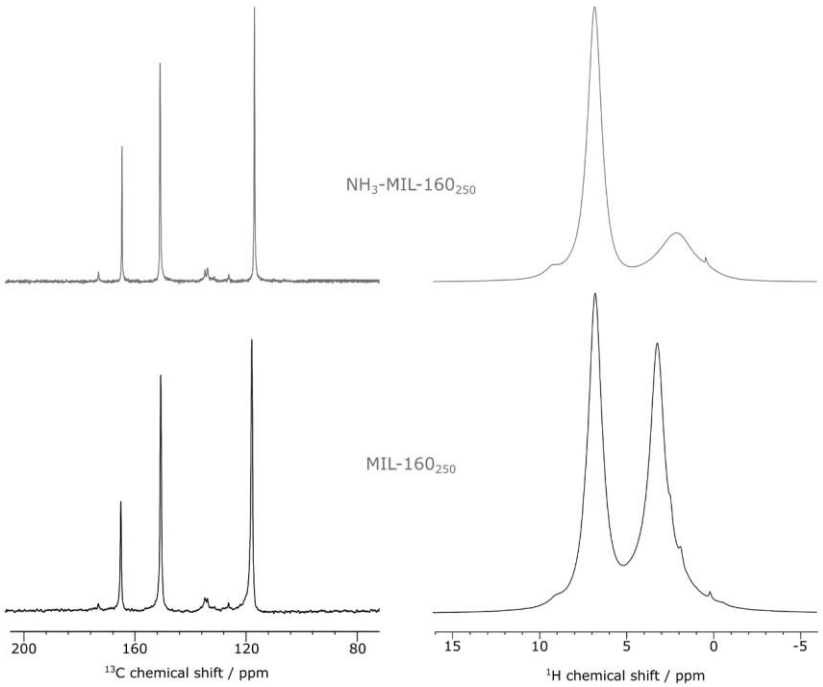

Supplementary Figure 3.17. Comparison of {^{1}H-}^{13}C CPMAS (left) and ^{1}H Hahn-echo MAS (right) NMR spectra of NH_3 loaded and desorbed (250 ºC) MIL-160 (top) and activated pristine MIL-160 that has undergone heating at 250 ºC (bottom). 1 rotor period was used as the delay either side of the π-pulse for the Hahn-echo.

11. Supplementary Tables

Table 3.1. Summary of the pore volume, NH_3 isothermal adsorption capacities and NH_3 packing density in stable MOF materials.

MOF	Measuring condition	Pore volume ($cm^3\ g^{-1}$)	NH_3 isothermal uptake ($mmol\ g^{-1}$)	NH_3 packing density/g cm^{-3}	Reference
MIL-160	**298 K 1.0 bar**	**0.45[a]**	**12.8**	**0.48**	**This work**
	273 K 1.0 bar		**15.5**	**0.59**	
CAU-10-H	**298 K 1.0 bar**	**0.32[a]**	**10.0**	**0.53**	**This work**
Al-fum	**298 K 1.0 bar**	**0.44[a]**	**8.9**	**0.34**	**This work**
MIL-53(Al)	**298 K 1.0 bar**	**0.31[a]**	**3.0**	**0.16**	**This work**
MOF-303	298 K 1.0 bar	0.55[a]	19.7	0.61 (293 K)	10
MFM-303(Al)	293 K 1.0 bar	0.191[b]	9.0	0.80	3
UiO-66-X (M=defect, Cu^{I}, Cu^{II})	273 K 1.0 bar	0.388[b]	11.8, 12.6, 16.9	0.52, 0.55, 0.74	2
MFM-300(M) (M=V^{III}, V^{IV}, Fe)	273 K 1.0 bar	0.49, 0.48, 0.46[a]	16.1, 17.3, 15.6	0.54, 0.61, 0.60	5
MFM-300(Sc)	298 K 1.0 bar	0.48[a]	13.1	0.46	6
MFM-300(Al)	273 K 1.0 bar	0.37[c]	15.7	0.72	8
Ni_acryl_TMA	298 K 1.0 bar	0.57[a]	23.5	0.70	11
Ni_acryl_TGA	298 K 1.0 bar	0.56[a]	17.4	0.53	11
M_2Cl_2BTDD (M=Mn, Co, Ni)	298 K 1.0 bar	n/a	15.5, 12.0, 12.0	n/a	7
M_2(dobpdc) (M=Mn, Co, Ni, Mg)	298 K 1.0 bar	1.18, 1.06, 1.11, 1.60[a]	13.3, 13.3, 20.8, 23.9	0.19, 0.21, 0.32, 0.25	4
$M_2(adc)_2$(dabco) (M=Zn, Co, Ni)	295 K 1.0 bar	0.25[a]	8.3, 11.2, 12.1	0.56, 0.76, 0.82	9
NU-1401	298 K 1.0 bar	0.23[a]	8.4	0.62	12
Al-PMOF	298 K 1.0 bar	n/a	7.7	n/a	13

[a]: pore volume determined from N_2 isotherms at 77 K.

[b]: pore volume from crystal structure.

[c]: pore volume determined from CO_2 isotherms at 273 K.

Supplementary Table 3.2. Crystal Data and details of the Structure Determination for ND_3 loaded MIL-160.

	MIL-160	MIL-160·$(ND_3)_{0.4}$	MIL-160·$(ND_3)_{1.5}$
Formula	[Al(OH)fdc], $C_6H_3AlO_6$	[Al(OH)fdc]·$(ND_3)_{0.4}$, $C_6H_3D_{1.2}AlO_6N_{0.4}$	$[Al(OH)_{0.176}(OD)_{0.824}$ fdc] ·$(ND_3)_{1.228}$·$(NH_3)_{0.274}$, $C_6H_3D_{4.5}AlO_6N_{1.5}$
Formula weight	198.1	206.1	223.5
Crystal system	Tetragonal	Tetragonal	Tetragonal
Space Group	*I*4$_1$/*amd* (141)	*I*4$_1$/*amd* (141)	*I*4$_1$/*amd* (141)
a, b (Å)	21.1298(1)	21.0660(12)	21.224(2)
c (Å)	10.6406(5)	10.6056(6)	10.4837(11)
Volume(Å^3)	4750.7(5)	4706.5(6)	4722.3(12)
ρ (calc) g/cm^3	1.10770	1.166	1.283
Radiation type	Neutron	Neutron	Neutron
Scan method	Time of flight	Time of flight	Time of flight
R_{exp} (%)	0.323	0.321	0.281
R_{wp} (%)	1.854	1.710	0.957
R_p (%)	1.514	1.498	0.821
GoF (χ^2)	5.739	5.329	3.401
CCDC	2219217	2219215	2219216

Supplementary Table 3.3. Host–guest interactions in MIL-160·$(ND_3)_{0.4}$.

MIL-160·0.5(ND_3)	Interactions	Distances (Å)	Colour
Site I	H (HO−Al)···N (site I)	2.36(2)	Blue
	D (site I)···C=C	2.99(4)	Red
	N (site I)···H−C	2.11(2)	Aqua
	D (site I)···O_{ligand}	2.20(1)	Dark yellow
	N (site I)···N (site II)	2.82(3)	Violet
Site II	D (site II)···O_{ligand}	3.17(2)	Rose
	N(site II)···N (site I)	2.82(3)	Violet

Supplementary Table 3.4. Host–guest interactions in MIL-160·$(ND_3)_{1.5}$.

MIL-160·0.5(ND_3)	Interactions	Distances (Å)	Colour
Site I	H (HO−Al)···N (site I)	2.31(2)	Blue
	D (site I)···O_{ligand}	2.32(4)	Dark yellow
	N (site I)···H−C	2.53(2)	Turquiose
	D (site I)···C=C	3.60(4)	Red
	N (site I)···N (site II)	4.11(2)	Lime
	N (site I)···N (site III)	3.79(4)	Violet
Site II	D (site II)···O_{ligand}	2.94(2)	Rose
	N (site II)···N (site I)	4.11(2)	Lime
Site III	N (site III)··· N (site I)	3.79(4)	Violet

Supplementary Table 3.5. Atomic positions for atoms in MIL-160·$(ND_3)_{0.4}$.

	x	y	z	Occupancy	Biso / Å^2
Al	0.3197(4)	0	0	1	1.3(3)
O1	0.25749(19)	0.00749(19)	0.125	1	3.00(9)
H1	0.2266(5)	0.0234(5)	0.125	1	3.60(10)
O2	0.3824(5)	0.0068(3)	0.1217(9)	1	3.00(9)
O3	0.3375(3)	0.0656(4)	0.2790(12)	1	3.00(9)
H3	0.4341(5)	0.1047(3)	0.4570(9)	1	2.36(8)
C1	0.3868(3)	0.0435(2)	0.2199(8)	1	1.96(7)
C2	0.45080(18)	0.05676(12)	0.2713(3)	1	1.96(7)
C3	0.4653(3)	0.0854(2)	0.3825(5)	1	1.96(7)
O4	0.5	0.04076(6)	0.20924(6)	1	3.00(9)
N1	0.4658(19)	0.3648(14)	0.811(3)	0.110(4)	1.0(12)
D1	0.484(6)	0.397(3)	0.872(7)	0.110(4)	1.2(15)
D2	0.486(5)	0.322(3)	0.834(8)	0.110(4)	1.2(15)
D3	0.484(4)	0.376(5)	0.724(5)	0.110(4)	1.2(15)
N2	0.8469(9)	0.0893(8)	0.7698(18)	0.1010(19)	4.6(8)
D1	0.848(3)	0.0546(17)	0.837(4)	0.1010(19)	5.5(10)
D2	0.8186(19)	0.1242(16)	0.805(4)	0.1010(19)	5.5(10)
D3	0.8226(17)	0.070(3)	0.696(3)	0.1010(19)	5.5(10)

Supplementary Table 3.6. Atomic positions for atoms in MIL-160·$(ND_3)_{1.5}$.

	x	y	z	Occupancy	Biso / Å^2
Al	0.3216(9)	0	0	1	4.3(6)
O1	0.2676(5)	0.0176(5)	0.125	1	6.6(2)
H1	0.2334(7)	0.0166(7)	0.125	0.176(14)	8.0(3)
D1	0.2334(7)	0.0166(7)	0.125	0.824(14)	8.0(3)
O2	0.3821(9)	0.0086(6)	0.1287(17)	1	6.6(2)
O3	0.3385(6)	0.0700(8)	0.273(2)	1	6.6(2)
H3	0.4354(9)	0.1200(6)	0.4494(17)	1	6.37(19)
C1	0.3863(5)	0.0472(5)	0.2192(15)	1	5.31(16)
C2	0.4495(3)	0.0630(2)	0.2693(6)	1	5.31(16)
C3	0.4669(6)	0.0968(4)	0.3762(10)	1	5.31(16)
O4	0.5	0.04322(10)	0.20678(10)	1	6.6(2)
N1	0.5	0.322(2)	0.675(5)	0.188(8)	1.3(18)
D1	0.502(9)	0.307(7)	0.767(7)	0.094(4)	2(2)
D2	0.493(7)	0.369(3)	0.680(15)	0.094(4)	2(2)
D3	0.460(3)	0.303(7)	0.639(15)	0.094(4)	2(2)
N2	0.509(3)	0.3861(6)	0.0865(13)	0.179(3)	7.7(7)
D1	0.541(6)	0.417(5)	0.125(3)	0.179(3)	9.3(8)
D2	0.489(4)	0.363(2)	0.162(2)	0.179(3)	9.3(8)
D3	0.474(4)	0.413(5)	0.049(4)	0.179(3)	9.3(8)
H1	0.1114(8)	0.421(3)	0.864(3)	0.137(2)	8.0(4)
H2	0.1848(11)	0.4267(16)	0.907(2)	0.137(2)	8.0(4)
H3	0.166(2)	0.4338(14)	0.7576(18)	0.137(2)	8.0(4)
N1	0.1559(5)	0.4088(5)	0.8383(11)	0.478(3)	6.7(4)
D1	0.1114(8)	0.421(3)	0.864(3)	0.341(4)	8.0(4)
D2	0.1848(11)	0.4267(16)	0.907(2)	0.341(4)	8.0(4)
D3	0.166(2)	0.4338(14)	0.7576(18)	0.341(4)	8.0(4)

11. Supplementary References

1. Cadiau, A.; Lee, J.; Borges, D.; Fabry, P.; Devic, T.; Wharmby, M.; Martineau, C.; Foucher, D.; Taulelle, F.; Jun, C.; Hwang, Y.; Stock, N.; Lange, M.; Kapteijn, F.; Gascon, J.; Maurin, G.; Chang, J.; Serre, C. Design of hydrophilic metal–organic framework water adsorbents for heat reallocation. *Adv. Mater.* **2015,** *27*, 4775–4780.
2. Ma, Y.; Lu, W.; Han, X.; Chen, Y.; Silva, I.; Lee, D.; Sheveleva, A.; Wang, Z.; Li, J.; Li, W.; Fan, M.; Xu, S.; Tuna, F.; McInnes, E.; Cheng, Y.; Rudic, S.; Manuel, P.; Frogley, M.; Cuesta, A.; Schröder, M.; Yang, S. Direct observation of ammonia storage in UiO-66 incorporating Cu(II) binding sites. *J. Am. Chem. Soc.* **2022,** *144*, 8624–8632.
3. Marsh, C.; Han, X.; Li, J.; Lu, Z.; Argent, S.; Silva, I.; Cheng, Y.; Daemen, L.; Ramirez-Cuesta, A.; Thompson, S.; Blake, A.; Yang, S.; Schröder, M. Exceptional packing density of ammonia in a dual-functionalized metal–organic framework. *J. Am. Chem. Soc.* **2021,** *143*, 6586−6592.
4. Kim, D.; Kang, D.; Kang, M.; Lee, J.; Choe, J.; Chae, Y.; Choi, D.; Yun, H.; Hong, C. High ammonia uptake of a metal–organic framework adsorbent in a wide pressure range. *Angew. Chem. Int. Ed.* **2020,** *59*, 22531−22536.
5. Han, X.; Lu, W.; Chen, Y.; Silva, I.; Li, J.; Lin, L.; Li, W.; Sheveleva, A.; Godfrey, H.; Lu, Z.; Tuna, F.; McInnes, E.; Cheng, Y.; Daemen, L.; McPherson, L.; Teat, S.; Frogley, M.; Rudic, S.; Manuel, P.; Ramirez-Cuesta, A.; Yang, S.; Schröder, M. High ammonia adsorption in MFM-300 materials: dynamics and charge transfer in host–guest binding. *J. Am. Chem. Soc.* **2021,** *143*, 3153−3161.
6. Guo, L.; Han, X.; Ma, Y.; Li, J.; Lu, W.; Li, W.; Lee, D.; Silva, I.; Cheng, Y.; Rudic, S.; Manuel, P.; Frogley, M.; Cuesta, A.; Schröder, M.; Yang, S. High capacity ammonia adsorption in a robust metal–organic framework mediated by reversible host–guest interactions. *Chem. Commun.*, **2022,** *58*, 5753−5756.
7. Rieth, A.; Tulchinsky, Y.; Dincă, M. High and reversible ammonia uptake in mesoporous azolate metal–organic frameworks with open Mn, Co, and Ni sites. *J. Am. Chem. Soc*. **2016,** *138*, 9401–9404.
8. Godfrey, H.; Silva, I.; Briggs, L.; Carter, J.; Morris, C.; Savage, M.; Easun, T.; Manuel, P.; Murray, C.; Tang, C.; Frogley, M.; Cinque, G.; Yang, S.; Schröder, M. Ammonia storage by reversible host−guest site exchange in a robust metal–organic framework. *Angew. Chem. Int. Ed.* **2018,** *130*, 14994−14997.
9. Cao, Z.; Landström, K.; Akhtar, F. Rapid ammonia carriers for CR systems using MOFs $[M_2(adc)_2(dabco)]$ (M=Co, Ni, Cu, Zn). *Catalysts.* **2020,** *10*, 1444–1454.
10. Wang, Z.; Li, Z.; Zhang, X.; Xia, Q.; Wang, H.; Wang, C.; Wang, Y.; He, H.; Zhao, Y.; Wang, J. Tailoring multiple sites of metal–organic frameworks for highly efficient and reversible ammonia adsorption. *ACS Appl. Mater. Interfaces* **2021,** *13*, 56025−56034.
11. Kim, D.; Kang, D.; Kang, M.; Choi, D.; Yun, H.; Kim, S.; Lee, S.; Lee, J.; Hong, C. High gravimetric and volumetric ammonia capacities in robust metal–organic frameworks prepared via double postsynthetic modification. *J. Am. Chem. Soc.* **2022,** *144*, 9672−9683.
12. Zhang, Y.; Zhang, X.; Chen, Z.; Otake, K.; Peterson, G.; Chen, Y.; Wang, X.; Redfern, L.; Goswami, S.; Li, P.; Islamoglu, T.; Wang, B.; Farha, O. A flexible interpenetrated zirconium-based metal-organic framework with high affinity toward ammonia. *ChemSusChem* **2020,** *13*, 1710–1714.

13. Moribe, S.; Chen, Z.; Alayoglu, S.; Syed, Z.; Islamoglu, T.; Farha, O. Ammonia capture within isoreticular metal−organic Frameworks with rod secondary building units. *ACS Mater. Lett.* **2019,** *1*, 476–480.
14. Olovsson, I.; Templeton, D. X-ray study of solid ammonia. *Acta Cryst.* **1959,** *12*, 832–836.
15. Olovsson, I.; Templeton, D. The crystal structure of ammonia monohydrate. *Acta Cryst.* **1959,** *12*, 827–832.
16. Fortes, A.; Suard, E.; Cailleau, M.; Pickard, C.; Needs, R. Crystal structure of ammonia monohydrate phase II. *J. Am. Chem. Soc.* **2009,** *131*, 13508–13515.
17. Wilson, C.; Bull, C.; Stinton, G.; Loveday, J. Pressure-induced dehydration and the structure of ammonia hemihydrate-II. *J. Chem. Phys.* **2012,** *136*, 094506.
18. Loveday, J.; Nelmes, R.; Marshall, W.; Besson, J.; Klotz, S.; Hamel, G. Structure of deuterated ammonia IV. *Phys. Rev. Lett.* **1996,** *76*, 74.
19. Fung, B.; Khitrin, A.; Ermolaev, K. An improved broadband decoupling sequence for liquid crystals and solids. *J. Magn. Reson.* **2000,** *142*, 97–101.
20. Massiot, D.; Fayon, F.; Capron, M.; King, I.; Calv´e, S.; Alonso, B.; Durand, J.; Bujoli, B.; Gan, Z.; Hoatson, G. Modelling one- and two-dimensional solid-state NMR spectra. *Magn. Reson. Chem.* **2002,** *40*, 70–76.

Appendix III: Supporting information for Chapter 4

Supporting Information

1. Experimental Section

Synthesis of MFM-300(Sc)

MFM-300(Sc) was synthesised by a solvothermal method according to the literature.[1] Scandium triflate (900 mg, 1.83 mmol) and biphenyl-3,3',5,5'-tetracarboxylic acid (H_4L, 300 mg, 0.91 mmol) were mixed in dimethylformamide (DMF, 105 mL), H_2O (15 mL) and HCl (36.5 %, 3 mL). The mixture was stirred until complete dissolution occurred. The solution was then placed in a pressure tube and heated in an oil bath to 80 ^oC for 72 h. The tube was then cooled to room temperature, and the colourless crystalline product was separated by filtration, washed with DMF three times and stored in acetone. Yield: 70% (based on ligand).

Characterisations

Powder X-ray diffraction (PXRD) patterns was performed for the as-synthesised, post-isotherm and post-cycling experiments samples of MFM-300(Sc) on a Philips X'pert X-ray diffractometer (40 kV and 30 mA) using Cu-Kα radiation (λ = 1.5406 Å). The data were collected at room temperature in a 2θ range of 5-50 with a scan speed of 4° min^{-1}. TGA was conducted on a TA Instrument Q600 under N_2 flow of 50 mL min^{-1}. 10 mg sample was added into an alumina pan and heated from room temperature with a ramp rate of 5 °C min^{-1} up to 800 °C.

BET surface areas were obtained from N_2 isotherms recorded on a 3-flex instrument at 77 K. The pre-dried acetone-exchanged materials (100-150 mg) were loaded into a sample cell and subjected to a dynamic vacuum (1×10^{-7} mbar) at 443 K for 10 h. Measurements of static adsorption isotherms (0-1.0 bar) for NH_3 were undertaken on an IGA gravimetric sorption analyser (Hiden Isochema, Warrington, UK). NH_3 gravimetric sorption isotherms were recorded at 273, 283, 293, 298, 303,

and 313 K under ultra-high vacuum produced by a turbo pumping system with the temperature controlled using a programmed water bath and furnace bath. Research-grade NH_3 was purchased from BOC and used as received. In a typical gas adsorption experiment, 40 mg of acetone-exchanged MFM-300(Sc) was loaded into the IGA system and outgassed dynamic vacuum (1×10^{-8} mbar) at 453 K for 12 h. For the cycling experiments, the pressure of NH_3 was increased from vacuum (1×10^{-8} mbar) to 200 mbar and the uptake recorded. The pressure was then reduced to regenerate the sample without heating. This cycling process was repeated 90 times.

Breakthrough experiments were conducted on a Hiden Isochema IGA-003 with ABR attachments and a Hiden Analytical mass spectrometer using a fixed-bed tube packed with 410 mg of MFM-300(Sc). The sample was activated by heating under a flow of He at 423 K for 12 h. The fixed-bed was then cooled to 298 K. A breakthrough curve was collected with a flow of 1000 ppm NH_3 diluted in He. The flow rate of the entering gas was maintained at 25 mL min^{-1}, and the concentration of NH_3 in the exhaust gas was determined by mass spectrometry and compared with the inlet concentration C_0, where $C/C_0 = 1$ indicates complete breakthrough. The MFM-300(Sc) sample framework density is 1.08 g cm^{-3}, occupied a volume of 0.38 mL (assuming 100% purity and no framework collapse), leading the dead volume is determined to be 4.2 mL.

For tests of chemical stability, 20 mg of MFM-300(Sc) was placed in a small vial and immersed under solutions of various pH values (pH = 7-12) and different organic solvents. The vial was sealed and retained at room temperature for 12 h.

The structural determination of the binding positions of ND_3 in MFM-300(Sc) was conducted using WISH, a long wavelength powder and single crystal neutron diffractometer at the ISIS neutron and muon facility at Rutherford Appleton

Laboratory (UK). The instrument has a solid methane moderator providing a high flux of cold neutrons with a large bandwidth, transported to the sample via an elliptical guide. The WISH system of divergence jaws allows tuning of the resolution according to the need of the experiment; in this case, it was setup in high resolution mode. The WISH detectors are 1m long, 8mm diameter pixelated 3He tubes positioned at 2.2m from the sample and arranged on a cylindrical locus covering a 2θ scattering angle of 10-170°. To reduce the background from the sample environment, WISH was equipped with an oscillating radial collimator that defines a cylinder of radius of approximately 22 mm diameter at 90° scattering. The sample of desolvated MFM-300(Sc) was loaded into a cylindrical vanadium sample container with an indium vacuum seal connected to a gas handling system. The sample was degassed at $1x10^{-7}$ mbar and at 100 °C for 4 days with He flushing to remove any remaining trace of guest water. The sample was dosed with ND_3 using the volumetric method after being warned to room temperature to ensure that the gas is well dispersed throughout the crystalline structure of MFM-300(Sc). Data collection for desolvated MFM-300(Sc) and three subsequent loadings of ND_3 (1.0 and 1.5 ND_3 molecules per OH functionality) were performed controlled using a He cryostat (10 ± 0.2 K). In NH_3 loaded MOF frameworks, typically binding interactions including hydrogen bonding, electrostatic interactions, and intermolecular interactions can occur, contributing to the overall stability of the system. Hydrogen bonding (X–H···Y) involves the interaction between a hydrogen atom bonded to an electronegative atom (X) and a lone pair or electronegative atom (Y). The typical range for hydrogen bond distances is 1.5 to 3 Å, a longer hydron bond distance usually means the weaker hydrogen bonding. Electrostatic interactions are long-range interactions that arise from the attraction or repulsion between charges, occurring between the adsorbed gas molecules and the ligand rings. The bond distances generally involved in electrostatic interactions are typically longer than those hydrogen bonding. The intermolecular

interactions involve the physical proximity of the adsorbed gas molecules and can include Van der Waals forces, dipole-dipole interactions, or other weak intermolecular forces. The distance of this interaction is typically ranging from approximately 2 to 4 Å.

In situ synchrotron infrared micro-spectroscopy experiments were carried out at multimode infrared imaging and micro spectroscopy (MIRIAM) beamline at the Diamond Light Source, UK. The instrument is comprised of a Bruker Hyperion 3000 microscope in transmission mode, with 15x objective and condenser lenses and a small element (50 μm) liquid N_2 cooled MCT detector, coupled to a Bruker Vertex 80 V Fourier Transform IR interferometer using radiation generated from a bending magnet source. Spectra were collected (512 scans) in the range 400-4000 cm^{-1} at 4 cm^{-1} resolution and an infrared spot size at the sample of approximately 15 × 15 μm. A microcrystalline powder of MFM-300(Sc) was scattered onto a 0.5 mm thick ZnSe infrared window and placed within a Linkam FTIR 600 gas-tight sample cell equipped with 0.5 mm thick ZnSe windows, a heating stage and gas inlet and outlet. Ultrapure N_2 and anhydrous NH_3 gases were used as supplied from the cylinder. The gases were flowed through the gas delivery system prior to connection to the Linkam cell to remove air and moisture. The gases were dosed volumetrically to the sample cell using mass flow controllers, and the total flow rate being maintained at 100 mL min^{-1} for all experiments. The exhaust from the cell was directly vented to an extraction system and the total pressure in the cell was therefore 1 bar for all experiments. The sample was desolvated under a flow of dry N_2 at 100 mL min^{-1} and 443 K for 5 h, and was then cooled to 298 K under a continuous flow of N_2. Dry NH_3 was then dosed as a function of partial pressure, maintaining a total flow of 100 mL min^{-1}. The MOF sample was regenerated with a flow of dry N_2.

Magic angle spinning (MAS) NMR spectra were recorded using a Bruker 9.4 T (400 MHz 1H Larmor frequency) AVANCE III spectrometer equipped with a 4 mm HFX MAS probe. Samples were treated and packed into 4 mm o.d. zirconia rotors under inert conditions and sealed with a Kel-F rotor cap. Experiments were acquired at ambient temperature using a MAS frequency of 12 kHz. ^{1}H-pulses of 100 kHz were used for excitation and SPINAL-64[2] heteronuclear decoupling, ^{45}Sc-pulses of 0.5 μs duration (small flip angle with radio frequency field amplitude of ~70 kHz) were employed for ^{45}Sc direct excitation (DE)MAS experiments, and ^{13}C-pulses and spin-locking at 50 kHz were used for {^{1}H-}^{13}C CPMAS experiments with corresponding ramped (70-100%) ^{1}H spin-locking at ~73 kHz (100%) for 2 ms; s Hahn-echo τ_r–π–τ_r sequence of 2 rotor periods total duration was applied to ^{13}C after CP to circumvent receiver dead-time. For the ^{1}H-^{45}Sc 2D CP (HETCOR) dipolar correlation experiments, 500 μs of CP spin-locking was applied with fixed-amplitude RF irradiation of ~28 kHz for ^{1}H and ~4 kHz for ^{45}Sc. 24 complex t_1 increments were acquired with an indirect dimension dwell time of 83.33 μs, and spectral deconvolution and peak fitting were performed in the solid lineshape analysis (SOLA) module v2.2.4 in Bruker TopSpin v4.0.9. ^{1}H and ^{13}C chemical shifts are given with respect to TMS (0 ppm) and ^{45}Sc chemical shifts are referenced to a 0.06 M $Sc(NO_3)_3$ in D_2O solution.

INS spectra were collected on the TOSCA beamline at ISIS Neutron and Muon Source (UK). The sample of desolvated MFM-300(Sc) was loaded into a cylindrical vanadium sample container with an indium vacuum seal and this was connected to a gas handling system. The sample was degassed at 393 K and 10^{-7} mbar for 24 h to remove any residual trace of guest water. The temperature during data collection was controlled using a closed cycle refrigerator cryostat (10 ± 0.1 K). The loading of NH_3 was performed volumetrically at room temperature, and subsequently the temperature

was reduced to 10 K in order to minimize achievable thermal motion of the framework and adsorbed NH_3 molecules in the scattering measurements. Background spectra of MFM-300(Sc) were subtracted to obtain the difference spectra.

Modelling by Density Functional Theory (DFT) of the bare and NH_3-loaded MFM-300(Sc) was performed using the Vienna Ab initio Simulation Package (VASP).[3] The calculation used Projector Augmented Wave (PAW) method[4,5] to describe the effects of core electrons, and Perdew-Burke-Ernzerhof (PBE)[6] implementation of the Generalized Gradient Approximation (GGA) for the exchange-correlation functional. Energy cutoff was 800 eV for the plane-wave basis of the valence electrons. The lattice parameters and atomic coordinates determined by neutron powder diffraction in this work were used as the initial structure. The electronic structure was calculated on the Γ-point for the unit cell (144 atoms for the blank MOF). The total energy tolerance for electronic energy minimization was 10^{-8} eV, and for structure optimization it was 10^{-7} eV. The maximum interatomic force after relaxation was below 0.001 eV/Å, and the optB86b-vdW functional for dispersion corrections was applied.[7] The vibrational eigen-frequencies and modes were then calculated by solving the force constants and dynamical matrix using Phonopy.[8] The OClimax software was used to convert the DFT-calculated phonon results to the simulated INS spectra.[9]

2. Structure of MFM-300(Sc)

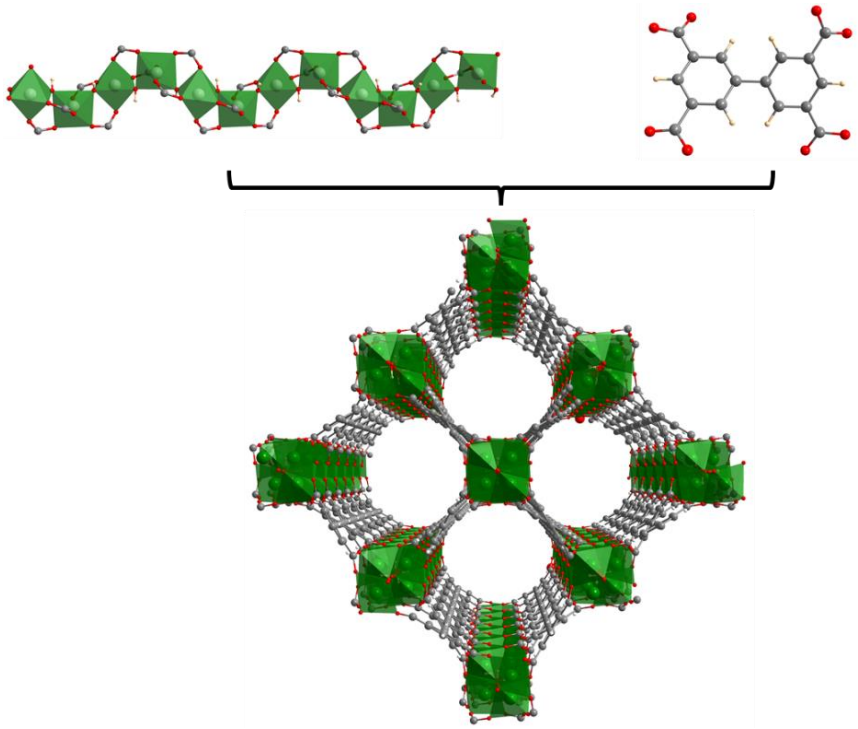

Supplementary Figure 4.1. View of the three-dimensional framework structure of MFM-300(Sc). Colour code for atoms: Sc, green; O, red; C, grey; H, tan; N, blue.

3. Characterisation of Porosity

Prior to the measurement, MFM-300(Sc) was activated under dynamic vacuum at 180 °C for 12 h. The adsorption-desorption isotherms for N_2 were carried out at 77 K. **Supplementary Figure 4.2** shows a type-I profile with a surface area of 1390 m^2 g^{-1}.

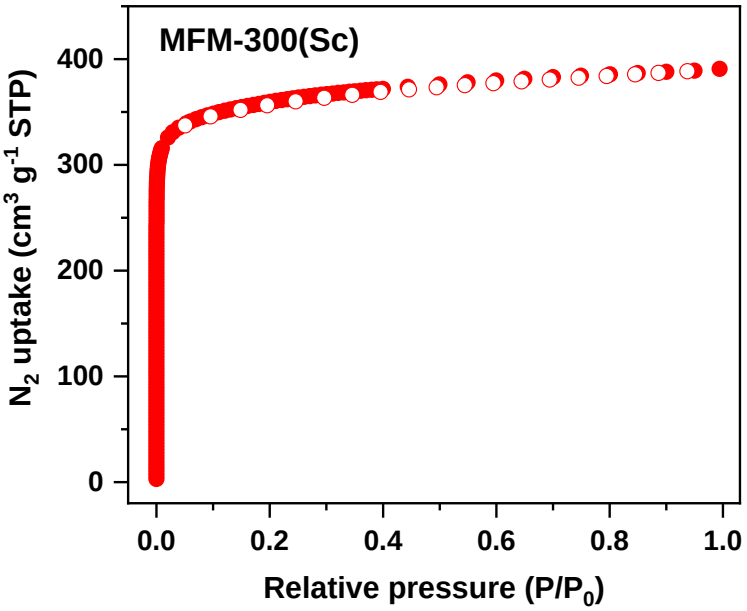

Supplementary Figure 4.2. Adsorption isotherm for N_2 in MFM-300(Sc) at 77 K (solid symbols: adsorption; hollow symbols: desorption).

4. Thermogravimetric Analysis

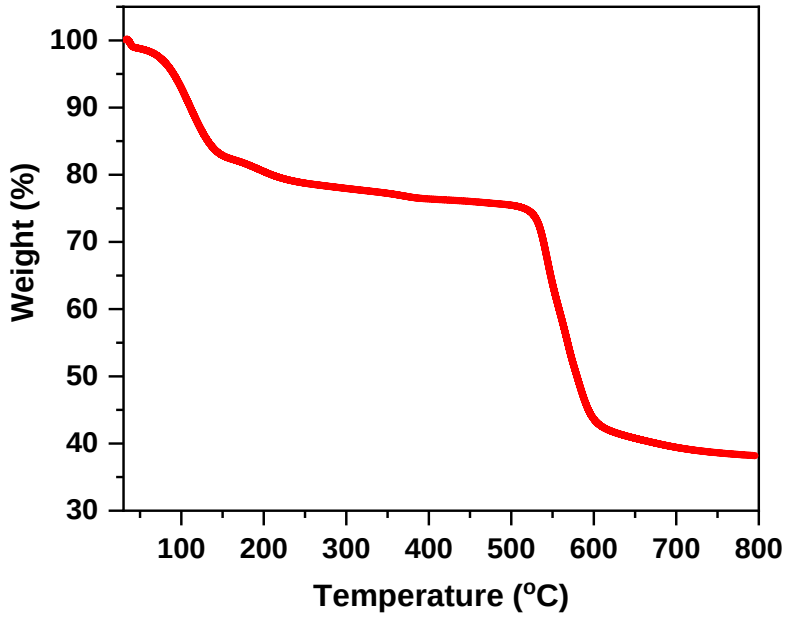

Supplementary Figure 4.3. Thermogravimetric analysis of acetone-exchanged MFM-300(Sc) under a flow of N_2 at a heating rate of 5 °C min^{-1}.

5. Stability Tests

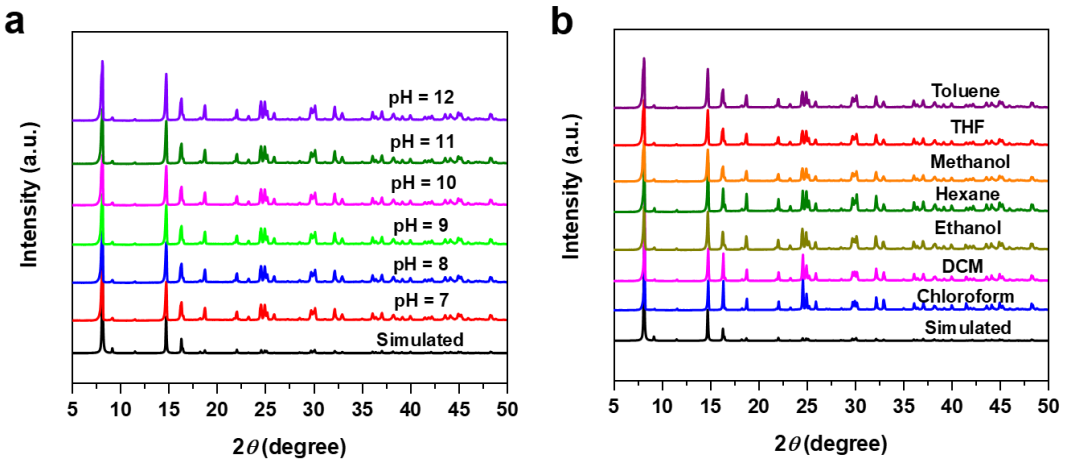

Supplementary Figure 4.4. PXRD patterns of MFM-300(Sc) after being immersed in (a) solutions at pH 7 to pH12, and (b) different organic solvents.

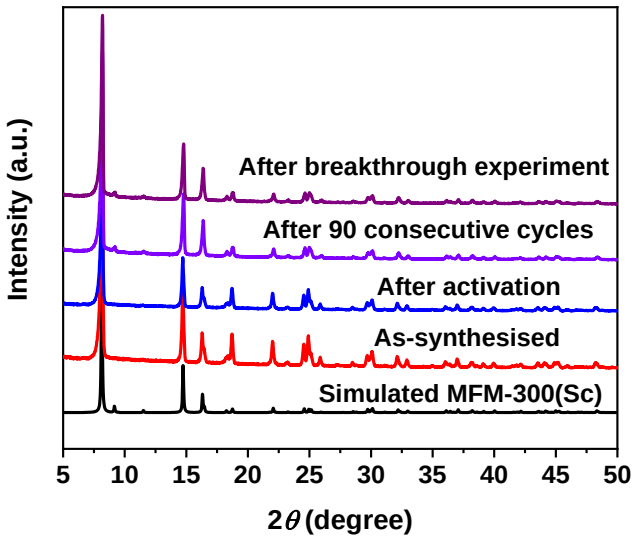

Supplementary Figure 4.5. PXRD patterns of as-synthesised MFM-300(Sc), activated sample, and samples after 90 consecutive cycles of adsorption of NH_3 and after NH_3 breakthrough experiment.

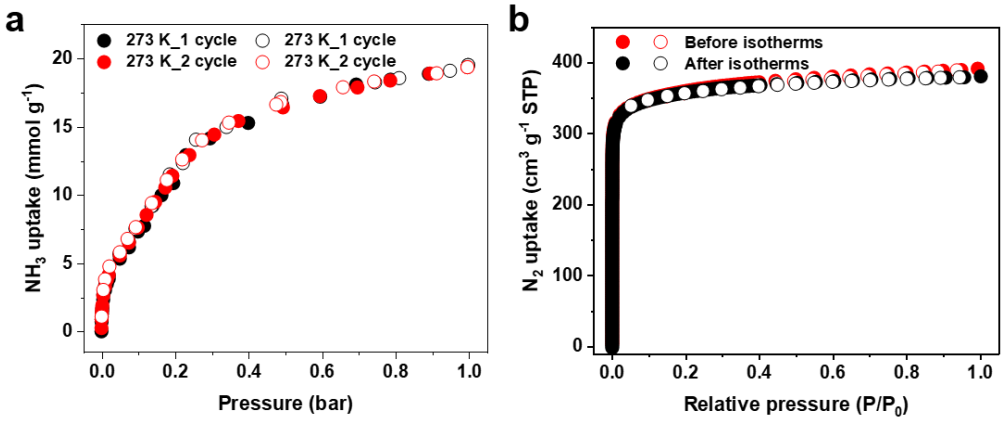

Supplementary Figure 4.6. (a) Adsorption isotherms for NH_3 in MFM-300(Sc) at 273 K, first cycle (black) and second cycle (red). (b) Adsorption isotherms for N_2 at 77 K in MFM-300(Sc) before and after two cycles NH_3 adsorption. Solid symbols: adsorption; hollow symbols: desorption.

6. Calculation of Isosteric Heats of Adsorption

To calculate the differential enthalpies (ΔH_n) and entropies of adsorption (ΔS_n) for NH_3 uptake as a function of gas adsorption (n), isotherms were measured over a range of temperatures and fitted to the van't Hoff isochore (Equation 1).

$$\ln(p)_n = \frac{\Delta H_n}{RT} - \frac{\Delta S_n}{R} \quad (1)$$

Liner fitting of the plot of ln(p) versus 1/T at constant gas loading allows the isosteric heats of adsorption (Q_{st}) and entropies of adsorption (ΔS_n) to be determined from the slope and the intercept of the line, respectively.

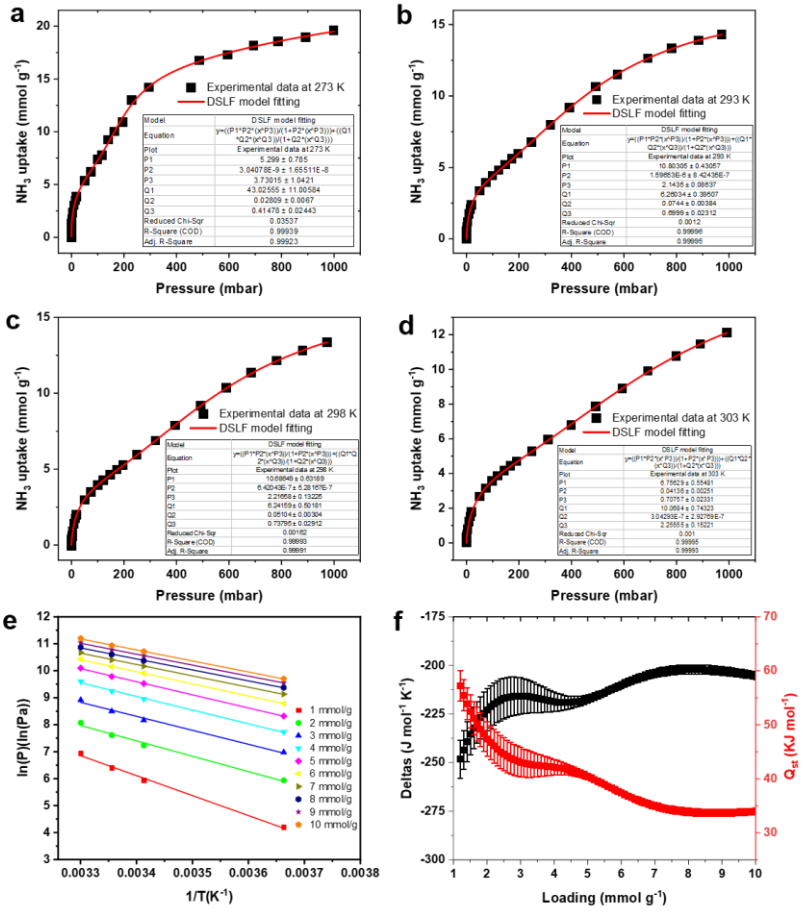

Supplementary Figure 4.7. (a-d) Fitting of isotherm by Dual-Site Langmuir Freundlich (DSLF) model for NH_3-loaded MFM-300(Sc) at different temperatures and up to 1.0 bar. (e) van't Hoff linear fittings and (f) isosteric enthalpy and entropy of adsorption for NH_3 in MFM-300(Sc) at different loadings.

7. Neutron Powder Diffraction

Rietveld refinements of the NPD patterns of the bare MOF and samples at various ND_3 loadings were performed using the TOPAS software package. In this treatment the guest molecules are treated as rigid bodies; we first refined the centres of mass, orientations, and occupancies of the adsorbate, followed by full profile Rietveld refinement, including the positions of metals and linkers together with their corresponding lattice parameters, resulting in satisfactory R-factors. The final refinements on all parameters including fractional coordinates, thermal parameters, occupancies for both host lattice and adsorbate molecule, and background/profile coefficients yielded very good agreement factors.

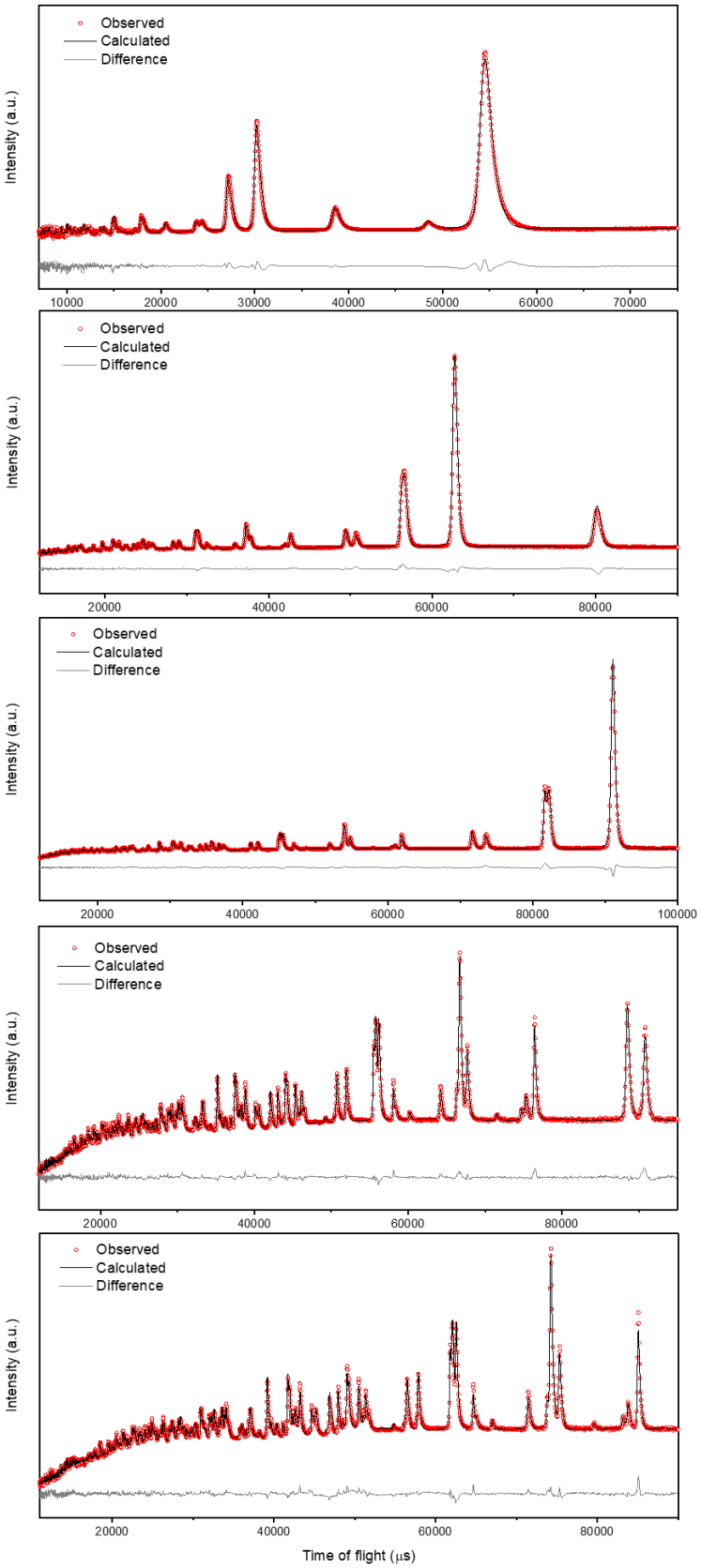

Supplementary Figure 4.8. Neutron diffraction patterns and Rietveld refinement of bare MFM-300(Sc) (bank 1 to 5).

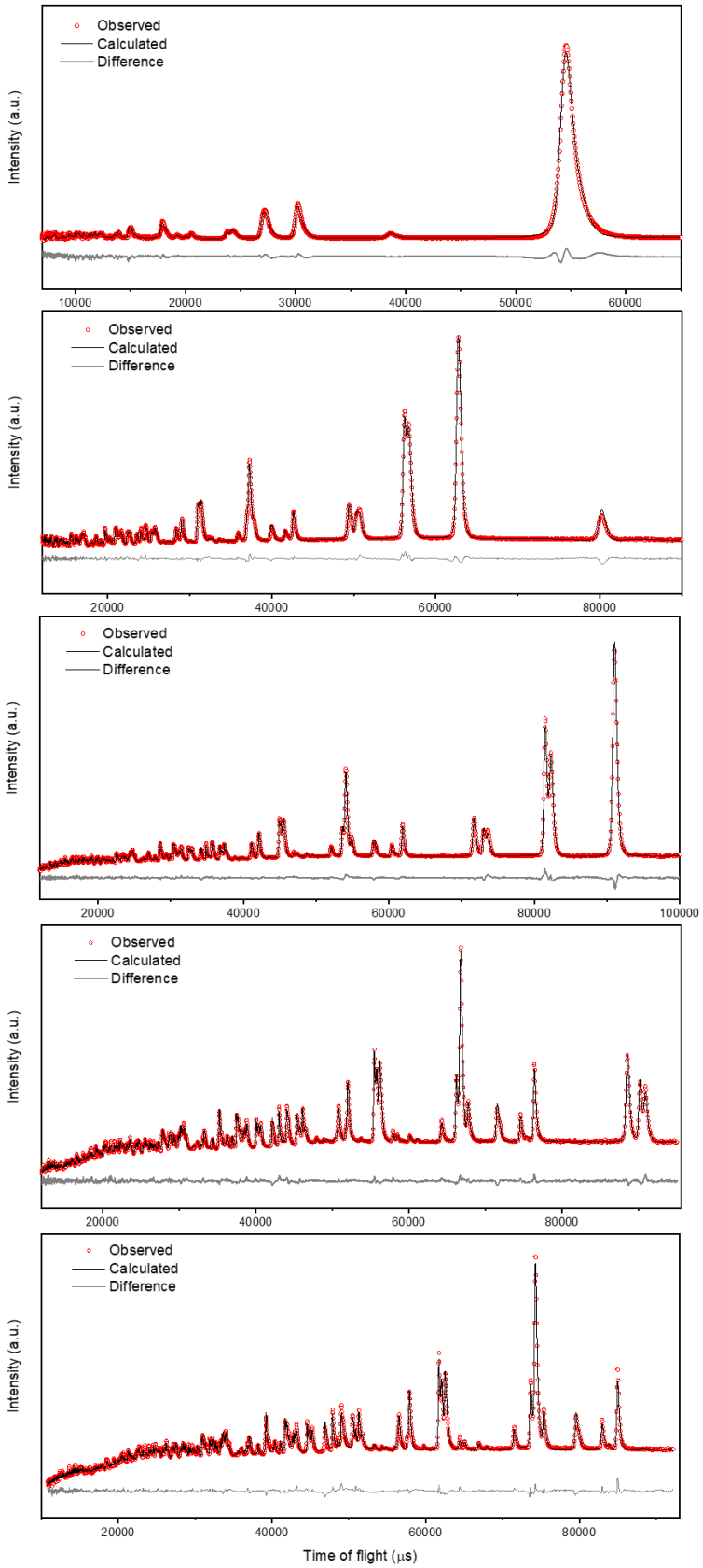

Supplementary Figure 4.9. Neutron diffraction patterns and Rietveld refinement of MFM-300(Sc)·$(ND_3)_{1.25}$. (bank 1 to 5).

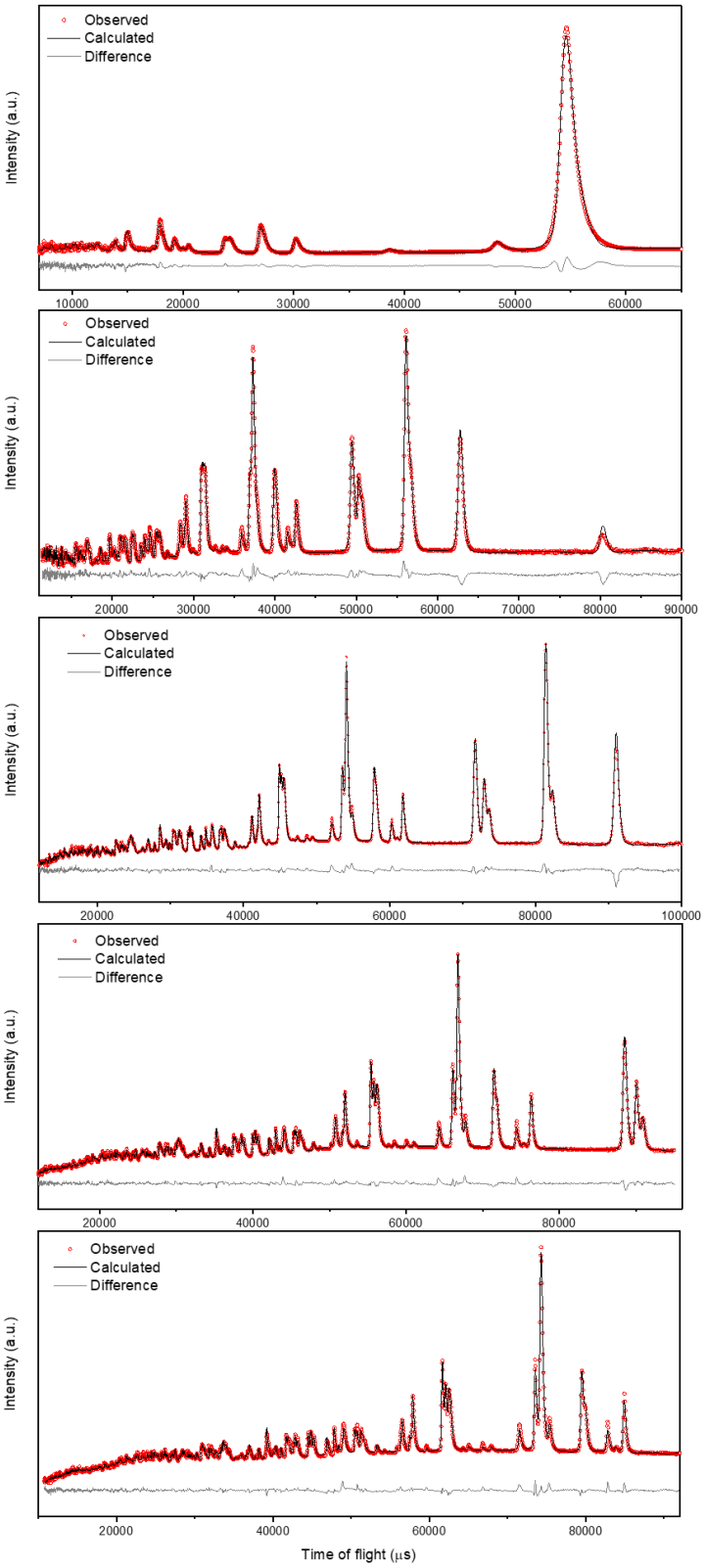

Supplementary Figure 4.10. Neutron diffraction patterns and Rietveld refinement of MFM-300(Sc)·$(ND_3)_{2.6}$. (bank 1 to 5).

8. Solid-state NMR spectroscopy

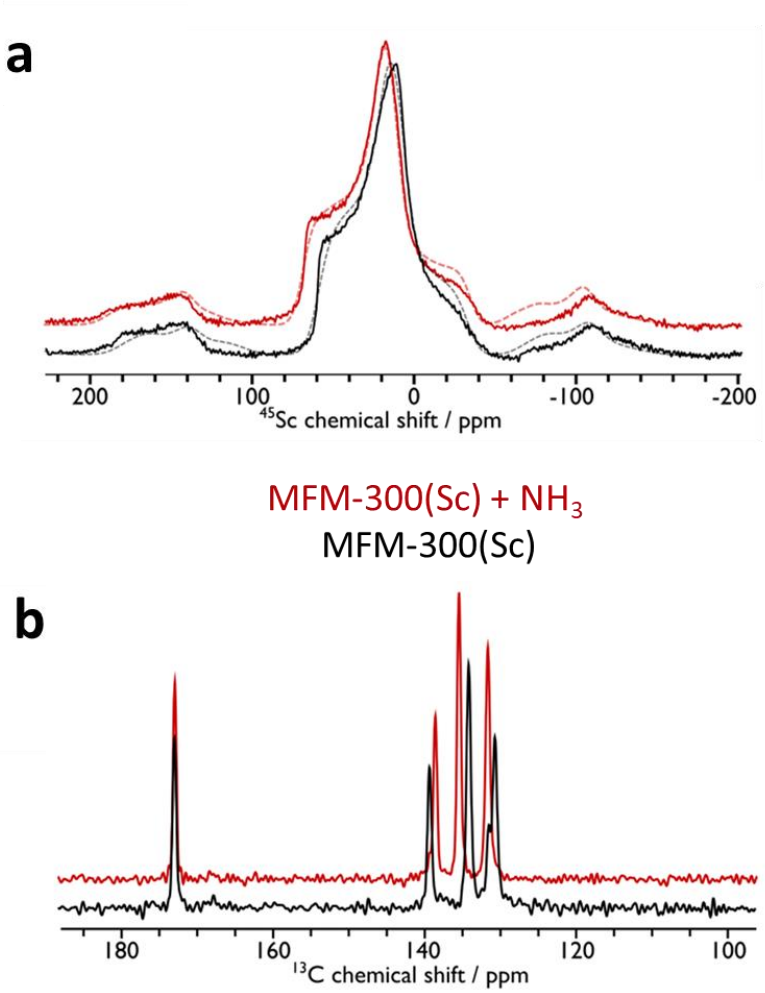

Supplementary Figure 4.11. (a) ^{45}Sc and (b) {^{1}H-}^{13}C CP MAS NMR spectra of pristine (black) and NH_3-loaded (red) MFM-300(Sc). The dashed lines in (a) are from simulated spectra with the following parameters: δ_{iso} = 59.6 ppm, C_Q = 10.8 MHz, η_Q = 1, Gaussian broadening = 1.41 kHz for pristine MFM-300(Sc) and δ_{iso} = 68.6 ppm, C_Q = 11.5 MHz, η_Q = 1, Gaussian broadening = 1.14 kHz for NH_3-loaded MFM-300(Sc).

9. Inelastic neutron scattering

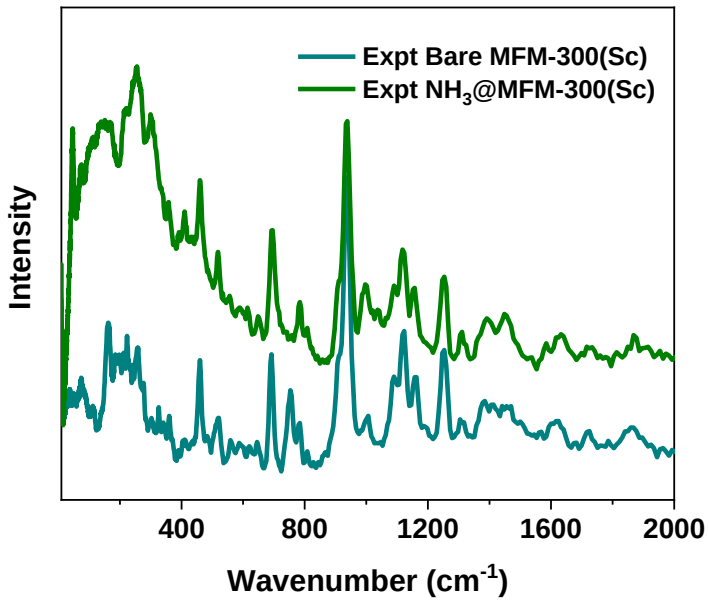

Supplementary Figure 4.12. Experimental INS spectra of bare MFM-300(Sc) (dark cyan) and of NH_3-loaded MFM-300(Sc) (olive).

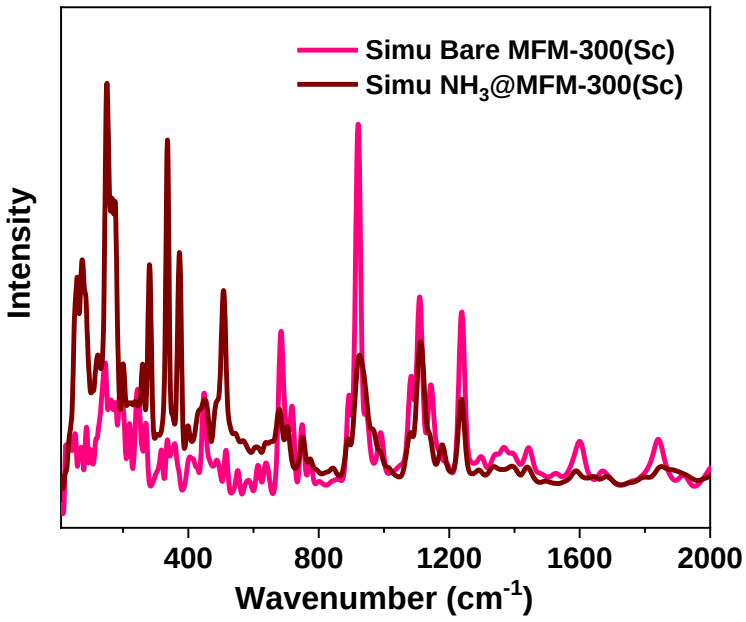

Supplementary Figure 4.13. Simulated INS spectra of bare MFM-300(Sc) (pink) and NH_3-loaded MFM-300(Sc) (wine).

10. Supplementary Tables

Table 4.1. Comparison of the total uptake of NH_3 in selected MOF materials at 1.0 bar.

MOF	Capacity (mmol/g)	Structure	Stability	Reference
MOF-5 MOF-177	12.2 (298 K)	-	loss of crystallinity after adsorption	10
DUT-6 OH-DUT-6	12, 16.4 (298 K)	hydroxyl functionality	irreversible adsorption and structural degradation	11
Mg-MOF-74	16.2 (298 K)	Open metal sites	capacity reduced after first ads/des cycle	12
Fe-MIL-101-SO_3H	17.8 (298 K)	Brønsted acid	-	13
M_2Cl_2BTDD[a] M=Mn,Co, Ni	15.5, 12.0, 12.0 (298 K)	Open metal sites	reversible for three ads/des cycles	14
MIL-101	10 (298K)	-	uptake maintained for five ads/des cycles	15
M_2Cl_2BBTA[b] M=Cu,Co, Ni	19.8, 18.0, 14.7 (298 K)	Open metal sites	Ni_2Cl_2(BBTA) retains crystallinity upon exposure	16
NU-300	8.28 (298 K)	Free carboxylate group	crystallinity decreases	17
NU-1401	8.41 (298 K)	hydroxyl groups	hysteresis loops between ad/desorption	18
MFU-4	17.7 (298 K)	hydroxyl groups	-	19
M_2(dobpdc)[c] M=Mg,Ni, Zn, Co,Mn	23.9, 20.8, 15.2, 13.3, 13.3 (298 K)	Open metal sites	Mg_2(dobpdc) shows five reversible ads/des cycles under wet conditions	20
UiO-67 UiO-bpydc[d]	~8.4 (298 K)	hydroxyl groups	Hysteresis loop	21
MFM-300(M) M=Al,Cr,V^{I} ^{II},Fe,V^{IV}	15.7, 14.0, 15.6, 16.1, 17.3 (273 K)	bridging hydroxyl	MFM-300(Al,Cr,Fe V^{III}) shows three reversible ads/des cycles	22, 23
MFM-300(Sc)	13.1 (298 K)	Sc-N interactions	4 % of NH_3 uptake capacity reduced after 5 adsorption cycles	24
MFM-303	9.9 (273 K)	free carboxylate and hydroxyl groups	- Keep crystalline after cycles experiment	25

UiO-67 Uio-67-vac UiO-67-ox-Cu	6.1-10.5 (298 K)	accessible carboxylate group and copper sites	-	UiO-67 and UiO-67-ox-Cu missed about 28.32% and 44.6% of their surface area after five NH_3 recycles.	[26]
MFM-300(Sc)	19.5 (273 K) 13.5 (298 K)	bridging hydroxyl groups	-	MFM-300(Sc) shows at least two reversible ads/des cycles and keep crystalline after 90 cycles experiment	**This work**

Note: a) BTDD = bis(1*H*-1,2,3-triazolo[4,5-b],[4′,5′-*i*])dibenzo[1,4]dioxin; b) BBTA = 1*H*,5*H*-benzo(1,2-d:4,5-*d*′)bistriazole; c) dobpdc = 4,4-dioxidobiphenyl-3,3-dicarboxylate; d) bpydc = 2,2′-bipyridine-5,5′- dicarboxylate

Supplementary Table 4.2. Crystal Data and Details of the Structure Determination for ND_3 loaded MFM-300(Sc).

	MFM-300(Sc)	MFM-300(Sc)·$(ND_3)_{1.25}$	MFM-300(Sc)·$(ND_3)_{2.6}$
Formula	$C_8H_4ScO_5$	$C_8H_4D_{1.9}ScO_5N_{0.6}$	$C_8H_4D_{3.9}ScO_5N_{1.3}$
Formula weight	225.07	237.5	251.21
Crystal system	Tetragonal	Tetragonal	Tetragonal
Space Group	$I4_122$	$I4_122$	$I4_122$
a, b (Å)	15.3819(3)	15.3970(3)	15.4020(3)
c (Å)	12.4454(2)	12.4104(2)	12.3825(3)
Volume($Å^3$)	2944.6(12)	2942.1(13)	2937.4(14)
ρ (calc) g/cm^3	1.073	1.073	1.136
Radiation type	Neutron	Neutron	Neutron
Scan method	Time of flight	Time of flight	Time of flight
R_{exp} (%)	0.41	0.37	0.36
R_{wp} (%)	1.54	1.54	1.54
R_p (%)	1.42	1.35	1.39
GoF (χ^2)	3.77	4.15	4.34
CCDC	2142629	2142631	2142630

Supplementary Table 4.3. Host–Guest Interactions in MFM-300(Sc)·$(ND_3)_{1.25}$.

MFM-300(Sc)·$(ND_3)_{1.25}$	Interactions	Distance (Å)	Colour
Site	H (HO-Sc)···N (site I)	1.96(1)	pink
	D (site I)···Benzene	3.05(1)	blue
	D (site I)···O (ligand)	3.22(1)	turquoise

Supplementary Table 4.4. Host–Guest Interactions in MFM-300(Sc)·$(ND_3)_{2.6}$.

MFM-300(Sc)·$(ND_3)_{2.6}$	Interactions	Distances (Å)	Colour
Site I	H (HO-Sc)···N (site I)	1.93(1)	pink
	N (site I)···D (site II)	2.30(3)	bright green
	D (site I)···Benzene	3.13(1)	blue
	D (site I)···N (site II)	2.24(2)	red
	D (site I)···O(ligand)	3.24(1)	turquoise
Site II	N (site II)···D (site I)	2.24(2)	red
	D (site II) ···N (site I)	2.30(3)	bright green

Supplementary Table 4.5. Atomic positions for atoms in MFM-300(Sc)·$(ND_3)_{1.25}$.

	x	y	z	Occupancy	Biso / Å^2
Sc	0.6876(1)	0.3124 (1)	0.5	1	1.91(7)
O1	0.7437(3)	0.25	0.625	1	0.50(6)
O2	0.6061(4)	0.3751(4)	0.6148(3)	1	0.50(6)
O3	0.5969(4)	0.2897(2)	0.7580(3)	1	0.50(6)
C1	0.5827(3)	0.3611(2)	0.7109(2)	1	1.05(5)
C2	0.5372(1)	0.4302 (1)	0.7699(2)	1	1.05(5)
C3	0.5	0.5	0.7132(2)	1	1.05(5)
C4	0.5372(10)	0.4302(1)	0.8832(1)	1	1.05(5)
C5	0.5	0.5	0.9399(1)	1	1.05(5)
H1	0.8021(7)	0.25	0.625	0.406(3)	0.50(6)
D1	0.8021(7)	0.25	0.625	0.594(3)	0.50(6)
H3	0.5	0.5	0.6286(4)	1	1.05(5)
H4	0.5650(2)	0.3781(2)	0.9255(2)	1	1.05(5)
N1	0.75	0.0706(3)	0.375	0.625(2)	12.8(3)
D1	0.6891	0.0457(3)	0.375	0.2135(13)	12.8(3)
D2	0.7804	0.0457(3)	0.3096	0.2135(13)	12.8(3)
D3	0.7804	0.0457(3)	0.4404	0.2135(13)	12.8(3)
H1	0.6891	0.0457(3)	0.375	0.0990(5)	12.8(3)
H2	0.7804	0.0457(3)	0.3096	0.0990(5)	12.8(3)
H3	0.7804	0.0457(3)	0.4404	0.0990(5)	12.8(3)

Supplementary Table 4.6. Atomic positions for atoms in MFM-300(Sc)·$(ND_3)_{2.6}$.

	x	y	z	Occupancy	Biso / Å^2
Sc	0.6895(1)	0.3105(2)	0.5	1	2.37(8)
O1	0.7452(4)	0.25	0.65	1	0.65(6)
O2	0.6072(4)	0.3755(4)	0.6130(3)	1	0.65(6)
O3	0.5972(4)	0.2894(3)	0.7583(4)	1	0.65(6)
C1	0.5839(3)	0.3613(2)	0.7102(2)	1	1.32(5)
C2	0.5394(2)	0.4315(1)	0.7698(2)	1	1.32(5)
C3	0.5	0.5	0.7131(3)	1	1.32(5)
C4	0.5394(2)	0.4315(1)	0.8833(2)	1	1.32(5)
C5	0.5	0.5	0.9401(2)	1	1.32(5)
H1	0.8080(6)	0.25	0.625	0.254(4)	0.65(6)
D1	0.8080(6)	0.25	0.625	0.746(4)	0.65(6)
H3	0.5	0.5	0.6283(4)	1	1.32(5)
H4	0.5688(2)	0.3803(2)	0.9257(2)	1	1.32(5)
N2	0.2636(5)	0.4537(9)	0.6766(10)	0.1522(11)	7.83(16)
D1	0.2721(15)	0.4110(16)	0.7377(16)	0.1522(11)	7.83(16)
D2	0.3085(17)	0.439(2)	0.6198(18)	0.1522(11)	7.83(16)
D3	0.280(3)	0.5130(13)	0.706(2)	0.1522(11)	7.83(16)
N1	0.75	0.0669(18)	0.375	1.000(2)	7.83(16)
D1	0.6892	0.0421(2)	0.375	0.3757(14)	7.83(16)
D2	0.7804	0.0421(2)	0.3095	0.3757(14)	7.83(16)
D3	0.7804	0.0421(2)	0.4405	0.3757(14)	7.83(16)
H1	0.6892	0.0421(2)	0.375	0.3757(14)	7.83(16)
H2	0.7804	0.0421(2)	0.3095	0.1243(7)	7.83(16)
H3	0.7804	0.0421(2)	0.4405	0.1243(7)	7.83(16)

11. Supplementary References

1. Zhang, X.; Silva, I.; Godfrey, H.; Callear, S.; Sapchenko, S.; Cheng, Y.; Yrezabal, I.; Frogley, M.; Cinque, G.; Tang, C.; Giacobbe, C.; Dejoie, C.; Rudic, S.; Cuesta, A.; Denecke, M.; Yang, S.; Schröder, M. Confinement of iodine molecules into triple-helical chains within robust metal–organic frameworks. *J. Am. Chem. Soc.* **2017**, *139*, 16289–16296.
2. Fung, B.; Khitrin, A.; Ermolaev, K. An improved broadband decoupling sequence for liquid crystals and solids. *J. Magn. Reason.* **2000**, *142*, 97–101.
3. Kresse, G.; Furthmüller, J. Efficient iterative schemes for *ab* initio total-energy calculations using a plane-wave basis set. *Phys. Rev. B*, **1996**, *54*, 11169–11186.
4. Blochl, P. Projector augmented-wave method. *Phys. Rev. B*, **1994**, *50*, 17953–17979.
5. Kresse, G.; Joubert, D. From ultrasoft pseudopotentials to the projector augmented-wave method. *Phys. Rev. B*, **1999**, *59*, 1758–1775.
6. Perdew, J.; Burke, K.; Ernzerhof, M. Generalized gradient approximation made simple. *Phys. Rev. Lett.*, **1996**, 77, 3865–3868.
7. Klimeš, J.; Bowler, D.; Michaelides, A. A critical assessment of theoretical methods for finding reaction pathways and transition states of surface processes. *J. Phys.: Cond. Matt.* **2010**, *22*, 074203.
8. Togo, A.; Tanaka, I. First principles phonon calculations in materials science. *Scr. Mater.* **2015**, *108*, 1–5.
9. Cheng, Y.; Daemen, L.; Kolesnikov, A.; Ramirez-Cuesta, A. Simulation of inelastic neutron scattering spectra using OCLIMAX. *J. Chem. Theory Comput.* **2019**, *15*, 1974–1982.
10. Saha, D.; Deng, S. Ammonia adsorption and its effects on framework stability of MOF-5 and MOF-177. *J. Colloid. Interf. Sci.* **2010**, *348*, 615–620.
11. Spanopoulos, I.; Xydias, P.; Malliakas, C.; Trikalitis, P. A straight forward route for the development of metal–organic frameworks functionalized with aromatic −OH groups: synthesis, characterization, and gas (N_2, Ar, H_2, CO_2, CH_4, NH_3) adsorption properties. *Inorg. Chem.* **2013**, ***52***, 855–862.
12. Kajiwara, T.; Higuchi, M.; Watanabe, D.; Higashimura, H.; Yamada, T.; Kitagawa, H. A systematic study on the stability of porous coordination polymers against ammonia. *Chem.* **2014**, *20*, 15611–15617.
13. Humbeck, J.; McDonald, T.; Jing, X.; Wiers, B.; Zhu, G.; Long, J. Ammonia capture in porous organic polymers densely functionalized with Brønsted acid groups. *J. Am. Chem. Soc.* **2014**, *136*, 2432–2440.
14. Rieth, A.; Tulchinsky, Y.; Dinca, M. High and reversible ammonia uptake in mesoporous azolate metal–organic frameworks with open Mn, Co, and Ni sites. *J. Am. Chem. Soc.* **2016**, *138*, 9401–9404.
15. Chen, Y.; Zhang, F.; Wang, Y.; Yang, C.; Yang, J.; Li, J. Recyclable ammonia uptake of a MIL series of metal–organic frameworks with high structural stability. *Micropor. Mesopor Mat.* **2018**, *258*, 170–177.
16. Rieth, A.; Dinca, M. Controlled gas uptake in metal–organic frameworks with record ammonia sorption. *J. Am. Chem. Soc.* **2018**, *140*, 3461–3466.
17. Chen, Y.; Zhang, X.; Ma, K.; Chen, Z.; Wang, X.; Knapp, J.; Alayoglu, S.; Wang, F.; Xia, Q.; Li, Z.; Islamoglu, T.; Farha, O. Zirconium-based metal–organic framework with 9-connected nodes for ammonia capture. *ACS Appl. Nano M.* **2019**, *2*, 6098–6102.

18. Zhang, Y.; Zhang, X.; Chen, Z.; Otake, K.; Peterson, G.; Chen, Y.; Wang, X.; Redfern, L.; Goswami, S.; Li, P.; Islamoglu, T.; Wang, B.; Farha, O. A flexible interpenetrated zirconium-based metal–organic framework with high affinity toward ammonia. *ChemSusChem* **2020**, *13*, 1710–1714.
19. Cao, R.; Chen, Z.; Chen, Y.; Idrees, K.; Hanna, S.; Wang, X.; Goetjen, T.; Sun, Q.; Islamoglu, T.; Farha, O. Benign integration of a Zn-azolate metal–organic framework onto textile fiber for ammonia capture. *ACS Appl. Mater. Inter.* **2020**, *12*, 47747–47753.
20. Kim, D.; Kang, D.; Kang, M.; Lee, J.; Choe, J.; Chae, Y.; Choi, D.; Yun, H.; Hong, C. High ammonia uptake of a metal–organic framework adsorbent in a wide pressure range. *Angew. Chem. Int. Ed.* **2020**, *132*, 22720–22725.
21. Yoskamtorn, T.; Zhao, P.; Wu, X.; Purchase, K.; Orlandi, F.; Manuel, P.; Taylor, J.; Li, Y.; Day, S.; Ye, L.; Tang, C.; Zhao, Y.; Tsang, S. Responses of defect-rich zr-based metal–organic frameworks toward NH_3 adsorption. *J. Am. Chem. Soc.* **2021**, *143*, 3205–3218.
22. Godfrey, H.; Silva, I.; Briggs, L.; Carter, J.; Morris, C.; Savage, M.; Easun, T.; Manuel, P.; Murray, C.; Tang, C.; Frogley, M.; Cinque, G.; Yang, S.; Schröder, M. Ammonia storage by reversible host–guest site exchange in a robust metal–organic framework. *Angew. Chem. Int. Ed.* **2018**, *57*, 14778–14781.
23. Han, X.; Lu, W.; Chen, Y.; Silva, I.; Li, J.; Lin, L.; Li, W.; Sheveleva, A.; Godfrey, H.; Lu, Z.; Tuna, F.; McInnes, E.; Cheng, Y.; Daemen, L.; McPherson, L.; Teat, S.; Frogley, M.; Rudic, S.; Manuel, P.; Cuesta, A.; Yang, S.; Schröder, M. High ammonia adsorption in MFM-300 materials: dynamics and charge transfer in host–guest binding. *J. Am. Chem. Soc.* **2021**, *143*, 3153–3161.
24 Lyu, P.; Wright, A.; Olvera, A.; Mileo, P.; Zárate, J.; Ahumada, E.; Martis, V.; Williams, D.; Dincă, M.; Ibarra, I.; Maurin, G. Ammonia capture *via* an unconventional reversible guest–induced metal-linker bond dynamics in a highly stable metal–organic framework. *Chem, Mater.* **2021**, *33*, 6186–6192.
25. Marsh, C.; Han, X.; Li, J.; Lu, Z.; Argent, S.; Silva, I.; Cheng, Y.; Daemen, L. L.; Cuesta, A.; Thompson, S.; Blake, A.; Yang, S.; Schröder, M. Exceptional packing density of ammonia in a dual-functionalized metal–organic framework. *J. Am. Chem. Soc.* **2021**, *143*, 6586–6592.
26. Binaeian, E.; Li, Y.; Tayebi, H.; Yuan, D. Enhancing toxic gas uptake performance of Zr-based MOF through uncoordinated carboxylate and copper insertion; ammonia adsorption. *J. Hazard. Mater.* **2021**, *416*, 125933.

Appendix IV: Supporting information for Chapter 5

Supporting Information

1. Experimental Section

Synthesis of MFM-300(In). H_4L (330 mg, 1.00 mmol), $In(NO_3)_3 \cdot 5H_2O$ (585 mg, 1.50 mmol) were mixed in a DMF/MeCN mixture (30 ml, 2:1 v/v) with conc. HNO_3 (1.0 mL) in a 250 mL glass pressure reactor. Then the vessel sealed and heated at 80 °C for 48 h. The resultant flaky white precipitate was then washed with DMF and immersed in an excess of acetone for 3 days with frequent exchange of solvent.[1] Yield: 347 mg (42% yield based upon solvent content from microanalysis).

Gas Adsorption Isotherms. Gravimetric isotherms (0-1000 mbar) were recorded at 273, 283, 293, 303, and 308 K (temperature controlled water-bath) for C_2H_2, C_2H_4, C_2H_6, C_3H_4, C_3H_6 and C_3H_8 and at 195 K (dry ice/acetone) for C_2H_2, C_2H_4, C_2H_6. Data were collected using an IGA-003 system (Hiden Isochema, Warrington, UK) equipped with a turbomolecular pumping system. Acetone exchanged samples were loaded into the system and degassed at 120 °C and 1×10^{-6} mbar for 20 h to give a dry, desolvated material of typical mass ca. 50 mg. Ultra-pure research grade (99.99 %) gases were purchased from Air Liquide or BOC and used as received. C_2H_2 was purified by dual-stage cold trap systems operated at 195 K (dry ice) and an activated carbon filter before introduction to the IGA system.

Dynamic Breakthrough Experiments. Dynamic breakthrough experiments were conducted on a Hiden Isochema IGA-003 with ABR attachments and a Hiden Analytical mass spectrometer by using a fixed-bed tube (7mm diameter × 120 mm length, bed volume: 5.0 mL) packed with 750 mg of MFM-300(In) powder. The sample was heated at 120 ºC under a flow of dry He for 12h for activation, and then cooled to room temperature (293 K). Single-component gas breakthrough experiments with an inlet gas flow rate of 2 mL min^{-1} diluted in a flow of He (total

flow rate of 20 mL min^{-1}) were measured through a fixed-bed packed with MFM-300(In). For equimolar mixtures of hydrocarbons, the flow rate of 2.0 mL min^{-1}/2.0 mL min^{-1} diluted in He (total flow rate of 20 mL min^{-1}) was applied. Dynamic breakthrough experiments for 1:99 mixtures of C_2H_2/C_2H_4, C_2H_2/C_2H_6, and C_2H_4/C_2H_6 were conducted at the rate of 0.2 mL min^{-1}/19.8 mL min^{-1}. All breakthrough experiments were conducted at a total flow of 20 mL min^{-1} at 293 K. The concentration of hydrocarbon gas at the outlet was determined by mass spectrometry and compared with the inlet concentration C_0, where C/C_0 = 1 indicates complete breakthrough. The MFM-300(In) sample framework density is 1.32 cm^{-3}, occupied a volume of 0.57 mL (assuming 100% purity and no framework collapse), leading the dead volume is determined to be 4.43 mL.

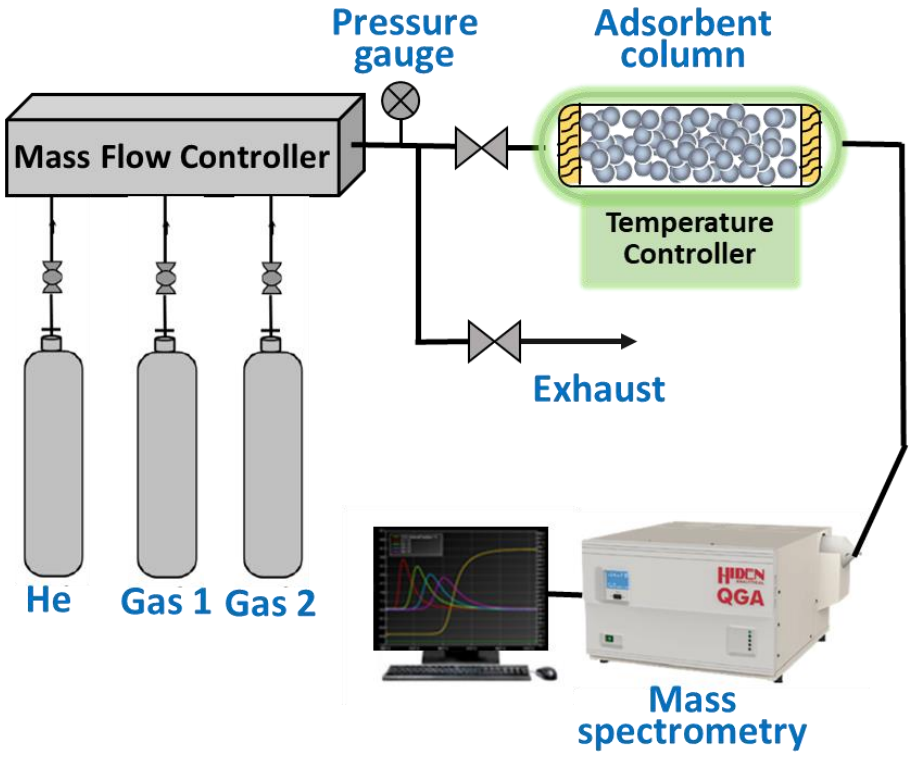

Supplementary Figure 5.1. Scheme of the column dynamic breakthrough experiments.

In a typical column dynamic breakthrough experiment for binary gas separation, the fixed bed column is initially charged with the MOF sample. The gases are then introduced into the column from the inlet port and flow through the packed MOF sample (Supplementary Figure 5.1). During the entire experimental process, the composition of the outlet gas is continuously monitored by the mass spectrometry to determine when the breakthrough of one of the gas components occurs. The "breakthrough" is defined as the moment when one of the gas components begins to appear in the outlet stream. This indicates that the adsorption capacity of the MOF sample for that gas component has been saturated, and it has begun to break through the column. By monitoring the breakthrough time and the changes in the composition of the outlet gas after breakthrough, the performance and separation capacity of the MOF sample can be assessed.

2. Powder X-ray Diffraction

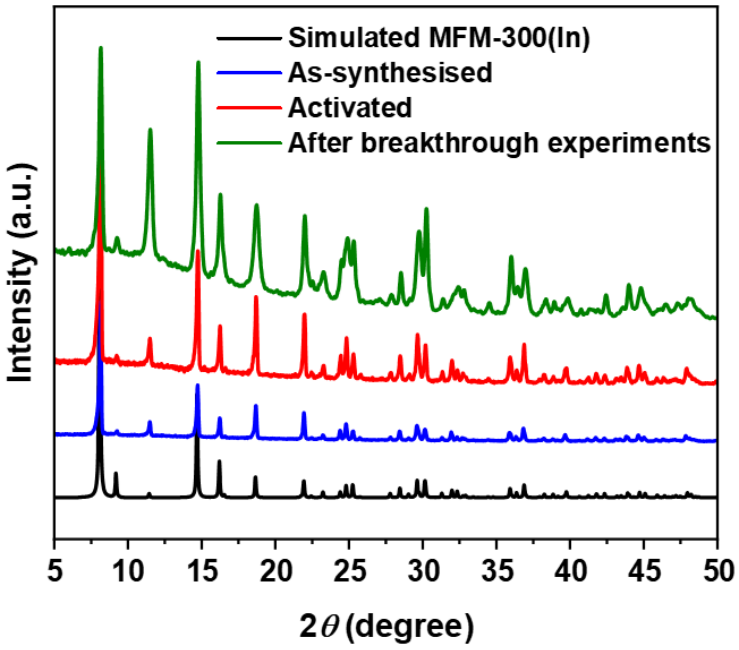

Supplementary Figure 5.2. PXRD patterns of as-synthesised, activated MFM-300(In), and sample after breakthrough experiments (black: simulated MFM-300(In); blue: as-synthesised; red: activated; olive: after breakthrough experiments).

3. Thermogravimetric Analysis

The as-synthesised, acetone exchanged and activated MFM-300(In) were heated from room temperature to 510 °C at a rate of 5 °C min^{-1} under a flow of air. The result shows that the MFM-300(In) can tolerate up to 400 °C confirming its high thermal stability.

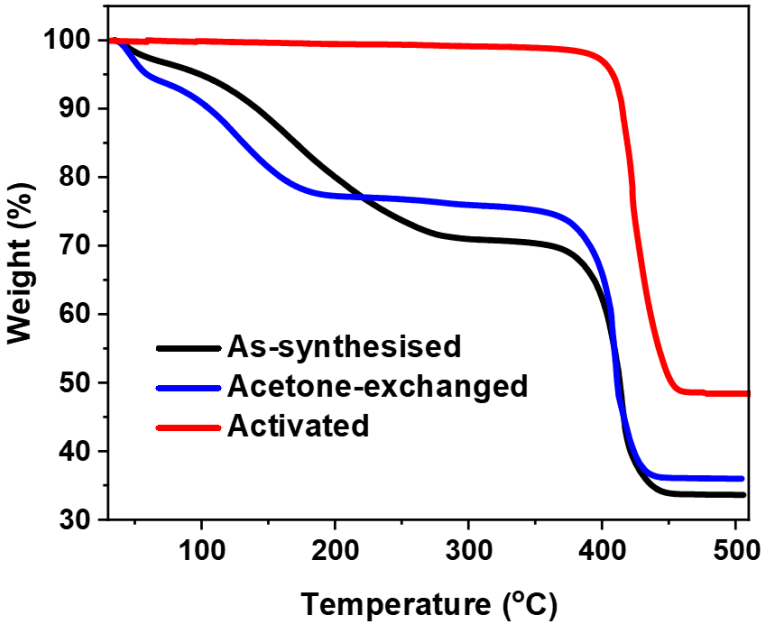

Supplementary Figure 5.3. TGA curves for as-synthesised (black), acetone-exchanged (blue) and activated MFM-300(In) (red).

4. Characterisation of Porosity

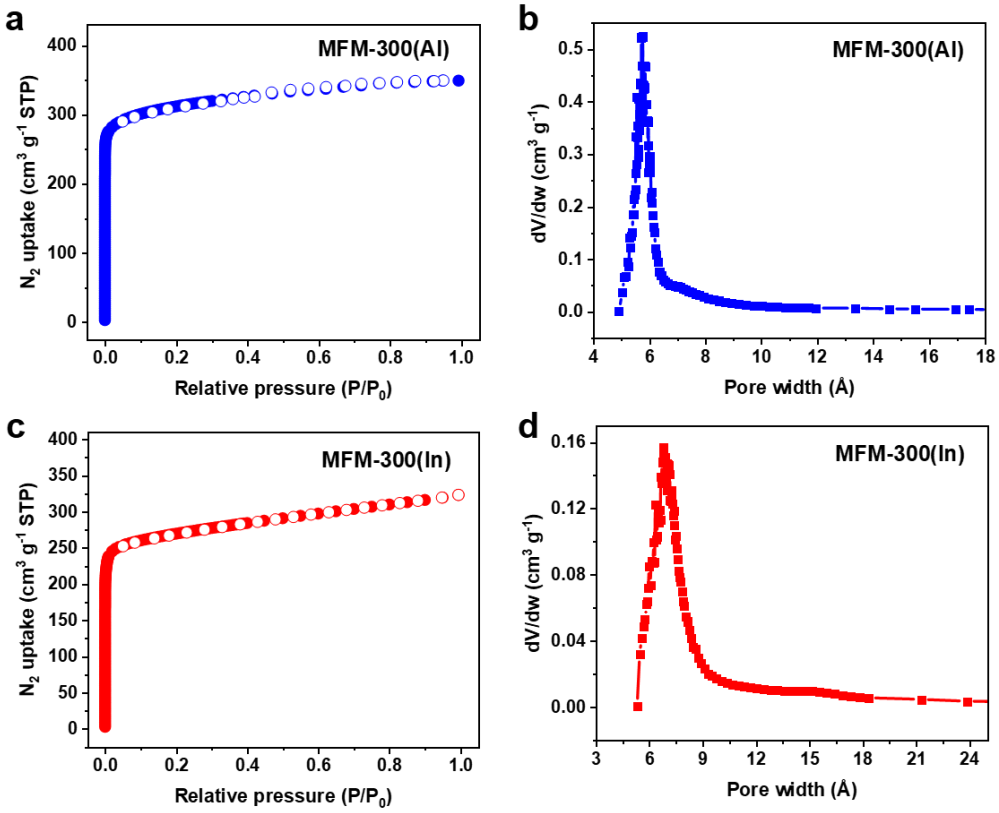

Supplementary Figure 5.4. N_2 adsorption/desorption isotherms for (a) MFM-300(Al) and (c) MFM-300(In) at 77 K (solid symbols: adsorption; hollow symbols: desorption). Micropore size distribution plots for (b) MFM-300(Al) and (d) MFM-300(In).

5. Additional Gas Adsorption Isotherms

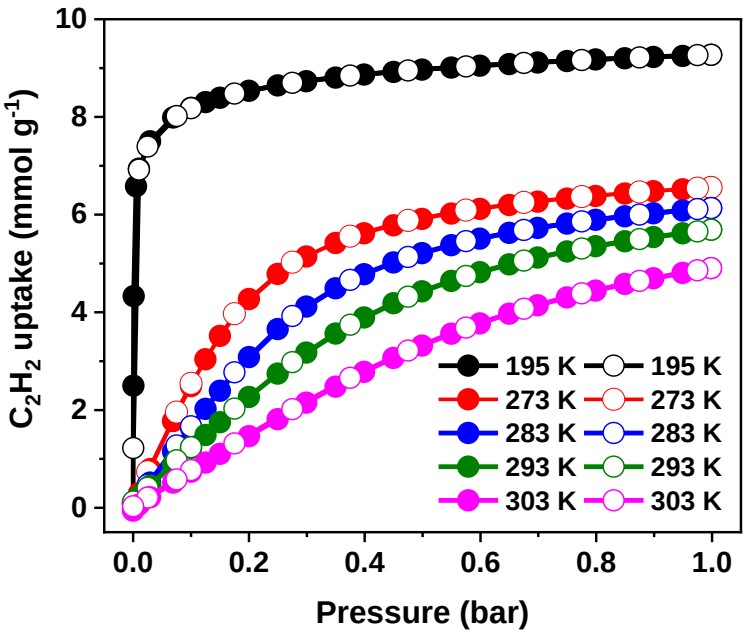

Supplementary Figure 5.5. Adsorption/desorption isotherms for acetylene in MFM-300(In) (black: 195 K; red: 273 K; blue: 283 K; olive: 293 K; magenta: 303 K) (solid symbols: adsorption; hollow symbols: desorption).

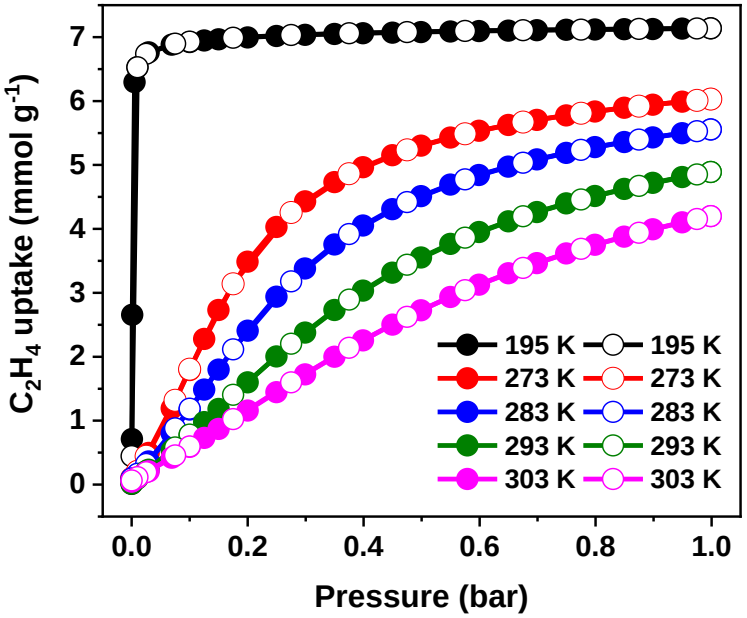

Supplementary Figure 5.6. Adsorption/desorption isotherms for ethylene in MFM-300(In) (black: 195 K; red: 273 K; blue: 283 K; olive: 293 K; magenta: 303 K) (solid symbols: adsorption; hollow symbols: desorption).

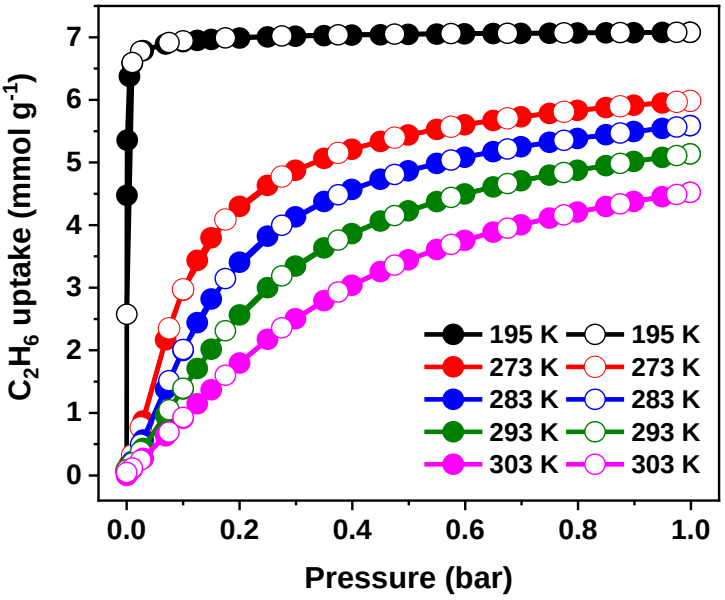

Supplementary Figure 5.7. Adsorption/desorption isotherms for ethane in MFM-300(In) (black: 195 K; red: 273 K; blue: 283 K; olive: 293 K; magenta: 303 K) (solid symbols: adsorption; hollow symbols: desorption).

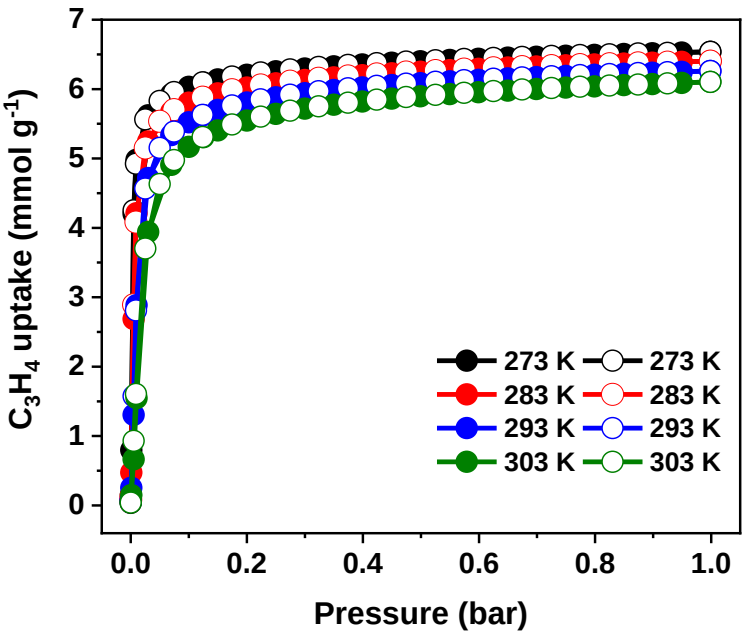

Supplementary Figure 5.8. Adsorption/desorption isotherms for propyne in MFM-300(In) (black: 273 K; red: 283 K; blue: 293 K; olive: 303 K) (solid symbols: adsorption; hollow symbols: desorption).

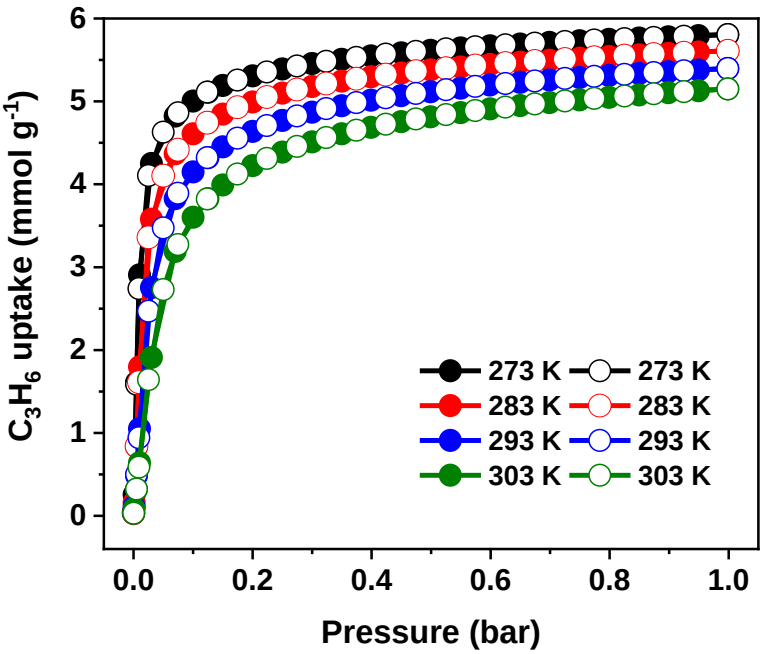

Supplementary Figure 5.9. Adsorption/desorption isotherms for propene in MFM-300(In) (black: 273 K; red: 283 K; blue: 293 K; olive: 303 K) (solid symbols: adsorption; hollow symbols: desorption).

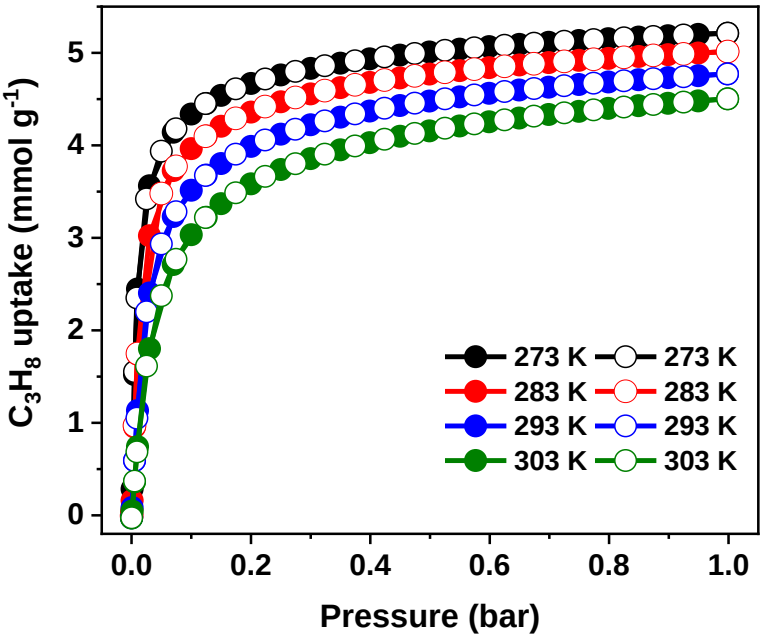

Supplementary Figure 5.10. Adsorption/desorption isotherms for propane in MFM-300(In) (black: 273 K; red: 283 K; blue: 293 K; olive: 303 K) (solid symbols: adsorption; hollow symbols: desorption).

6. Comparison of C_2H_2, C_2H_4, C_2H_6, C_3H_4, C_3H_6 and C_3H_8 isotherms

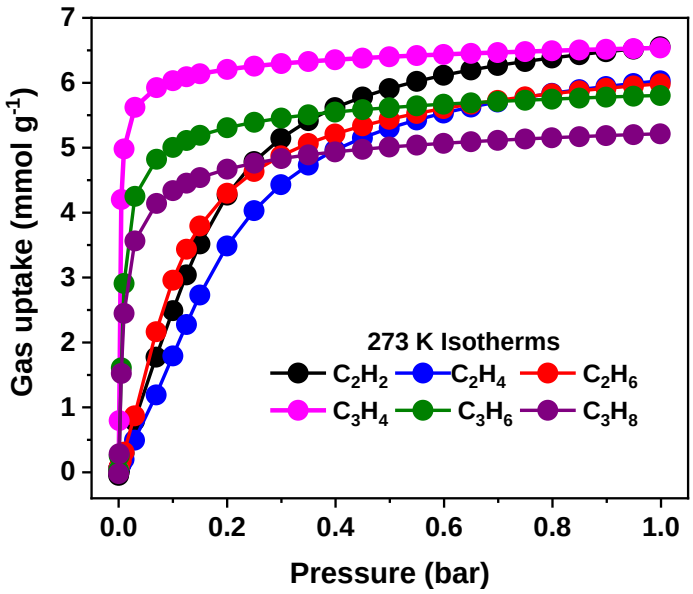

Supplementary Figure 5.11. Adsorption isotherms at 273 K of C_2H_2 (black), C_2H_4 (blue), C_2H_6 (red), C_3H_4 (magenta), C_3H_6 (olive) and C_3H_8 (purple) in MFM-300(In) to a pressure of 1 bar. Desorption isotherms are omitted for clarity; the nature of reversible adsorption has been demonstrated above.

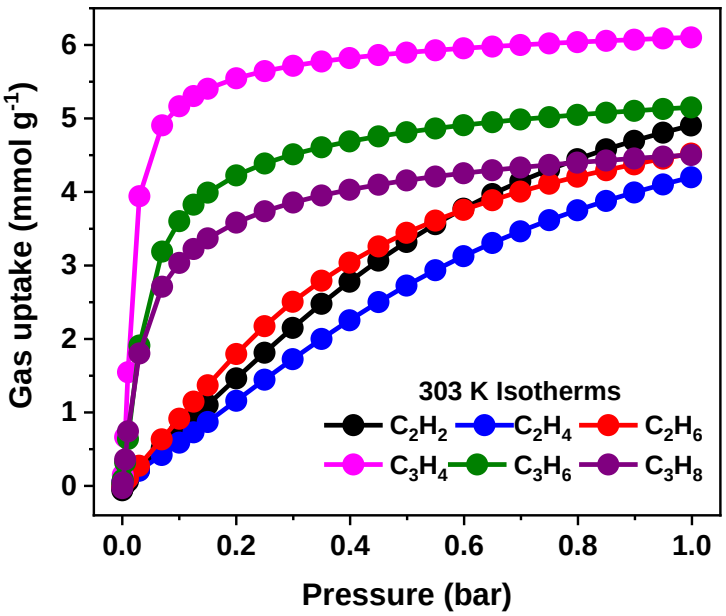

Supplementary Figure 5.12. Adsorption isotherms at 303 K of C_2H_2 (black), C_2H_4 (blue), C_2H_6 (red), C_3H_4 (magenta), C_3H_6 (olive) and C_3H_8 (purple) in MFM-300(In) to a pressure of 1 bar. Desorption isotherms are omitted for clarity; the nature of reversible adsorption has been demonstrated above.

7. Analysis and Derivation of the Isosteric Heats of Adsorption

To estimate the isosteric enthalpies (ΔH) for adsorption of C_2H_2, C_2H_4, C_2H_6, C_3H_4, C_3H_6 and C_3H_8 isotherms between 273–308 K were fitted to the Van t' Hoff equation;

$$\ln P = \frac{\Delta H}{RT} - \frac{\Delta S}{R} \quad (1)$$

where p is pressure in Pa, T is the temperature, and R is the ideal gas constant. All linear fittings show R^2 above 0.99 indicating the consistency of the isotherm data and of the fitting.

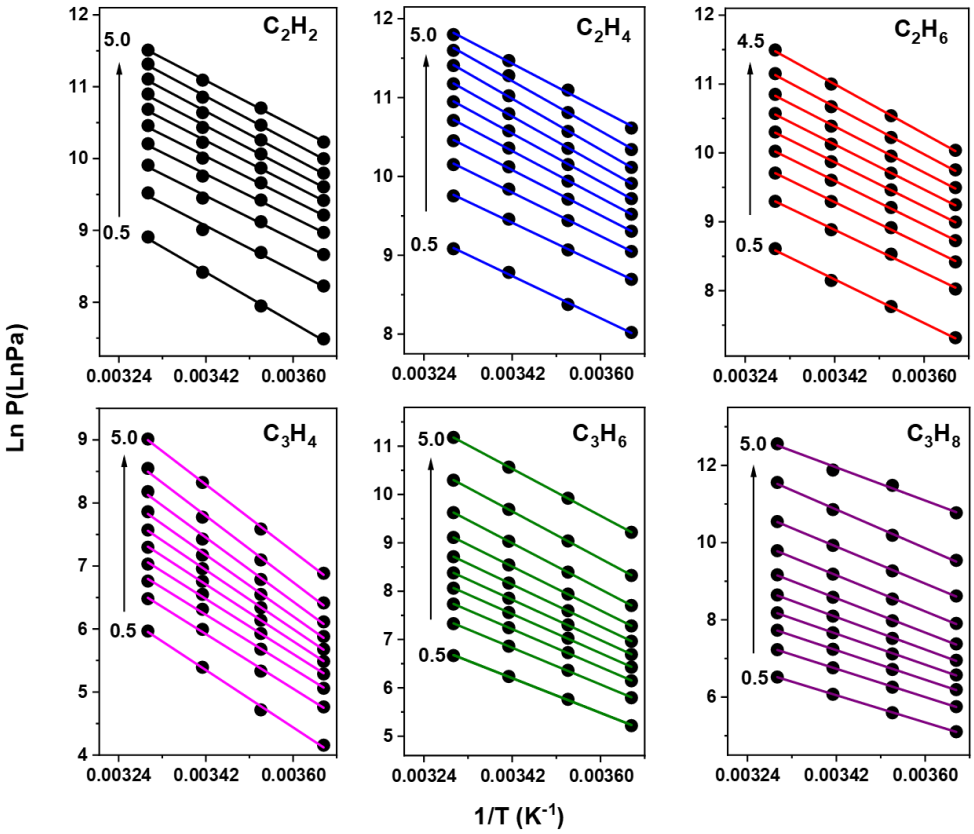

Supplementary Figure 5.13. Linear fitting of 1/T vs LnP at intervals of 0.1 mmolg^{-1} for substrates in MFM-300(In) to determine the isosteric heat of adsorption by the Van t' Hoff method.

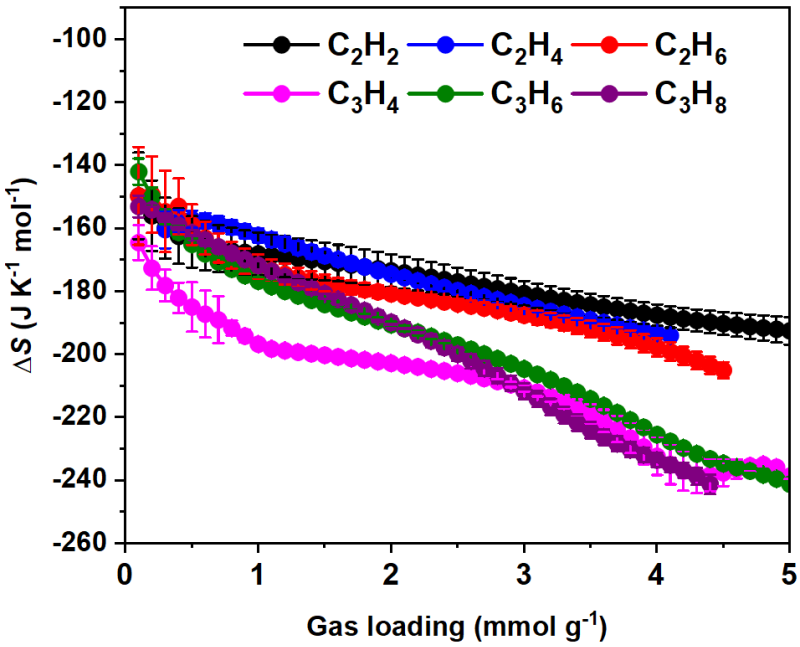

Supplementary Figure 5.14. Entropy of adsorption for C_2 and C_3 hydrocarbons in MFM-300(In) calculated from isotherm data. C_2H_2 (black), C_2H_4 (blue), C_2H_6 (red), C_3H_4 (magenta), C_3H_6 (olive) and C_3H_8 (purple).

8. Calculation of IAST selectivity for gas adsorption.

To estimate the selectivity observed for each substrate isotherm data at 293 K were fitted using the dual-site Langmuir-Freundlich (DSLF) model (equation 2).

$$N^{\circ}(f) = \frac{q_1 b_1 P^{v_1}}{1 + b_1 P^{v_1}} + \frac{q_2 b_2 P^{v_2}}{1 + b_2 P^{v_2}} \qquad (2)$$

where *P* is the pressure of the bulk gas at equilibrium with the adsorbed phase, q_i is the maximum adsorption amount, b_i is the the affinity constant and n_i is the deviation from the simple Langmuir equation. Using this fitting, the IAST selectivity can be calculated by equation 3.

$$S = \frac{x_1/y_1}{x_2/y_2} \qquad (3)$$

where x_{i} is the amount of each component adsorbed and y_{i} is the mole fraction of each component at equilibrium.

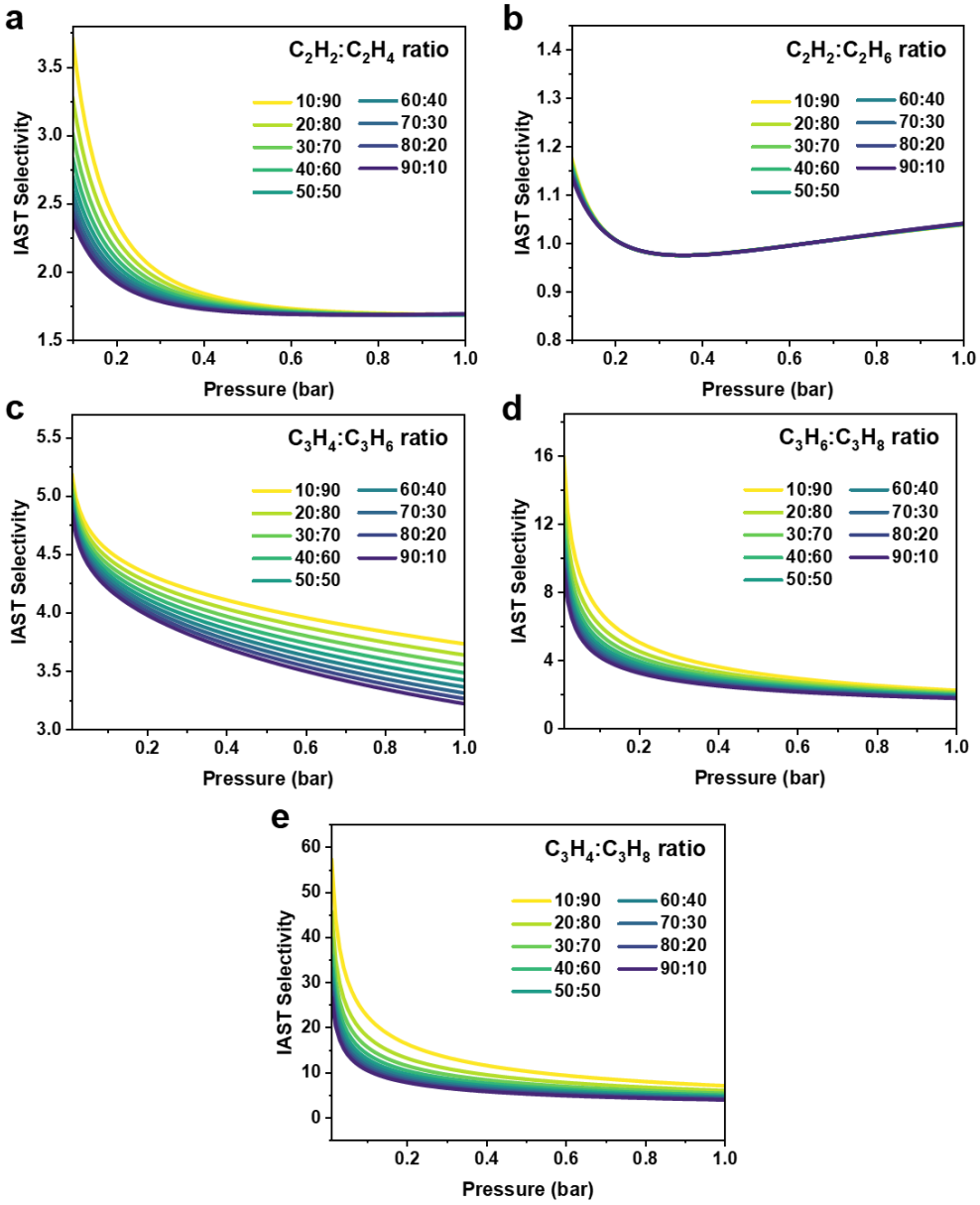

Supplementary Figure 5.15. Selectivities as a function of pressure for C_2 and C_3 hydrocarbons in MFM-300(In) calculated by IAST from single component adsorption isotherms.

9. Dynamic Breakthrough Experiments

Calculation of dynamic adsorption capacity and productivity

To determine the dynamic adsorption capacity, the uptake of each component (n_m) was calculated based on the breakthrough curves by the equation described as follows:

$$V_m = \frac{\int_0^t v_{gas\ out}\, d_t - V_{dead}}{W_{MOF}} \qquad (4)$$

$$n_m = \frac{PV_m}{\mathrm{R}T} \qquad (5)$$

where $v_{\text{gas out}}$ is the flow rate of the target gas with the unit of mL min^{-1}; V_{dead} is the dead volume of the system (mL); W represents the mass of MFM-300(In) packed in the breakthrough bed (g); t is the retention time for the specific gas (min); P is atmospheric pressure (Kpa); R is the ideal gas constant. T is the measurement temperature (K).

The productivity (q_m) of C_2H_4 and C_3H_6 was determined through the breakthrough amount of C_2H_4 and C_3H_6, which is calculated by integration of the breakthrough curves during a period from t_1 to t_2 during which the gas purity is greater than 99.9%:

$$q_m = \frac{\int_{t1}^{t2} v_{gas\ out}\, d_t - V_{dead}}{W_{MOF}} \qquad (6)$$

where $v_{\text{gas out}}$ is the flow rate of target gas with the units of mL min^{-1}; V_{dead} is the dead volume of the system (mL); W represents the mass of MFM-300(In) packed in the breakthrough bed (g);

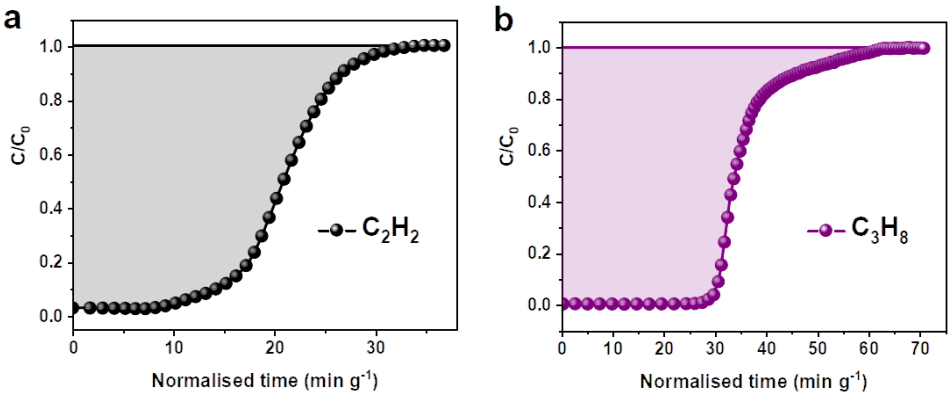

Supplementary Figure 5.16. Breakthrough plots for single component (a) C_2H_2 and (b) C_3H_8 with an inlet gas flow rate of 2.0 mL min^{-1} diluted in He through MFM-300(In) at a total flow of 20 mL min^{-1} at 293 K.

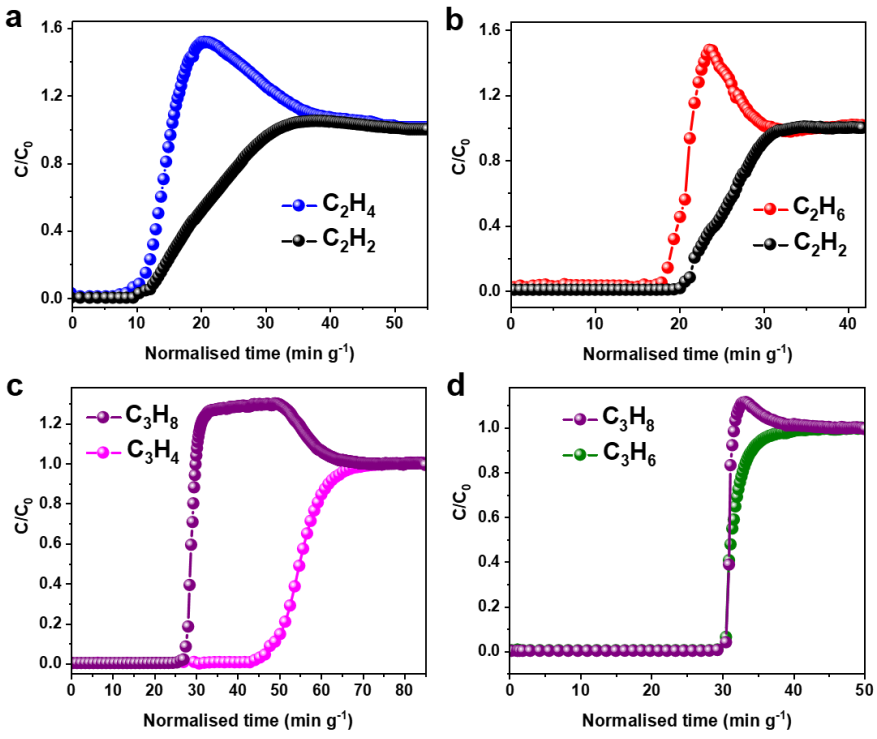

Supplementary Figure 5.17. Dynamic breakthrough plots for equimolar mixtures of (a) C_2H_4/C_2H_2, (b) C_2H_6/C_2H_2, (c) C_3H_8/C_3H_4 and (d) C_3H_8/C_3H_6 with an inlet gas flow rate of 2.0 mL min^{-1}/2.0 mL min^{-1} diluted in He through a fixed-bed packed with MFM-300(In) at a total flow of 20 mL min^{-1} at 293 K. C_2H_2 (black), C_2H_4 (blue), C_2H_6 (red), C_3H_4 (magenta), C_3H_6 (olive) and C_3H_8 (purple).

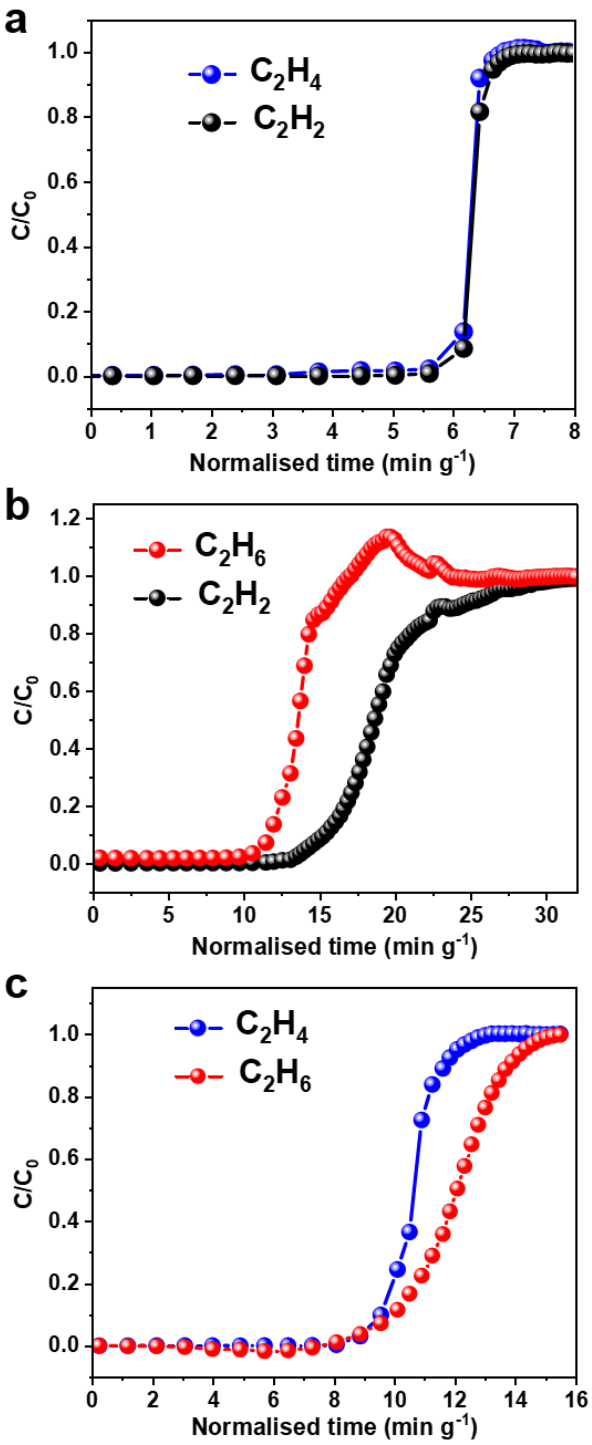

Supplementary Figure 5.18. Dynamic breakthrough experiments for 1:99 mixtures of (a) C_2H_2/C_2H_4, (b) C_2H_2/C_2H_6, and (c) C_2H_4/C_2H_6 with an inlet gas flow rate of 0.2 mL min^{-1}/19.8 mL min^{-1} through a fixed-bed packed with MFM-300(In) at a total flow rate of 20 mL min^{-1} at 293 K. C_2H_2 (black), C_2H_4 (blue), and C_2H_6 (red).

10. Neutron Powder Diffraction

Neutron powder diffraction experiments were undertaken at the WISH diffractometer at the ISIS Facility. MFM-300(In) was loaded into a 6 mm diameter vanadium sample can and outgassed at 1×10^{-7} mbar and 100 °C for 1 day. The sample was loaded into a liquid helium cryostat and cooled to 7 K for data collection. C_2H_2, C_2H_4, C_2H_6, C_3H_4, C_3H_6 and C_3H_8 gas were introduced by warming the samples to 298 K and the gas dosed volumetrically from a calibrated volume. The gas-loaded sample was then cooled to 7 K over a period of 2 h to ensure good mobility of adsorbed species within the crystalline structure of MFM-300(In) and for a further 30 mins to ensure thermal equilibrium. Rietveld structural refinements were carried out on the NPD data using the TOPAS software package.[21] The binding interactions between MFM-300(In) and light hydrocarbons involve three common types, which are hydrogen bonding, electrostatic interactions, and intermolecular interaction. The bond lengths associated with these bonding types are similar to those discussed in Chapter 2 and 3, which could be referring to previous chapters where the bonding characteristics and lengths were discussed.

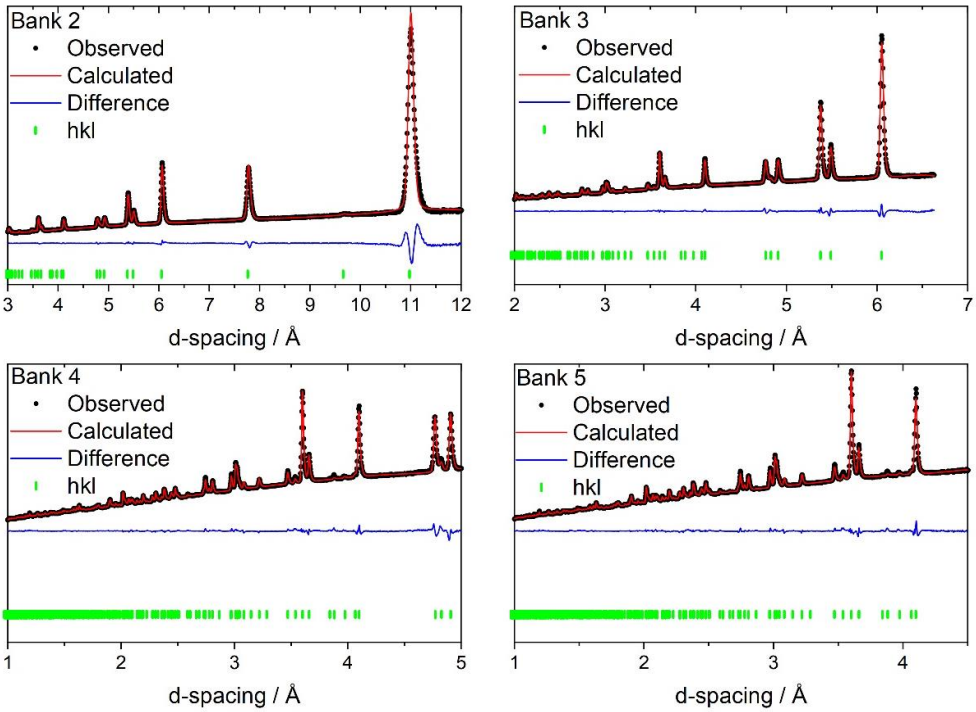

Supplementary Figure 5.19. Rietveld fit profiles of the NPD data of MFM-300(In)·1.32(C_2D_2).

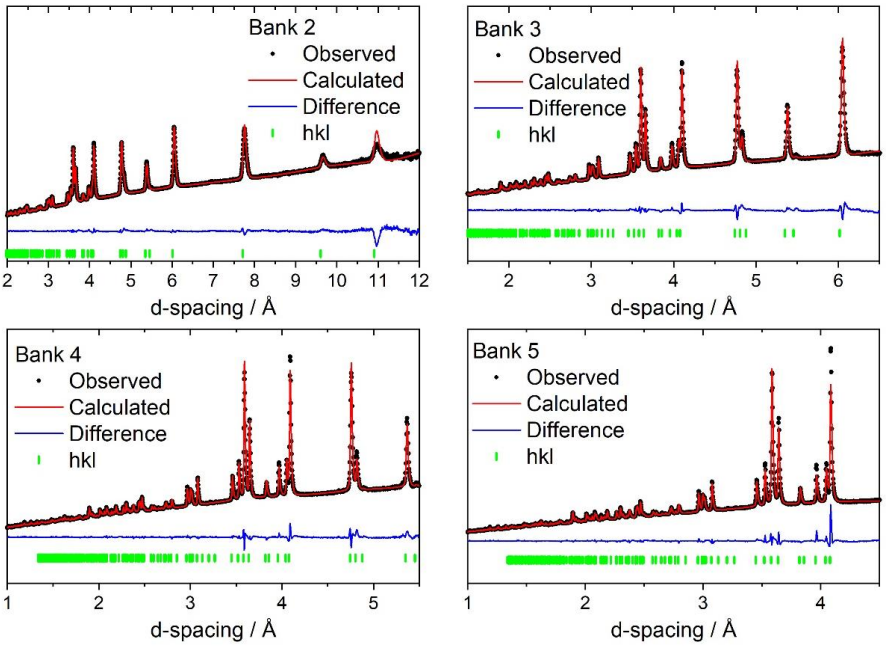

Supplementary Figure 5.20. Rietveld fit profiles of the NPD data of MFM-300(In)·1.66(C_2D_4).

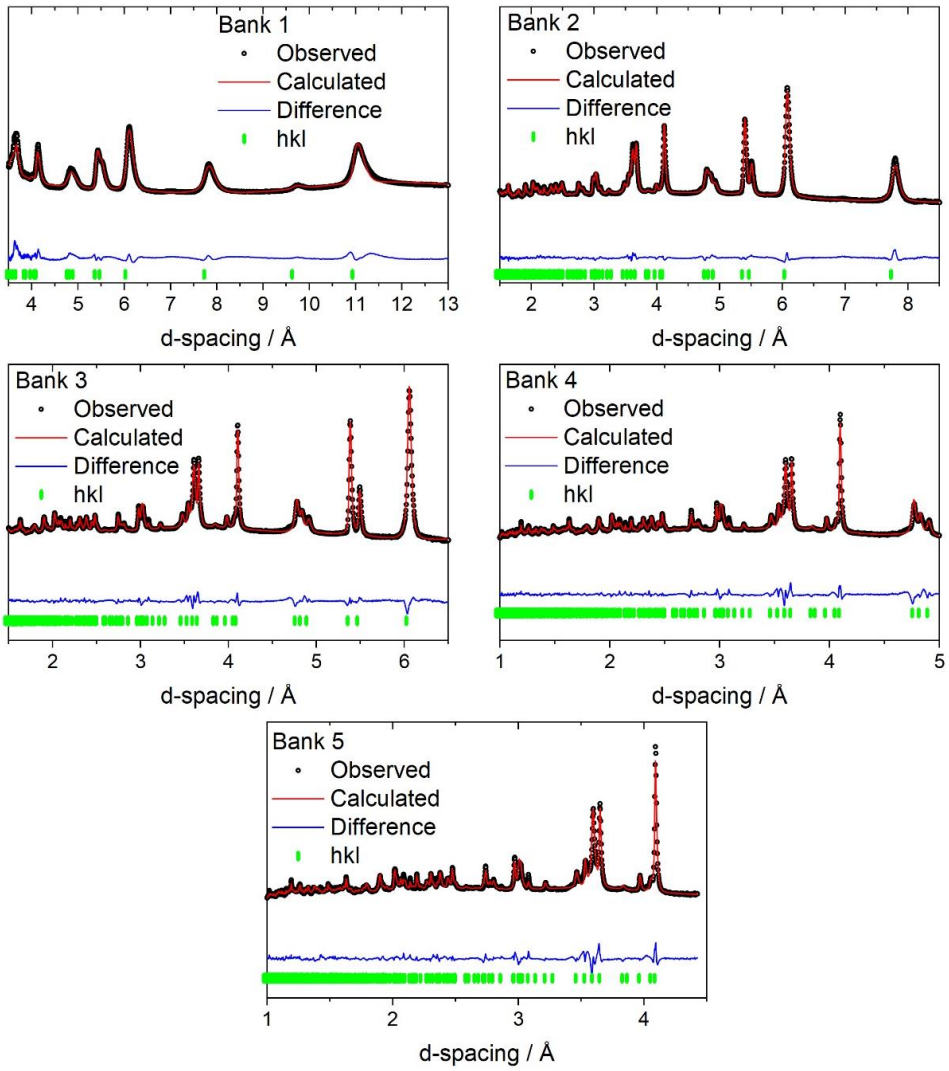

Supplementary Figure 5.21. Rietveld fit profiles of the NPD data of MFM-300(In)·0.72(C_2D_6).

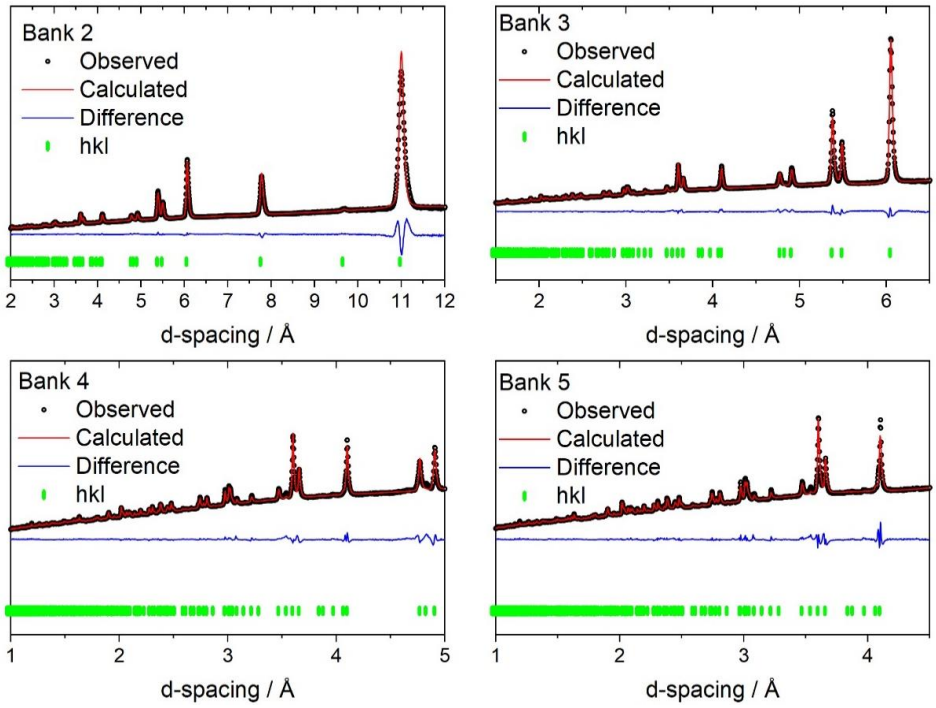

Supplementary Figure 5.22. Rietveld fit profiles of the NPD data of MFM-300(In)·0.2(C_3D_4).

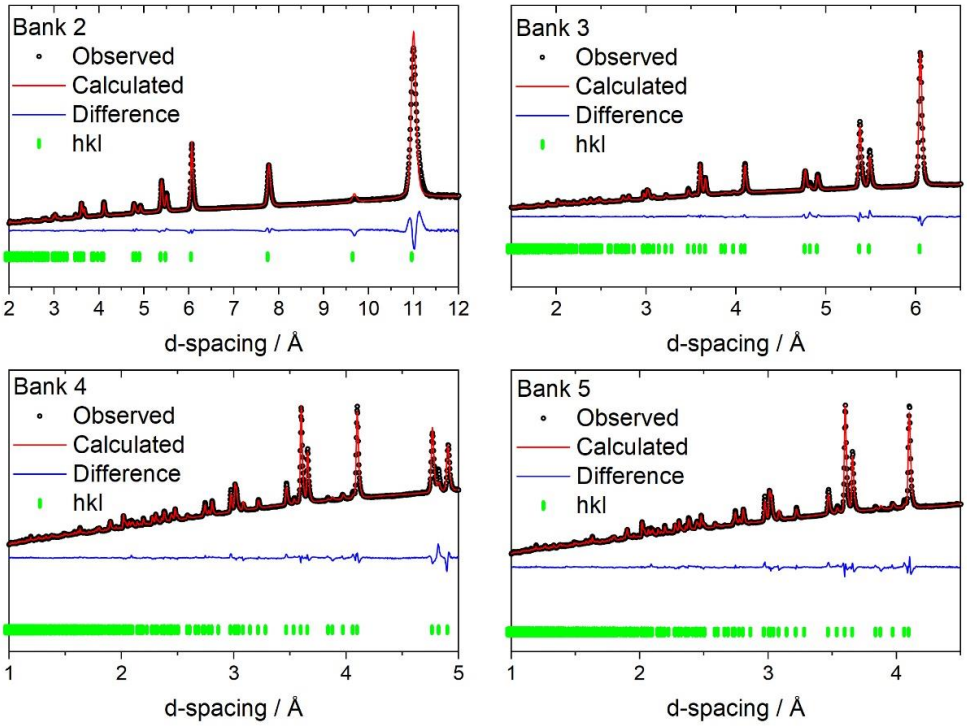

Supplementary Figure 5.23. Rietveld fit profiles of the NPD data of MFM-300(In)·0.48(C_3D_6).

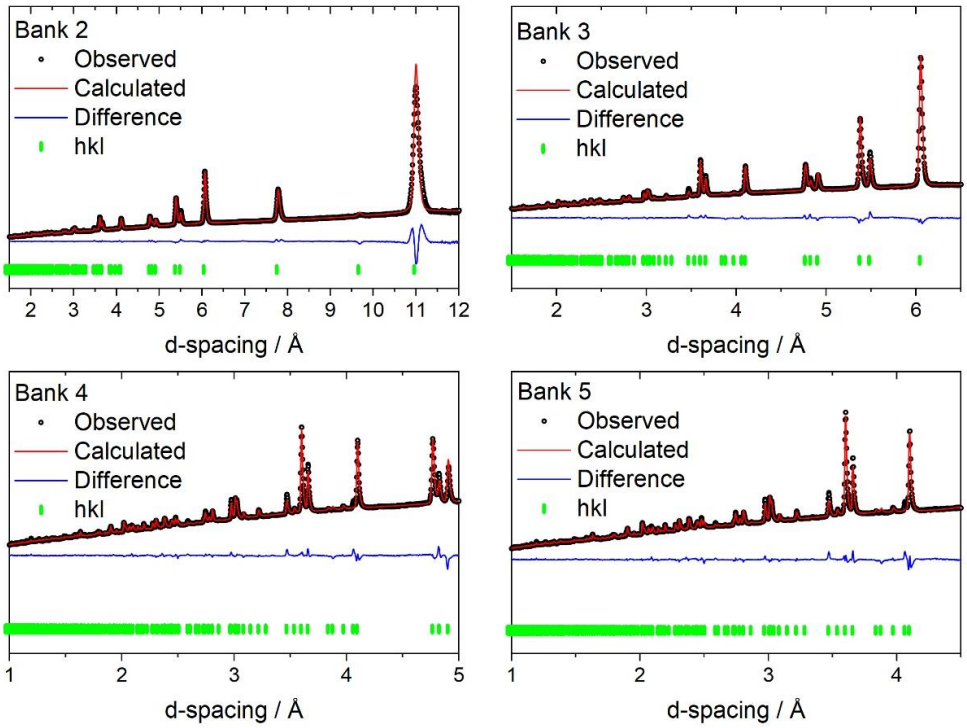

Supplementary Figure 5.24. Rietveld fit profiles of the NPD data of MFM-300(In)·0.46(C_3D_8).

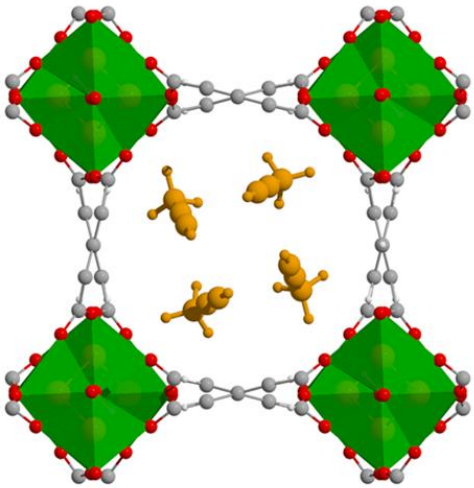

Supplementary Figure 5.25. NPD structure of MFM-300(In)·0.2(C_3D_4).

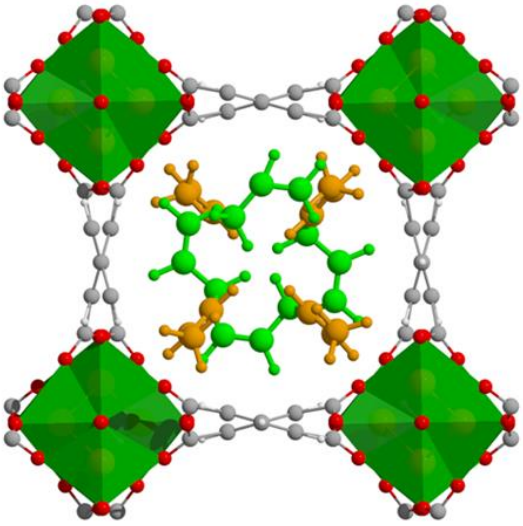

Supplementary Figure 5.26. NPD structure of MFM-300(In)·0.48(C_3D_6).

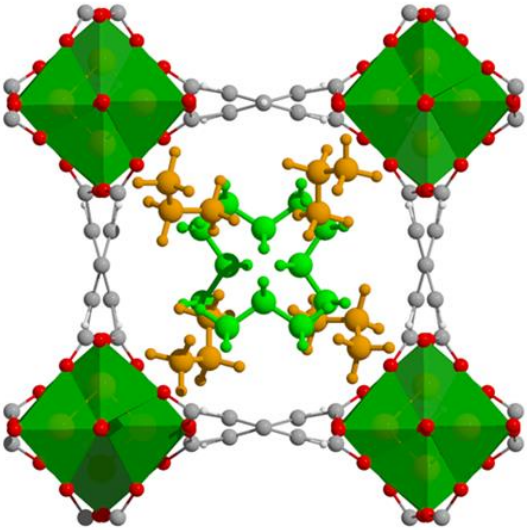

Supplementary Figure 5.27. NPD structure of MFM-300(In)·0.46(C_3D_8).

11. Inelastic Neutron Scattering Measurement

Inelastic neutron scattering (INS) experiments were undertaken using the TOSCA spectrometer at the ISIS Facility. MFM-300(In) was loaded into an 11 mm diameter vanadium sample can and outgassed at 1×10^{-7} mbar and 100 °C for 1 day. The sample was loaded into a helium closed cycle refrigerator (CCR) cryostat and cooled to 11 K for data collection. C_2H_2, C_2H_4 and C_2H_6 gas were introduced by warming the sample to 298 K and the gas was dosed volumetrically from a calibrated volume. The gas-loaded sample was then cooled to 7 K over a period of 2 h to ensure good mobility of adsorbed species within the crystalline structure of MFM-300(In). The sample was kept at 7 K for an additional 30 mins before data collection to ensure the thermal equilibrium.

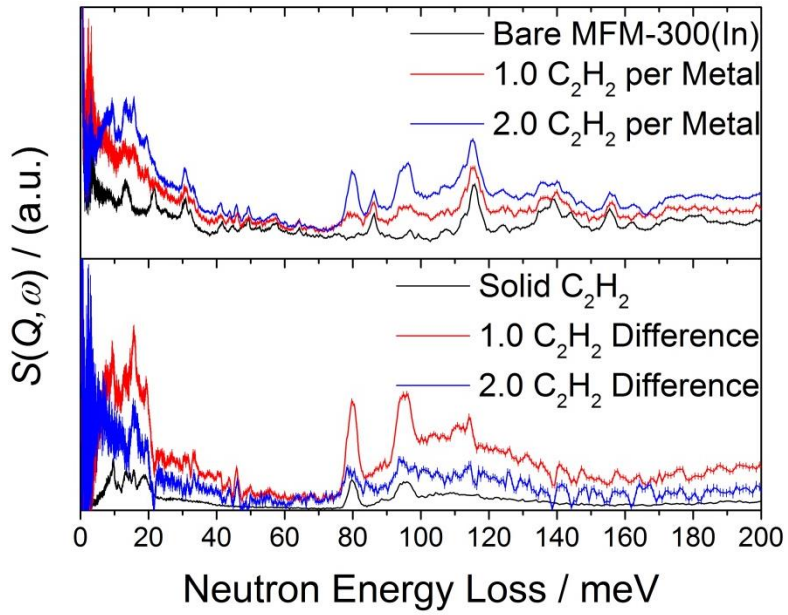

Supplementary Figure 5.28. Comparison of bare and C_2H_2 loaded MFM-300(In) (black: bare MFM-300(In); red: 1.0 C_2H_2 per metal; blue: 2.0 C_2H_2 per metal).

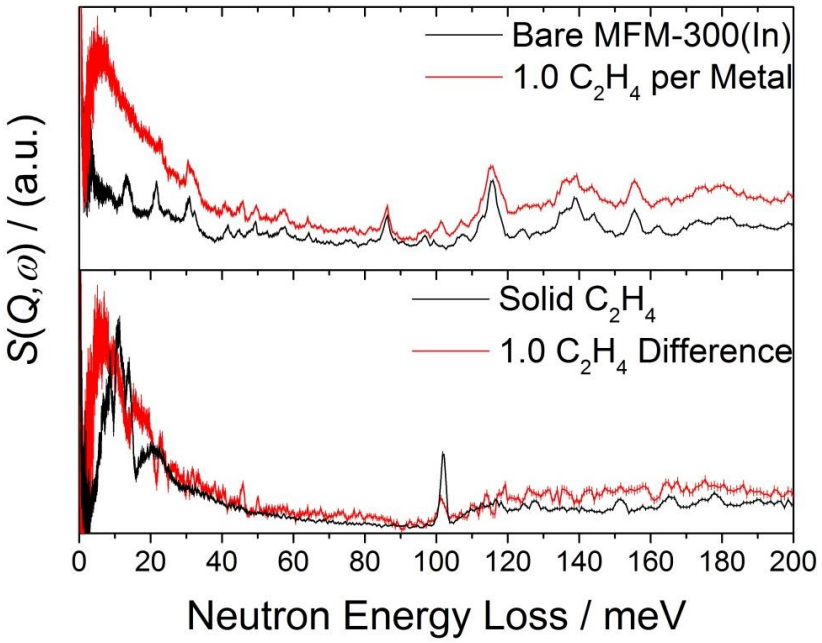

Supplementary Figure 5.29. Comparison of bare and C_2H_4 loaded MFM-300(In) (black: bare MFM-300(In); red: 1.0 C_2H_4 per metal).

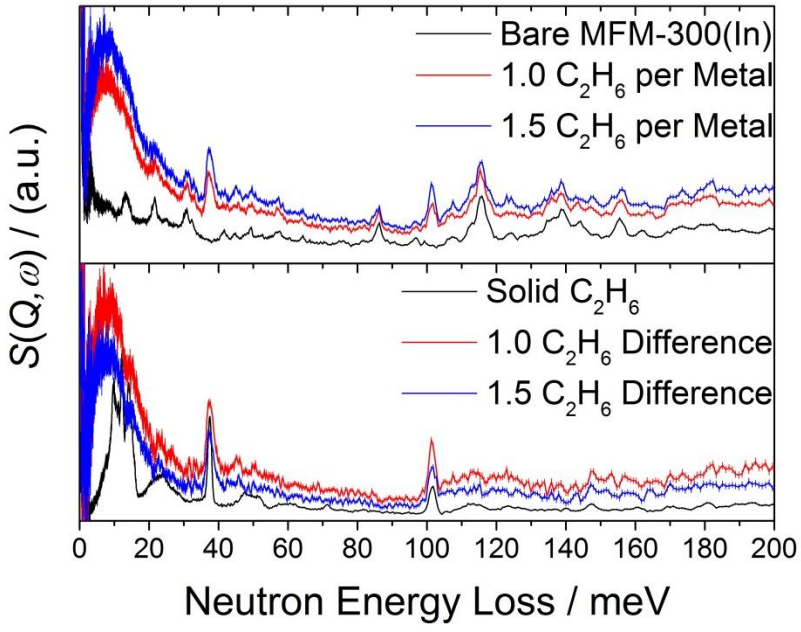

Supplementary Figure 5.30. Comparison of bare and C_2H_6 loaded MFM-300(In) (black: bare MFM-300(In); red: 1.0 C_2H_6 per metal; 1.5 C_2H_6 per metal).

12. Supplementary Tables

Supplementary Table 5.1. Physical parameters for C_2 and C_3 hydrocarbons.[2-8]

Gas	Molecular size (Å^3)	Boiling point (K)	Kinetic diameter (Å)
C_2H_2	3.3 × 3.3 × 5.7	188.40	3.3
C_2H_4	3.3 × 4.2 × 4.8	169.42	4.2
C_2H_6	3.8 × 4.1 × 4.8	184.55	4.4
C_3H_4	4.0 × 4.1 × 6.5	249.8	4.8
C_3H_6	4.2 × 5.3 × 6.4	225.46	4.7
C_3H_8	4.2 × 4.8 × 6.8	231.02	4.3-5.1

Supplementary Table 5.2. Dynamic adsorption of substrates on MFM-300(In) based on the breakthrough experiments.

	Amount adsorbed (mmol g^{-1})
C_2H_2	1.4
C_2H_4	1.0
C_2H_6	1.6
C_3H_4	4.4
C_3H_6	3.5
C_3H_8	3.1
C_2H_4 in equimolar C_2H_6/C_2H_4 mixture	0.7
C_2H_6 in equimolar C_2H_6/C_2H_4 mixture	1.4
C_3H_4 in equimolar C_3H_4/C_3H_6 mixture	4.6
C_3H_6 in equimolar C_3H_4/C_3H_6 mixture	3.1

Supplementary Table 5.3. Comparison of separation performance for several reported MOFs.

MOF	Pore size (Å)	Pore volume (cm^3 g^{-1})	BET surface area (m^2 g^{-1})	Uptake (mmol g^{-1}) C_2H_6/C_2H_4	Selectivity C_2H_6/C_2H_4 : 50/50	Q_{st} (kJ mol^{-1}) C_2H_6/C_2H_4	C_2H_4 Productivity (L/kg)
MFM-300(In) This work	**6.8**	**0.43**	**1030**	**5.1/4.9 (293 K)**	**1.7**	**30/28**	**4.6 L/kg**
MFM-300(Al)[9]	6.5	0.43	1370	0.85/4.28 (293 K)	C_2H_6/C_2H_4=48.7		/
JNU-2[10]	3.4, 4.6, 6.7 Å	0.56	1219	4.19/3.68 (298 K)	1.6	/	21.2 L/kg
TJT-100[11]	8.7 × 11.6	0.39	890	~3.66/3.4 (299 K)	1.2	29/25	/
IRMOF-8[12]	17.5	0.69	1360	2.16/1.25 (298 K)	1.8	52.5/50	2.5 L/kg
PCN-250[13]	5.9, 6.8, 9.3	0.56	1470	5.21/4.22 (298 K)	1.9	23/21	10 L/kg
MUF-15[14]	8.5 × 3.5, 7 × 3.8, 3.2 × 1.2	0.51	1130	4.69/4.15 (293 K)	1.96	28.2/29.2	14 L/kg
$Cu(Qc)_2$[15]	3.3	0.11	240	1.85/0.78 (298 K)	3.4	29/25.4	4.3 L/kg
$Ni(bdc)(ted)_{0.5}$[16]	7.94	0.79	1701	5.0/3.4 (298 K)	2	21.5/18.2	/
PCN-245[17]	10	0.71	1743	3.27/2.39 (298 K)	1.9	20.5/23.0	5.8 L/kg
$Fe_2(O_2)$dobdc[18]	/	/	1073	3.45/2.68 (298 K)	4.4		19.3 L/kg
ZIF-4[19]	/	0.38	300	2.3/2.2 (293 K)	1.7	/	
ZIF-8[20]	3.4	0.73	1844	2.54/1.5 (293 K)	1.8	17.2/16.1	/

Supplementary Table 5.4. Host–Guest Interactions in MFM-300(In)·1.32(C_2D_2).

MFM-300(In)·1.32(C_2D_2)	Interactions	Distances (Å)	Colour
Site I	H (HO-In)···C≡C (site I)	2.52(1)	Violet
	H (site I)···C≡C (site II)	3.73(1)	Bright green
	C≡C (site I)···phenyl groups	3.83(1)	Orange
		4.04(1)	
Site II	C≡C (site II)···H (site I)	3.73(2)	Bright green

Supplementary Table 5.5. Host–Guest Interactions in MFM-300(In)·1.66(C_2H_4).

MFM-300(In)·1.66(C_2H_4)	Interactions	Distances (Å)	Colour
Site I	H (HO-In)···C=C (site I)	3.85(1)	Violet
	H (site I)···C=C (site II)	3.91(1)	Bright green
		4.01(1)	
	H (site I)···phenyl groups	2.92(1)	Orange
		3.03(1)	
		3.73(2)	
		4.40(1)	
Site II	C=C (site II)···H (site I)	3.91(1)	Bright green
		4.01(1)	
	H (site II)···phenyl groups	4.27(1)	Pink

Supplementary Table 5.6. Host–Guest Interactions in MFM-300(In)·0.72(C_2H_6).

MFM-300(In)·0.72(C_2H_6)	Interactions	Distances (Å)	Colour
Site I	H (HO-In)···C (site I)	3.22(2)	Violet
	H (site I)···C (site II)	2.99(4)	Bright green
	H (site I)···phenyl groups	2.65(2)	Orange
		3.30(2)	
		3.68(1)	
		4.18(2)	
Site II	C (site II)··· H (site I)	2.99(4)	Bright green

Supplementary Table 5.7. Host–Guest Interactions in MFM-300(In)·0.2(C_3H_4).

MFM-300(In)·0.2(C_3H_4)	Interactions	Distances (Å)	Colour
Site I	H (HO-In)···C_3D_4	3.26(6)	Violet
	H (site I)···phenyl groups	3.18(6)	Orange
	C≡C (site I)··· phenyl groups	3.56(1)	Green

Supplementary Table 5.8. Host–Guest Interactions in MFM-300(In)·0.48(C_3H_6).

MFM-300(In)·0.48(C_3H_6)	Interactions	Distances (Å)	Colour
Site I	H (HO-In)···C=C (site I)	3.37(1)	Violet
	H (site I)···phenyl groups	3.03(2)	Orange
		4.17(2)	
	C=C (site I) ··· phenyl groups	3.89(1)	Blue
Site II	C=C (site II)··· H (site I)	1.91(2)	Bright green
	H (siteII)···phenyl groups	4.07(1)	Orange

Supplementary Table 5.9. Host–Guest Interactions in MFM-300(In)·0.46(C_3H_8).

MFM-300(In)·0.46(C_3H_8)	Interactions	Distances (Å)	Colour
Site I	H (HO-In)···C (site I)	2.72(2) Å	Violet
	H (site I)···C (site II)	2.92(2)	Bright green
	C (site I)···H (site II)	3.19(2)	
	H (siteI)···phenyl groups	3.17(2)	Orange
		4.87(2)	
		4.02 (2)	
		3.37(2)	
Site II	C (site II)···H (site I)	2.92(2)	Bright green
	C (site I)···H (site II)	3.19(2)	
	H (site II)··· phenyl groups	3.35(1)	Pink
		3.02(1)	

13. Supplementary References

1. Savage, M.; Cheng, Y.; Easun, T.; Eyley, J.; Argent, S.; Warren, M.; Lewis, W.; Murray, C.; Tang, C.; Frogley, M.; Cinque, G.; Sun, J.; Rudic, S.; Murden, R.; Benham, M.; Fitch, A.; Blake, A.; Ramirez-Cuesta, A.; Yang, S.; Schröder, M. Selective adsorption of sulfur dioxide in a robust metal–organic framework material. *Adv. Mater.* **2016**, *28*, 8705–8711.
2. Li, J.; Kuppler, R.; Zhou, H. Selective gas adsorption and separation in metal–organic frameworks. *Chem. Soc. Rev.* **2009**, *38*, 1477–1504.
3. Geng, S.; Lin, E.; Li, X.; Liu, W.; Wang, T.; Wang, Z.; Sensharma, D.; Darwish, S.; Andaloussi, Y.; Pham, T.; Cheng, P.; Zaworotko, M.; Chen, Y.; Zhang, Z., Scalable room-temperature synthesis of highly robust ethane-selective metal–organic frameworks for efficient ethylene purification. *J. Am. Chem. Soc.* **2021**, *143*, 8654–8660.
4. Wang, S.; Wang, F.; Dong, Y.; Shivanna, M.; Dong, Q.; Mu, X.; Duan, J.; Yang, Q.; Zaworotko, M.; Yang, Q. Reversed C_2H_6/C_2H_4 separation in interpenetrated diamondoid coordination networks with enhanced host–guest interaction. *Sep. Purif. Technol.* **2021**, *276*, 119385.
5. Liu, P.; Wang, Y.; Chen, Y.; Yang, J.; Wang, X.; Li, L.; Li, J. Construction of saturated coordination titanium-based metal–organic framework for one-step $C_2H_2/C_2H_6/C_2H_4$ separation. *Sep. Purif. Technol.* **2021**, *276*, 119284.
6. Gao, J.; Qian, X.; Lin, R.; Krishna, R.; Wu, H.; Zhou, W.; Chen, B. Mixed metal–organic framework with multiple binding sites for efficient C_2H_2/CO_2 separation. *Angew. Chem. Int. Edit.* 2020, *59*, 4396–4400.
7. Ding, Q.; Zhang, Z.; Yu, C.; Zhang, P.; Wang, J.; Kong, L.; Cui, X.; He, C. H.; Deng, S.; Xing, H., Separation of propylene and propane with a microporous metal–organic framework via equilibrium–kinetic synergetic effect. *AIChE J.* **2020**, *67*, 17094.
8. Kim, S.; Lee, P.; Chang, J.; Nam, S.; Park, Y. Preparation of carbon molecular sieve membranes on low-cost alumina hollow fibers for use in C_3H_6/C_3H_8 separation. *Sep. Purif. Technol.* **2018,** *194*, 443–450.
9. Yang, S.; Ramirez-Cuesta, A.; Newby, R.; Garcia-Sakai, V.; Manuel, P.; Callear, S.; Campbell, S.; Tang, C.; Schröder, M. Supramolecular binding and separation of hydrocarbons within a functionalized porous metal–organic framework. *Nat. Chem.* **2015**, *7*, 121–129.
10. Zeng, H.; Xie, X. J.; Xie, M.; Huang, Y. L.; Luo, D.; Wang, T.; Zhao, Y.; Lu, W.; Li, D., Cage-Interconnected Metal-Organic Framework with Tailored Apertures for Efficient C_2H_6/C_2H_4 Separation under Humid Conditions. *J. Am. Chem. Soc.* **2019**, *141*, 20390–20396.
11. Hao, H. G.; Zhao, Y. F.; Chen, D. M.; Yu, J. M.; Tan, K.; Ma, S.; Chabal, Y.; Zhang, Z. M.; Dou, J. M.; Xiao, Z. H.; Day, G.; Zhou, H. C.; Lu, T. B., Simultaneous Trapping of C_2H_2 and C_2H_6 from a Ternary Mixture of $C_2H_2/C_2H_4/C_2H_6$ in a Robust Metal–Organic Framework for the Purification of C_2H_4. *Angew. Chem. Int. Edit.* **2018**, *130*, 16299–16303.
12. Pires, J.; Pinto, M. L.; Saini, V. K., Ethane Selective IRMOF-8 and its Significance in Ethane-Ethylene Separation by Adsorption. *ACS Appl. Mater. Interfaces* **2014**, *6*, 12093–12099.
13. Chen, Y.; Qiao, Z.; Wu, H.; Lv, D.; Shi, R.; Xia, Q.; Zhou, J.; Li, Z., An Ethane-Trapping MOF PCN-250 for Highly Selective Adsorption of Ethane over Ethylene. *Chem. Eng. J.* **2018**, *175*, 110–117.

14. Qazvini, O. T.; Babarao, R.; Shi, Z. L.; Zhang, Y. B.; Telfer, S. G., A Robust Ethane-Trapping Metal-Organic Framework with a High Capacity for Ethylene Purification. *J. Am. Chem. Soc.* **2019**, *141*, 5014–5020.
15. Lin, R. B.; Wu, H.; Li, L.; Tang, X. L.; Li, Z.; Gao, J.; Cui, H.; Zhou, W.; Chen, B., Boosting Ethane/Ethylene Separation within Isoreticular Ultramicroporous Metal-Organic Frameworks. *J. Am. Chem. Soc.* **2018**, *140*, 12940–12946.
16. Liang, W.; Xu, F.; Zhou, X.; Xiao, J.; Xia, Q.; Li, Y.; Li, Z., Ethane Selective Adsorbent Ni(Bdc)(Ted)$_{0.5}$ with High Uptake and Its Significance in Adsorption Separation of Ethane and Ethylene. *Chem. Eng. J.* **2016**, *148*, 275–281.
17. Lv, D.; Shi, R.; Chen, Y.; Wu, Y.; Wu, H.; Xi, H.; Xia, Q.; Li, Z., Selective Adsorption of Ethane over Ethylene in PCN-245: Impacts of Interpenetrated Adsorbent. *ACS Appl. Mater. Interfaces* **2018**, *10*, 8366–8373.
18. Li, L.; Lin, R. B.; Krishna, R.; Li, H.; Xiang, S.; Wu, H.; Li, J.; Zhou, W.; Chen, B., Ethane/Ethylene Separation in a Metal-Organic Framework with Iron-peroxo Sites. *Science* **2018**, *362*, 443–446.
19. Hartmann, M.; Bohme, U.; Hovestadt, M.; Paula, C., Adsorptive Separation of Olefin/Paraffin Mixtures with ZIF-4. *Langmuir* **2015**, *31*, 12382–12389.
20. Bohme, U.; Barth, B.; Paula, C.; Kuhnt, A.; Schwieger, W.; Mundstock, A.; Caro, J.; Hartmann, M., Ethene/Ethane and Propene/Propane Separation via The Olefin and Paraffin Selective Metal-Organic Framework Adsorbents CPO-27 And ZIF-8. *Langmuir* **2013**, *29*, 8592–600.
21. Coelho, A. A., TOPAS And TOPAS-Academic: An Optimization Program Integrating Computer Algebra and Crystallographic Objects Written in C^{++}. *J. Appl. Cryst.* **2018**, *51*, 210–218.